

Institute of Geology named after Academician N.P. Yushkin
Komi Scientific Center of the Ural Branch
Russian Academy of Sciences

Manuscript copyright

Piskunova Natalia Nikolaevna

**Layer-by-layer growth and dissolution
of crystals on defects**

Scientific speciality 1.6.4. Mineralogy, crystallography.
Geochemistry, geochemical methods of mineral exploration.

Dissertation submitted for the doctoral degree in
geology and mineralogy

Translation from Russian

Scientific Advisor:
Doctor Sci.
in Geology and Mineralogy,
Academician of RAS
A.M. Askhabov

Syktvkar

2024

Table of contents

Introduction	4
 Chapter 1. Defect–assisted Crystal Growth and the History of its Study by AFM	
1.1 Defects. Layer-by-layer growth and dissolution on defects	14
1.2 Atomic force microscopy of crystal growth: new possibilities	19
1.3 Atomic force microscopy of crystal growth today	24
1.4 History of AFM studies of the growth-dissolution reversibility and the influence of mechanical impact during crystal growth	25
 Chapter 2. Experimental Modeling	
2.1 Instruments	29
2.2 Materials	31
2.2.1 Structure and properties of the model crystal	32
2.2.2 Solutions for experiments	35
2.3 Experimental methodology	
2.3.1 Conditions	43
2.3.2 Special mechanical impact. Methodology of sample preparation and AFM analysis	44
2.3.2.1 Growth and dissolution on the scratch.....	45
2.3.2.2 Incorporation of foreign particles.....	48
2.3.2.3 Growth in a limited space.....	50
2.3.2.4 Growth and dissolution on cracks.....	52
2.3.2.5 Methods of other <i>in-situ</i> experiments with special mechanical impact.....	52
2.4 Calculations of the growth rate and fluctuations	55
2.4.1 Obtaining data from AFM images	56
2.4.2 Accuracy of coordinate data	58
2.4.3 Optimization of the data production process	59
2.4.4 Calculation of the rate and its fluctuations	60
2.5 Artefacts. Instrumental influence on the surface processes and correctness of experimental results	
2.5.1 Artefacts	64
2.5.2 Instrumental influence on the processes and layer-by-layer growth kinetic.....	68
2.6 Applicability of <i>in-situ</i> AFM results to reconstruction of crystal growth in nature	77
2.7 AFM–videos	80
 Chapter 3. <i>In-situ</i> AFM Experiments	
3.1 Transition from dissolution to growth through the saturation point	82

3.1.1 Pit on the screw dislocation	84
3.1.2 Hillock on the screw dislocation	92
3.1.3 Influence of diffusion and convection	98
3.1.4 Transition from dissolution to growth through the saturation point. Conclusions	104
3.2 Dynamics and kinetics of layer-by-layer growth and dissolution without mechanical impact	
3.2.1 Growth of monomolecular steps on screw dislocations	106
3.2.2 Growth of macrosteps and large hillocks	118
3.2.3 Dissolution without mechanical impact	123
3.3 Effect of scratches	
3.3.1 Effect of scratches on the surface dissolution	124
3.3.2 Effect of scratches on layer-by-layer growth characteristics	127
3.4 Incorporation of the solid foreign particles	134
3.4.1 Dislocation formation on the captured particle	135
3.4.2 Dislocation propagation through growth layers	139
3.4.3 Dislocation formation before cavity sealing	142
3.4.4 Mechanism of dislocation formation initiated by solid inclusion	143
3.4.5 3D reconstruction of inclusion in the crystal	149
3.4.6 Average growth rates and their fluctuations during solid particle capturing	150
3.5 Layer-by-layer growth processes at the crystal intergrowth boundary ...	153
3.6 Processes of layer-by-layer growth and dissolution in the crack area	167
3.7 Observation of a constrained crystal face in solution	177
3.8 Processes of layer-by-layer growth (regeneration) and dissolution on the cleavage surface. Influence of neighboring crystals	184
 Chapter 4. <i>Ex-situ</i> AFM study of Mineral Crystals: Evidence of Growth and Dissolution on Defects	190
 Conclusion	204
References	208

Introduction

Relevance of the Research. The processes that take place on the growing crystalline surface, the successive growth of which completely determines the internal structure and controls the defectiveness of the crystal, have long attracted the attention of specialists. The study of the morphology of natural crystals and the observation of crystallisation processes under laboratory conditions almost immediately confirmed the layered nature of surface growth, which soon led to the discovery of screw dislocations as one of the main causes of the formation of layers on the surface (Frank, Read, 1950, Forty, 1954, Lemmlein, Dukova 1956, Frank, 1958). The next major step was the development of methods that allowed us to detail the structure of layers, to determine the mechanisms of their behaviour during growth and dissolution at the micro level (Lemmlein, 1973, Chernov et al., 1980 a, 1980 b, Chernov et al. 1986). A breakthrough in the visualisation of the relief of growing crystal surfaces was the advent of atomic force microscopy (AFM), which made it possible to obtain nanoscale and molecular relief of the crystal surface directly during their growth and dissolution (Malkin et al., 1996, Pina et al., 1998 a,b, Kuznetsov et al., 1999, Land et al., 1999). The use of AFM has allowed direct observation of theoretically predicted structural components of layer-by-layer growth, such as screw dislocation channels (De Yoreo, 1997 a). With its help, processes that had previously been the subject of purely theoretical analysis were recorded: the formation and evolution of dislocation spiral mounds on the crystal face, the movement of steps of elementary height for a given substance, the interaction of steps with each other and with impurities, the formation and decay of macrosteps (Vekilov, Alexander, 2000, De Yoreo et al., 2001, Gvozdev, 2001, Rashkovich et al., 2002, McPherson et al., 2003).

Direct observations of such processes are necessary to complement existing theoretical mechanisms of various crystal growth phenomena and to develop new ones. The AFM method is currently the only way to obtain information about crystallogenic processes occurring on the surface at the nano- and molecular scale. Direct monitoring of processes at the elementary scale is also important for solving problems of

crystallogenic modelling and industrial production of the required quality crystals for various industries, from energy and optoelectronics to pharmaceuticals (Nelea et al., 2021, Pampudi et al., 2021, Shtukenberg et al., 2022, Nakano et al., 2022). Deciphering the mechanisms of crystal dissolution at the nanoscale under the influence of various factors can help solve the pressing problem of non-toxic dissolution of mineral deposits for the purpose of environmentally friendly nature management (Dong et al., 2020, Geng et al., 2021, Chalina et al., 2022, Miyata et al., 2022, Chasnitsky et al., 2023).

Direct observations of growth at the nanoscale are also relevant to the genetic interpretation of the growth relief of the surface of mineral crystals. The surfaces of natural crystals are difficult to study at this level, and reconstructing the conditions of their formation is difficult due to the many factors that must be taken into account, including the complex composition of the environment, mechanical action, PT conditions, and many more. A growth experiment is designed to determine the influence of individual conditions, in order to extend the research possibilities by adding other factors. An interesting task in this respect is to determine the dynamic and kinetic patterns of movement of elementary layers under the influence of various mechanical factors. During their formation, mineral crystals come into contact with each other and with mechanical impurities, rest against the walls of cavities, crack and are subject to other mechanical influences. While researchers are at least somewhat familiar with live images of such processes in the optical regime, it is rare to trace them at the unit cell scale (Elhadj et al., 2008, Zhong et al., 2018, Zareepolgardani et al., 2019). Obtaining correct AFM images for such processes, interpreting the detected phenomena taking into account artefacts, and calculating various kinetic parameters based on AFM data will help to establish fundamental patterns of crystal growth, replenish the scientific base for reconstructing similar processes during mineral formation, and develop methods for the efficient use of mechanical factors for crystal growth technology.

Objectives of the Research:

- (1) Selection of model crystals, adaptation of the atomic force microscopy method to visualise and record their surface topography at the nanoscale during growth and

dissolution from solutions (in situ). Conducting methodical experiments to determine the instrumental influence on surface processes for a specific substance.

(2) Experimental modelling of the effect of various mechanical factors on the crystal surface in solution using atomic force microscopy and obtaining an adequate representation of nano- and micro-scale processes in the area of scratches, cracks, at the boundary of intergrowth of individuals, in the area of capture of large solid impurities, in confined conditions, at the surface of a fracture, etc.

(3) Analysis of the experiments: determination of the characteristics of the registered phenomena, comparison with literary examples, development of the mechanisms of the phenomena.

(4) Extraction of kinetic features of step motion from finished AFM images in sufficient quantity for statistical processing. Data processing and analysis of the experiments in the light of the results obtained.

(5) To carry out an ex situ study of the elementary relief of the growth surfaces of natural crystals based on the results of the in situ experiments.

(6) Production of videos based on AFM images for use in the educational process.

Objects and Methods of the Research. Atomic force microscopy is the main method of this work, and all direct observations of growth and dissolution processes have been made on model crystals of dioxidine (hydroxymethylquinoxaline dioxide) $C_{10}H_{10}N_2O_4$ using an atomic force microscope Ntegra Prima (NT-MDT, Russia). It was also used to study the growth surfaces of natural crystals of quartz, pyrite, topaz, alabandine, zircon and phenacite, kindly provided by colleagues listed in the *Conclusion* in *Acknowledgements* section. In addition to the AFM, the equipment of the Centre for Collective Use "Geoscience" (Syktyvkar), listed at the beginning of the *Methods* chapter (26 p.), was also used.

Scientific novelty of the study.

(1) In each of the experiments presented in the thesis, the novelty is determined by the fact that specific nanoscale growth and dissolution phenomena have been recorded and their mechanisms subsequently described. Some phenomena have been observed

for the first time at the nanoscale. For example, the process of dislocation growth through the massive layers covering it has been filmed step by step.

(2) For the first time, direct AFM observations were made of layer-by-layer processes at the fusion boundary of individuals, in the region of cracks and on faces compressed from opposite sides. The occurrence of different types of defects under such influences was recorded, and their significant influence on the surface morphology, dynamics and kinetics of micro- and nanoscale processes was demonstrated.

(3) A three-stage mechanism for the appearance of a screw dislocation initiated by an embedded impurity particle is proposed, consisting of stress relaxation around the particle by the formation of one or more dislocations before its overgrowth in the first stage, the joining of edge dislocations to them at the moment of overgrowth in the second stage, the appearance of the resulting dislocation and its growth through the covering layers in the third stage.

(4) An original method of extracting coordinate data from AFM images has been developed; the data obtained allow large-scale kinetic calculations to be carried out. It was found that scratching induces a fluctuation-dissipative restructuring of the surface and the appearance of self-oscillations of the rate, whereas a surface that has captured many solid particles is characterised by a smooth rate and small fluctuations.

(5) Growth and dissolution at the nanoscale have been shown to be non-reversible processes.

The practical relevance of the work is determined by the importance of the fundamentally new information obtained about micro- and nanoprocesses on growing crystal faces for the control of industrial crystal growth processes and the development of a scientific basis for the reconstruction of natural mineral formation processes. Understanding nano- and microscale crystal growth processes is the most important prerequisite for establishing fundamental patterns, constructing new concepts of mineral formation, and developing technologies for synthesising high quality, defect-free crystals for the optoelectronic and pharmaceutical industries.

Methods have been developed to determine, using AFM, the influence on surface processes of 1) short term mechanical action with formation of scratches; 2) large impurity particles; 3) cracks; 4) neighbouring crystals in intergrowths; 5) compression of the crystal face from different sides. Such studies can contribute to the development of a scientific basis for the use of mechanical factors to accelerate desirable and suppress undesirable crystallisation in various areas of industry.

A new model object, dioxide, has been introduced into the practice of growth experiments. It is accessible and easy to use. For the first time, solubility values at different temperatures and data on the viscosity of its saturated and unsaturated solutions have been obtained.

As an example of the direct application of research results, 9 digital films made from AFM data demonstrating various crystal growth phenomena are used in educational programmes at Syktyvkar State University. The videos are available via the link and QR code:

<https://geo.komisc.ru/divisions/laboratory/experimental-mineralogy-laboratory?view=article&id=759:piskunova&catid=189:experimental-mineralogy-laboratory>



Research Approbation. The results of various sections of the work carried out since 2008 were reported personally by the author at the mineralogical seminars of the Syktyvkar branch of the Russian Mineralogical Society, at the Geological Congresses of the Komi Republic in 2009, 2014 and 2019, at the International Mineralogical Seminars and All-Russian Mineralogical Seminars with International Participation held in Syktyvkar in 2009, 2010, 2011, 2012, the Mineralogical Seminars with International Participation "Yushkin's Readings" held in Syktyvkar in 2013, 2016, 2018, 2022, at the 16th International Conference on Crystal Growth in Beijing (2010), the 22nd Congress of the International Crystallographic Union in Madrid (2011), the First European Mineralogical Conference in Frankfurt am Main (2012), the 17th International Conference on Crystal Growth and Epitaxy in Warsaw (2014), the International Congress on Microscopy in Manchester (2014), the International Scientific Conference

"Fedorovskaya Session" and the Annual Meetings of the RMS in St. Petersburg in 2016, 2017 and 2023, the International Scientific Conference on Scanning Probe Microscopy in Yekaterinburg (2019), the 18th Russian Meeting on Experimental Mineralogy in Irkutsk (2022), the 13th All-Russian School of Young Scientists on Experimental Mineralogy, Petrology and Geochemistry in Chernogolovka (2022), the All-Russian Seminar on Experimental Mineralogy, Petrology and Geochemistry VESEMPG in Moscow (2023) and the 20th International Meeting on Crystal Chemistry, X-ray Diffraction and Spectroscopy of Minerals in St. Petersburg (2024).

Publications. 59 works works related to the topic of the dissertation have been published on, including a monograph, sections in 6 collective monographs (four are in English), 17 articles in peer-reviewed scientific journals (15 articles in journals belonging to the Scopus and Web of Science list) and 35 proceedings of Russian and international conferences.

Personal contribution of the author. The author is responsible for setting up the tasks, developing the methods and performing the *in-situ* and *ex-situ* AFM experiments, collecting and processing the kinetic data, interpreting the results and making videos. Until 2021 the experiments were performed with the help of AFM operator V. A. Radaev, later the author became the AFM operator himself.

Scope and structure of the dissertation. The dissertation contains the following sections: "Introduction"; "Chapter 1. Defect-stimulated crystal growth and the history of its study using AFM"; "Chapter 2. Experimental methodology"; "Chapter 3. *In-situ* experiments using AFM", which presents the results of 44 experiments ranging from 1.5 to 6 hours; "Chapter 4. *Ex-situ* AFM study of mineral crystals"; "Conclusion" and "List of References", including 199 sources, 33 of which are Russian and 166 – in English. The dissertation is presented on 229 pages, illustrated with 2 tables and 132 figures.

Main scientific results:

(1) The work significantly expanded the possibilities of AFM studies of growth processes, including modelling the influence of various factors on them and interpretation of the observed patterns, detailed analysis of the types of artifacts, assessment of the instrumental influence on surface growth and dissolution processes, methods for calculating kinetic characteristics based on AFM data have been developed (Piskunova, Rakin, 2005 (P. e1662), Piskunova, Askhabov, 2007 (P. 1290-1292), Piskunova, 2010 (P. 198, 199), Piskunova, 2018 c (P. 98, 99), Piskunova, 2024 b (P. 3, 4, 11)).

(2) For the first time, the process of dislocation growth (inheritance) through massive growth layers covering it was recorded at the nanoscale. The mechanism of this phenomenon consists in the transfer of stresses in the form of plastic deformations (shear) along the dislocation line from the depth of the crystal to the nearest point of the free surface and the stopping at this point of a small segment of the step, which wraps around it and forms a new screw mound (Piskunova, 2023 (P. 86), Piskunova, 2023 (P. 5)).

(3) The transition from dissolution to growth through the saturation point was followed on the steps of the same dislocation pit and on the monomolecular steps of the same dislocation mound. It has been shown that, technically, during growth the substance is not always incorporated in the same places on the surface from which it was removed during dissolution, due to the presence and type of defects (Piskunova, 2024 b (P. 5, 7)).

(4) Growth and dissolution have been shown to be irreversible, non-equivalent processes at the nanoscale in both dynamics and kinetics. With a smooth transition from dissolution to growth, complete non-equivalence of tangential and normal rates at the same monomolecular steps has been established. Growth and dissolution are also not comparable in terms of the nature of the rate fluctuations (Piskunova, 2024 b (P. 9, 10)).

1. It has been found that the directed action of an AFM needle on the crystal surface with a force of only $\sim 10^{-7} - 10^{-6}$ N causes the appearance of grooves-scratches up to 1

micron wide in a slightly supersaturated dioxidine solution, which are caused by point defects created by the needle. Selective dissolution in the direction of needle movement in an undersaturated solution, as well as loss of morphological stability of the surface and dissolution events far from the contact zone in a supersaturated solution, indicate that shear stresses from the needle provoked the appearance of edge defects (Piskunova, Askhabov, 2017 (P. 165-167), Piskunova, 2021 (P.3, 7, 8)).

2. Kinetic calculations for the experiment on the growth of a dislocation mound showed that scratching its top provoked a fluctuation-dissipative rearrangement of the surface and the appearance of self-oscillations of rate (Piskunova, 2021 (P. 9, 10), Piskunova, 2022 (P. 123, 124)).

(5) In an AFM experiment on the trapping of solid foreign particles by a growing crystal at the nanoscale, the process of formation of a screw dislocation initiated by an impurity particle was recorded. To explain the process theoretically, a three-stage mechanism is proposed, which consists of stress relaxation around the impurity particle by forming one or more dislocations before its overgrowth in the first stage, joining edge dislocations to them at the time of overgrowth in the second stage, the appearance of the resulting dislocation and its growth after sealing the cavity with the particle in the third stage (Piskunova, 2023 a (P. 93)). It is shown that the entrapment of a large number of solid particles does not cause jumps in the rate of the steps in the scanning section or an increase in the rate fluctuations. The proposed mechanism allows to explain the paradoxical weak defectiveness of the surface and the whole crystal with a significant amount of trapped solid impurities. It is shown that a screw dislocation cannot form from the surface of a crystal as a result of misalignment of flat lattices during the counter-movement of steps of different heights or sagging (Piskunova, 2023 b (P. 6-8)).

3. In growth experiments on a specially created crack, its boundary is an obstacle to the passage of steps, due to screw dislocations that occur along it. AFM was used to record the appearance of screw dislocations along the entire boundary between crystals in the intergrowth, caused by the mutual pressure of the crystals. The crystal face constrained on both sides shows a distinct direction of step movement, both during

dissolution and during growth, which coincides with the direction of compression. The occurrence of edge dislocations was recorded along the compression direction. Thus, the special mechanical effect on the surface of the crystal in solution is accompanied by the occurrence of new point, linear and three-dimensional structural defects, which begin to significantly affect the surface morphology at the micro- and nanoscale, as well as the dynamics and kinetics of the crystallisation process (Piskunova, Askhabov, 2017 (P.165-167), Piskunova, 2024 a (P. 637-646)).

4. Ex situ AFM studies of the growth surfaces of several natural crystals have revealed identical evidence of defect-stimulated growth and dissolution at the nano- and microscale for crystals of different genesis - growth steps, including elementary ones, dislocation spiral hillocks and dissolution pits on defects (Treyvus, Piskunova et al, 2011b (P. 62, 63), Sokerina, Piskunova, 2011 (P. 183, 184), Sokerina et al., 2013 (P. 96, 97), Mashina et al., 2015 (P. 115-117), Perovsky, Piskunova, 2017 (P. 7-9), Piskunova, 2020 (P. 32), Piskunova, 2024 b (P. 634-636)).

Main provisions of the dissertation:

1. The influence of mechanical factors during crystal growth and dissolution at the micro- and nanoscale is expressed in the formation of various types of structural defects that impede the advancement of layers, are propagated through macrolayers, induce rate oscillations, stimulate the appearance of micro-sized pits both during dissolution and during growth, and lead to the loss of morphological stability of the surface far from the point of direct mechanical impact.
2. The appearance of a screw dislocation triggered by the trapping of an impurity particle is caused by the relaxation of stresses around the impurity particle through the creation of dislocations even before the cavity is sealed, and the propagation of the resulting dislocation after the particle is completely trapped. Growth involves the plastic transfer of stress through the cladding layers, the stopping of surface steps at a stress point and the twisting of the steps around this point into a screw hillock.
3. The array of coordinate values measured on successive AFM images of a real growth experiment is a source of information about the kinetic and dynamic patterns of layer-by-layer (dislocation) growth of crystals and the behaviour of the system as a whole on a time scale, allowing us to indicate self-organising processes for some systems, as opposed to other systems which have a smooth rate and small fluctuations.
4. The kinetic parameters and dynamics of the continuous transition from dissolution to growth through the saturation point on the same monomolecular steps indicate that growth and dissolution are non-reversible processes in the kinetic regime.

Chapter 1. Defect–assisted Crystal Growth and the History of its Study by AFM

1.1 Defects. Layer-by-layer growth and dissolution on defects

Defects associated with the crystal surface determine how that surface will grow or dissolve, especially in slightly supersaturated and slightly undersaturated solutions. In such solutions the surface grows by a layer-by-layer mechanism. Normal growth, where the surface grows at each of its points, was not observed in the work. Layer-by-layer growth is a sequential deposition of elementary or macrolayers of a substance in which growth steps spread out from growth centres (Figure 1.1). The latter may be screw dislocation exits to the surface or two-dimensional nuclei.

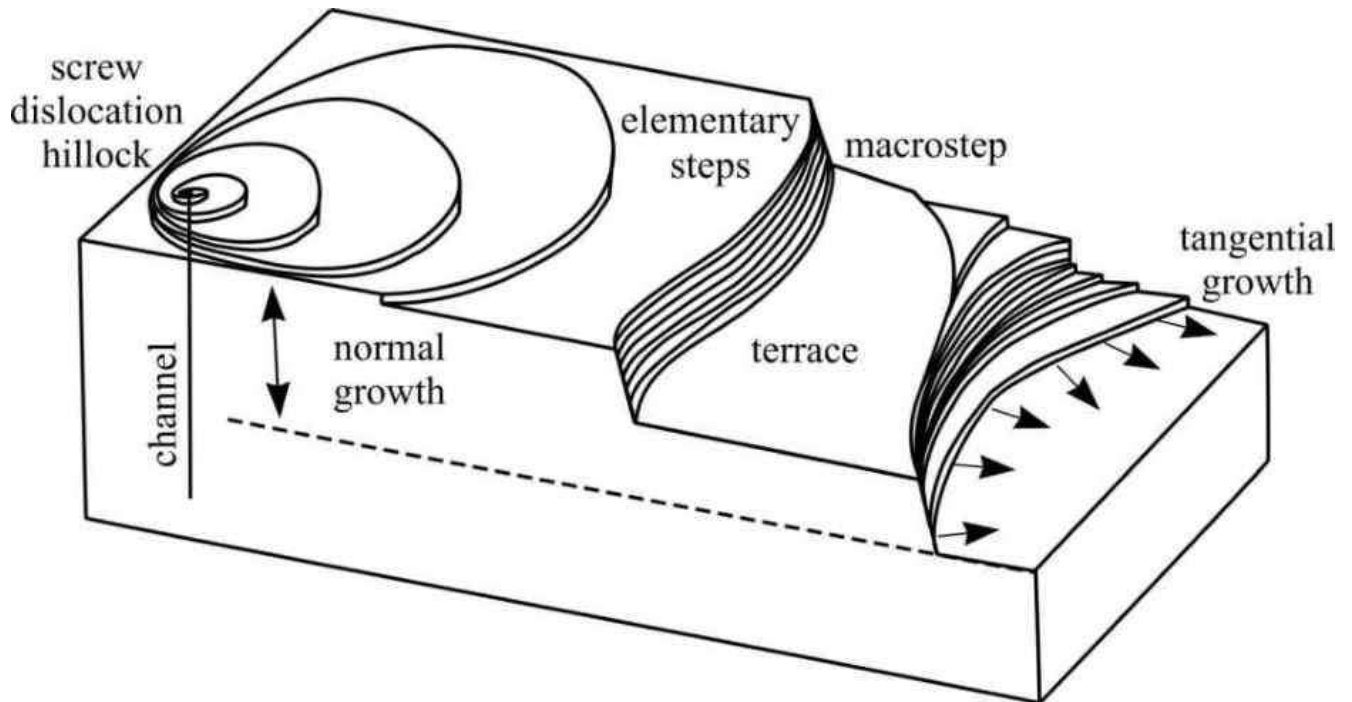


Figure 1.1 – Tangential and normal growth on a crystalline surface

The probability of two-dimensional nuclei appearing at supersaturations below 50% is low, whereas real crystals grow at the observed rates at supersaturations of 1% and below. At such supersaturations the layer-by-layer growth is exclusively dislocation in nature (Figure 1.1). The end of the step at the dislocation exit point is motionless; as

it grows, the step curls up around this point and takes the form of a spiral. From the centre of the spiral, new turns are constantly ejected, forming a hillock. If elementary steps (corresponding to the diameter of the smallest unit for a given substance, or one of the parameters of the crystal lattice, or the cluster size) or macrosteps are found on a surface, then the source of these steps – the dislocation exit – must be on that surface.

The edges of elementary steps (especially fractures) are the site of preferential attachment of building units. The more rounded the step, the more fractures it contains. At low supersaturations, building units do not join the terraces between the steps. The advance of the edge of the steps along the face is called as tangential growth, the general increase of the face upwards is called as normal growth. The English crystallographer Frederick Charles Frank is believed to have been the first to suggest in 1949 that surface growth should occur on the steps of the screw hillocks. However, it was Georgy Glebovich Lemmlein who, in 1945 in the Bulletin of the USSR Academy of Sciences (No. 4, p. 119), based on interferometric observations, described the discovered "spiral layers" as "the primary form of surface growth". In 1951, the well-known dislocation theory of growth was presented by Barton, Cabrera and Frank in *Philosophical Transactions A*.

Screw dislocations, like edge dislocations, are linear (one-dimensional) defects in the crystal structure. Two-dimensional defects include twin boundaries and the crystal surface itself is such a defect. Gas, gas–liquid and solid inclusions are volumetric (three-dimensional) defects. An edge dislocation is an extra half-plane inserted into the structure, or a shift in the plane of the lattice, while a screw dislocation is a perpendicular shift of a section of the lattice (Figure 1.2).

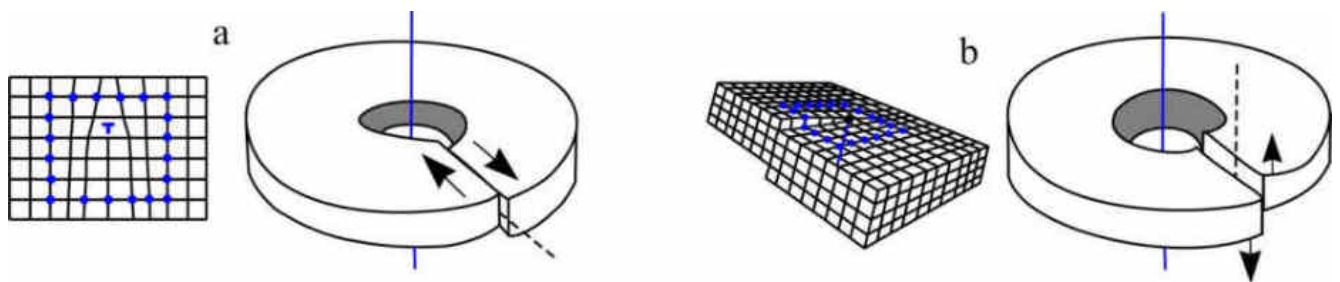


Figure 1.2 – Edge (a) and screw (b) dislocations as defects in the crystal structure

Plastic deformation, including that due to the mechanical effects considered in this work, is responsible for the appearance of edge and screw dislocations. An edge dislocation forming on the surface does not create a step, but a field of mechanical stress is created around it, increasing the free energy of this region of the crystal. At low supersaturations, these stressed regions are thermodynamically unstable: instead of growth, dissolution is observed. There is also lattice deformation around three-dimensional defects, which creates a stress field, and if the stresses during the capturing of these inclusions exceed certain critical values under certain conditions, screw dislocations can be formed from such inclusions. In the stress region, the chemical potential for the addition of a substance is increased.

Attachment of substance to defects

The chemical potential is the adiabatic energy of adding a particle to a system without doing work and is associated with the readiness of a substance to change from one state to another. In the region of a point defect, edge dislocation or the exit point of a screw dislocation, the chemical potential will be higher than on an ideal surface. This is due to the energy of the particles already there. Particles on the surface have increased energy because they realise only part of the possible interactions (chemical bonds) and have excess potential (free) energy in the field of action of asymmetric attractive forces. In addition, there is an excess of kinetic (thermal) energy due to the greater mobility of the particles near the surface. When a dislocation occurs (D in Figure 1.3), such increased energy is also acquired by particles along the line or plane of shear, it is even greater than that of the surface particles, since along the dislocation line the stresses can spread over several layers. The resultant of the forces acting on a molecule in the surface layer ("2" and along the dislocation "3" in Figure 1.3) is directed inwards, and the interaction of the molecules with their neighbours in the volume ("1") is approximately equivalent. But the particles along the line (or plane) of the dislocation on the surface itself ("4" in Figure 1.3) have the highest energy for the same reasons. The presence of uncompensated attractive forces at the surface leads to the appearance

of a tangential force (together with excess surface energy). This force is called surface tension and prevents the interphase surface from expanding. Uncompensated bonding in the dislocation channel region also involves surface tension. The interface at the exit of the channel is curved, and the action of the surface tension forces there leads to the appearance of a difference in normal pressures in the phases, which depends on the intensity of the surface tension and on the principal radii of curvature of the surface. The surface tension in the region of the dislocation exit ("II" in Figure 1.3, right) is significantly greater than the surface tension on the surrounding surface ("I" in Figure 1.3, right) and the excess energy of the surface particles at the point of dislocation exit makes the addition of new material at this location extremely energy consuming.

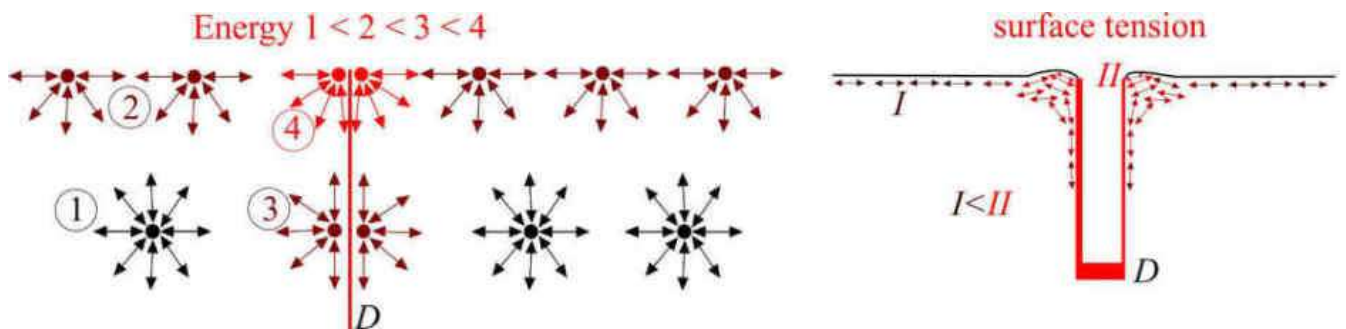


Figure 1.3 – Increased surface energy of particles (left) and increased surface tension (right) at the exit of a dislocation (D), preventing an increase in the interphase surface, i.e., the incorporation of the substance to the exit point of a dislocation during growth

Thus, during growth, the substance is not incorporated exactly into the defect area, but the separation of the substance during dissolution begins precisely at the defects. The formation of etch pits at these locations destroys the stress field and releases the energy of elastic deformation.

Detachment of the substance from the defects

Work of formation of hollow dissolution nuclei on dislocation ΔG_{real} and work on an ideal, undisturbed surface ΔG_{ideal} are related by the following expression (Heiman, 1975):

$$\Delta G_{real} = \Delta G_{ideal} \sqrt{1 - \xi}, \quad (1.1)$$

that is ΔG_{real} exactly by a $\sqrt{1 - \xi}$ less than on a perfect surface. Here ξ :

$$\xi = \frac{Gb^2h^2}{2\pi^2\rho^2\Omega} \Delta g \quad (1.2)$$

where G – dislocation shear modulus, ρ – specific free edge energy, h and r – depth and radius of the hollow nuclei, b – Burgers vector of a dislocation, Δg – change of the free enthalpy during dissolution, equal to $kT \ln(C_0/C)$ plus a parameter responsible for the lattice deformation, depending on the type of dislocation, T is the temperature, k – Boltzmann's universal constant, C and C_0 – the concentration of the solution near the defect is both equilibrium and Ω is the atomic volume.

For edge and screw dislocations the factor Δg is slightly different, but the general principle remains unchanged. At the slightest decreasing of the concentration C dissolution on defects quickly becomes predominant and intense, since ξ is proportionally to $\ln(C_0/C)$. The work required to produce a hollow dissolution nucleus on an ideal surface and at the exit of a dislocation is shown graphically in Figure 1.4.

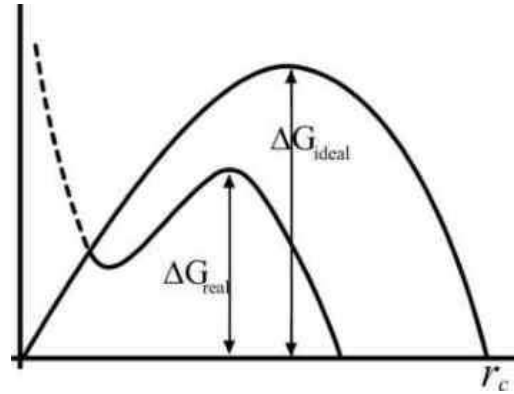


Figure 1.4 – Work of formation of a hollow nucleus on a dislocation ΔG_{real} is less of this kind of work on a perfect undisturbed surface ΔG_{ideal} (Johnston, 1962), which makes dissolution in the area of surface defects preferential

1.2 Atomic force microscopy of crystal growth: new possibilities

Until the 1980s, most growth observations were made using optical methods, the most common being the measurement of linear displacements of facets when viewed in profile. Such measurements gave an accuracy of 100–200 μm , and when analysing twenty times magnified profile prints using crystal defects as reference points, the accuracy was $\approx 3 \mu\text{m}$. The resolving power of Fourier spectroscopy in the near infrared was up to 25 μm (Maillard, 1972); such setups also allowed studies in liquids, but the resolution was significantly reduced. For direct growth observations, a high-temperature optical microscope and in-situ X-ray diffractometry have sometimes been used simultaneously (Aswal et al., 1998). In this case, objects no smaller than 10 μm were clearly visible in the photographic plane. The spatial resolution of in-situ X-ray topography methods is determined by the resolution of the photographic plates or imaging systems and is in the range of 1–50 μm . (Chirawa, 1974; Smolski et al., 1979; Chernov et al., 1980). For direct observations, an in-situ interference microscope (Rashkovich, Kronskey, 1997) and a method combining *in-situ* X-ray topography for studying the defect structure of crystals and a laser interference method for measuring the facet growth rate (Chernov et al., 1986) have also been successfully used. The resolution limit in the lateral plane of these methods allowed differentiation but did not allow detailed dislocation sources.

Atomic force microscopy has made significant advances in the phenomenological recording of crystal growth processes at the micro-, nano- and even atomic scale. In 1993, Hillner et al (1993) presented the first real-time AFM results. They measured the rate of step growth on calcite and fluorite, modelled surface poisoning by impurities and, for the first time, obtained atomic resolution for fluorite in solution. In 1996, Giocondi et al (1996) showed that the surface growth of 6H-SiC crystals from the gas phase occurs via a spiral mechanism. De Yoreo and co-authors performed AFM measurements of rates on the (101) face of KDP in a small range of solution supersaturations; they were the first to visualise theoretically

predicted screw dislocation channels with a width of units and a few tens of nanometres (De Yoreo et al., 1997a). In the same year, Hong and co-authors (Qi Hong et al., 1997) performed dissolution experiments in a liquid AFM cell with known hydrodynamics and simulated convection-diffusion. They showed the evolution of each dissolution pit with time in a solution flow. The authors found good quantitative agreement between the Barton-Cabrera-Frank theory data and direct AFM measurements. Also in 1997, the first publication by L.N. Rashkovich in collaboration with De Yoreo (De Yoreo et al., 1997b) appeared, after which AFM appeared at Moscow State University. In early 1998, Pina and co-authors studied the growth of the (001) face of barite crystals (Pina et al., 1998a). The growth steps on barite were found to be half the height of the unit cell, as predicted by Hartmann's theory of periodic chains of bonds (PCB) (Lemmlein, 1973). The authors followed two-dimensional nucleation and showed that the direction of step motion and the orientation of the two-dimensional islands depend on a specific crystallographic direction.

Further studies by Pina et al. (1998b) showed some limitations of the periodic chain and Barton-Cabrera-Frank theories. Then Teng et al. (1998) studied the surface area of growing calcite in a flowing solution, the dependence of the step rate on its length, and the dependence of the critical step length on supersaturation. They determined the effect of adding aspartic acid to the solution on the morphology and energy of the surface. They found that with the addition of acid, the hillock became asymmetric, the step corners became strongly rounded and the width of the terraces became smaller.

In late 1999, Land, De Yoreo and Martin demonstrated the structure of dislocation hillocks and step dynamics as a function of supersaturation on KDP surfaces, as well as the effect of impurities on step formation and movement (Land et al., 1999). In 1998, the first entirely russian paper on AFM crystal growth was published in English by L. N. Rashkovich, N. V. Gvozdev and I. V. Yaminsky (Rashkovich et al., 1998). The authors described the propagation of elementary

layers along the (010) face of a rhombic lysozyme crystal taken at molecular resolution.

In 2000, P. Vekilov's group (Yau et al., 2000) not only achieved molecular resolution on an apoferritin crystal, but also recorded the step-by-step process of incorporating a molecule into step fractures. They used a special manipulator to introduce a foreign molecule, creating a point defect in the apoferritin lattice. They calculated the rate fluctuations using AFM data (Vekilov, Alexander, 2000). At the same time, the growth of protein crystals, in particular enzymes, was studied (Kuznetsov et al., 1999; Malkin et al., 2001; Astier et al., 2001).

Shindo et al (2000) showed that molecular resolution can also be achieved on ionic crystals of NaCl and NaF using liquid AFM. The authors initiated the growth of a microcrystal at the pressure point by applying prolonged tip pressure to the surface of sodium fluoride. In 2000, L.N. Rashkovich, O.A. Shustin, and T.G. Chernevich determined the time dependence of the rate fluctuations of the steps on the faces of a prism and a bipyramid of potassium dihydrogen phosphate (KDP) crystals in solution in single-line scanning mode. During the experiment, the authors alternated between growth and dissolution so that the step was not lost from view. They showed that the fluctuations increased according to the law $t^{1/4}$ (where t is time) and not $t^{1/2}$ as for a single diffusing particle. The authors found that on the prism face the fluctuations are larger during dissolution than during growth (Rashkovich et al., 2000).

A little later, Bartelt et al. (2001) studied the surface dynamics during the growth of KDP from solution, as well as calcite, brushite, proteins and viruses. An unexpected result was the recovery of the surface in the "dead zone" with an increase in supersaturation, not by the movement of elementary steps (as predicted by the Cabrera-Vermilia models), but by the movement of macrosteps (the unification of hundreds of elementary steps) and supersteps (the unification of thousands of elementary steps).

For crystals such as insulin and canavaline in solution, molecular resolution was rapidly achieved even in the lateral plane, and many phenomena were recorded

during the interaction of steps, dislocation groups and two-dimensional islands (Land, De Yoreo, 2000; Waizumi et al., 2003).

Silnikova M.I. and Gvozdev N.V. studied the morphology and kinetics of lysozyme growth in 2001. They showed that there are no fundamental differences between the growth mechanism of lysozyme crystals in solution and crystals of low molecular weight compounds – both grow by a layered spiral mechanism (Silnikova, Gvozdev, 2001). In 2002, L.N. Rashkovich, N.V. Gvozdev, M.I. Silnikova and A.A. Chernov studied the formation of a dislocation spiral on the (101) face of the monoclinic modification of lysozyme and showed that the face grows by a dislocation mechanism and that the fluctuations in the rate of the steps are proportional to the fourth root of time (Rashkovich et al., 2002).

Direct visualisation of the growth of macromolecular crystals using AFM has been a powerful breakthrough in determining the mechanisms and kinetics of dislocation growth, the effect of impurities and defects on the growth and dissolution of crystals of proteins, nucleic acids and viruses (McPherson et al., 2003; Sours et al., 2005; Geng et al., 2005; Friddle et al., 2011).

The findings and regularities obtained have also been confirmed on inorganic substances, in particular analogues of natural crystals, which have helped to reconstruct the conditions of mineral crystal growth. It is not possible to achieve a wide range of pressure and temperature values in AFM, but the growth and dissolution of the most "amenable" minerals, such as calcite, brushite, aragonite, barite, etc., have been extensively studied using AFM (Stipp et al., 1994; Vavouraki et al., 2010; Wang, et al., 2011; Araki et al., 2012; Klasa et al., 2013; Kuwahara et al., 2016). Patricia Dove was one of the pioneers in this direction (Dove, Platt, 1996), and her group continues such studies today. A comprehensive review of AFM scanning of mineral surfaces is given in (Jupille, 2014).

AFM studies of growing crystals have shown that organic and inorganic crystals with any type of bonding – ionic, covalent or molecular – crystallising from solutions at up to 40 °C grow by screw dislocations (Figure 1.5), the polygonisation of the steps of which depends on the degree of supersaturation and syngony (De Ng

et al, 1997; Yoreo et al. 2001; McPherson et al. 2003; Shöâèè et al. 2008; Karino et al. 2008; Pers et al. 2016; Wenge et al. 2017; Putnis et al. 2021).

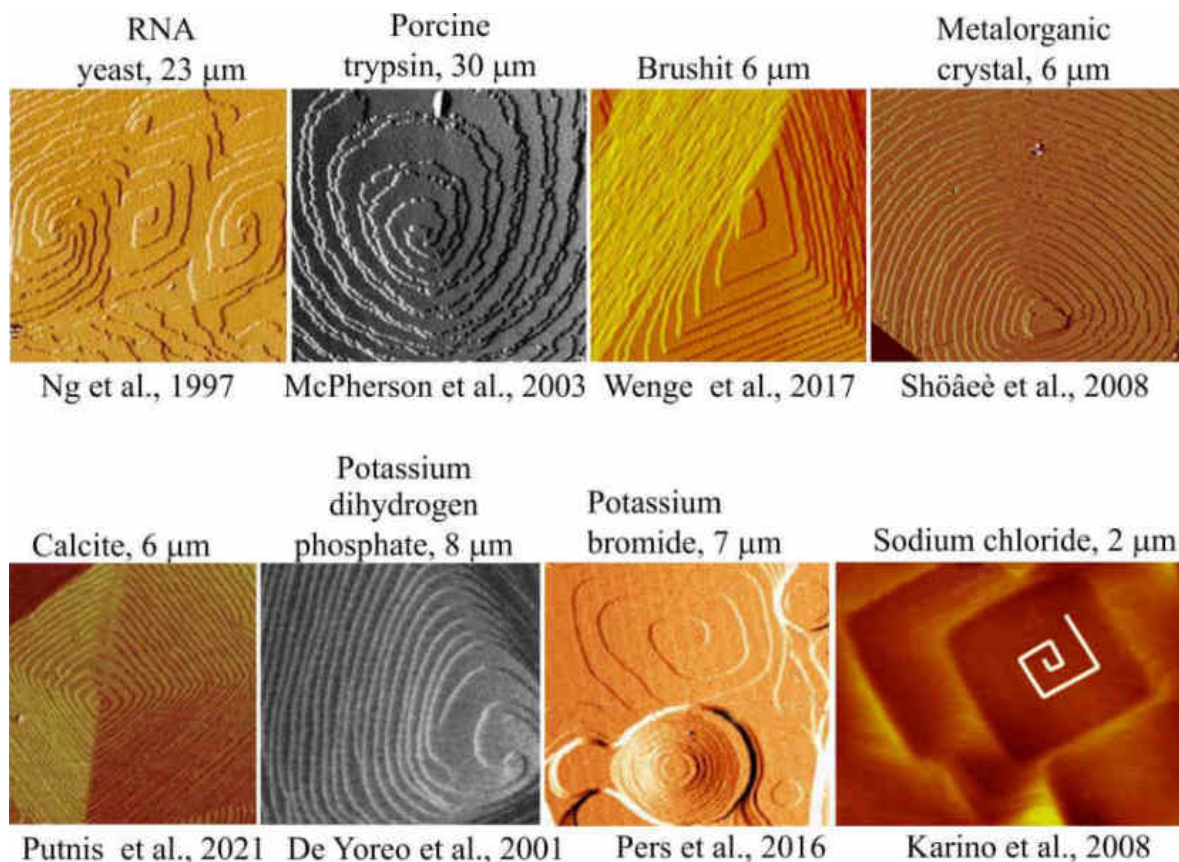


Figure 1.5 – AFM images of screw dislocations on different types of crystals (literature data). The scanning window width is indicated for each image

In Russia, growth experiments using atomic force microscopy in solution have been carried out at Moscow State University, St Petersburg State University and the Syktyvkar Institute of Geology (Piskunova, 2005, 2007, 2010). As shown above, the largest number of publications belongs to the group of L.N. Rashkovich of Moscow State University, whose assets include cooperation with world leaders in the field – J. De Yoreo, A.A. Chernov, P. Vekilov, K. Orme, N. Zaitseva, T.A. Land (Chernov et al., 2005; Chernov et al., 2007; Rashkovich et al., 2006). Under the supervision of L.N. Rashkovich and with the assistance of I. Yaminsky (Yaminsky et al., 2002; Yaminsky, 2004), N.V. Gvozdev defended his Ph.D. thesis on AFM crystal growth. (Gvozdev, 2001) and Petrova E.V. (Petrova, 2004).

At St. Petersburg State University, under the supervision of A.E. Glikin, the difficult to observe processes of metasomatic replacement and mixed crystallisation were recorded using AFM (Glikin, 2007; Glikin et al., 2010), including in collaboration with the Institute of Crystallography (Voloshin et al., 2003) and foreign researchers (Woensdregt, Glikin, 2005).

1.3 Atomic force microscopy of crystal growth today

AFM experiments are currently being carried out on both polymer and organic crystals to explore their potential as organic semiconductors, solar cells, field effect transistors, etc. (Chakrabarti, 2021; Zhang et al., 2020; Nelea, 2021; Chi, 2021). The growth of organometallic crystals for medical applications will be investigated (Pambudi, 2021). There are AFM data on the effect of blocking proteins on ice crystal growth, which partially explains the mechanism of survival of organisms in ice (Chasnitsky, 2023). In the field of mineralogy, dissolution experiments are underway (Liu, 2023), including calcite dissolution, to explain one of the most important processes of post-growth mineral transformation (Gershonowitz, 2019; Miyata et al., 2022; Cho et al., 2021). AFM has successfully modelled the removal of chromium from the environment via incorporation into growing calcite (Gurena, 2020), and the dissolution of calcite in seawater has been studied to elucidate the mechanism of this natural reaction that helps regulate atmospheric CO₂ (Dong, 2020). The problem of harmful mineral scale has stimulated AFM studies of dissolution in the presence of both caustic and environmentally friendly inhibitors such as alginate (Chaliha, 2022; Geng, 2021). Publications on the automation of the data acquisition process from AFM images are appearing (Söngen et al., 2017; Corrias et al., 2023). AFM studies of crystallisation of a fundamental nature are underway (Choudhary, 2020; Darkins, 2022; Zaitseva et al., 2022; Van Driessche, 2023; Cho, 2023). In 2024, P. Vekilov's group (Chakrabarti et al., 2024) combined AFM with X-ray, optical methods and molecular dynamics modelling and showed that dissolved etioporphyrin molecules reach the steps directly from the

solution, near the steps they lose part of their hydration shell and attach to the molecules of the fractures with bonds different from those characteristic of their state in the crystal. In the second stage, these initial bonds are broken and the substance is finally incorporated into the fracture. The authors point out that the stability of the intermediate state can be controlled by solvents and additives, which can suppress unwanted or accelerate favourable crystallisation in industry. Among the fundamental studies, those that have direct implications for the development of methods to treat and prevent undesirable crystallisation in the human body stand out. For example, the work (Shtukenberg et al., 2022) identified the main growth mechanisms and the effect of inhibitors on the layer-by-layer growth of *L*-cystine crystals.

In Russia today, the main emphasis is on *ex-situ* AFM studies of various properties of solid surfaces to solve problems of micro- and ultra-small-scale organisation of matter – mainly for the creation of effective ferroelectric compositions and for biological/medical applications.

1.4 History of AFM studies of the growth-dissolution reversibility and the influence of mechanical impact during crystal growth

No examples were found of *in-situ* AFM observations of growth or dissolution at the boundary of growth twins and at the boundary between individuals. The literature notes the importance of information on grain and twin boundary processes for understanding natural processes and for industry, particularly alloys, but mainly provides results from *ex situ* AFM scanning (Pramanick et al., 2009). Similarly, the effects of plastic deformation, strain and compression, vibration of various types, and fracture and crack healing on crystal growth and dissolution have been studied by various methods, but no data on *in situ* observations at the molecular level in solution have been found. Literature references on the history of the study of the influence of these factors on other methods are given in the appropriate sections of the paper. Below

is a literature review of AFM publications in the field of three experimental problems that are reflected in the main provisions defended.

Scratches

The first to use an AFM tip on the surface of a growing crystal was Shluger et al. (1994), who succeeded in doing so on alkali halide crystals with the finest monoatomic steps. The effect of scratches was then studied in three other papers (Elhadj et al., 2008; Yanagiya, Goto 2012; Zareeipolgardani et al., 2019). In the paper (Elhadj et al., 2008), the voltage applied by the AFM probe to the surfaces of biotic and abiotic calcite simultaneously suppressed growth and "modified the crystalline phase of the material". The authors of the work (Zareeipolgardani et al., 2019) observed how, when scratching the surface of lysozyme, small steps were generated from the edges of the scratch and combined into macrosteps, and the surface was subsequently levelled. The work (Yanagiya, Goto 2012) investigated the processes of groove healing and tubercle dissolution that occurred after scratching the (100) faces of KDP with an AFM tip. The authors explained the alignment of grooves and tubercles by minimising the free energy of the surface.

Impurity particles

There are many examples of AFM studies where an impurity solution is added to the main solution. For example, McPherson and Kuznetsov (2014) showed the effect of such impurities on the growth of lysozyme, canavaline and other crystals. In addition, the effect of impurity ions added to the solution on the dynamics of surface processes was studied in (Land et al., 1999; Nakada et al., 1999; Pastero et al., 2004; Kamiya et al., 2004; Klapper et al., 2010; Lee-Thorp et al., 2017). All authors noted the stopping of the steps at low supersaturations, kinetic anisotropy and non-linear kinetics of the steps, which is in agreement with theoretical data (Lee-Thorp et al., 2017). Experiments adding organic impurities to the solution are also known (Nakada et al., 1999; Hendley

et al., 2018). In 2000, P. Vekilov's group (Yau et al., 2000) used a manipulator to introduce particles, create point defects in the apoferritin lattice and monitor their overgrowth.

When the particles are not fixed, they can be moved using an AFM tip, and the entry of particles into the crystal can be identified by the holes above them, which do not overgrow for a long time (Poornachary et al., 2008). Some authors have used the long-term influence of elemental organic and inorganic particles added to the solution as a factor controlling the crystal habit (Abbona et al, 2010; Bisker-Leib, Doherty, 2003; Capellades et al, 2022). The most comprehensive analysis and review of the literature on the influence of impurity solutions is presented in the work (Lucre`ce et al., 2019).

At the same time, there are very few examples of AFM being used to study the introduction of large mechanical particles. McPherson and Kuznetsov in the same paper (McPherson, Kuznetsov, 2014) showed the introduction of affinity crystals, which grew into the crystal without forming defects due to their affinity. McPherson himself, in 1995, conducted a 7–minute observation of a large foreign particle interfering with the steps and growing into the mother liquor. This experiment is described in detail in the same paper (McPherson, Kuznetsov, 2014). Finally, in 2017, a paper was published on the introduction of pyrite into the surface of *L*-cystine {0001} (Zhong et al., 2018). The particles in this experiment were adherent to the material of the growing layers and were introduced without forming cavities between them and the host crystal, i.e. without trapping the solution. The authors of the paper (Zhong et al., 2018) were the first and only ones who managed to gradually record the appearance of a screw dislocation above an impurity particle using AFM.

Reversibility and symmetricity of growth and dissolution

The idea of general symmetricity and reversibility of the growth and dissolution processes follows from the common physical laws underlying these two aspects of crystallisation. The advent of AFM should have helped to resolve the issue of reversibility, since in AFM it is possible to follow dissolution and then growth on the

same steps of the same dislocation hillock. As mentioned above, in 2000 L.N. Rashkovich and co-authors showed that during the growth–dissolution transition on the face of the KDP prism, the fluctuations during dissolution were greater than during growth. However, most authors of AFM publications tend to confirm the reversibility of growth and dissolution. For example, Bose (2008) speaks of a reversible adsorption mechanism controlling the dissolution of barite. Pina (2009) compared the kinetics of steps in solution near the saturation point of anhydrite and argues that the mechanisms of stepwise dissolution and growth are virtually identical. However, it is Dove et al. who have paid the most attention to this issue, insisting that, similar to growth, the release of a substance into solution occurs at a rate determined by the overcoming of energy barriers with the formation of hollow cores on dislocation defects or the nucleation of two–dimensional vacancy islands on impurities. In their work (Dove et al., 2005, Dove, Han, 2007) they experimented with the dissolution of quartz and calcite and then compared the results with published data on the growth and dissolution of feldspar and kaolinite. According to their data, growth and dissolution are analogous but inverse processes and, depending on the factors controlling their mechanisms, each stage of growth and dissolution gives the same nanoscale picture (Figure 1.6).

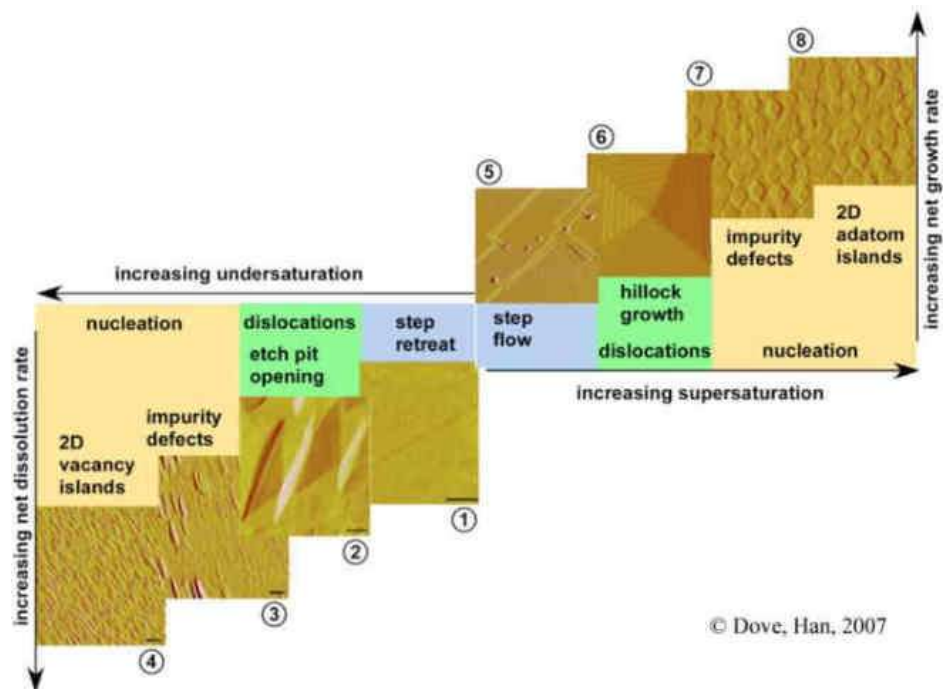


Figure 1.6 – AFM demonstration of growth and dissolution as equivalent but inverse processes. From (Dove, Han, 2007)

Chapter 2. Experimental Modeling

2.1 Instruments

The work was carried out using the Ntegra Prima atomic force microscope (NT-MDT, Russia). Standard silicon cantilevers were used (NanoProbe (UK), Veeco (USA) and NT-MDT, Russia). Cantilever characteristics: tip radius of 1.5, 2.5 and 5 nm, length of 405–495 nm, width of 45–55 nm, resonance frequency of 10–16 kHz, stiffness of 0.2 N/m. Calibration of the piezo scanners was performed on optical diffraction gratings with a pitch of 16 and 1.2 μm .

Atomic force microscopy is the main method of this work, in addition to which the following devices were used as auxiliaries:

1. Diffractometer Shimadzu XRD-6000, radiation – $\text{CuK}\alpha$, internal standard – Si (operator – Yu. S. Simakova).

2. Inductively coupled plasma mass spectrometer Agilent 7700x (USA), operator – G. V. Ignatiev. Concentrations were calculated from calibration curves constructed using standard solutions of high-purity standards at a concentration of 10 mg/l.

3. Raman spectrometer (modification of DFS-24 spectrometer, Lomo, Russia), operator – A.A. Kryazhev. Half-width of the instrumental function is not more than 1 cm^{-1} , laser – DPSS 532 nm, thermally stabilised, half-width of the line 1 cm^{-1} , quartz glass cuvette, pumped.
4. Optical microscope Nikon Eclipse E400 with fluorescence.

5. Scanning electron microscope Tescan Vega 3 (Czech Republic). Elemental analysis was performed using an X-Max energy dispersive detector (area 50 mm^2) (Oxford Diffraction). Operator – A.A. Kryazhev.

6. Scanning electron microscope Axia ChemiSEM (ThermoFisher Scientific, USA). Operator – V. A. Radaev.

7. Analytical balance SHINKO VIBRA HT-224RCE (Japan), accuracy 0.0001 g, platform size 80 mm, built-in calibration.

8. JAVOS VS-10 vacuum drying oven.

The equipment belongs to the Geosciences Collective Use Centre (Institute of Geology, Syktyvkar).

The principle of AFM

The atomic force microscope, which is part of the scanning probe microscopy group, is currently the only method that allows in-situ observation of the evolution of a crystal surface in solution at the level of individual molecules. In the AFM, the crystal surface is probed with a sharp tip whose tip is brought to the surface at the distance of the interatomic potentials (Figure 2.1).

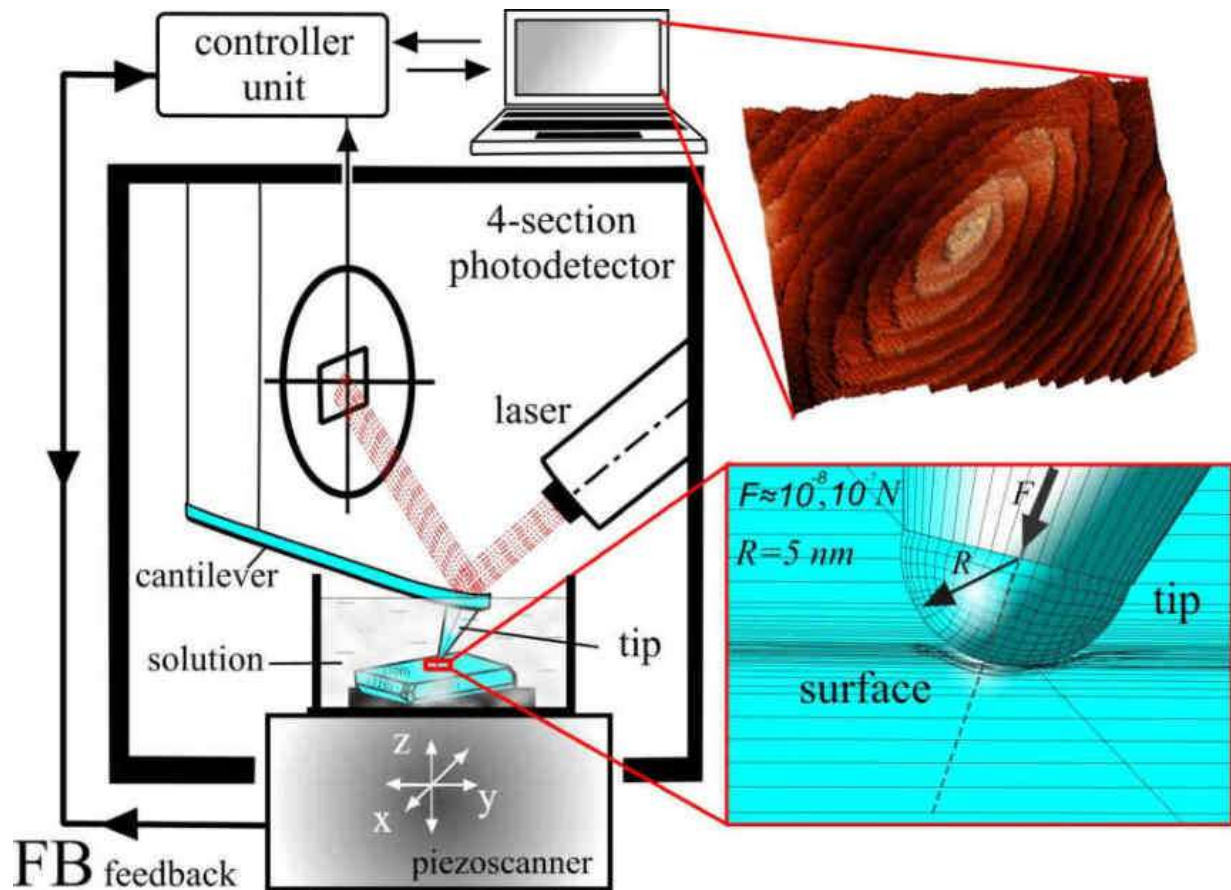


Figure 2.1 – Principle of atomic force microscopy

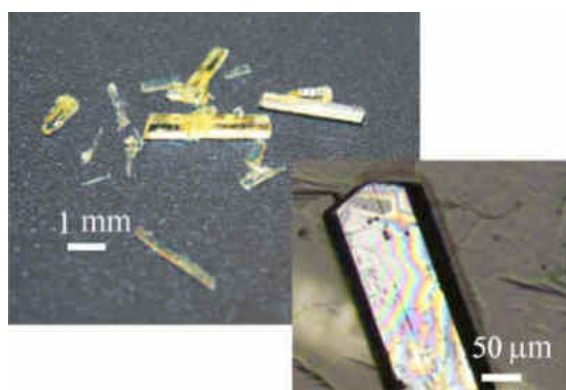
The basic operating principle of the AFM is the effect of forces from the sample surface on the tip of the probe. During surface scanning, the stylus moves up and down; to record its angstrom shift, an optical system is used consisting of a semiconductor laser focused on the tip of the stylus holder, whose beam is reflected into the centre of a

four-section diode photodetector connected according to a differential circuit. The tip deflections are recorded as a differential mismatch signal from the photodiode windows.

The scanning is done by the sample under the tip, but physically it still looks like the tip is 'walking' line by line across a square area of the surface. The tip registers the interaction force according to the settings, e.g. at 256 points in each of the 256 lines. The lowest position of the tip is then assigned the darkest colour, the highest the lightest. This produces an image of the surface relief, similar to an optical image.

AFM can work in one of the following modes. In contact mode, also known as repulsion mode, the tip of the AFM probe is in soft physical contact with the sample and its deflection is caused by the mutual repulsion of the tip and surface atoms due to the overlap of their electron shells and the Coulomb repulsion of the nuclei. The magnitude of the force varies from 10^{-8} N to a more typical working range of 10^{-7} ... 10^{-6} N. In the non-contact mode, also known as the attraction mode, the AFM monitors the attractive van der Waals forces between the tip of the scanning probe and the sample. All images in solutions were taken in contact mode. Ex-situ images of natural crystals in air were obtained in the semi-contact mode – the tapping mode.

2.2 Materials



(Piskunova, 2011).

All in-situ experiments in this work were performed on solutions and crystals of dioxidine (hydroxymethylquinoxaline dioxide, $C_{10}H_{10}N_2O_4$), which was first introduced into the practice of growth studies by the author

Other objects studied by ex-situ AFM are metacrystals of Ural pyrite and pyrite from the Navahun deposit (Spain), alabandine crystals from Vysokogornoye deposit (Yakutia), rock crystal from Zhelannoye deposit (subpolar Urals), small quartz crystals

from the Sinilga ore deposit (subpolar Urals), topaz (Sherlovaya Gora, Transbaikalia), datolite (Dalnegorsk borosilicate deposit, Primorye), phenakite (Ural emerald mines) and zircon (Manhambo Massif, subpolar Urals). Electron microscopy was used to study the surface topography of gold from the Kyvvozh gold placer field (Volsko–Vymskaya Ridge, Middle Timan).

2.2.1 Structure and properties of the model crystal

Dioxidine is one of two antimicrobial drugs, derivatives of quinoxaline di-N-oxide, developed as a result of basic research in the period 1960–1980 at the All-Union Chemical-Pharmaceutical Research Institute (Dvoryantseva et al., 1990). Dioxidine crystallises as tabular crystals in monoclinic syngony, space group P21/n, elementary cell parameters: $a = 8.795$, $b = 15.745$, $c = 7.994$ Å, $\beta = 102.29^\circ$, $V = 1081.58$ Å³ (according to our data). Its crystal structure (Figure 2.2) was entered into the Cambridge SOKGAA structural database by G.G. Dvoryantseva's team. The dioxidine molecule (1,4-di-N-oxide 2,3-bis(oxymethyl)quinoxaline) is a syn-isomer (Figure 2.2 (a)). The structure of dioxidine monohydrate contains a system of intra- and intermolecular hydrogen bonds, including hydrogen bonds with water molecules, in which the dioxidine molecule acts as both an acceptor and a donor of active hydrogen atoms. Two intramolecular H-bonds are formed by the mobile hydroxyl hydrogen atoms of the oxymethyl groups and the oxygen atoms of the N-oxide functions: O(3)H–O(1) and O(4)H–O(2) with the closure of two six-membered rings (Figure 2.2 (a)), while the O(3)H–O(1) bond is significantly weakened compared to the second one due to the competition with the water molecule. The water molecule acts as an acceptor of the hydroxyl hydrogen atom HO(3) and as a donor of the hydrogen atom in the H-bond with the oxygen atom of the N(1)–O(1) group. The hydroxyl hydrogen of the oxymethyl group at C(1) thus participates in the formation of an asymmetric fork H-bond. The hydroxyl hydrogen of the oxymethyl group at C(2) is also involved, forming, in addition

to the indicated intramolecular H–bond, an intermolecular H–bond O(4)H with the oxygen atom O(2) of another molecule (lower part of Figure 2.2).

The crystallisation water molecule also participates in the formation of hydrogen bonds with dioxidine molecules: one of its hydrogen atoms, bound to the oxygen atom of the N(1)–O(1) group of one molecule, is simultaneously bound to the oxygen atom of the O(4)–oxymethyl group of another molecule. The second hydrogen atom of the water molecule forms an H–bond with the O(1) of another molecule.

Due to the hydrogen bonds considered (except for the last one), the dioxidine and water molecules are combined into double chains along the crystallographic direction $[201\bar{1}]$, and these chains are combined into layers parallel to (010).

In the chains, in addition to H–bonding by water molecules, stacking interactions occur between the dioxidine molecules with distances of 3.3 and 3.7 Å between the planes of the antiparallel quinoxaline cores (Figure 2.2 (e)). Dioxidine and crystallisation water molecules belonging to different layers (010) form a three–dimensional framework in the crystal.

Using AFM, interesting phenomena of layer-by-layer growth of the smallest elementary layers were observed on dioxidine. For example, on the (010) side they averaged 3.5 Å (Figure 2.3). This is one of the sizes of the dioxidine molecule. In the following, the steps on the (010) face will be referred to as monomolecular.

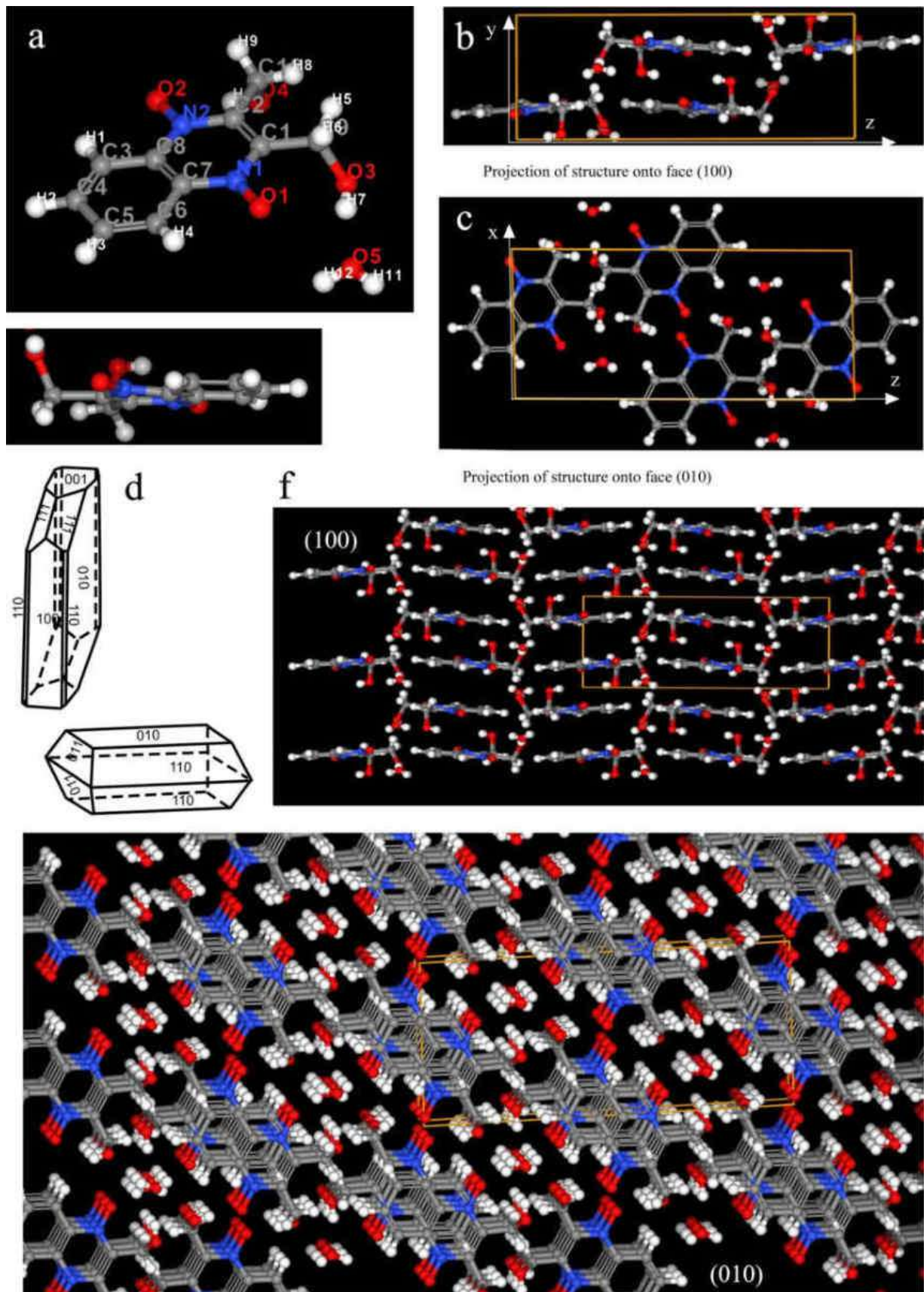


Figure 2.2 – Crystal structure of dioxidine (1,4–di–N–oxide of 2,3–bis(oxymethyl)quinoxaline) $C_{10}H_{10}N_2O_4$, images from Cambridge Crystallographic Data Centre, (d) – dioxidine crystal habit

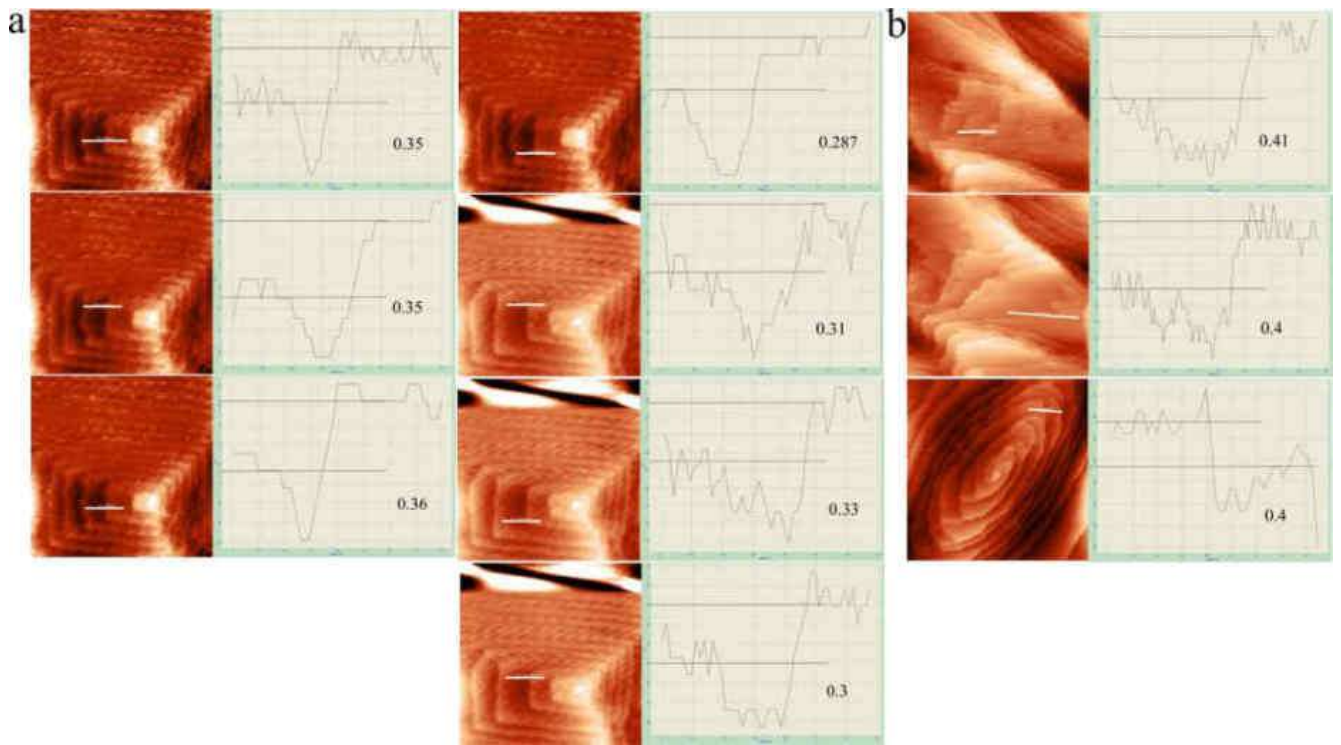


Figure 2.3 – Height measurements in nanometers of elementary steps on the (010) face: (a) – on one step at different times in one experiment, (b) – in two other experiments

2.2.2 Solutions for experiments

The choice of dioxidine as a model object for atomic force microscopy of growth processes is due to its properties of growth and dissolution at room temperature, as well as the transparency of its solutions, which is important for the unimpeded passage of the laser beam. Numerical data on the solubility of dioxidine are not yet available, but it is widely reported in medical literature and patents that dioxidine is a poorly soluble substance. Perhaps the only source of solubility data is the paper (Kustov, Smirnova, 2017). It gives a value of 0.74 g / 100 g H₂O for a temperature of 15.15 °C, determined by drying to constant weight.

Solubility

To determine the solubility of dioxidine at a temperature of 35°C, 24°C and 18.6°C, i.e. in the range of conditions of the AFM experiments, the method of drying to constant weight was used. Solutions with precipitated crystals were kept for 12 hours at three specified temperatures, a saturated solution for each temperature was collected, weighed and then dried in a vacuum drying cabinet. Drying was carried out at 75°C for 12 hours, then the temperature was increased for a further 4 hours to extract capillary water. The weight was determined to within 4 decimal places. The solubility of dioxidine was 1.69 g per 100 g water at 35°C, 1.13 g/100 g H₂O at 24°C and 0.87 g/100 g H₂O at 18.6°C (Figure 2.4). For comparison, the solubility of KDP at these temperatures is 22 times higher and that of NaCl and KCl almost 30 times higher.

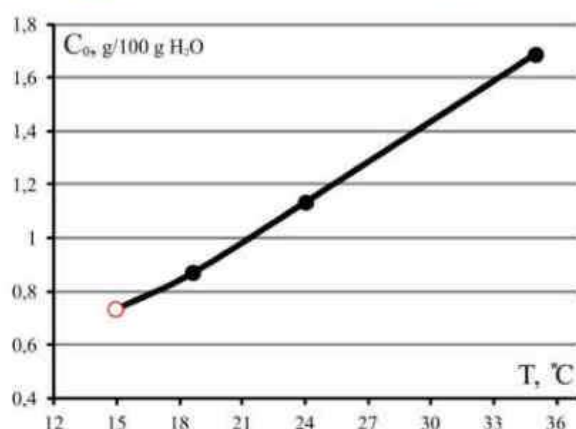


Figure 2.4 – Solubility curve of dioxidine C₁₀H₁₀N₂O₄ in water based on drying to constant weight for 16 hours. The point “15.15 °C” corresponds to the value from the work (Aleksandrov et al., 2015)

If the concentration of pharmaceutical solutions is 10 mg/ml, then below 20 °C crystals should precipitate in the ampoules. This does not happen because the onset of nucleation of crystalline hydrates is more difficult than for non-crystalline hydrates (Aleksandrov et al., 2015). In addition, the concentration of the solution determined by drying to a constant weight for four different ampoules from a package of dioxidine labelled "10 mg/ml" turned out to be different – 0.55, 0.87, 0.89 and 0.82 g/100 g H₂O, respectively. Dry crystals of dioxidine kept in a drying cabinet lost a further 0.42 g of their 40 g weight over 12 hours, which is also associated with structural water. So dioxidine is indeed a poorly soluble substance.

The low growth rates of dioxidine, which amount to fractions of nanometres per second, compared to the rates measured for NaCl and KCl (Piskunova, 2007), which amount to tens of nanometres per second, allow us to observe various crystal growth phenomena at the nanoscale more effectively and for longer periods of time using dioxidine.

For a correct AFM image it is important that the processes are not too fast and that all fluctuations in the scan window are realised and the particles fall into place, as the AFM tip will not pick up an unfixed particle and will often remove it from the scan field. For this reason, AFM films slow growth and dissolution well – about 1–2% for dioxidine on both sides of the saturation point. The growth surfaces of most natural crystals carry information about this stage of near-equilibrium growth. Therefore, in the experiments, the lowest possible initial supersaturation was chosen for growth and the lowest possible undersaturation for dissolution.

In the absence of standardised methods, the parameters of the solutions were selected in methodical experiments:

– by evaporating the pharmaceutical solution, a saturated solution was prepared for a given temperature, a very important condition was the precipitation of the excess substance into crystals. – The solution above the crystals was collected, a certain amount of dry matter or a few drops of water were added, the initial supersaturation/undersaturation was calculated, then the solution was poured into the AFM cell from above onto the fixed crystal.

– the undersaturation "step" was one drop (0.005 ml) of double deionised water from an insulin syringe added to 1 ml of solution. If a successful surface scan was obtained, this supersaturation/undersaturation was considered to be working from that moment on in the remaining similar experiments.

Viscosity

The viscosity of dioxidine solutions was determined according to State standard GOST 10028–81 using a “VPS 2” viscometer (capillary diameter 0.56 mm, the accuracy of time measurement by an electronic stopwatch is 0.01 sec.). The viscosity was calculated using a formula that includes the viscosity and density of water, as well as its flow rate in the same capillary. The viscosity was determined, among other things, for the minimum temperature relative to the experimental temperature of -18.6°C , and the solution was run saturated. Nevertheless, the obtained value is comparable with the value for the viscosity of water. The viscosity of a slightly undersaturated dioxidine solution turned out to be close to the viscosity of water (Figure 2.5). For comparison, the viscosity of an undersaturated NaCl solution at a temperature of 20°C is twice as high. That is, the greatest value for increasing the viscosity of the dioxidine solutions used is not the concentration of the solution, but the temperature.

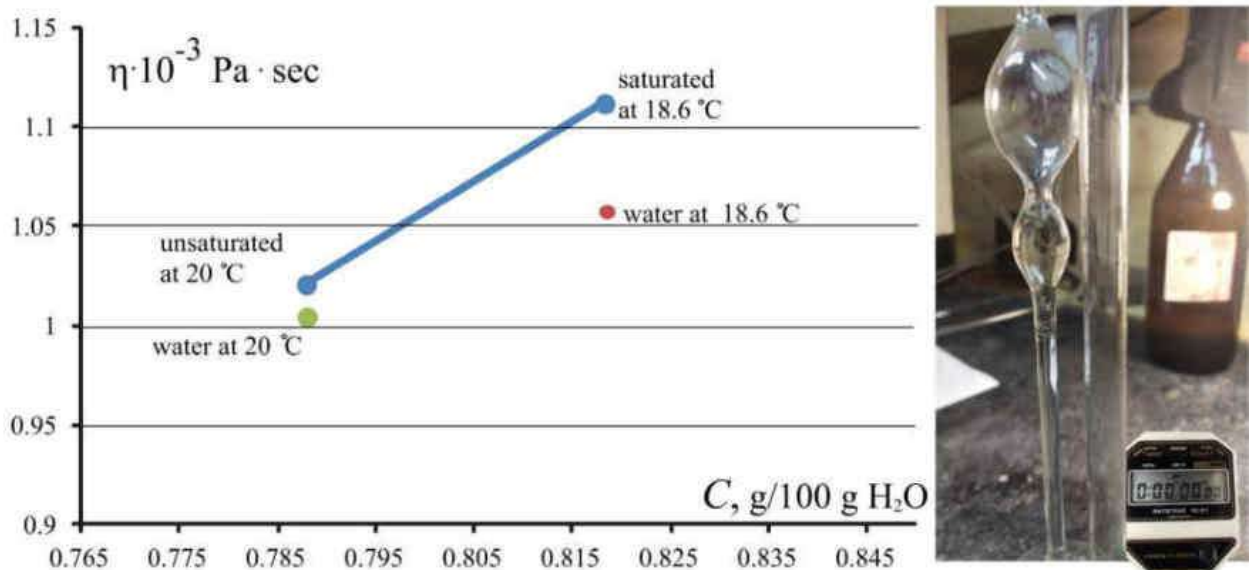


Figure 2.5 – Dynamic viscosity of dioxidine solutions compared to the viscosity of water

The experiment to compare the growth and dissolution processes near the saturation point described in Section 3.1.2 of Chapter 3 (Figure 3.5) was carried out at a temperature of 25 °C. In this experiment it was important to show that the viscosity of a slightly undersaturated solution does not differ from the viscosity of a slightly supersaturated solution at the same temperature. However, the precipitation of crystals from a supersaturated solution would falsify measurements of the solution flow time, so an experiment was carried out to change the flow time of dioxidine by lowering the temperature from 24 °C to 18.6 °C. The temperature was controlled by immersing the viscometer in a thermostat. The initial solution had a concentration slightly above the equilibrium concentration for 18.6 °C, i.e. it started out undersaturated at 24 °C and ended up slightly supersaturated at 18.6 °C. The results are shown in Figure 2.6 in comparison with the corresponding data for water. If the temperature slope is subtracted from the viscosity curve, it can be seen that the viscosity remains virtually unchanged during the transition from dissolution to growth.

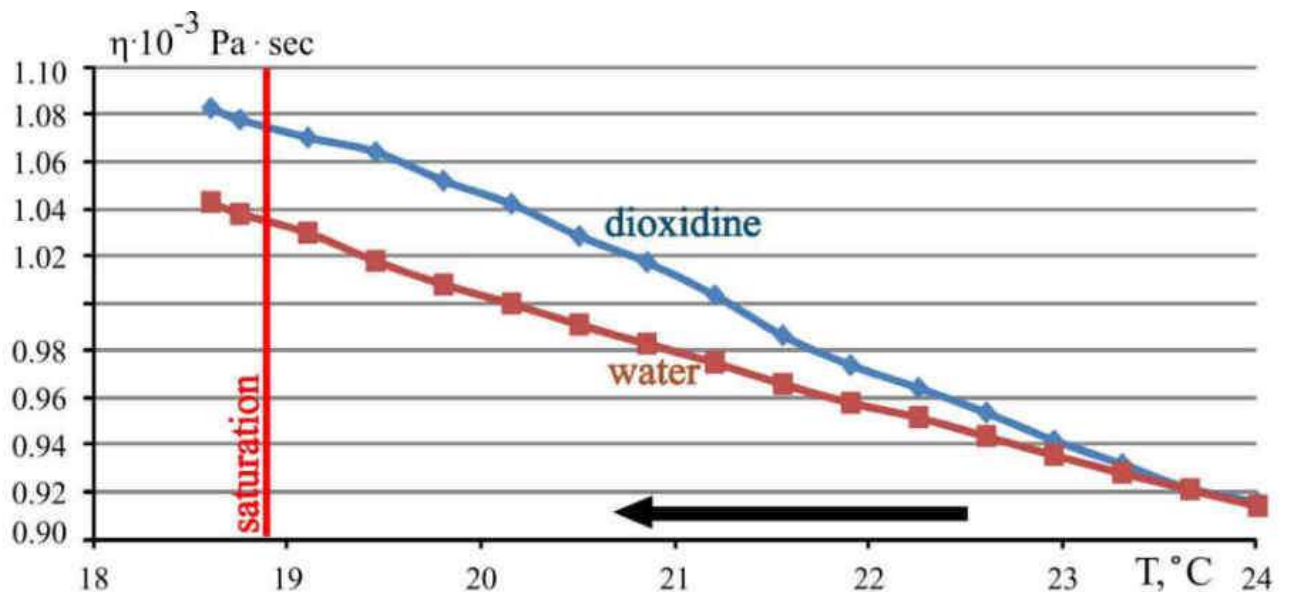


Figure 2.6 – Dynamic viscosity of a solution of dioxide as it changes from 24 °C (undersaturated solution) to a temperature of 18.6 °C (supersaturated). The corresponding curve for water is shown for comparison

Purity of solutions

This work investigates the influence of various mechanical factors on the growth and dissolution of crystals at the nano- and microscale. Often such an influence is expressed as a loss of morphological stability and surface restructuring. Since the loss of morphological stability of the surface can be observed in the case of non-uniform trapping of impurities (Nakada et al., 1999; Klapper H., Rudolph, 2015; Lee-Thorp et al. 2017), special attention was paid to the proof of purity of the solutions. Dioxidine is indeed produced in sufficient purity, which was demonstrated by testing its solutions using an inductively coupled plasma mass spectrometer. Three types of solution were studied: a pharmacy solution from an ampoule, double deionised water with a crystal dissolved in it, and a depleted pharmacy solution left over after extraction of the grown crystal. Concentrations were calculated using calibration curves constructed from standard solutions of high-purity standards at a concentration of 10 mg/l. The results showed (Table 1) that all dioxidine solutions contain trace concentrations of impurities that are not included in the crystal during crystallisation.

Since clusters can also act as impurities, blocking the bends in the steps, it was necessary to determine whether clustering is characteristic of dioxidine solutions at different concentrations. Using Raman spectroscopy, it was found that no clusters formed in dioxidine solutions.

Raman spectroscopy allows the shift along the axis of the vibrational frequencies to be recorded with high accuracy, and the binding of molecules, even into dimers, reduces the vibrational frequency, shifting the peak to the left. This method was developed long ago (Rusli et al., 1989), the approach is to obtain spectra of solutions of different concentrations at different temperatures with an interval of 0.5 °C. The peaks obtained are decomposed into three Gaussian components responsible for free, hydrated and clustered ions.

At the Institute of Geology of the Komi Scientific Centre of the Ural Branch of the Russian Academy of Sciences, this method was used to obtain comparative spectra of numerous inorganic compounds, four alcohols and dioxidine. The same instrumental

conditions were observed during the recording, the position of the cuvette was not changed, and solutions were changed by pumping.

Table 1. Concentration of impurities in dioxidine solution

Elements with concentrations above zero	Concentration (mg/l)		
	Double deionised water with a crystal dissolved in it	Solution after extraction of the grown crystal	Pharmaceutical solution, new ampoule
7 Li	0.000	0.000	0.007
9 Be	0.001	0.000	0.000
11 B	bdl ¹	0.108	0.091
24 Mg	bdl	0.001	0.001
27 Al	bdl	0.072	0.070
28 Si	0.118	0.209	0.168
39 K	bdl	0.113	bdl
44 Ca	0.080	0.236	0.218
45 Se	0.001	0.000	0.001
51 V	0.006	0.004	0.007
52 Cr	0.019	0.014	0.023
60 Ni	0.007	0.007	0.00
63 Cu	bdl	0.007	bdl
66 Zn	0.045	0.057	0.034
75 As	bdl	0.001	bdl
78 Se	bdl	0.001	bdl
88 Sr	bdl	0.004	0.002
137 Ba	0.002	0.025	0.016
209 Bi	0.000	0.167	0.000
bdl – below detection limit.			

Dioxidine was one of the few substances studied where no frequency shift, i.e. clustering, was detected (Figure 2.7). KNO_3 , for example, has clusters even in undersaturated solutions. The NO peak was chosen as an illustration because of its most contrasting behaviour. In the dioxidine structure, the expected change in the oscillation

frequency of the NO bond should be characterised by the largest shift, since the oxygens O(1) and O(2) (Figure 2.2 (a)) are the first to bind to neighbouring molecules.

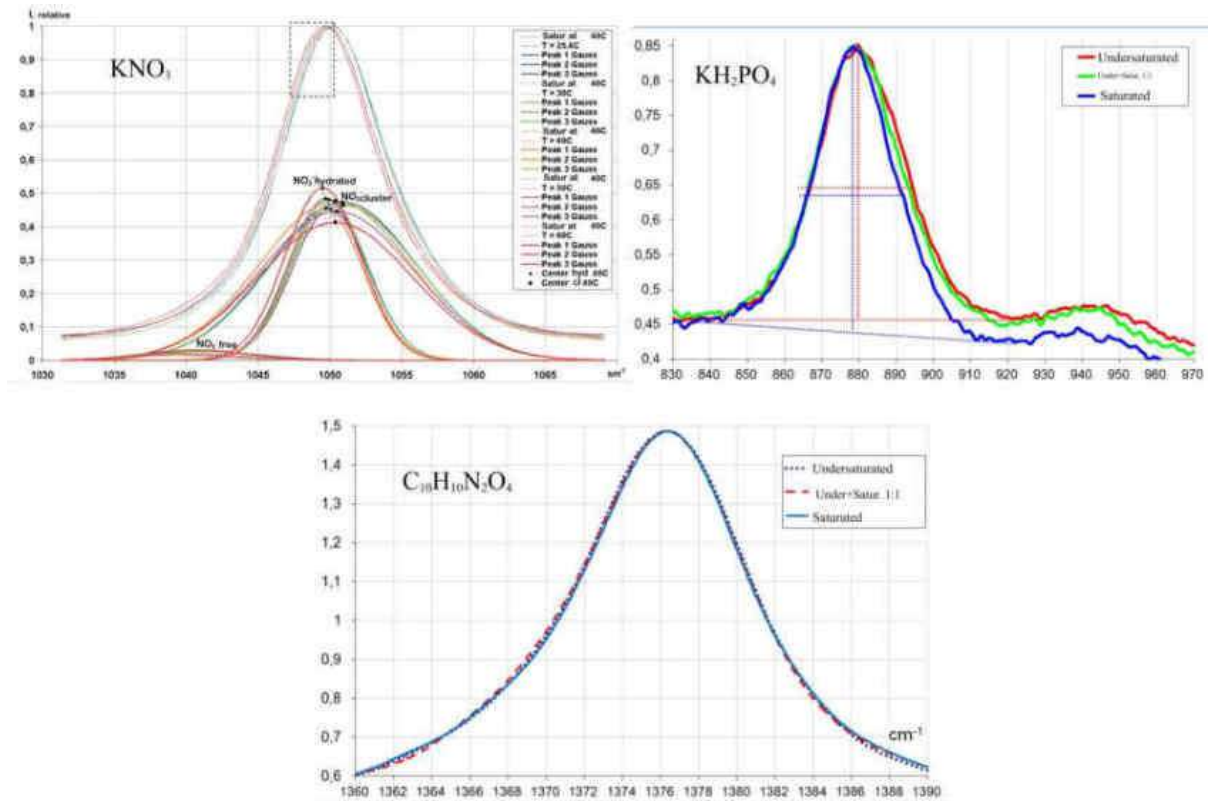


Figure 2.7 – Raman spectra of potassium nitrate, KDP and dioxidine of different concentrations: on the left – frequency shift of the NO_3 anion of potassium nitrate (with decomposition into three Gaussian components); on the right – three peaks of KDP solutions of different saturation; at the bottom – three peaks (N–O) of different concentrations of dioxidine, which do not change their position as the system moves toward saturation, indicating the absence of clusters


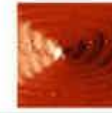











When using this method, it is important to observe the OH peak at the same time: for KNO_3 , the broadening of this peak at some point indicated the release of OH groups due to the clustering of the substance. This was not the case for dioxidine, which did not show the slightest frequency shift in any of its peaks. The ability of pure dioxidine solutions to remain unbound in clusters is one explanation for its high antimicrobial potential. This is also the reason for its easy release from the polymer base during targeted drug delivery.

2.3 Experimental methodology

2.3.1 Conditions

The studies were carried out at room temperature and the temperature and humidity data for the different experiments are given in Table 2.

Table 2. Task and conditions (temperature (T) and relative humidity (RH)) for solution experiments

Saturation point 0 nm/c DISSOLUTION GROWTH		RH=25.0 % T=25.0 °C	Scratch GROWTH		RH=26.2 % T=24.0 °C	Dislocation Hillocks GROWTH		RH=40.5 % T=24.0 °C	Dislocation Hillocks GROWTH		RH=40.0% T=25.0 °C
Saturation point 0 nm/c DISSOLUTION GROWTH		RH=25.0 % T=25.0 °C	Scratch GROWTH		RH=30.0 % T=24.5 °C	Dislocation Hillocks GROWTH		RH=43.0% T=25.4 °C	Dislocation Hillocks GROWTH		RH=34.0% T=24.0 °C
Impurity Particles GROWTH		RH=27.0 % T=26.0 °C	Scratch DISSOLUTION		RH=26.0 % T=24.1 °C	Propagation Dislocation GROWTH		RH=36.7% T=28.5 °C	Dislocation Hillocks GROWTH		RH=36.0% T=27.1 °C
Impurity Particles GROWTH		RH=27.2 % T=24.0 °C	Close Proximity of Crystals GROWTH		RH=45.0 % T=27.00 °C	Dislocation Hillocks DISSOLUTION GROWTH		RH=45.0% T=27.1 °C	Growth on Defects GROWTH		RH=26.0 % T=25.2 °C
Impurity Particles GROWTH		RH=27.2 % T=26.0 °C	Channel Shape GROWTH		RH=26.5 % T=24.3 °C	Dislocation Hillocks GROWTH		RH=43.0% T=28.1 °C	Growth on Defects GROWTH		RH=25.2 % T=25.4 °C
Crack DISSOLUTION GROWTH		RH=45.1 % T=26.7 °C	Dissolution on Defects DISSOLUTION GROWTH		RH=25.0 % T=25.0 °C	Dislocation Hillocks GROWTH		RH=40.0% T=25.1 °C	Dislocation Hillocks GROWTH		RH=35.1 % T=26.0 °C
Crack DISSOLUTION GROWTH		RH=46.6 % T=28.6 °C	Acoustic Impact E2 GROWTH		RH=40.0 % T=33.7 °C	Dislocation Hillocks GROWTH		RH=45.2% T=24.0 °C	Dislocation Hillocks GROWTH		RH=25.0% T=25.9 °C
Intergrowth Boundary GROWTH		RH=36.9% T=28.4 °C	Acoustic Impact E2 GROWTH		RH=41.2 % T=30.6 °C	Dislocation Hillocks GROWTH		RH=27.7% T=24.0 °C	Dislocation Hillocks GROWTH		RH=40.0% T=25.8 °C
Limiting Space DISSOLUTION GROWTH		RH=38.8 % T=27.6 °C	Limiting Space DISSOLUTION GROWTH		RH=51.5 % T=26.9 °C	Dislocation Hillocks GROWTH		RH=28.0% T=22.1 °C	Dislocation Hillocks GROWTH		RH=50.0 % T=30.0 °C
Limiting Space GROWTH		RH=50.2 % T=26.0 °C	Limiting Space DISSOLUTION GROWTH		RH=51.5 % T=26.9 °C	Dislocation Hillocks GROWTH		RH=27.6% T=25.7 °C	Dislocation Hillocks GROWTH		RH=26.0% T=23.1 °C
Limiting Space GROWTH		RH=50.4 % T=25.9 °C	Limiting Space GROWTH		RH=44.2 % T=30.3 °C	Dislocation Hillocks GROWTH		RH=30.2 % T=26.6 °C	Dissolution on Defects GROWTH		RH=25.0 % T=25.1 °C
Limiting Space GROWTH		RH=50.0 % T=26.0 °C	Limiting Space GROWTH		RH=44.6 % T=30.0 °C	Dislocation Hillocks GROWTH		RH=30.2 % T=26.6 °C	Growth on Defects DISSOLUTION GROWTH		RH=25.2 % T=30.0 °C

The temperature and humidity in the immediate vicinity of the AFM cell were read from the corresponding displays (accuracy – two decimal points). These parameters were kept constant for one experiment to an accuracy of one decimal place by the climate system and additionally by an evaporation humidifier attached to a room heater. When necessary, a protective cap was used on the scanning system.

Table 2 shows the special conditions under which the experiments were carried out, depending on the tasks set. Some of them do not require a separate methodological section, such as experiments where growth on defects was observed, in particular on screw dislocations. In these cases, the recording was made on a glued crystal with a solution poured on top, or on a crystal grown directly in the AFM cell. When it was necessary to record a continuous transition from dissolution to growth up to the saturation point, the solution was prepared slightly undersaturated or saturated for a given temperature. Descriptions of the methods used in other experiments where it was necessary to create special conditions are given below.

2.3.2 Special mechanical impact. Methodology of sample preparation and AFM analysis

Natural mineral systems, especially those where crystals grow from solutions, are difficult to model because of the many components that need to be replicated, both chemically, physically and temporally (Piskunova, 2018, Perovski, 2017). In this paper the influence of only mechanical factors is modelled – scratches, large foreign particles, fractures, cracks, confined conditions, the mechanical influence of neighbouring individuals and the mutual influence of individuals in intergrowths. The AFM allows the influence of each of these factors to be "looked at" separately and with good quality, and the results can also be compared with a "standard" (Piskunova, 2024 b). The standard is an experiment carried out under similar conditions, but without any influence. If the AFM registers unusual phenomena or a shift in the kinetic

characteristics at the boundary of the twins in a solution free of impurities and in the absence of other influences, the cause is precisely the mutual influence of two individuals. When observing growth in confined conditions, the appearance of atypical defects will be associated precisely with the influence of stresses that arise when the space for the crystal facet to advance is limited. Since the size of the crystals ranges from 0.5 to 2 mm, all preparatory manipulations were carried out under a binocular microscope. A non-toxic gel was used which polymerises completely and rapidly under UV radiation.

2.3.2.1 Growth and dissolution on the scratch

The surface scratches were made by the AFM tip itself during the experiment. First, the growth or dissolution of the desired surface area was recorded for some time, then, without leaving the contact, the scan window size was reduced, for example from $10 \times 10 \mu\text{m}^2$ to $0.5 \times 0.5 \mu\text{m}^2$. The resulting small square (Figure 2.8) moved along the trajectory of the future scratch.

If, during scanning, the tip hits high areas (increasing the tip-sample interaction force) due to feedback being switched on, the instrument will usually command the piezo scanner to move the sample away from the tip. This is necessary to maintain a constant force value and protect the sample and tip from damage. To achieve the opposite goal – deliberate damage to the surface – it was sufficient to forcibly pull the tip to a higher area and, without bringing the tip back into contact, immediately draw the trajectory of the future scratch. Since the tip can only be moved between scans when the feedback is not working, and since the tip movement occurs at a higher section with the old settings, the effect of the tip on the surface becomes noticeable and has a force one or two orders of magnitude higher than before. In experiments in a slightly supersaturated solution, the tip movement described above resulted in the formation of deep grooves – micrometre-wide scratches – on the crystal surface (Figure 2.8 (a, b, c)).

This is due to the advantage of defective areas of the surface during near equilibrium dissolution (Heiman, 1975). The interaction of the growing steps with these scratches was then recorded, with the steps slowing down over time, their profile bending, a loss of morphological stability of the surface being observed, and even the phenomenon of simultaneous dissolution and growth in close areas within a step (Piskunova, 2017, 2019, 2021).

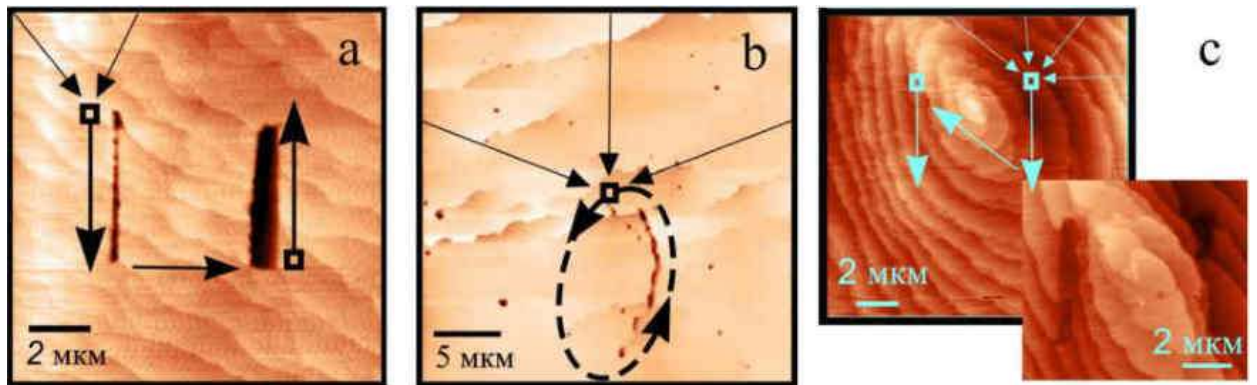


Figure 2.8 – Scratching procedure

With feedback enabled, the pressure force of the tip in the contact is 10^{-9} N. We estimated the pressure force at the moment of jumping off the step, based on the characteristics from the cantilever pass and the device parameters at the moment of calibration, taking into account the disabled FB, to be $\sim 10^{-7}$ N. In the work (Yanagiya, Goto, 2012), the scratching force of lysozyme crystals was $\sim 10^{-6}$ N, for the KDP crystal in the work (Elhadj et al, 2008), a much larger force was required – 10^{-5} N. Obviously, the probability and rate of occurrence of defects at a given impact force depends on a specific substance, which is confirmed by studies in air (Li et al., 2015; Zhu et al., 2004; Amit, Weinan, 2016). In Chapter 3 (3.3) it will be shown that it is not so much the normal probe pressure that is important, which produces Type I defects, the location of which is shown in Figure 2.9 (vacancies and screw dislocations), but the shear stress that it produces during directed motion, which produces Type II defects (edge dislocations and interstitial atoms).

The vertical pressure of the tip creates point defects, whose increased chemical potential initiates local dissolution and a scratch is formed. The stopping of the tip and

the further transfer of shear stresses stimulates the occurrence of edge dislocations at some distance from the contact point, which subsequently causes the loss of morphological stability of the surface over a large area.

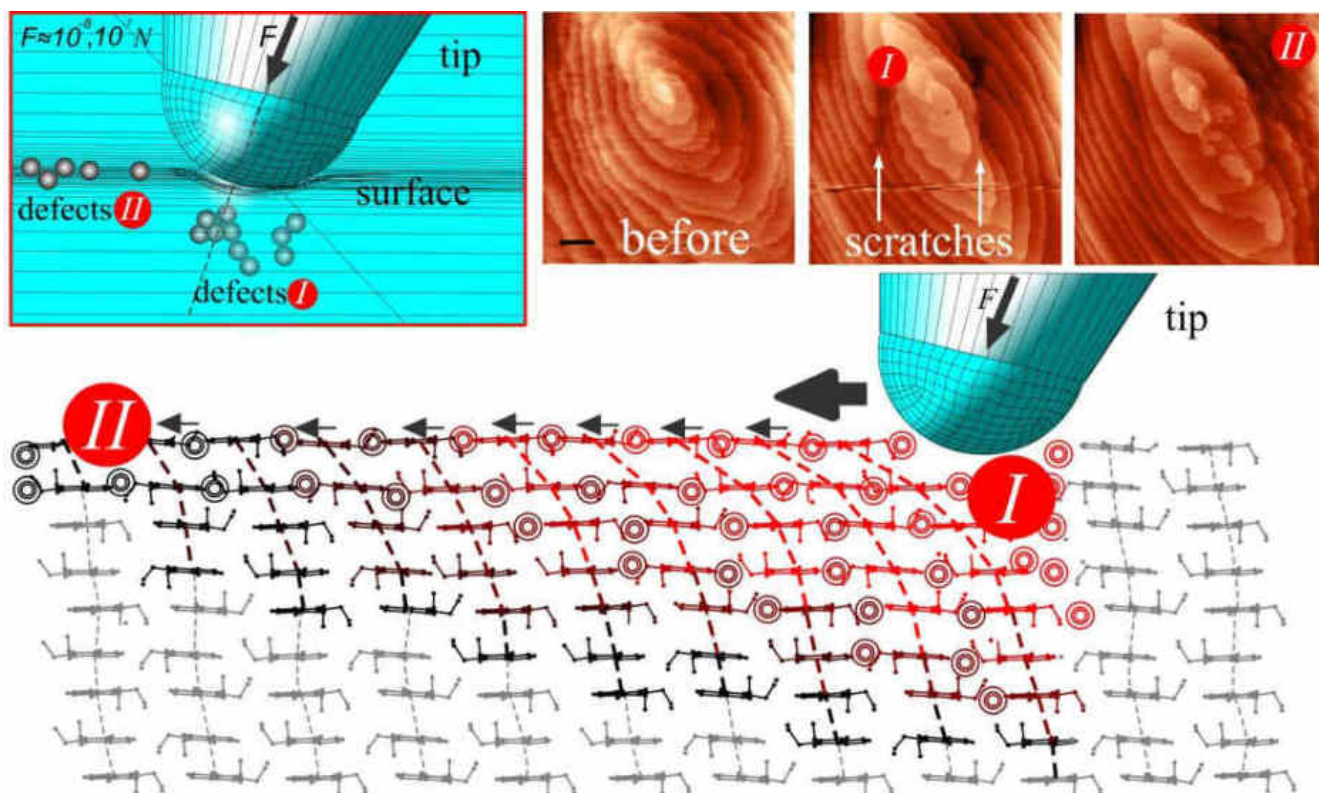


Figure 2.9 – The AFM tip acting with a small force normal to the surface causes the appearance of type I defects (point defects) on which dissolution and a scratch occur (indicated by arrows in the second image above, scale segments are $2\ \mu\text{m}$). The lower part of the figure shows the projection of the dioxidine structure on the $\{100\}$ plane as the tip moves along the $[010]$ surface: the transmitted shear stresses are responsible for the appearance of type II defects (edge dislocations and interstitial defects) at a significant distance from the point of action, leading to a loss of morphological stability far from the scratch (third image above).

The appearance of edge dislocations far from the scratch in the experiment shown in Figure 2.8 (c) led to local dissolution as the surface continued to grow. It is possible that it is the stacking interaction between the levels of the quinoxaline nuclei in the $\{100\}$ plane that allows the stress to be transferred as the tip moves along the (010)

surface to some depth, and that during subsequent growth this stress is relieved by the formation of an edge dislocation.

As early as 1934, G.G. Lemmlein raised the question of creating defects by mechanical action on the crystal. By gently rubbing crystals removed from the solution with a glass rod and immersing them back into the solution, he achieved the appearance of screw hillocks in the contact zone after some time (Lemmlein, 1934). Screw dislocations were later obtained by Forty using a needle on the crystal (Forty, 1954). Why do scratches cause only edge dislocations in an AFM experiment? The reason lies in the magnitude of the forces and the nature of the action: in an AFM, the pressure of the tip along the normal is not sufficient to produce screw dislocations.

2.3.2.2 Incorporation of foreign particles

In nature, the trapping of solid inclusions in a crystal produces crystals of impressive beauty, such as rutilated quartz. In order to register the effect of a solid foreign impurity entering a crystal at the level of an elementary cell, direct observations of such a process have been made in AFM. Typically, model crystals for observation have been grown directly in the AFM cell, so that their growth can be recorded at very small sizes and their surface is not damaged by drying. However, this method is technically difficult to combine with the controlled introduction of impurities: at sizes suitable for AFM, no material sinks or fixes to the surface, and unfixed particles are moved by the AFM tip and often removed completely from the observation zone. Such particles do not have time to grow into the crystal in a short time due to the low supersaturation characteristic of AFM imaging. Therefore, the foreign particle has to be specially pressed. Many attempts have been made to press the particles, including using a magnet and magnetisable particles. None of them produced the desired result. For example, magnetic particles (an alloy of magnesium and iron oxides), due to their size, stuck to the cantilever and the tip faster than they were attracted by a weak magnet and

grew into the crystal. The main conclusion from the methodical experiments was that a foreign particle should be half grown for observation. At the same time, its raised part should not be too high: in an AFM image, a detail as small as 1 μm appears fully illuminated, while thin details around it appear completely black.

Crystals for experiments were therefore pre-grown in solution in the presence of solid neutral particles (Figure 2.10).

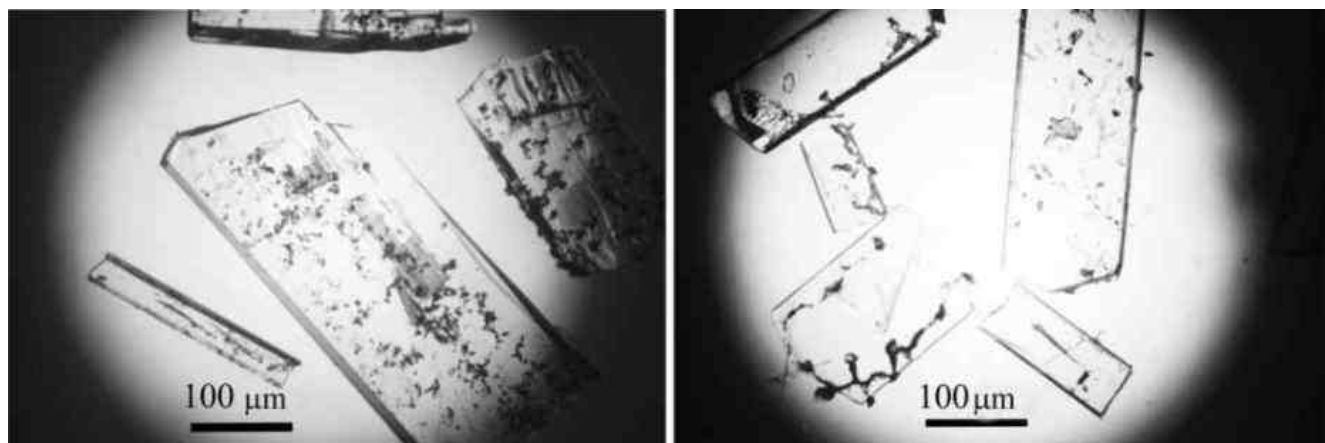


Figure 2.10 – Dioxidine crystals with incorporated foreign particles

When the crystals reached a size of about 500 μm , they were dried and glued into the AFM cell. A pure dioxidine solution was then poured in, a section with embedded particles was found (in Figure 2.11 the impurity particles rise above the surface by 400 nm) and observation began. It was necessary to ensure that the substance did not adhere to these particles during the growth process.

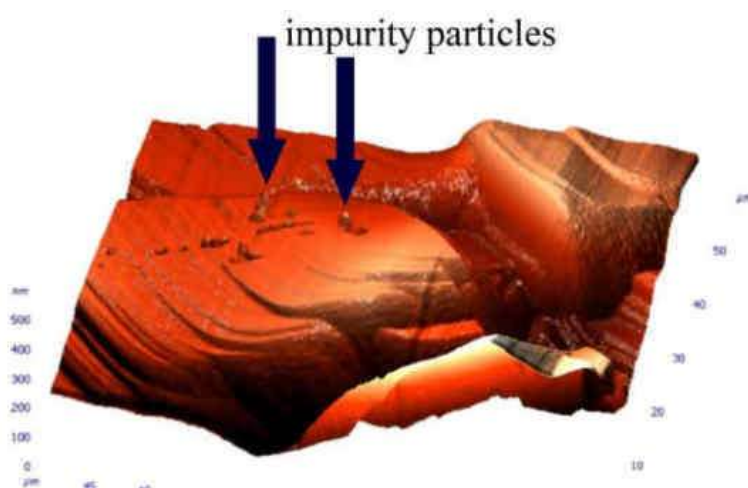


Figure 2.11 – Surface area of dioxidine 50 \times 50 μm with semi-ingrown foreign particles

The particles used in the experiments as mechanical impurities were obtained by grinding a black tourmaline crystal (Sherlovaya Mountain, Transbaikalia) to powder in a mortar.

After washing out all the salts from the liquid inclusions in an ultrasonic bath, the substance was identified by SEM as the mineral species schorl $\text{NaFe}_3(\text{Al,Fe})_6\text{Si}_6\text{O}_{18}(\text{BO}_3)_3(\text{OH})_4$. The tourmaline particles had no specific shape and varied in size from 0.5 to 5 μm . The choice of impurity was determined by the desire to achieve minimal adhesion to the host crystal. In addition, the Schorl powder particles are uniform in size and composition, not too large for AFM (like gold particles or microcrystals) but not too small (like fullerenes). In order to position the AFM tip precisely on the impurity particles, they had to be distinguished in the AFM optical system while still in solution, and the glassy lustre of schorl played an important role in this. At high resolution, these particles looked like sharp fragments and were therefore easily identified in AFM images where it is impossible to visually distinguish similar relief details of different elemental compositions. The colour of the impurity was very important and the Schorl dust particles remained black, making them easy to distinguish in the crystallizer and in transmitted light (Figure 2.10). Good wettability of the impurity was very important – for this reason carbon black was not suitable, although it was ideal in terms of particle size and shape.

2.3.2.3 Growth in a limited space

The constrained face experiments were designed to simulate the conditions in natural cavities that somehow limit the space for the advancement of growing crystal faces. AFM scanning was performed on the (010) face and a pair of diametrically opposed faces on its sides were completely blocked (Figure 2.12). For example, the side of the crystal with faces $(011\bar{1})$ – (011) and the diametrical side, or the side with faces (110) – $(11\bar{0})$ and also the diametrical side of the crystal were clamped. The constraint blocks were of two types: sawn glass blocks that completely repeated the crystal profile

from the side (Figure 2.13 (a)) or assembled blocks of the thinnest glass, glued layer by layer to apply uniform pressure (Figure 2.13 (b) and the first and last images of Figure 2.12).

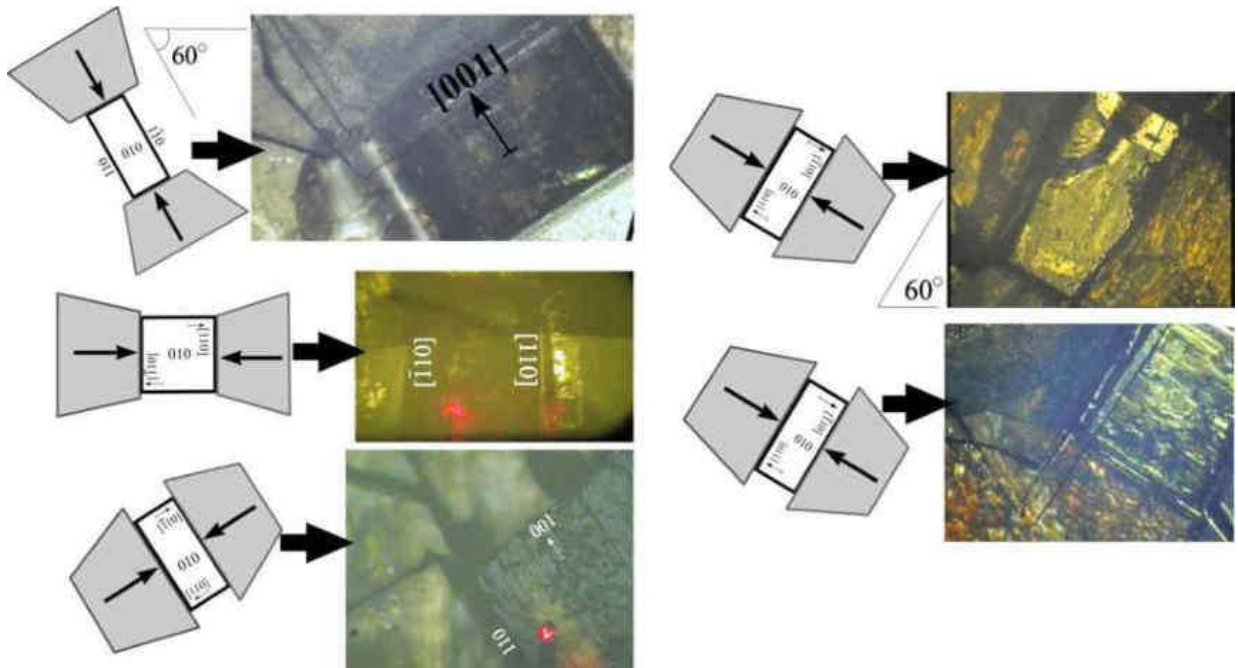


Figure 2.12 – Constrained crystals prepared for the experiment

The upper edge of the constraint blocks was higher than the level of the (010) facet in order to squeeze the upward growing facet for a sufficiently long time. However, the blocks were not made too high so that the cantilever would not touch them when the tip was brought into contact with the surface. The crystal, together with the constraining blocks, was fixed with a fast-curing UV gel. A solution (saturated or slightly supersaturated) was poured on top and shooting began.

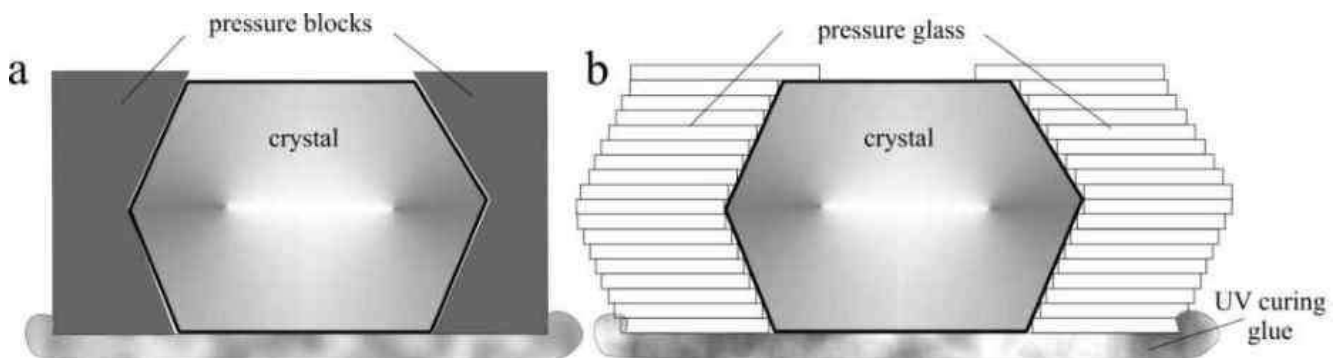


Figure 2.13 – Two types of space-bounding blocks that restrict the growth of side faces

2.3.2.4 Growth and dissolution on cracks

It was planned to use AFM to record elementary processes on the surface of a crystal in solution that occur in the crack area. If, in preparation for such experiments, the crystal is fractured and the edges rejoined, the height difference at the fracture site will be the limit for AFM imaging, since a height difference of more than 5–7 μm threatens to break the tip. Therefore, to achieve this goal, the crystal was glued to a UV gel and then stress was applied by pressing on its opposite edges, resulting in a slight crack without displacement (Figure 2.14). The solution was poured in from above, a spot was selected using the AFM optical system, and shooting began.

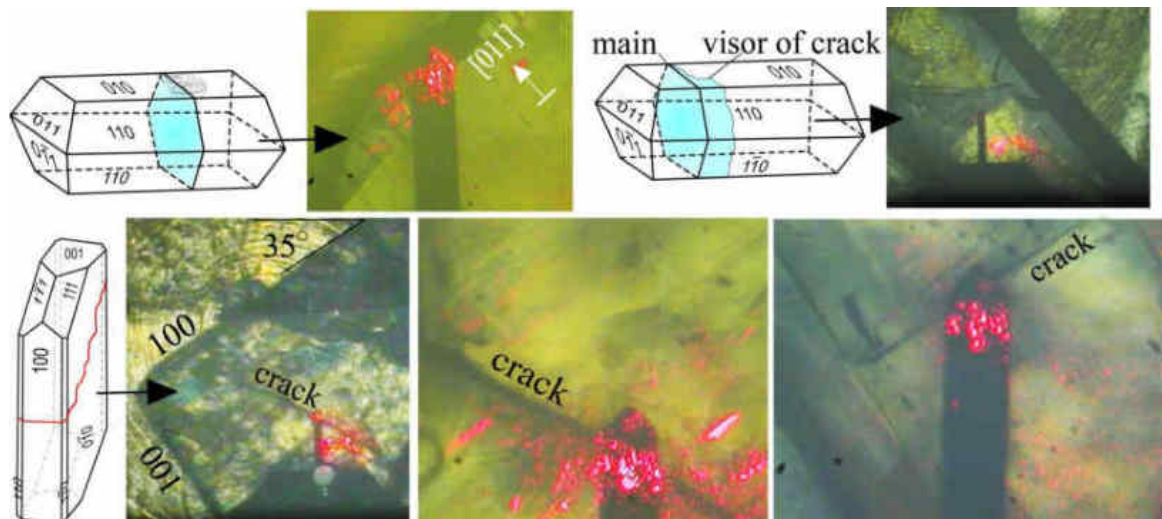


Figure 2.14 – Location of cracks on the dioxidine crystal, in the area of which the shooting was carried out. The cantilever console and the reflection of the laser beam are visible in the optical images

2.3.2.5 Methods of other in-situ experiments with special mechanical impact

Regeneration surfaces

Regeneration is the restoration of the cleavage planes in the feed solution. In the experiments, it was planned to observe the processes on the transverse fractures of the

dioxidine crystals, corresponding approximately to the $\{001\}$ plane (Figure 2.15). As expected, it is not possible to photograph such a growing surface with AFM for a long time, because the regeneration surface becomes uneven, multi-headed growth begins, the result of which after removing the crystal from the solution is shown in Figure 2.16.

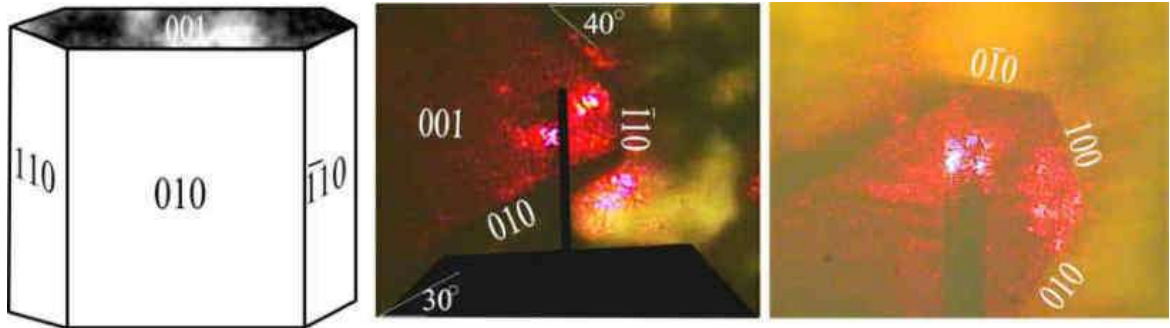


Figure 2.15 – A crystal of dioxidine broken along the $\{001\}$ plane and its image in the AFM camera

As it is physically impossible to record the simultaneous growth of many heads growing in the normal direction by fast right-left tip movements in the AFM, weak dissolution on the fracture surfaces was reconstructed in four experiments and the very beginning of the growth of the regeneration surface was recorded at the nanoscale.

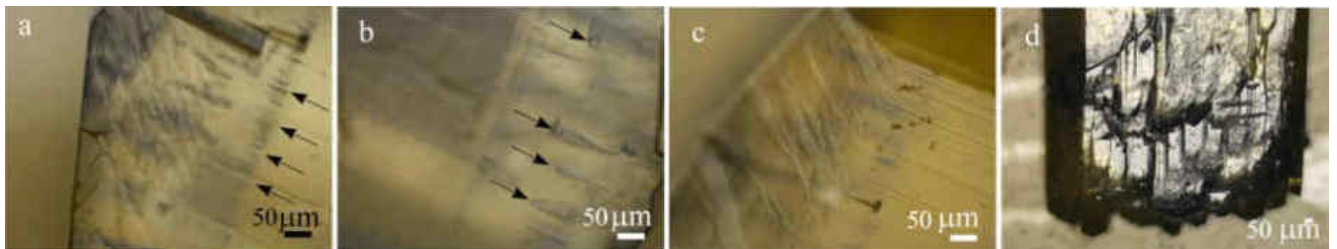


Figure 2.16 – Capture of inclusions with solution (indicated by arrows in (a) and (b)) between many growing heads (d) on the regeneration surface of dioxidine.

Collective growth of crystals

It was planned to observe the elementary processes at the point of close contact between two crystals over a long period of time, in order to study the mutual influence

and the characteristics of the formation of induction surfaces. However, many attempts to record phenomena from above exactly above the boundary between two closely pressed natural faces (100) or (010) of different crystals were unsuccessful (Figure 2.17), because at the scales at which the AFM records, satisfactory contact was prevented by 'bevels' in the form of even the narrowest faces (110). However, it was possible to obtain an unusual shape of dislocation channel at the top of the hillock in the centre of one of these pressed crystals.

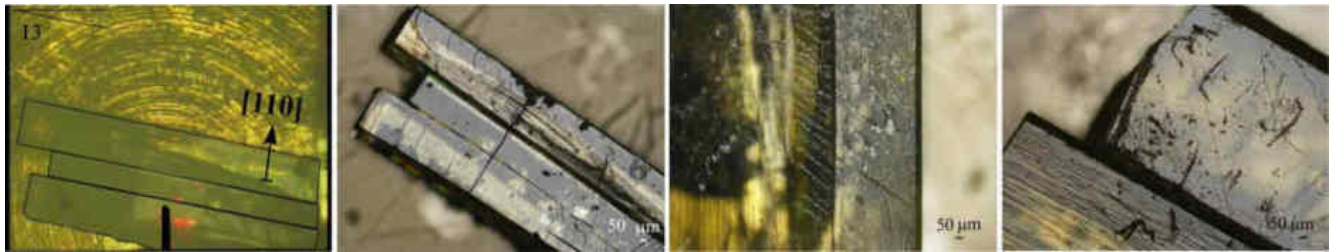


Figure 2.17 – Samples prepared for an experiment to study the influence of neighboring crystals

Twins boundary

Twins were selected from a variety of small crystals grown from a highly supersaturated solution. The angle between the twins was often 120 degrees, but as no X-ray studies were carried out it is more accurate to call them intergrowths of crystals in a twinning position. The crystals were glued at such an angle that when the tip was brought to the boundary of the intergrowths between the (010) face of one crystal and the (010) face of the second crystal, the bracket did not touch either crystal (Figure 2.18).

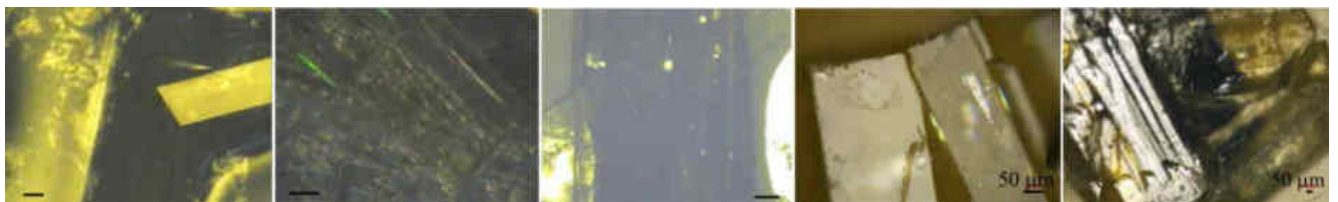


Figure 2.18 Crystal intergrowths prepared for the experiment. Scale bar 50 μm

In one of the experiments (Figure 2.19), which lasted almost 6 hours, the phenomenon of dislocation growth was recorded at such a boundary between crystals.

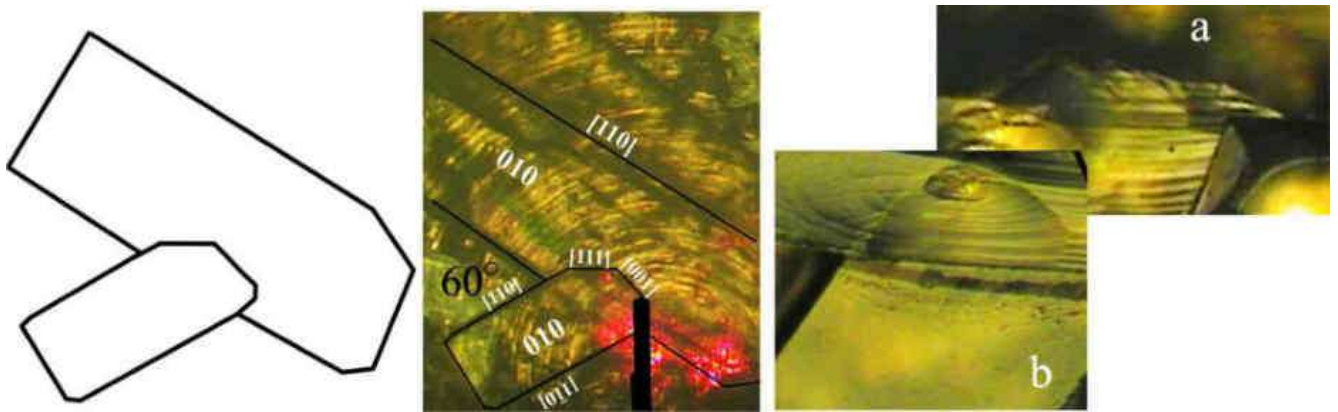


Figure 2.19 – Intergrowth of crystals and optical image of the boundary between two intergrowing crystals before experiment (a) and after 6 hours of AFM experiment (b)

2.4 Calculations of the growth rate and fluctuations

An important result of the work is the calculation of the growth and dissolution rate of elementary steps along the surface (tangential rate), as well as the normal growth rate of a facet section, from AFM images.

In crystal growth experiments, temperature has always been a factor in supersaturation modelling. It is indeed convenient when other forms of modelling are not available. AFM does not allow temperature to be varied over a wide range, but a much more accurate parameter is available – the tangential rate of the steps. It characterises the supersaturation in the immediate vicinity of the growth step and is measured with very high accuracy in the AFM. The essence of the rate measurement method is to carefully collect the coordinates of a set of points at the edge of each monomolecular and macrostep in the scan area at each instant, and to further process these data. With any type of AFM, the result of the work is a file in which each scan is associated with an array of xyz coordinates of all the 256×256 points passed. However, it is impossible to isolate only the coordinates of the points on the edges of the steps in this array, let alone find them in the next array. The rate cannot be calculated

automatically: the number, profile and direction of the steps are unique. It is therefore necessary to manually set the points to take the coordinates on each image.

2.4.1 Obtaining data from AFM images

1. The direction of the step movement, its shape and propagation principle were determined. This was necessary to develop a special grid that was superimposed on each image (Figure 2.20). The grid was a system of numbered parallel lines oriented at an angle or had a more complex radial structure. The grid lines should be perpendicular to the front of the step movement. The lines were drawn as densely as possible; they could be drawn at 35, 43, 55, 100 and 500 nanometres, depending on the size of the scan window.

2. The point of intersection of the step contour and the i -th grid line at time t_1 was assumed to be the point of intersection of the new position of the same step with the same i -th grid line at time t_2 .

3. The coordinates (x_i, y_i) of each point on the profile of each step were recorded at 35, 43, etc. nanometres. Depending on the number of steps for each image, the number of coordinates could reach one and a half thousand. The data were entered into *Excel* sheets in cells whose position was determined according to three parameters: the grid line number, the image number and the step number. Sometimes the data for different parts of the scanned area were recorded separately, and even the rates for them were reflected in different graphs. For example, scratches affected the behaviour of the steps to the left and right of the top of the hillock differently, because in one case the tip moved in the direction of the steps, and in the other it moved against them, creating a different number of defects. The distribution by rate turned out to be bimodal and the data had to be split into "left" and "right" data.

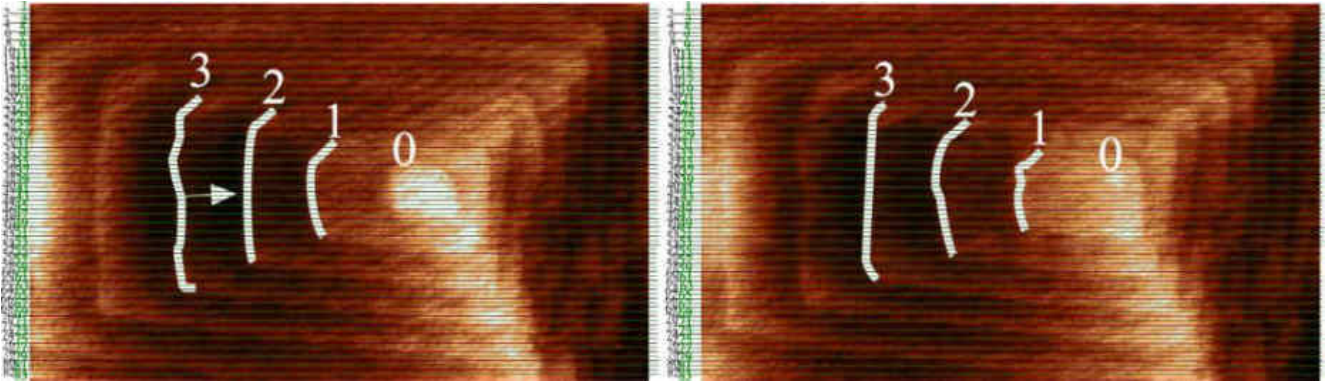


Figure 2.20 – Resolution at 0, 1, 2, etc. steps – contraction of the steps towards the centre of the dislocation. The time interval between images is 4.5 minutes. A simple numbered grid is shown; a similar vertical grid has been superimposed to measure the growth of the upper and lower parts of the steps

On the hillock in Figure 2.20, the data have been taken separately for the left steps and correspondingly separately for the right, top and bottom steps. This was done to simplify the grid, although it is clear that the first step on the right, the first step on the left, the first step at the top and the first step at the bottom are parts of a closed step emitted by the growth analogue of the Frank–Read dislocation source. In Figure 2.20 it is clear that in the next picture the step could become shorter and start from a different grid line, which was immediately reflected in the tables (Figure 2.21): if the step is drawn back to the top that emitted it during dissolution, becoming shorter and shorter, the column of numbers also becomes shorter.

grid line number

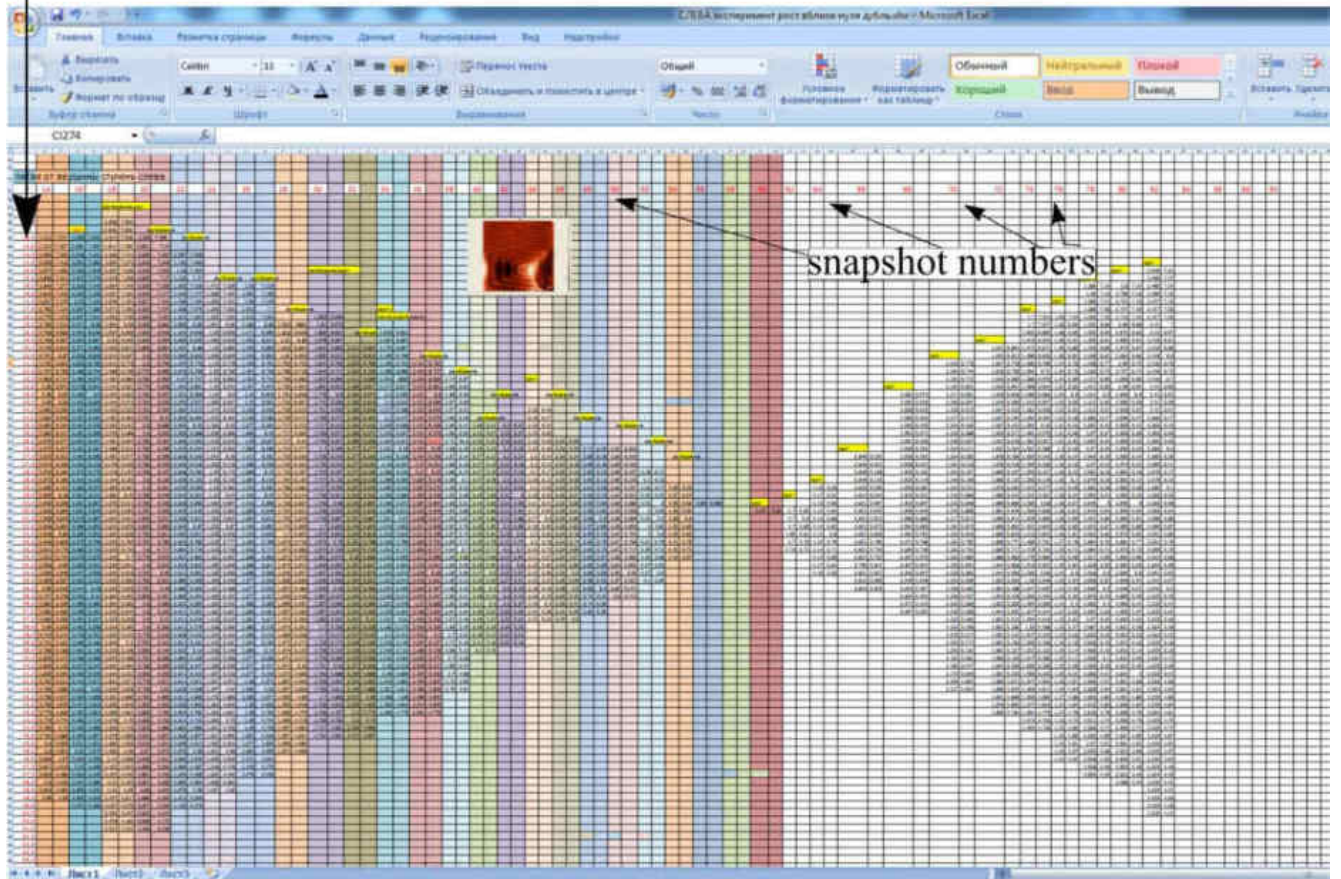


Figure 2.21 – An example of a table of data for the points on the left edge of the fifth step from the top in Figure 2.17. The jumper in the centre shows that the step disappears completely, but after the system passes the saturation point (58th snapshot) it reappears and starts to grow, its left edge lengthens and the column of numbers becomes longer

2.4.2 Accuracy of coordinate data

For a 1920×1680 monitor, the minimum distance that a mouse sensor (with a CPI of 400) can detect is 0.0625 mm. Thus, for an AFM image occupying almost half the screen and corresponding to an AFM size of 15×15 μm^2 (the scratch experiment), this mouse step corresponds to 6 nm. This is the accuracy of data acquisition in the XY plane. For the hill in Figure 2.1, which grew without any influence, the accuracy of data acquisition was 2 nm. In the experiment with impurities, the size of the scanning area was quite large – 50×50 μm^2 , and data was acquired every 500 nm. Therefore, the

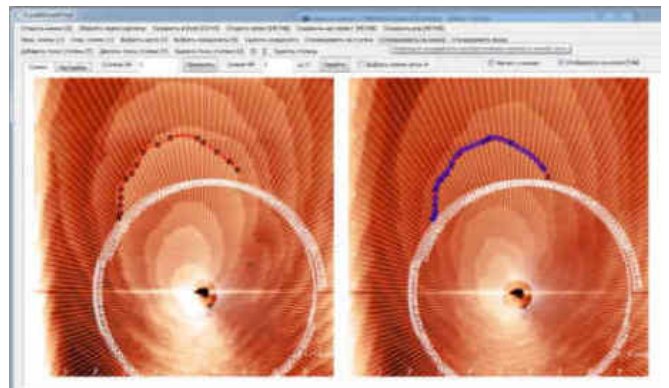
accuracy in the lateral plane was also rough – 60 nm. The best accuracy of data acquisition in the lateral plane was achieved on a $2.5 \times 2.5 \mu\text{m}^2$ area and was 0.01 nm, but this was the only short experiment in this thesis where high quality images of the growth of such a small area were obtained (Figure 2.29). Section 2.6 explains why it is not always possible to scan the growth and dissolution process on small areas.

Failure to acquire data on all steps in the scan window will shift the average rate value, so for reliability it is necessary to capture as much detail in the image as possible and to acquire each step in equal detail. In the scratch experiment, coordinates were acquired along each step every 55 nm, in the experiment shown in Figure 2.20 – every 35 nm, in some experiments – every 100 nm, and so on.

The exponential nature of the relationship between the distances from the surface and the force of the tip–sample interaction gives a very high resolution of the AFM in the normal direction. The accuracy of data acquisition in the normal direction is then much higher than in the lateral plane – 0.1 Å. However, this accuracy does not make much sense, as Figure 2.3 shows how much interference there is in the measurement of the height of an elementary step on the (010) surface, which is determined by the average value and is 3.5 Å.

2.4.3 Optimization of the data production process

In cooperation with mathematicians at Syktyvkar State University have developed an application with *Python* that does not record the coordinates of each point, but generates them at the intersections of the step profile drawn by the operator using a much smaller number of points with the grid lines. As the grid can be drawn very densely by machine, the application allows a large number of coordinates to be obtained in a short time, but it is still in the debugging stage. All the data presented in



this paper has been obtained manually.

2.4.4 Calculation of the rate and its fluctuations

1. Using the coordinates of the i -th point at time $t_1 - (x_{1i}, y_{1i})$ and its coordinates at time $t_2 - (x_{2i}, y_{2i})$, the distance travelled by the point during the 4.5 minutes between images was calculated and, accordingly, its rate v_i . In order to take into account the changes in the lower part of the surface during the scanning of the upper part, a time correction $c(y)$ was introduced into the formula for the rate of the i -th point, depending on the input data of the experiment and the y -th coordinate:

$$v_i = \frac{\sqrt{(x_{2i}-x_{1i})^2-(y_{2i}-y_{1i})^2}}{(t_2-t_1)+c(y_{2i})} \quad (2.1)$$

2. For each pair of images, empirical distributions (probabilities) of the tangential rates of all stages were constructed. For example, for the experiment in Figure 2.20, this took 38 Excel sheets. Each distribution was approximated by a lognormal distribution curve using the method of least squares (Figure 2.22). The lognormal distribution was chosen based on examples of its use in scientific problems because of the asymmetric nature of the distribution and the influence of factors that have a one-sided effect on the spread of values. In this case, such a one-sided factor is the supersaturation of the solution. The average tangential rates \bar{v} have been determined as the values of the mathematical expectation of the distribution at each instant. Their fluctuations δv represent the standard deviation of the lognormal distribution.

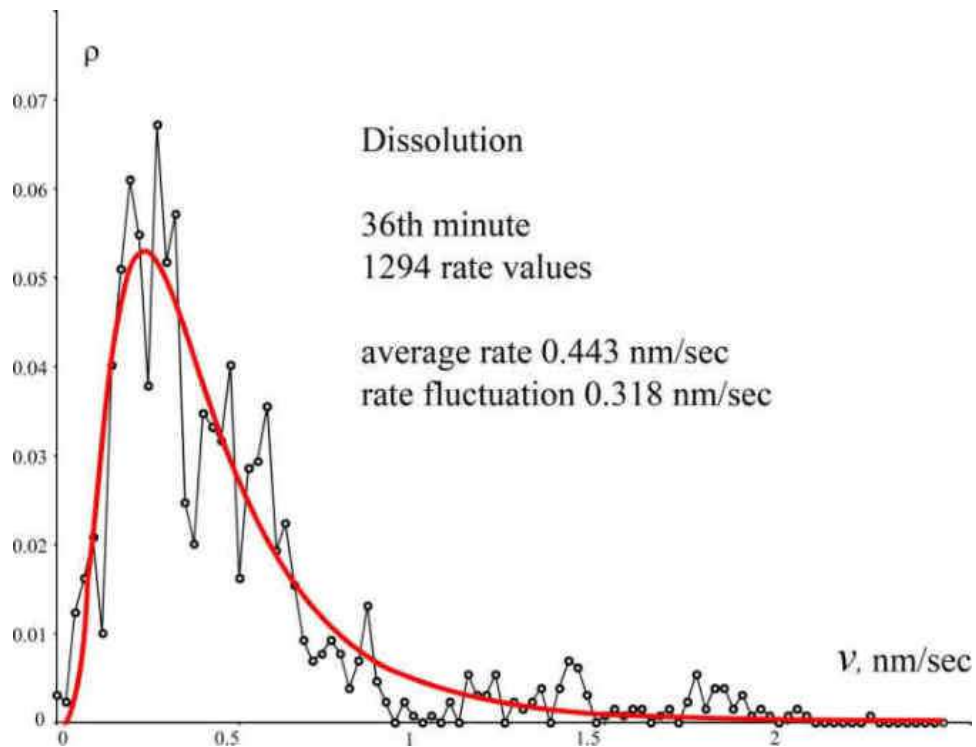


Figure 2.22 – Example of plotting the distribution of points on the steps by rate. Approximated by a log normal distribution (red line). Near equilibrium, rate fluctuations are often comparable to the rate value itself

3. The average rate values determined for each pair of images were plotted sequentially on a time graph, and the fluctuation values at each time point were plotted up and down as a confidence interval (Figure 2.23). Near equilibrium at the nanoscale, the fluctuations are large and a dissolution step may grow in one part at one moment and then dissolve again: this sudden growth during dissolution was considered a deviation and its rates were added to the dissolution fluctuations plotted upwards. Similarly, the recorded episodes of dissolution during growth were considered anomalies and added to the growth fluctuations plotted downwards. In this way, fluctuations in the tangential rate of points along the entire front of each monomolecular step in a given area were recorded using atomic force microscopy.

4. Since the rate obtained at each point is a characteristic of supersaturation directly at the growing surface, and the scale of the measurements is nanoscale, the AFM

is capable of registering thermodynamic fluctuations within the Gibbs approach (Rudoï, Sukhanov, 2000).

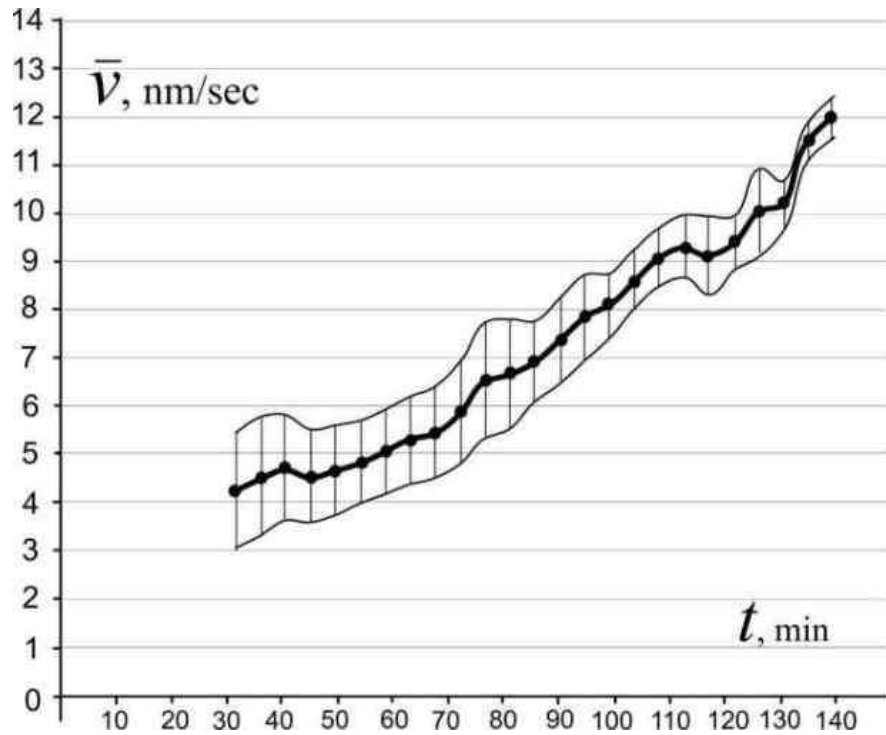


Figure 2.23 – Example of a graph of the average tangential rate of the stages during a 140 minute test with contamination. Each highlighted point was calculated using the method shown in Figure 2.22. In total, over 16 thousand rate values were used to plot the graph

Similarly, for each image, the distances between the steps (terrace widths) were calculated for each point on the grid lines. As shown in Figure 2.22., distributions by terrace width were constructed – another 38 sheets for the experiment given as an example. The mean distances \bar{x} and their fluctuations δx were calculated. They were needed to calculate the normal growth rate.

The normal rate R is equal to the product of the tangential rate v , the height h and the step frequency ε :

$$R = v \cdot \varepsilon \cdot h \quad (2.2)$$

Steady state growth is characterised by a constant concentration gradient that generates the zero fluctuations of the steps and, therefore, a constant normal growth rate

R . As for the fluctuations of the normal growth rate δR , it is proportional to the error of the fluctuations to the steps δR , which is constant and therefore its error is zero. The fluctuations of the normal growth rate δR are therefore equal to 0 in the steady state.

To find δR , formula (2.2) must be transformed using the formula for the relative error of the product:

$$\frac{\delta R}{\bar{R}} = \frac{\delta v}{\bar{v}} + \frac{\delta \varepsilon}{\bar{\varepsilon}} \quad (2.3)$$

The method for obtaining the rate v and its fluctuations δv is described above, which allows us to calculate the first term of formula (2.3). The second term: since the frequency of the steps ε is related to the height h and the distance between adjacent steps, $\frac{\delta \varepsilon}{\varepsilon}$ is equal:

$$\frac{\delta \varepsilon}{\varepsilon} = \frac{h \cdot \delta x \cdot \bar{x}}{\bar{x}^2 \cdot h} \cdot \frac{\delta x}{\bar{x}} \quad (2.4)$$

where \bar{x} is the average distance between adjacent steps, δx is the fluctuation of the distance between steps.

Having calculated the normal rate according to (2.2), and knowing both terms from formula (2.3), we can determine the value of the fluctuations in the normal growth rate:

$$\delta R = \bar{R} \cdot \left(\frac{\delta v}{\bar{v}} + \frac{\delta x}{\bar{x}} \right) \quad (2.5)$$

The normal rate plots were also plotted together with the confidence interval of the corresponding fluctuations.

Despite the fact that AFM is a truly three-dimensional method and measures the z -coordinate, it is impossible to compare this coordinate in two adjacent images because the instrument selects a new zero on the z -axis in each image. It is possible to approximate the normal rate by knowing the height of the steps and the number of steps that passed through the section during the observation time. Previously, in optical observations or interferometric experiments, the normal rate was determined by direct measurement of the facet displacement. The normal rate method described above gives a very accurate value for a real crystal in solution. Formally, according to the rules for

calculating errors for a formula value whose components are measured, the error in the normal rate for an experiment with a scratch on the top of a hillock is 0.01 nm/sec.

2.5 Artefacts. Instrumental influence on the surface processes and correctness of experimental results

2.5.1 Artefacts

An AFM image artefact is any detail that is not inherent to the crystal surface at the given time, but is present in the image. The image is formed by reading the movements of the tip, and if the tip makes the wrong movements, then false objects and effects will appear. The first of these are darkening and brightening. They are associated with the tip jumping (brightening in Figure 2.24, shown by the black arrow) due to the need to climb an obstacle, and its dips (darkening in Figure 2.24, shown by the white arrow) due to a sharp lowering when jumping off a step or 'squatting' before jumping. Physically, of course, the tip does not go below the level of the step, as shown by the red curve in the figure; in fact, this is a sharp decrease in the interaction force when the tip jumps off.

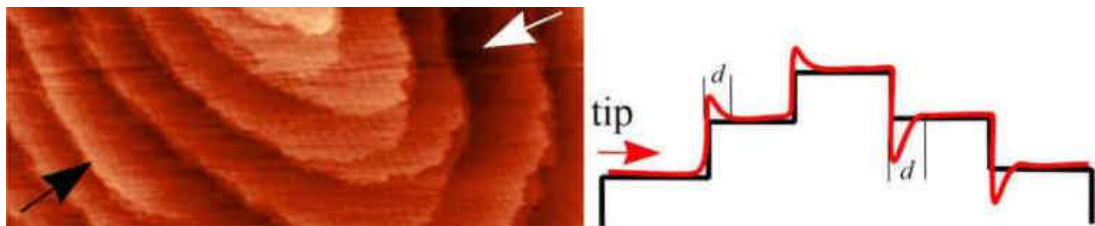


Figure 2.24 – Explanation of the appearance of pseudo-rise (light areas) and pseudo-descent (dark areas) as the tip moves from left to right. The profile also decreases in front of high obstacles, which can be clearly seen when measuring the height of the steps in Figure 2.3

The interaction force changes so much that when the tip passes through very deep holes, it forms broaches in both directions (Figure 2.25).

Artefacts, the causes of which must be well understood, are also compressions. The cantilever with the tip is attached to the end of a flexible bracket, the tip is brought into contact and the bracket no longer rises, it can only bend. If the surface of the crystal has grown strongly upwards, the cantilever will be so compressed that it can no longer bend and the relief at the highest point will practically not be drawn – a soapy area or highlight will appear (arrows in Figure 2.26), which will expand more and more as the surface grows.



Figure 2.25 – Artefacts caused by the tip falling into dislocation channels of considerable width

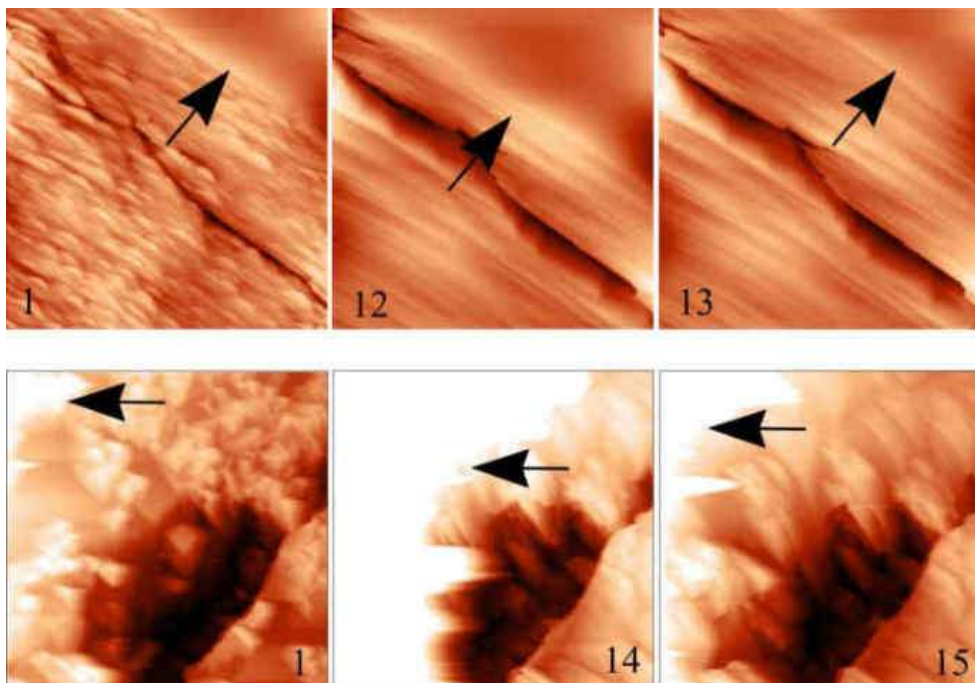


Figure 2.26 – Artefacts caused by the cantilever console being pressed by the highly elevated part of the scan area (indicated by arrows). Upper images – the fusion boundary with the raised upper twin, lower images – the growth to the left of the crack is very intense and the surface is raised

In order to continue the experiment, it is sometimes helpful to leave and re-enter the contact, and then with the new shooting parameters the console is not pressed as hard, despite the difference in height (for example, compare pairs 12–13 and 14–15 in Figure 2.26).

There are several other types of minor and interpretable artefacts. But the most important part of this section is to explain the reason for the appearance of such effects, which can be seen on the left in Figure 2.27. At low supersaturations close to equilibrium, in the presence of elementary steps on the surface, the crystal grows due to the incorporation of building units into the fractures at the ends of the steps. The edge of the step grows and it appears that the step is moving. The particle can attach to the terraces between the edges of the steps, but at low supersaturations it is likely to break away quickly.

At the edge of the step, the particle is also not immediately fixed, everything depends on the local supersaturation in the solution layer directly above the edge of the step. AFM records processes on the growth surface at the scale of thermodynamic fluctuations, which have a major impact on obtaining a high quality image. If the growth unit is still in the process of selection and has not completed the process of attachment, then the AFM tip will not clearly image it at the moment of passage. This means that if there is a fluctuation in the concentration of a substance on the scale of about 10 micrometres above the surface, the result of the scan will be an uninterpretable image, as shown in the first image above. A short time ago, however, the image in the same area was clear (Figure 2.27, right). After some time, the hill was again well registered, but at a different scale and is not shown in the figure.

If a local region (approximately 1.5 μm in diameter) of reduced supersaturation (or saturation) was created above the monomolecular steps, and the particles had not completed their attachment or detachment at the time the tip passed, this would appear visually in the AFM images as blurred boundaries of the step edge (arrows in Figure 2.28 (a)). After 4.5 minutes, the end of the attachment or detachment process coincided with the moment the tip passed, and the blurred areas of the step became clear again (Figure 2.28 (b)).

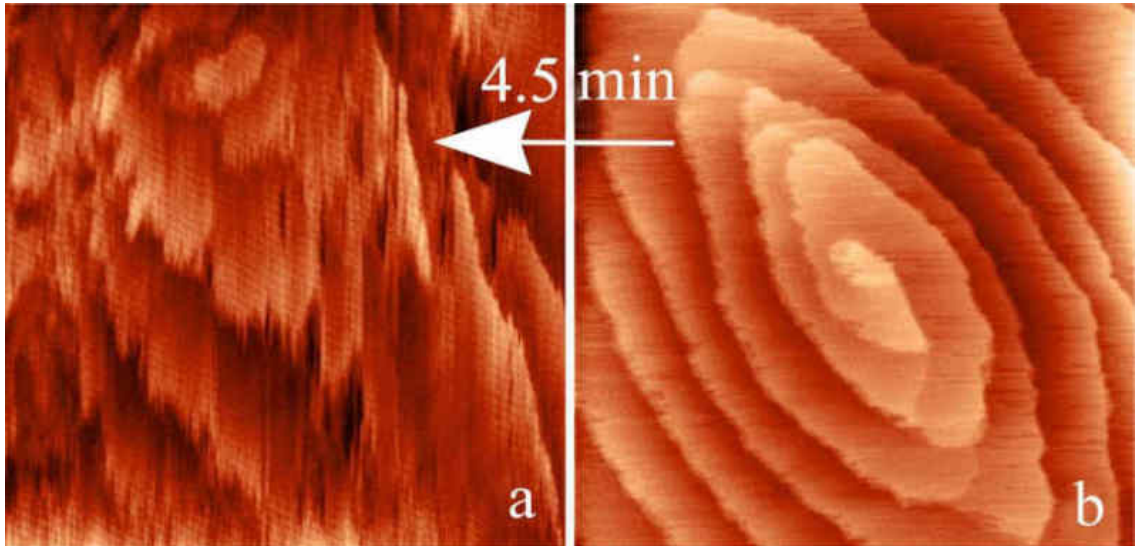


Figure 2.27 – Poor image quality due to incomplete fusion (a) and the same area 4.5 minutes ago (b). Window size $7 \times 7 \mu\text{m}^2$

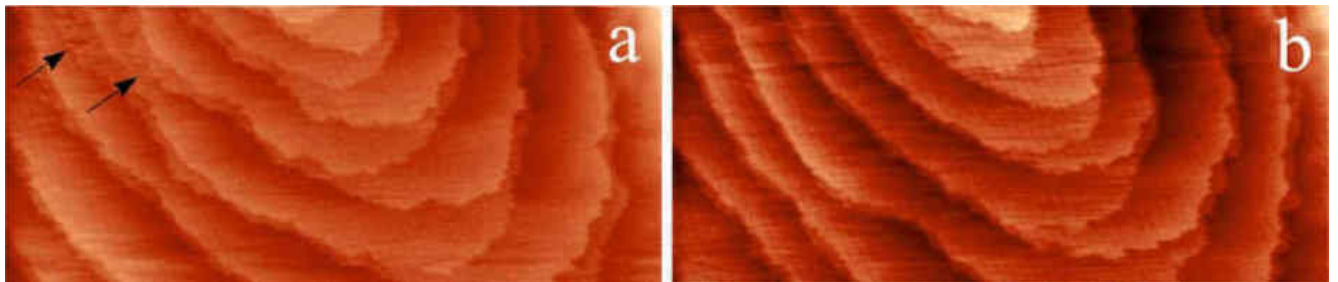


Figure 2.28 – Blurred edge of a step (arrows in (a)) due to local fluctuation and the same steps after 4.5 minutes (b). The window width is $10 \mu\text{m}$

Observations show that below a certain scan window size, surface processes in solution are unlikely to be recorded for the physical reasons described above. The nature of the substance, the characteristics of the instrument and the experimental conditions have a large influence; there are impressive examples of AFM observations at small scales in the literature (Vekilov, Alexander, 2000). Figure 2.29 shows the author's high-quality images of one-molecule-high steps growing on small areas in a solution of dioxidine. The author's monograph on AFM studies of growth and dissolution of inorganic salts includes experiments on growth on areas of 1.4×1.4 and $3.5 \times 3.5 \mu\text{m}^2$ (Piskunova, 2007). For long-term experiments with dioxidine, it is better not to set the

window size below $7 \times 7 \mu\text{m}^2$. Even if the processes are displayed qualitatively, a small scan window is not very useful for elucidating the mechanism of the phenomena because the steps quickly leave the observation zone.

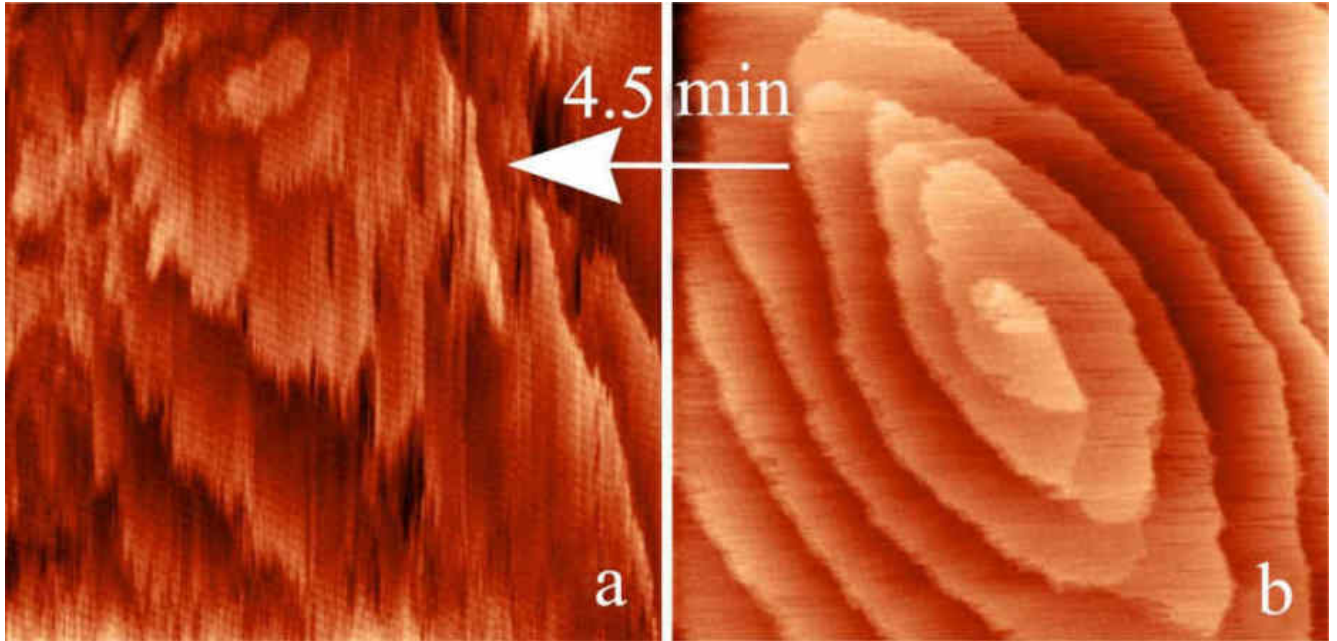


Figure 2.29 – Qualitative images of growth steps in a dioxidine solution in areas of $2.5 \times 2.5 \mu\text{m}^2$ and $4.7 \times 4.7 \mu\text{m}^2$

2.5.2 Instrumental influence on the processes and layer-by-layer growth kinetic

In addition to artefacts (the creation of unreal details in the image), an AFM, like any direct observation device, can also affect the processes themselves. In the case of AFM, the situation is further complicated by the occasional physical contact with the tip and the small scales at which imaging is performed. Bearing in mind that there is no other, more careful method of recording in solution at the molecular level, and adding to the results the influence of the instrument in each specific case, we can say that the overall result supports the main conclusions of the work.

Mechanical influence of the tip

The electrostatic interaction results in the existence of an adsorption layer on the crystal surface in which (1) the migration of the building units and (2) their incorporation into the crystal takes place. Some of the units leave the adsorption layer completely. Does the tip interfere with these processes? Scanning is done by reading the position of the tip at 256 points on each of the 256 lines that the tip passes through in 4.5 minutes. The tip is in contact with a particular point on the surface in this area for 0.004 seconds. Moreover, physically this is not contact – the tip is moved to a distance comparable to the range of interatomic potentials, the force is measured, and then the feedback keeps this force constant, preventing the tip from affecting the surface, even if it jumps off the hills. The distance between the points on the surface where "contact" occurs in the scratch experiment, for example, is 60 nm. This means that, taking into account the diameter of the tip, every 68 molecules from the adsorption layer along the edge of the step can freely attach to the surface of dioxidine without any interference, even where the tip is currently passing, which may affect 12 molecules, followed by another 68 molecules freely attaching. For the remainder of the scanning time, the tip does not return to the passed lines, and further attachment of building units in these areas occurs even more freely. The kinetic features of the evolution of the surface are determined on the basis of calculations in which the data are averaged over the entire scanning window, which generally allows us to trust the conclusions drawn.

The tip moves in one direction (e.g. from left to right) and it appears that as it moves, its contact with raised areas of the relief and the ends of the steps produces defects, mainly edge dislocations. However, due to feedback, the effect described does not occur even in dioxidine, a crystal with relatively weak bonds. This does not apply to special effects, such as in the scratching experiments, where edge dislocations actually occurred in the absence of feedback due to the rigid directional guidance of the tip.

Evaporation effect

The cell containing the solution has a capacity of just over 1 ml, a diameter of 1.9 cm, a crystal is usually placed in the central part and a prism with a fixed cantilever is immersed in the solution above (Figure 2.30 (a)). To estimate the amount of liquid evaporated through the free surface of the solution during the experiments, an experiment was carried out in which a structure replicating the experimental conditions was placed above the cell on the scale (Figure 2.30 (b)). The loss of mass of the solution was determined to an accuracy of 4 decimal places. The scale was not completely closed in order to estimate the maximum evaporation effect. As the duration of the experiments in the work ranges from 70 to 360 minutes, the simulation of evaporation at maximum and minimum temperatures also lasted 360 minutes. It was found that evaporation is uniform and does not depend much on whether an undersaturated or supersaturated solution is evaporating. Evaporation is stronger with increasing temperature, in just 6 hours 11% of the liquid evaporated at 19 °C and 14% at 29 °C. The blue curve in Figure 2.30 reproduces the conditions of the experiment from Section 3.1.2 of Chapter 3, where a slightly undersaturated solution was poured onto a large number of crystals, they first dissolved for 2 hours, then transitioned to growth on the same crystals for 1 hour. The dissolution and growth curves in the described experiment did not show a tendency towards growth (Figure 2.31), indicating that evaporation does not have a dramatic effect on the observed processes, it only moves the crystallisation. In the experiment in Figure 2.31, the depletion of the solution should have reduced the rate by the end of the experiment, but as can be seen from the graph, the evaporation was such that it allowed the rate to be maintained at a constant level.

Effect of evaporation and tip movement on the solution and surface processes

The scale of the AFM allows fluctuations in the tangential and normal growth rates to be recorded.

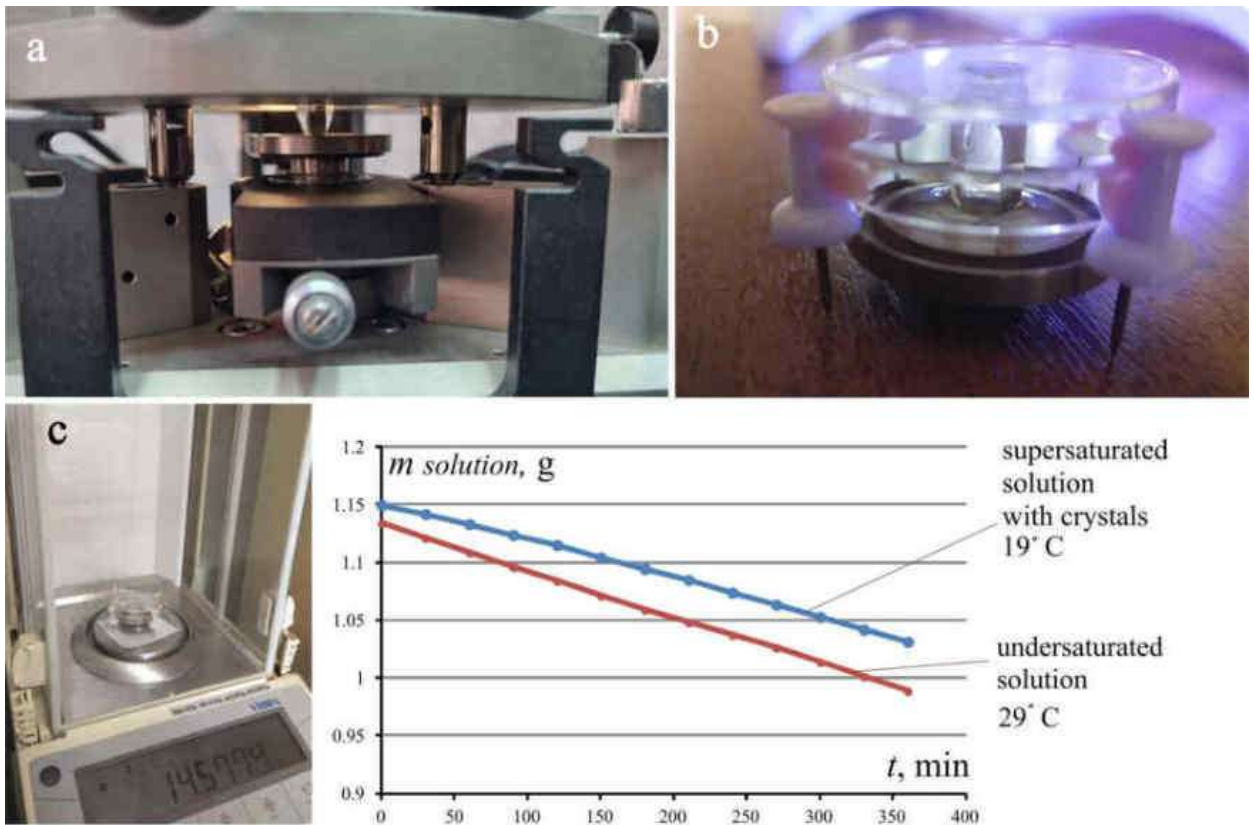


Figure 2.30 – Estimation of evaporation in the ASM cell over 6 hours due to evaporation

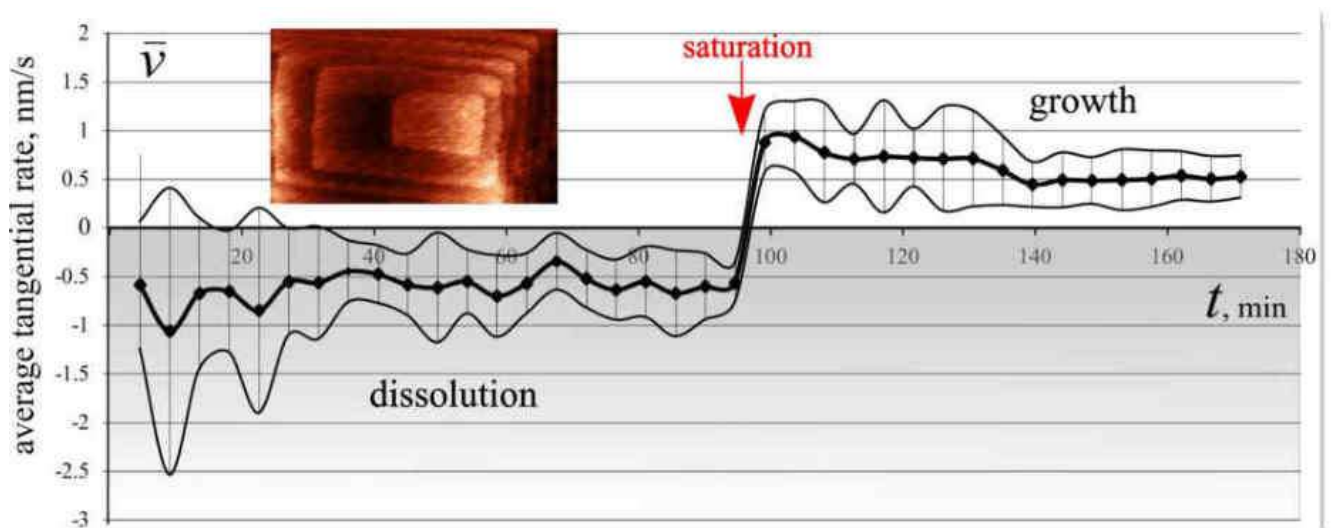


Figure 2.31 – Behaviour of the dissolution (left part of the graph) and growth (right part of the graph) rates, indicating that evaporation in the AFM cell does not have a serious effect on the processes at the surface

They are caused by local fluctuations of the concentration near the surface and are not caused by the instrumental influence, since fluctuations of the contact area of the tip with the surface, fluctuations of the force of their interaction and fluctuations of laser heating in the AFM (Rekhviashvili, 2001) are 1–3 orders of magnitude smaller than those shown in the work. If the fluctuations were caused by these factors, they would not differ in different experiments or even in different parts of the crystal in the same experiment.

More pronounced oscillations of the scanning head, which moves the tip, should affect the recorded processes. Capillary perturbations due to arbitrary deformation of the free surface of the liquid, which manifest themselves as a pair of waves running along the surface, only occur at small wave numbers (Andreev et al., 2000). The wave number is the number of spatial wave bumps per 2π metre. If the AFM tip sweeps $15\ \mu\text{m}$ in one direction in 1 second, the wave number must be large. In addition, the block stops between scans and the periodicity is interrupted. The resulting short wavelength perturbations are stabilised by surface tension forces. The appearance of resonance or a standing wave by reflection from the meniscus walls, which could cause the appearance of areas of condensation and rarefaction of the substance density, is impossible because the oscillations of different parts are not coordinated, most of the column of a small amount of liquid moves together with the block, the angles of the meniscus on different sides are not the same.

However, the movements of the scanning head affect the diffusion processes in the solution. Let us estimate their contribution. The main consequence of significant mixing of the solution is the rapid replenishment of the substance deficiency during growth and the removal of its excess across the step during dissolution, i.e. the rapid equalisation of concentration gradients. This means that, in contrast to the measured value (the black middle curve in Figure 2.32), growth with mixing should be smoother (the smoothed red curve in Figure 2.32, sign "1"). The rate fluctuations during mixing are not only smoother, they should also be smaller in amplitude (the sign "2" in Figure 2.32). Since the black curve obtained in the experiment is the growth under conditions of instrumental mixing, in order to present the results of the experiment without mixing, it

is necessary to add the black and red curves from Figure 2.32 (a). Figure 2.32 (b) shows the result of the addition: indeed, if the oscillations of the black curve in Figure 2.32 (a) are indeed smoothed and reduced in magnitude, then in the absence of mixing its oscillations should be more pronounced and even larger in magnitude. It is therefore clear from Figure 2.32 (b) that if we remove the mixing of the solution, the conclusion of the experiment about the oscillatory nature of the rate of overgrowth of the surface around the scratches and the unprecedented rate oscillations become even more obvious.

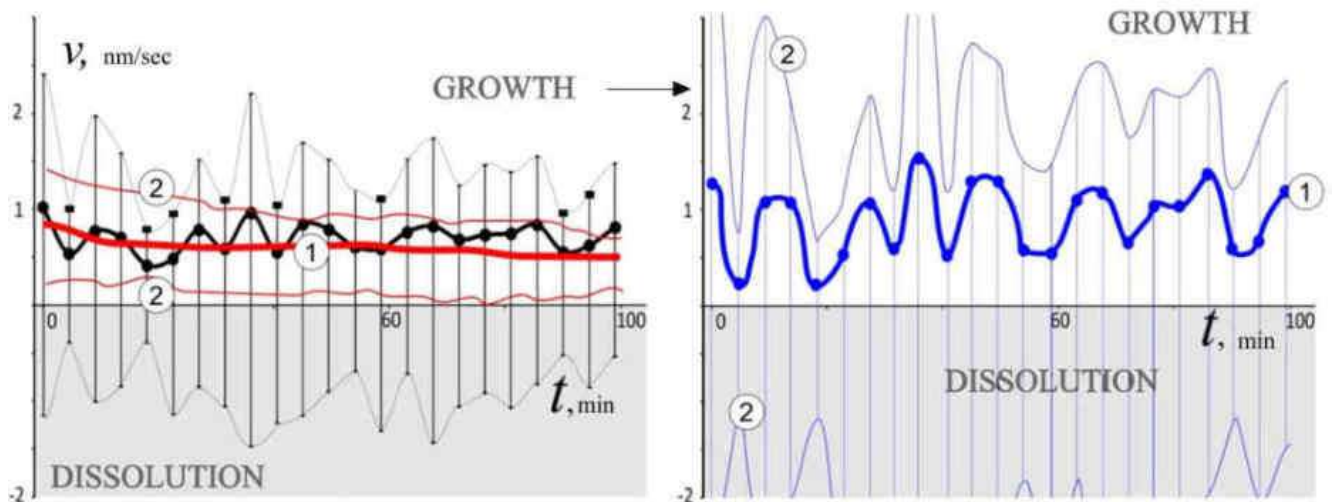


Figure 2.32 – Effect of solution mixing by rapid movement of the AFM tip on the layer-by-layer growth rate and its fluctuations: (a) – black lines reflect the experimental results, red lines show that, hypothetically, growth with mixing should be more uniform and with much smaller fluctuations; (b) – resulting rate and fluctuation curves when the effect of the device is removed

The next experiment is the transition from dissolution through the saturation point to growth on the same steps of the dislocation hillock. Figure 2.33 shows that stirring affects the dissolution from the first minute – it does not allow the substance to accumulate above the surface, which means that the dissolution is more intense from the start (the red curve below the black one) and does not show significant fluctuations (Figure 2.33 (a), sign "1"). If the dissolution is more intense and the solution is stirred, then less substance accumulates above the surface, which means that the jump in rate

after the saturation point is smaller – Figure 2.33 (a), sign "2". The growth should also be more uniform (Figure 2.33 a, sign "3") as the deficit of substance is replenished by the influx of substance from the volume of the solution due to stirring. The addition of the red and black curves is shown in Figure 2.33(b): if the oscillations of the black curve in Figure 2.33(a) are actually aligned, this means that in reality these oscillations are even more intense, as shown by the blue curve in Figure 2.33(b). Figure 2.33(b) reinforces the main conclusion of the experiment about the irreversibility of growth–dissolution: the oscillations of the rate during dissolution became even more intense (indicated by arrows), the growth jump after the saturation point became even higher (Figure 2.33(b), sign "4").

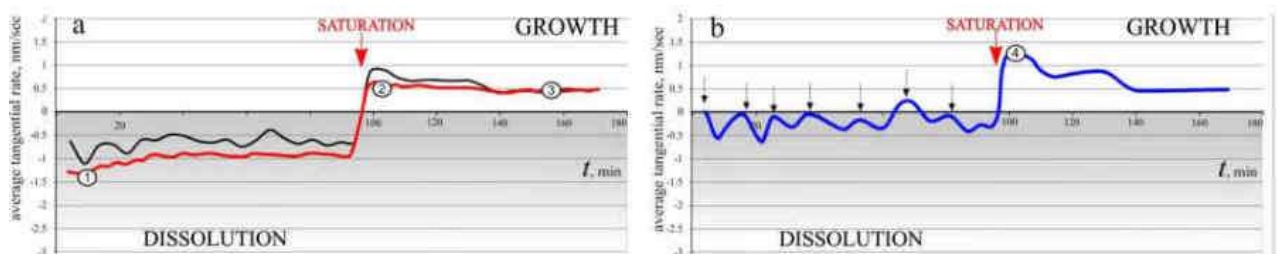


Figure 2.33 – Effect of fast movement of the AFM tip on the tangential rate: (a) – black line – result of the experiment, the red line shows that the hypothetical dissolution with forced stirring is more intense and uniform, the jump at the beginning of the growth, on the other hand, is smaller because the substance has not accumulated above the surface; (b) – new curve of the average tangential rate in the absence of instrumental stirring of the solution

Taking into account the stirring of the solution will also change the fluctuation plots. In Figure 2.34 (a), next to the black curve of the experiment, there is a red curve showing the hypothetical effect of stirring on the fluctuations: it is not known whether they are smaller in amplitude, but they certainly do not fluctuate as much (Figure 2.34 (a), sign "1"), since the concentration levels equalise over time. At the end of the third hour, the red curve coincides with the experimental curve – Figure 2.34 (a), sign "2". Figure 2.34 (b) shows the result of adding the red and black curves from Figure 2.34 (a).

Significant fluctuations are observed: if the fluctuations of the black curve in Figure 2.34 (a) are forcibly smoothed out, then in reality they are more intense. At the end of the experiment, practically stationary growth is observed. Thus, taking into account the forced stirring of the solution, the difference in the behaviour of growth and dissolution becomes even more obvious, reinforcing the conclusion about the irreversibility of growth and dissolution.

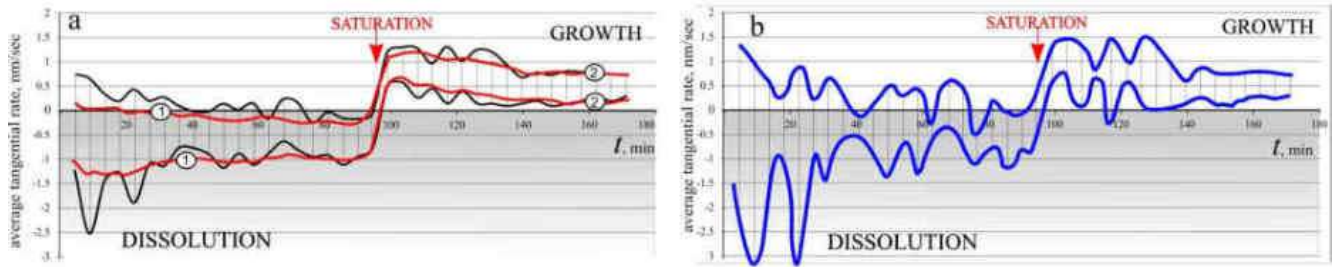


Figure 2.34 – Effect of stirring the solution by rapid movements of the AFM tip on rate fluctuations: (a) – black line – experimental result, red line shows that hypothetically the fluctuations should be more uniform as the gradients equalise in time; (b) – new rate fluctuation curve in the absence of instrumental influence

In the example experiment, growth events were recorded during global dissolution and single dissolution events when the system as a whole switched to growth. Without forced stirring, such local areas of increased or decreased substance concentration – concentration fluctuations – should be even more pronounced. The fluctuations detected in the scratch experiment should therefore be even more pronounced in the absence of forced stirring. In other words, instrumental stirring of the solution has an effect, but it does not create new phenomena, it only weakens the phenomena that are actually recorded.

Laser heating

Methodical experiments allowed us to determine that during three hours of laser operation the maximum increase in solution temperature was 0.4°C (thermocouple accuracy 0.1°C). Most measurements showed no increase in temperature, let alone an

avalanche. Effects of this type are always monotonous (Sebisi, Bradshaw, 1987) and heat transferred to the solution over a long period of time should lead to a significant increase in solution temperature, which does not happen. This means that the heat is successfully removed by the structural elements of the scanning unit and is also dissipated by mixing of the solution due to the movement of the scanning head. The laser heating does not stimulate any additional phenomena on the surface: on a larger scale, the area where the 3 hour scanning took place is not released in any way, although local undersaturation could be expected in the column of solution above it if the laser heating were not dissipated in any way. However, the heat transferred to the solution by the silicon cantilever can affect the rate of the steps. The maximum effect of laser heating on the experimental results (e.g. an experiment with a transition from dissolution to growth through the saturation point) can be hypothetically represented on the graph in Figure 2.35(a), where the black line is the experimental results and the red line is the hypothetical effect of laser heating. Initially the effect of the laser is minimal, so the red curve almost coincides with the black curve. After an hour and a half, heating should increase dissolution so that the red curve falls below the black curve (Figure 2.35, sign "1" in (a)). Since dissolution is more intense near the saturation point, more substance accumulates above the edge, so the growth jump after passing the saturation point is higher (Figure 2.35, sign "2" in (a)). However, after the jump, heating should greatly reduce the real rate. After three hours, the heat released by the laser increases even more, making the growth less and less intense (Figure 2.35, sign "3" in (a)). If we assume that the laser effect is maximal, then at the end of the third hour the growth should turn into dissolution (Figure 2.35, sign "4" in (a)), which was not observed in reality.

If this is how the laser shifts the real (no laser effect) rate, then the black line is the result of subtracting the red curve from the real (no heating) curve. This means that to construct a real curve without heating, it is necessary to add the two curves from Figure 2.35: indeed, if in (a) the black curve to the left of the saturation point is already underestimated, then in reality it should be higher. Figure 2.35 (b) shows a hypothetical curve of the average tangential rate in the absence of the thermal effect of the laser. As

can be seen, the main conclusion about the asymmetry and irreversibility of the growth–dissolution process is only strengthened.

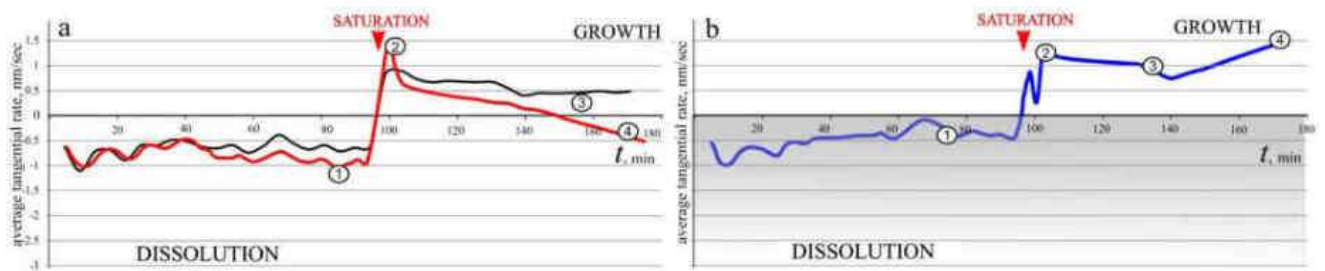


Figure 2.35 – Effect of laser heating: (a) – black line – experimental results, red line – hypothetical effect of laser heating. (b) – Result of adding the red and black curves, i.e. the hypothetical curve of the average tangential rate in the absence of the laser heating effect

The effect of the laser cannot be denied, but it is not dramatic. Taking into account the maximum possible effect of this kind only strengthens the main conclusions of the experiment. The main point is that the laser heating does not have a local effect, i.e. it does not cause local undersaturation and the appearance of a pit. This is prevented by mixing the solution, which equalises the thermal gradients.

2.6 Applicability of *in-situ* AFM results to reconstruction of crystal growth in nature

In order to detect nano- and microscale evidence of layer-by-layer growth and dissolution on defects in natural crystals, an *ex-situ* study of the growth faces of pyrite, alabandine, quartz and some other crystals was carried out. Typically, a small crystal or a section of the growth face of a large crystal was simply fixed in the AFM cell. The samples were pre-cleaned in an ultrasonic bath. In general, AFM studies of natural crystals are a very complex task because even the most ideal of them have undergone transfer, the rest are covered with oxidation films, have traces of dissolution, chips,

abrasions, etc., which sometimes make AFM imaging impossible. However, even on the basis of the results of successful photographs, it is impossible to carry out large-scale reconstructions, but on the basis of the results of direct observations on model crystals, some conclusions can be drawn about the characteristics of the final stage of growth of a particular natural crystal. How accurate is such a comparison? Is it possible to extend the results obtained on dioxidine, a model substance with a molecular structure, to natural crystals? Most mineral crystals are substances with ionic-covalent bonds (oxides, silicates) or a metallic type of chemical bond. In addition to the types of bonds, symmetry and size of the building units, they differ from model crystals in the conditions of formation, physical properties of the crystal-forming environment, duration and multistage transformations, etc.

Ex situ AFM studies of crystal surface morphology have shown that all crystals – organic and inorganic, from solutions, melts or gaseous environments, natural and synthetic (Perovskii, Piskunova, 2017), and even those growing inside the human body (Mashina et al., 2015) – have visually similar patterns on the growth surface at the microscale. These patterns are represented by layered relief, dislocation spiral hillocks, etch pits, including on defects, complex patterns of interaction of elementary and microscale steps with each other, impurities and other obstacles. The full set of features listed above will not necessarily be present on crystals from melts, for example, because the causes of the phenomena there are different from those in growth from solution. For example, dislocations are caused by plastic deformation rather than impurities. But if there is a dislocation, then the movement of steps, growth or etching on it will be represented in similar visual images and will develop according to the same mechanisms for crystals of different genesis.

Direct observations of growth at the nanoscale also indicate the similarity of the principles of surface construction. Comparison with the results of the AFM study of the crystallisation of inorganic water-soluble salts (Piskunova 2007) shows that the mechanisms of the processes were identical to those observed for dioxidine, except for dimensional nuances and geometric contours of hills and pits reflecting syngeneity. However, many phenomena on inorganic crystals could not be recorded: either they did

not occur, or the AFM tip was unable to draw a detailed relief across the entire scan window. The reason for this has already been described above – the size and time of the fluctuations. The AFM is an instrument that has the ability to register thermodynamic fluctuations in both size and time resolution. Fluctuations depend on the number of elementary particles in the microcanonical ensemble (microvolume).

Because of the difference in size between inorganic and organic particles, there will be more of the former than of the latter in the same volume. For the same reason, the building blocks in inorganic solutions are more mobile, often more reactive with impurity ions, more responsive to local variations in temperature and concentration, etc. Statistically, the probability that all the fluctuations in the scan window of an inorganic crystal will be realised by the time of the next scan and allow a correct image to be obtained in the AFM is even lower than for an organic crystal. It is important that the incorporation of elementary particles into the step breaks takes place because the AFM physically scans with a tip (in both contact and non-contact modes) and the tip does not pull unattached particles. The AFM therefore records more processes on organic crystals and films them longer and more clearly. A one-nanometre growth step visualised by AFM on the surface of sodium chloride corresponds to a bundle of several elementary (equal to the unit cell parameter) steps, i.e. it is essentially a macrostep. Observing the behaviour of a step of similar height on the surface of an organic crystal will be much more informative, as it will reveal the growth characteristics of the smallest steps for a given crystal.

The open question of the nature and size of the building blocks of crystal growth has been completely resolved in experiments with molecular crystals. Having understood the mechanism of the phenomenon using the example of the attachment of molecules to a growing surface, it is easier to understand more complex ways of laying down smaller units of matter for the same phenomenon.

Weak chemical bonds in molecular crystals allow us to see processes that would never be seen in crystals with, for example, ionic bonds. One example is the propagation of a dislocation through a macrostep covering it (Piskunova, 2023): in the experiment, the dislocation had enough energy to break hydrogen bonds in a 200 nm

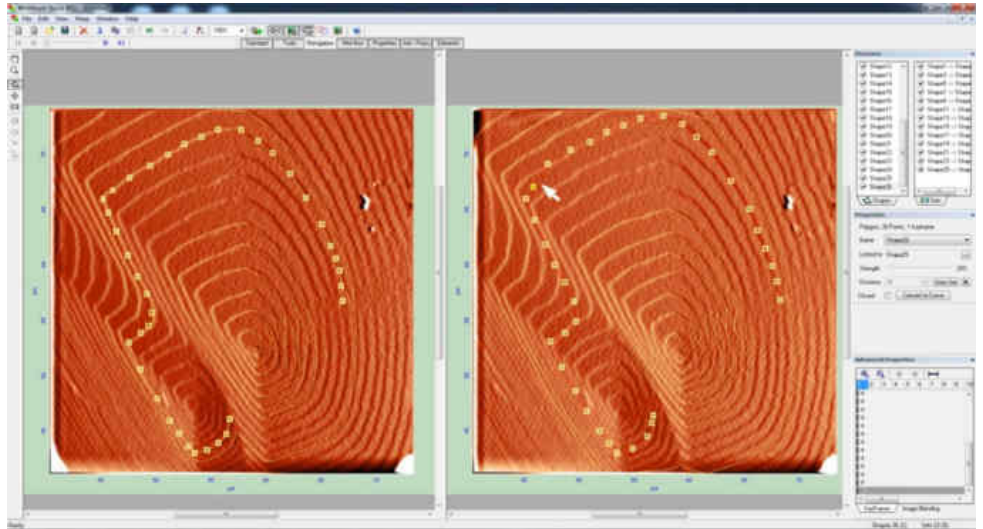
thick layer, and it was shown how, having barely found its way under the thick layer, the top of the dislocation hillock emerged through it, starting the development of a new hillock. This would be impossible to observe in inorganic model crystals at room temperature, although this process does occur in nature. There, the energies of high pressures and temperatures help dislocations to effectively overcome strong bonds in crystalline layers. However, it was in a model crystal with a molecular structure that this phenomenon was first observed at the nanoscale and its mechanics studied. Dioxidine, which was introduced into practical growth studies, proved to be a successful model crystal because it shows almost the same bright surface processes as lysozyme, but has a molecule that is tens of times smaller and the size of the elementary cell is slightly larger than that of quartz. Understanding the mechanisms of crystal growth and dissolution near equilibrium (supersaturation and undersaturation of solutions of about 1%), which are well captured by AFM, is important for reconstructing the processes that occurred under the same conditions at the final stage of mineral crystal growth. In molecular crystals at these supersaturations, the processes are recorded in greater detail and contrast.

Clearly, it is impossible to extrapolate experimental conclusions about molecular crystal growth rate values directly to crystal formation in nature. However, a balanced approach to making analogies between crystal growth mechanisms in the laboratory and in nature, based on the conclusions of atomic force microscopy as the only available tool for direct observations of crystal growth and dissolution at the molecular level in solution, seems entirely justified and allows us to identify new fundamental patterns.

2.7 AFM–videos

The result of in-situ AFM experiments are successive images of the surface, scanned at regular intervals. It is common practice for researchers to combine these images into movies for better viewing. The author's approach is to calculate up to a

hundred intermediate images using morphing programs that allow a smooth transition between the images. First, relief details are marked with dots, then these dots are moved to their new position in the next image.



Various films were made, including those showing growth and dissolution on a scratch, the introduction of foreign particles, and the transition from dissolution to growth in the same steps. Freely available programs were used for morphing and subsequent file joining. The films can be found at the following link and are also available via a QR code:

<https://geo.komisc.ru/divisions/laboratory/experimental-mineralogy-laboratory?view=article&id=759:piskunova&catid=189:experimental-mineralogy-laboratory>



Chapter 3. *In-situ* AFM Experiments

3.1 Transition from dissolution to growth through the saturation point

In a technical sense, growth and dissolution share the same mechanisms, involving two main steps: (1) mass transfer from/to the solution through the diffusion layer, (2) surface reaction and attachment/detachment of the substance from the crystal. Reversibility is the process of transitioning a thermodynamic system from one state to another, with the possibility of returning to its original state through the same sequence of intermediate states, but in reverse order.

Numerical modelling works, starting with Frank (1958), postulate the reversibility of growth and dissolution and consider them to have equivalent but inverse mechanisms (Madras and McCoy, 2004; Elts et al., 2017; Tilbury, 2017; Shen et al., 2018; Hill et al., 2021). Direct AFM observations are discussed in Section 1.4 of Chapter 1, and they largely support the reversibility of growth–dissolution. In direct observations using a confocal laser scanning microscope, Nakano et al. (2022) showed that the addition of chromium to the solution significantly increases the kinetic reversibility of the growth and dissolution of a silicon crystal. Rivzi (2020) also showed in his experiments that the dissolution behaviour of paracetamol mechanistically corresponds to the growth behaviour, and his analysis of the rates also indicates similarities. Some researchers are cautious about the idea of reversibility. Snyder et al (2007) showed that these two processes are reversible when modelling the final shape of the crystal using growth–dissolution cycles, but only if all their relative rates are equal and none of the growth faces disappear from the crystal during the dissolution stage. During growth, the crystal is covered with facets of high reticular density, whereas during dissolution the crystal has only rapidly dissolving facets. The vertices and edges are the first to dissolve, often resulting in rounded and curved dissolution shapes.

This makes it impossible to restore the original appearance of the semi–dissolved crystal during regeneration, even in the absence of impurities. And if traces of dissolution are visible when zoning is examined, it means that subsequent growth has not leveled them out, a process that is not completely opposite to dissolution under

certain conditions (Klepikov et al., 2020). J. Clark and colleagues (Clark et al., 2015) used coherent Bragg diffraction to study the electron density of calcite before growth, after growth and after dissolution, and found that defects formed during the growth process cause the formation of pits when dissolving on them over the next period. This contradicted their original assumption of the reversibility of growth and dissolution. In their work on the dissolution of zeolite crystals, Bozhilov et al. demonstrate reversibility by using dissolution as an *ex-situ* method to reveal growth details inaccessible by other methods (Bozhilov et al., 2021).

Those who argue against any reversibility of growth and dissolution have their own strong arguments. Theories that control the final crystal shape through growth-dissolution cycles are based solely on the anisotropy of growth and dissolution rates (Lovette et al., 2012; Neugebauer et al., 2018). Stack et al. (2012) demonstrate irreversibility using rare event theories to model the growth-dissolution of barite. In their review, Hadjittofis et al. (2018) emphasise the differences between crystal growth and dissolution: two processes that, in their view, are neither reversible nor opposite. Is it possible to demonstrate the reversibility of growth-dissolution at a subtle level? Once an experiment has been designed under practically ideal conditions, in the absence of modifying impurities, without nutritional restrictions and other influences, under constant conditions and a single variant of the attachment sites of the building units, i.e. on the same steps? Atomic force microscopy is a suitable tool for modelling such conditions.

This chapter presents the results of two experiments in which surface reactions were directly observed during the transition from dissolution to growth, in one case on the same dislocation pit and in the other on monomolecular steps of the same dislocation hillock (Piskunova, 2024 a). The system in these experiments had no impurities, no nutrient deficiency, no directed solution flow, no changes in conditions and no other influences. A slow continuous natural transition from dissolution to growth was simulated, controlled by uniform evaporation; the role of evaporation was evaluated in *section 2.5.2 of Chapter 2*. The possibility of irreversibility due to the influence of impurities was completely excluded: *section 2.2.2 of Chapter 2* showed

that the dioxidine solutions were chemically pure. It was also shown there that no clusters were formed in the solutions, i.e. the growth of dioxidine crystals, as well as the dissolution, was due to the attachment/detachment of identical units – individual molecules. If the growth occurred in clusters and the dissolution occurred by tearing individual molecules off the surface, it would be impossible to compare these processes.

The experiments were designed to answer the following questions

– Does the substance technically adhere to the same points during growth as it does during dissolution? – Is the shape of the same steps the same during growth and dissolution?

– Is there a period when all processes freeze and how long does it last, i.e. is it possible to visualise the equilibrium?

– If the surface dissolves at the beginning and grows at the end, is there mixed growth and dissolution in the transition region near the saturation point?

– What is the behaviour of the tangential growth and dissolution rates? Is it true that they are high far from the saturation point and minimal near the saturation point? Are the dissolution and growth curves symmetrical?

– How does the normal rate behave: does the hill regain its original shape during growth, lost during the period of symmetrical dissolution?

3.1.1 Pit on the screw dislocation

Dissolution

At the beginning of the first experiment, at slightly more than 1% undersaturation on the (010) side of the dioxidine, intense dissolution was observed: high relief details (from 890 to 1400 nm in height) quickly disappeared from the surface, while the tangential rate reached 68 nm/sec (the first three images in Figure 3.1). This process was similar to chemical polishing: high relief details in the normal direction quickly disappeared and there was almost no tangential dissolution. It should be noted that such 'polishing' also starts with defects as the weakest points, but due to the limited size of

the scan window this cannot be shown. Closer to equilibrium (at the 58th minute of scanning), careful dissolution began on dislocations (a triangular pit appeared, outlined in Figure 3.1), which did not extend beyond the scanning window and was recorded in stages. The sides of the pit dissolved at different tangential rates from 6 to 41 nm/sec.

Teng, who studied the dissolution of calcite, identified three dissolution modes: spontaneous pit formation at high undersaturation, dissolution at low undersaturation using existing steps, and dissolution at defects and steps at moderate undersaturation (Teng, 2004). He noted that little is known about the effect of saturation state. In the experiment shown in Figure 3.1, a pit formed on a dislocation just short of the saturation point was recorded.

Further observation of the pit provided a clear illustration of what Lasaga and Lutge described as the dissolution step wave mechanism (Lasaga and Lutge, 2001).

Developing the theory proposed by Frank and Cabrera that the strain field causes an etch pit to form in the hollow core of a screw dislocation, Lasaga and Lutge used Monte Carlo simulations to show that, from a certain undersaturation, the etch pits not only open but also become sources of step waves. These steps, which propagate as waves from the defect across the surface, can ultimately control the volumetric dissolution rate. In this mechanism, the progression of the steps within the pit and the spacing between them differ from those of the dissolution spirals rising above the surface. The main characteristic of the dissolution step waves is their closed nature. Closed dissolution steps were observed in the experimental work (Xu et al., 2010): they were generated at the exit point of a screw dislocation, and as the first steps moved along the surface, more and more new steps appeared at the exit point, not only widening the pit but also deepening it. Lasaga and Lutge (2001) present an equation for the dependence of the step rate on the distance from the exit point and show that, from a certain undersaturation, the external waves stop and the advantage in resolution goes to the centre – this is exactly the behaviour observed in the experiment in Figure 3.1 from 85.5 minutes. The global retreat of the face is caused by the closure of the outer steps of neighbouring pits, leading to their annihilation. In Figure 3.2 (a–c) the unification of neighbouring pits (circled areas) and the global retreat of the face are clearly visible.

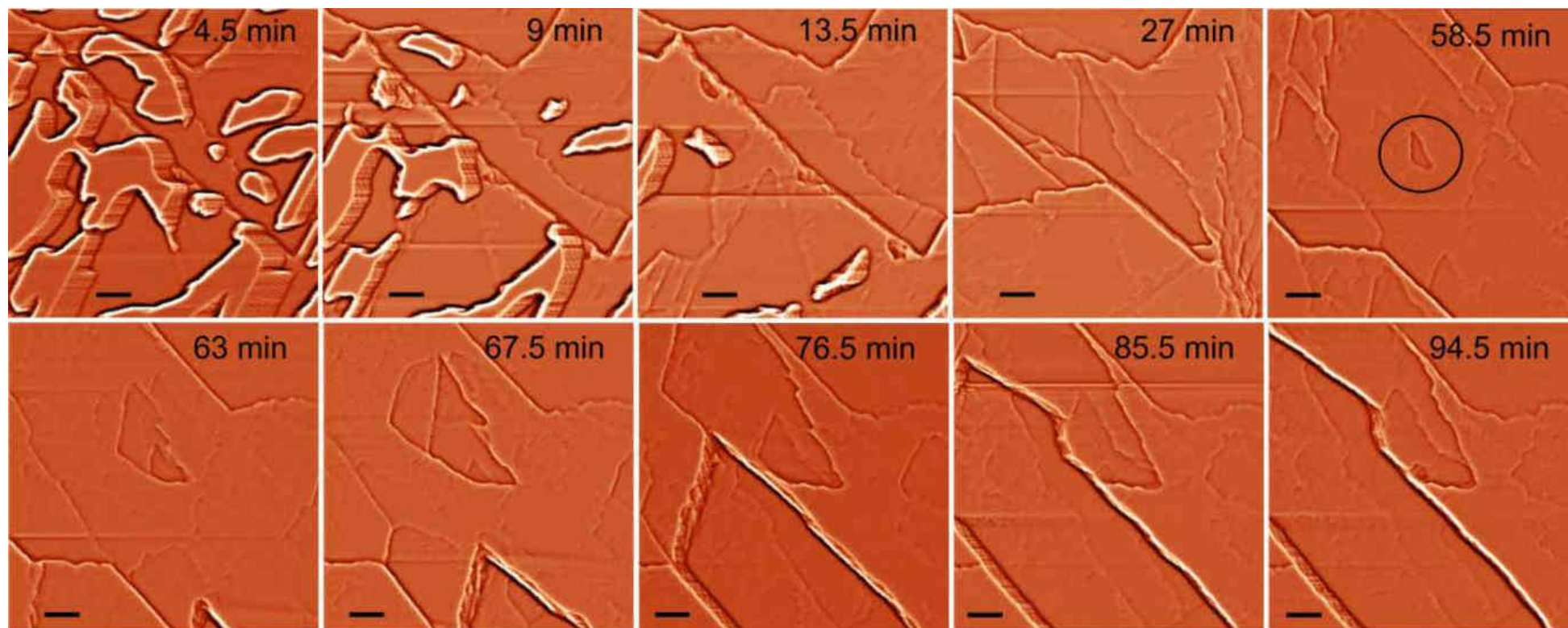


Figure 3.1 – The experiment starts from the dissolution similar to chemical polishing (first three images). The dissolution then continues with thin step retraction for 40 minutes. From the 58th minute a pit appeared on the screw dislocation (circled).

Time marks indicate intervals from the start of the experiment. Scale bars – 7 μm

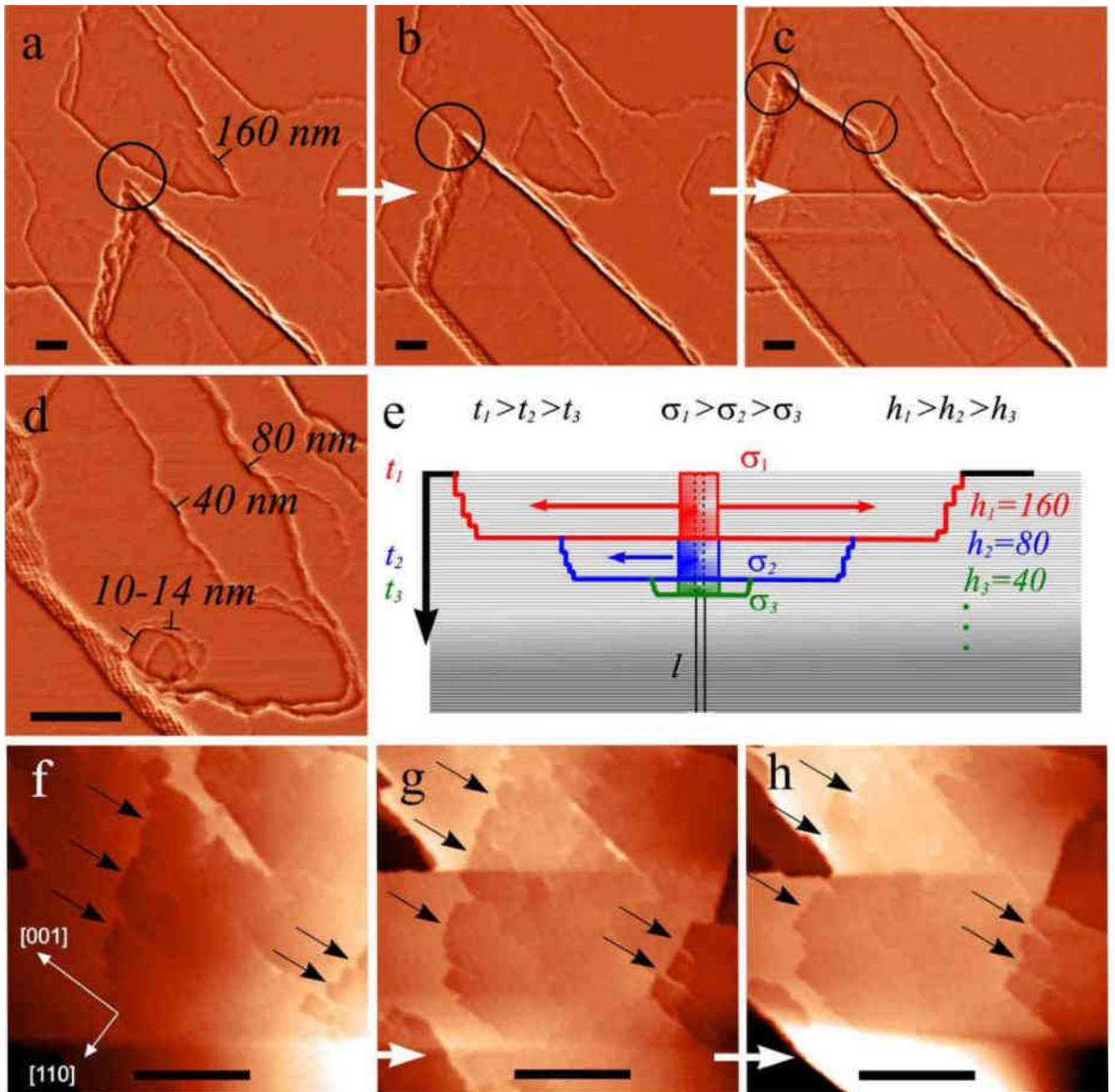


Figure 3.2 – Connection of pits in the wave mechanism of dissolution: the circled areas in (a), (b) and (c) are the meeting points of the steps of adjacent pits on the (010) face of dioxidine. The lower pit is significantly deeper than the upper, complete dissolution does not occur, and the dislocation axis of the upper pit begins to impede further advancement of the lower pit. (d) – different depths of steps moving from the dislocation exit point (explained in (e) and in the text). (e), (g), (h) – spreading of etch rays moving in the [001] direction (indicated by arrows). The time interval between frames is 4.5 minutes. Scale bars are 10 μm

The experiment in Figure 3.1 illustrates the theory of dissolution waves, but the data obtained on the dissolution of a real molecular crystal at the nanoscale allowed us to supplement this theory:

1. Dissolution waves formed at the surface can occur not only far from equilibrium, as predicted by Lasaga and Luttge (Lasaga, Luttge, 2001) and observed by Teng (2004) for the dissolution of calcite. In the experiment in Figure 3.1, this wave-like dissolution process occurred close to equilibrium. Obviously this depends on how many defects the crystal has close to the surface, which Teng does not deny. For example, the paper (Xu et al., 2010) shows AFM images of pits with closed steps formed on defects close to the saturation point, although the authors do not use the term "wave mechanism".

2. The above addition is related to the question of why closed step pits form on defects during dissolution (Teng, 2004; Wang et al., 2011). If an increased chemical potential due to local fluctuation triggers dissolution leading to the formation of negative two-dimensional cores, then the steps of pits formed on point defects should have a closed shape. The steps of the pits on edge dislocations will have the same shape. If the dissolution started on a screw hillock rising above the surface, then the layers will of course be removed along the path of their growth, i.e. by the screw mechanism. But if the dissolution started on a hidden screw dislocation, then there is no screw legacy in the growth layer covering it, it only contains lattice stress just above the core of the absorbed dislocation, which increases the chemical potential at that point. This is the origin of the dissolution pit, which is formed on a screw dislocation but will never become a screw itself. At first glance the pit in Figure 3.1 and especially in Figure 3.2 (g) appears to be a screw, but in reality its steps are closed.

3. The height of the step waves in the Lasaghi Monte Carlo model is one molecular unit, indicating a rapid concentration equalisation near the surface. The real nanoscale picture (Figure 3.2) proves that the depth of the subsequent step waves ($h_1, h_2 \dots$) near the saturation point depends on their ordinal number: the first macrostep emitted in the experiment had a depth of 160 nm (Figure 3.2 (d)), the second – 80 nm, the next has a total depth of 40 nm, etc., until the depth of the generated step reaches the elementary

value. In the absence of solution flow, the local undersaturation ($\sigma_1, \sigma_2...$) gradually decreases during the dissolution time ($t_1, t_2...$) due to the slow diffusion transfer of the detached substance that accumulates above the pit, and thus the depth of the steps also decreases. It should be taken into account that the scanning unit has a certain effect on the diffusion layer: the rapid movement of the tip mixes the solution and to some extent equalises the concentration levels. This leads to the conclusion that even if the steps of subsequent generations differ in depth with such equalisation, in a real crystalline medium, without the influence of the AFM, this should be even more pronounced.

4. When a macrostep disintegrates, its upper step may leave the group, but not its lower step. During growth, on the other hand, a lower elementary step may separate from the foot of the macrostep. Very rarely, this can take the form of an emission – a kind of protuberance; such a phenomenon is mainly caused by the non-equilibrium adsorption of impurities at the edge of the step. In dissolution, on the other hand, emissions are very common. For example, in Figure 3.2, snapshots (e), (g), (h) show oriented areas of negative relief on the (010) face of dioxidine, moving in a particular crystallographic direction [001]. Such emissions are the result of a combination of crystallographic vectors of preferential etching with step waves in opposite directions, and can be formally compared with the jet structures described by Putte et al. and later by Sangwal (Putte et al., 1978; Sangwal, 1987).

Transition to growth

When the dissolution of the outer steps of the pit slowed in the experiment in Figure 3.2, attention was focused on the very centre of the pit – the dislocation exit point (Figure 3.3). There the transition from dissolution (which took 117 minutes) to growth was observed. During the transition, the processes did not stop completely: dissolution in the centre of the pit was accompanied by the already initiated attachment of matter to the fractures of the upper steps. As time passed, the material became more active in attaching to the steps, but did not integrate into the dislocation exit point. The first two images in Figure 3.4 show the centre of the pit before and after two hours of

growth. It is clear that a screw hillock did not form on the pit, although it did initially form on a screw dislocation. The arrows in Figure 3.4 indicate the outer steps of the former dissolution pit, which are not growing despite the intense growth around them. In this experiment there is not even formal symmetry in growth and dissolution – the material was attached at different points during growth and dissolution, and growth was more intense than dissolution at equal distances from the saturation point. Giant steps of up to 400 nm in height then entered the observation zone. It can be seen that one of them slowed down and bent at an obstacle (represented by the red dot in Figure 3.4), around which its edges then closed. This point corresponds to the coordinate of the dislocation exit point (Figure 3.2 (g)), i.e. the obstacle to the attachment of the substance is the increased chemical potential above the dislocation nucleus.

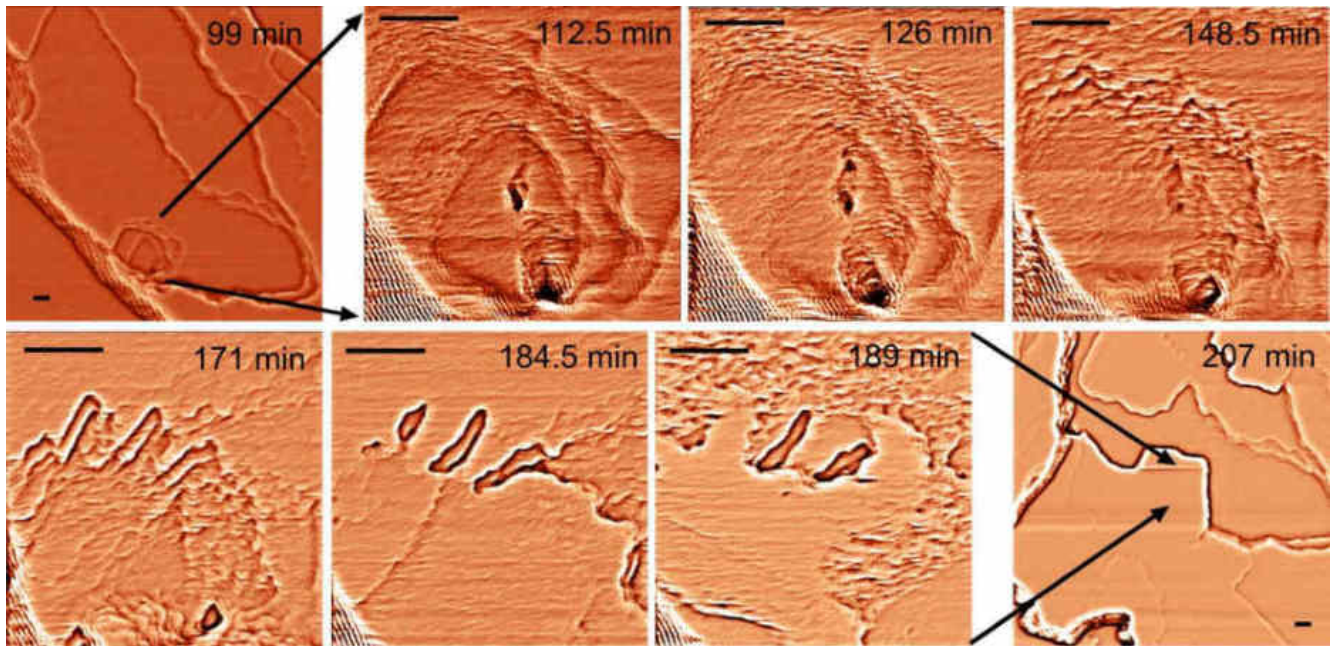


Figure 3.3 – Observation of growth at the centre of a dislocation pit at a scale of 4 μm : material is adhering to the edges of the steps but not to the exit point of the dislocation. The first and last images at 20 μm scale show the same pit before and after complete sealing. The time marks above indicate the intervals from the start of the experiment. Scale bars – 1 μm

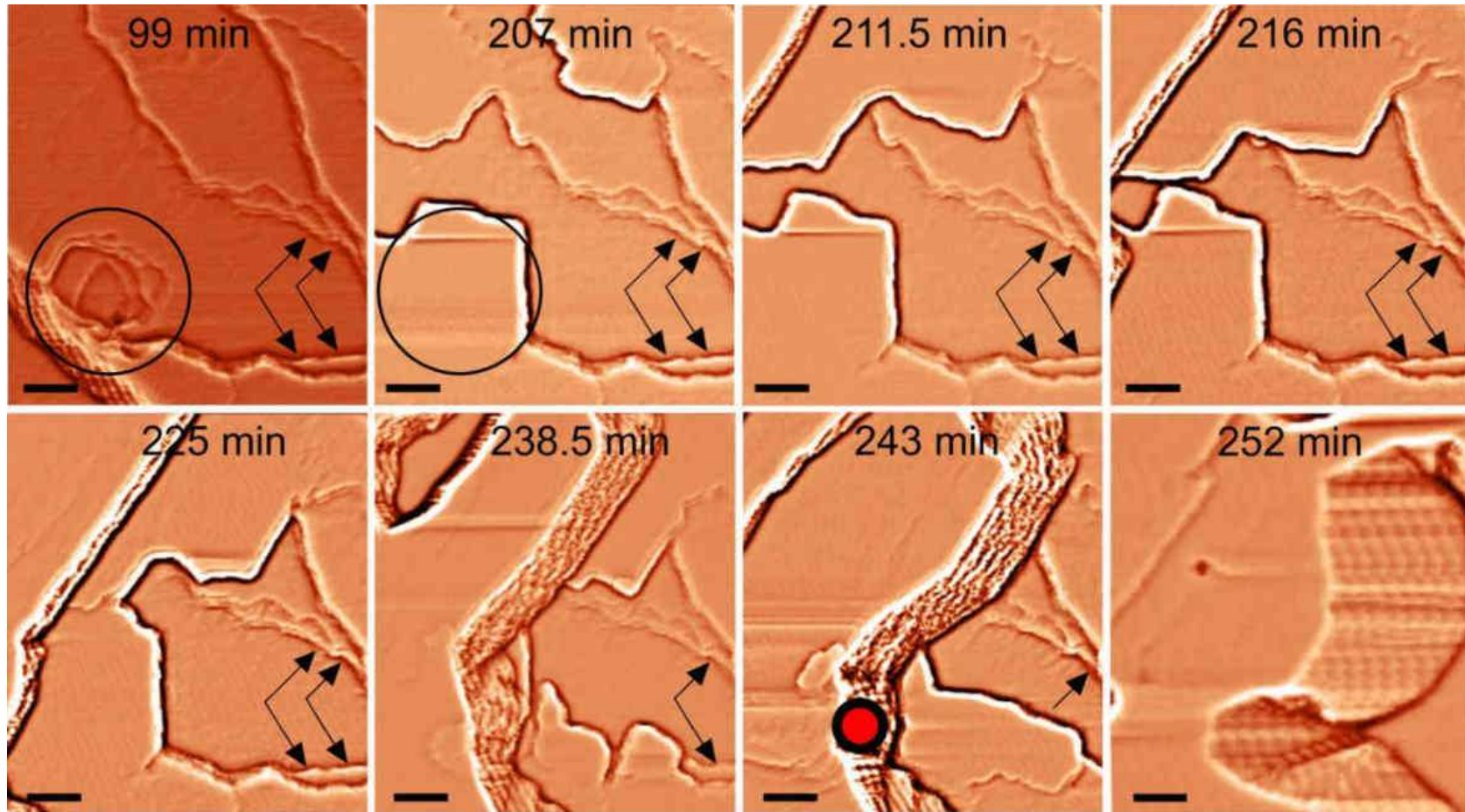


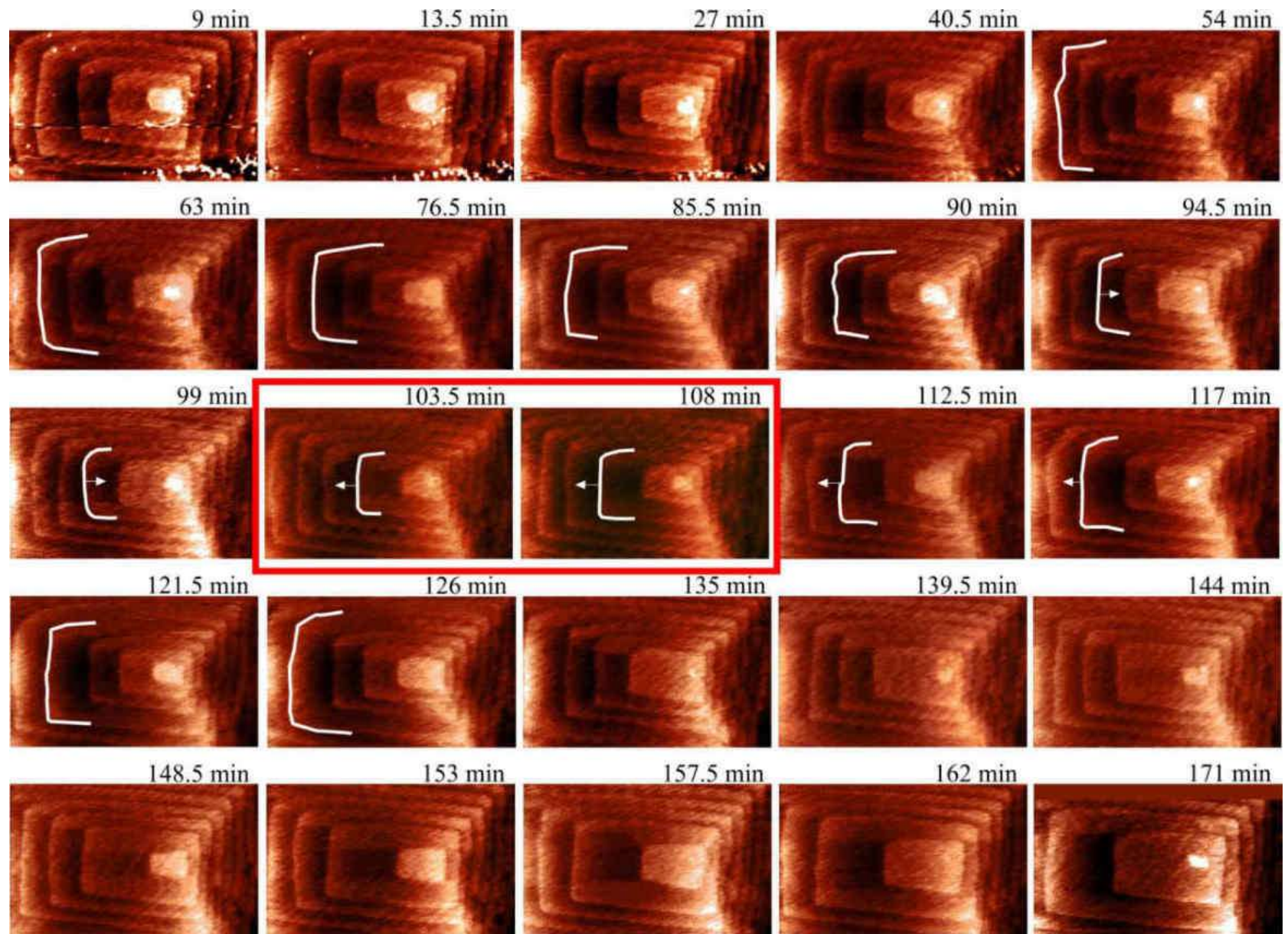
Figure 3.4. The centre of a pit (marked with a circle) on a screw dislocation, overgrown without forming a spiral hillock. During the overgrowth period, which lasted over 100 minutes, and beyond, the upper steps of the pit (marked with arrows) did not grow and no substance was attached to them. Time marks indicate intervals from the start of the experiment. 243 minutes – the giant step slows down and bends on an obstacle, which is where the dislocation emerges (shown in red). 252 minutes – the edges of this step are close to the obstacle. Scale bars – 1 μm

3.1.2 Hillock on the screw dislocation

The aim of the next experiment was to observe a slow transition from dissolution to growth on the same hill – a growth analogue of the Frank-Read dislocation source growth (Figure 3.5). At the top of the hillock, two dislocations of opposite sign form counter-rotating steps 3.5 Å high which merge into a closed step. The use of filters made it possible to isolate the moment when the steps form a complete loop at the top of the hill, but are visible as separate steps, and the distance between the two dislocations is less than 200 nm. The left dislocation produces steps with a large number of kinks, resulting in an overall anisotropy of the hillock shape. Some authors note that the closer to equilibrium the shape of the dislocation hillock steps becomes more polygonal (Kuwahara, Uehara, 2008), which is observed in Figure 3.5. Analysis of the shape of the same steps throughout the experiment does not allow us to assert any differences in their shape during growth and dissolution. Both growth and dissolution are accompanied by the formation of bulges in the front part of the steps, and the corners of the steps become rounded and then pointed (marked with a white outline in the images). A significant difference is that the number of steps in the scanning area is smaller during growth than during dissolution. This is clearly visible in the lower part of Figure 3.5: despite the intensive growth, it is difficult for the top of the hill to generate new closed steps. This leads back to the idea of asymmetry between growth and dissolution.

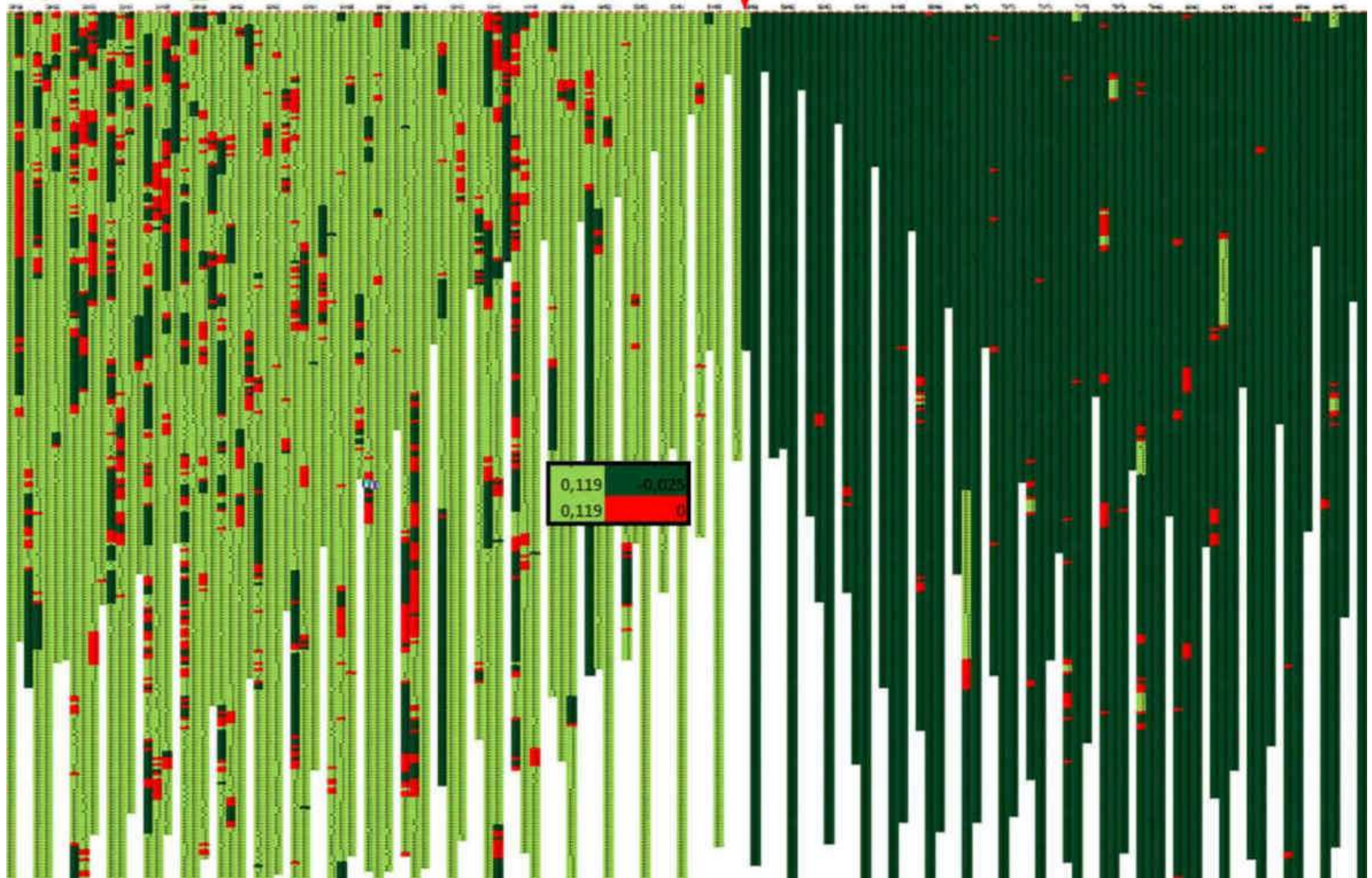
By taking the coordinates of points on the contours of the steps (every 35 nm on the top and bottom steps and every 43 nm on the left and right) for all 40 images and processing these data, a graphical representation of the experiment was obtained, a fragment of which is shown in Figure 3.6. The light areas on the left represent dissolution, the dark areas on the right represent growth. Calculations based on the data showed that there is growth activity (dark) in the left light dissolution zone and rare dissolution activity (light) in the right dark growth zone in Figure 3.6.

Figure 3.5 – Dissolution and subsequent growth of monomolecular steps of the same hillock – a growth analogue of the Frank-Read dislocation source. The contour of one of the steps is marked in white. The moment when the system crosses the saturation point is marked with a red rectangle. The time from the start of the experiment is marked on the images. Image size $4 \times 7 \mu\text{m}$



█ – dissolution
 saturation point
█ – growth

Figure 3.6 – Fragment of a graphical representation of the transition from dissolution to growth through the saturation point on the steps of the same dislocation hillock. In the left light dissolution zone, growth zones (dark) and stagnation regions (red) are visible. In the right dark growth zone, rare dissolution regions (light) and stoppage regions (red) are found. The colours assigned to the cells are based on calculations using AFM data (callout in the middle)



The difference also indicates that the growth and dissolution processes near equilibrium are not symmetrical. The growth during dissolution is visually apparent in the corresponding video. It is worth noting that around the saturation point, as can be seen in Figure 3.6, the colours are clear, i.e. contrary to expectation, dissolution and growth do not mix at the saturation point.

Simultaneous growth and dissolution near equilibrium recorded by AFM was first mentioned by Konnert et al. (1994).

What makes growth possible during dissolution near equilibrium? If the edge of a step has dissolved, this means that the concentration of the substance in the solution above the step has locally increased. Since the state near equilibrium is characterised by weak equalising currents, such a local increase in the concentration of the substance can be realised by a single act of growth on the same or an adjacent step. Figure 3.6 shows that growth activity sometimes occurs in very narrow areas, i.e. the fluctuation scale in this case is about 43 nm. But more often in this experiment the growth of one of the large segments was observed on the dissolving step. In these cases the fluctuation scale is 1–2 μm . Why is there almost no dissolution during nanoscale growth? During growth, the substance cannot deposit on the surface in excess to cause undersaturation because there is simply none at the surface. From this point of view, growth and dissolution look like essentially non-equivalent processes.

The average tangential rate for this experiment is shown in Figure 3.7. It is evident that growth and dissolution are not equivalent in kinetics. Growth does not show as much variation as dissolution. Immediately after passing the saturation point, the growth rate is twice as high as the dissolution rate. This difference in behaviour is often explained by the fact that dissolution can occur in elementary units, whereas growth occurs in clusters, leading to faster advancement of the step edges during the growth process. However, dioxidine grows and dissolves in molecules; there are no clusters in its solution. Thus, the more intense growth than dissolution in the experiment cannot be explained by the difference in size of the building blocks involved in these processes. A possible explanation for the jump in growth is that the substance, the excess of which had accumulated in the solution above the surface as a result of an hour's dissolution,

accumulated en masse after passing the saturation point. Phenomena caused by local thermodynamic fluctuations on such small scales, a few micrometres, can only be recorded by direct AFM observations.

The rate fluctuations were plotted up and down from each point in the form of a confidential interval (Figure 3.7).

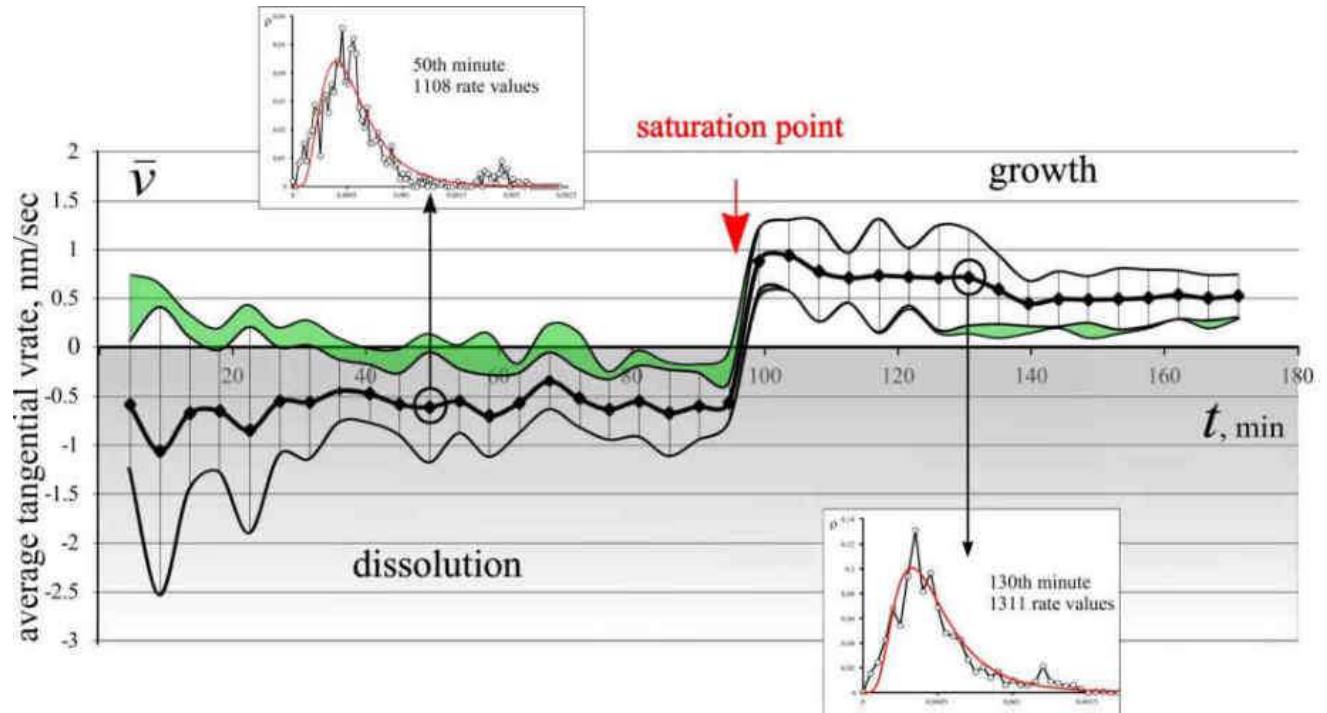


Figure 3.7 – Average tangential rate of monomolecular steps on the Frank–Read hillock during the transition from dissolution (left) to growth (right) through the saturation point. Each point on the graph is the result of processing a set of rate values, their total number on the graph is approximately 60,000. Fluctuations in rate are plotted up and down from each point. The green extensions of the fluctuations to the left and right are additions introduced by the detected growth events during general dissolution and dissolution events during growth

As can be seen from the graph, the dissolution rate fluctuations are large at the beginning of the experiment and only decrease in intensity as the saturation point is approached. Growth is characterised by smaller fluctuations which behave in the opposite way: they are largest when approaching the saturation point and smallest after

the 140th minute of the experiment: at the end of the experiment the system approaches a stable, almost stationary state. In kinetic terms, therefore, growth and dissolution at the nanoscale cannot be described as symmetrical.

The observed growth during dissolution and dissolution during growth (Figure 3.6) are deviations, i.e. fluctuations. Therefore, they have been plotted as additional fluctuations to the actual fluctuations of growth and dissolution. Individual growth events during the general dissolution of the crystal were added from above to the dissolution fluctuations on the left (green area on the left in Figure 3.7). Dissolution during growth was added from below to the natural growth fluctuations (small green area on the right in Figure 3.7). As can be seen, such additions did not make much difference to the overall picture: dissolution has large fluctuations even without them.

Experimental studies often present growth and dissolution rates combined in a single graph, as in Luttge or Schott et al. (2012). In many cases, such studies do not provide data on the saturation point, as they are often composite graphs containing the results of several different experiments, including literature data. Despite the lack of complete literature analogies, the general trend of the graph in Figure 3.7 corresponds to the trend of Eq. (22b) for dissolution on dislocations from the work of Dove and Han (2007). The next step was to calculate the step distances along a series of lines – every 35 nm – and plot the average step distance and its fluctuations (Figure 3.8. (b)). This allowed us to obtain the average normal rate with a step of 4.5 minutes (Figure 3.8 (a)). The normal rate is also not symmetrical on either side of the saturation point. Fluctuations in the normal rate for dissolution and growth are also very different in character. Figure 3.9 shows three profiles of a hillock: one hour before saturation, before dissolution (white profile), at the point of maximum dissolution (red profile) and after one hour of growth (green profile). It can be seen that growth and dissolution in the normal direction are also not kinetically equivalent, i.e. they are not reversible.

Formally, any nonequilibrium process is irreversible by definition. For a process to be reversible, it must be so slow that it can be considered as a continuous series of equilibrium states, i.e. it must be slow compared to the processes of establishing thermodynamic equilibrium in a given system. In this paper, the conclusion about

irreversibility is made on the basis of AFM data on the rate of normal growth (Figure 3.8 a), which are negligible modular average values - 0.001 nm/s. This and the fact that in the experiment there was a transition through the saturation point allows us to apply the concept of reversibility-irreversibility.

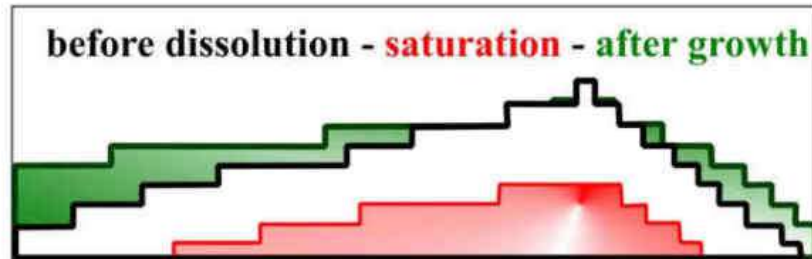


Figure 3.9 – Three profiles of a hillock (AFM data): one hour before the saturation point before dissolution (white profile), at the point of maximum dissolution (red profile) and after one hour of growth (green profile)

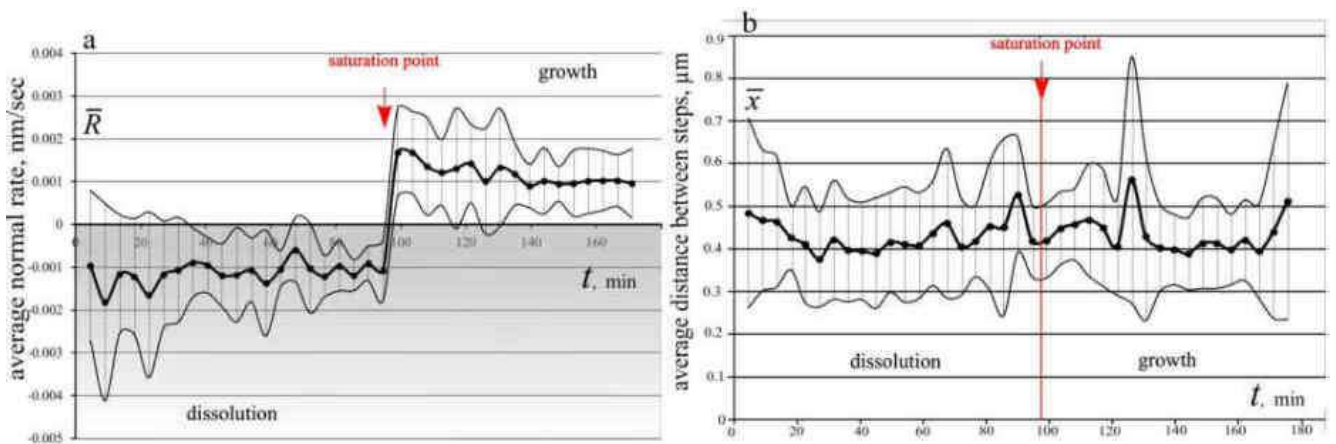


Figure 3.8 – Plots of the average normal rate and its fluctuations (a) and the average distance between steps with fluctuations (b) during the transition from dissolution to growth through the saturation point

3.1.3 Influence of diffusion and convection

Diffusion is caused by the random movement of elementary particles for a given system due to their thermal activation. In the diffusion layer around the crystal with a

thickness of δ such movement and the resulting process of concentration equalisation, which for a three-dimensional system can be called ∇C , occur. This process does not require the action of any force. However, if there is another force acting on the particles, then the flow produced by such a force, equal to the gradient of the corresponding potential, is added to the actual diffusion flux. Thus, evaporation in the AFM cell stimulates the gradient ∇I (Figure 3.9), just as convection, which is inevitably present, creates a gradient ∇K . But the gradients that limit the surface processes in the low-rate conditions will be those created as a result of excess and deficiency of matter near the surface itself (Figure 3.9, ∇R_d and ∇R_g icons in the callouts), on scales much smaller than the thickness of the diffusion layer. For layer-by-layer growth, the flow generated by surface migration is also important, both in the case of growth and in the case of dissolution (M_{xy} icon in the callouts in Figure 3.9).

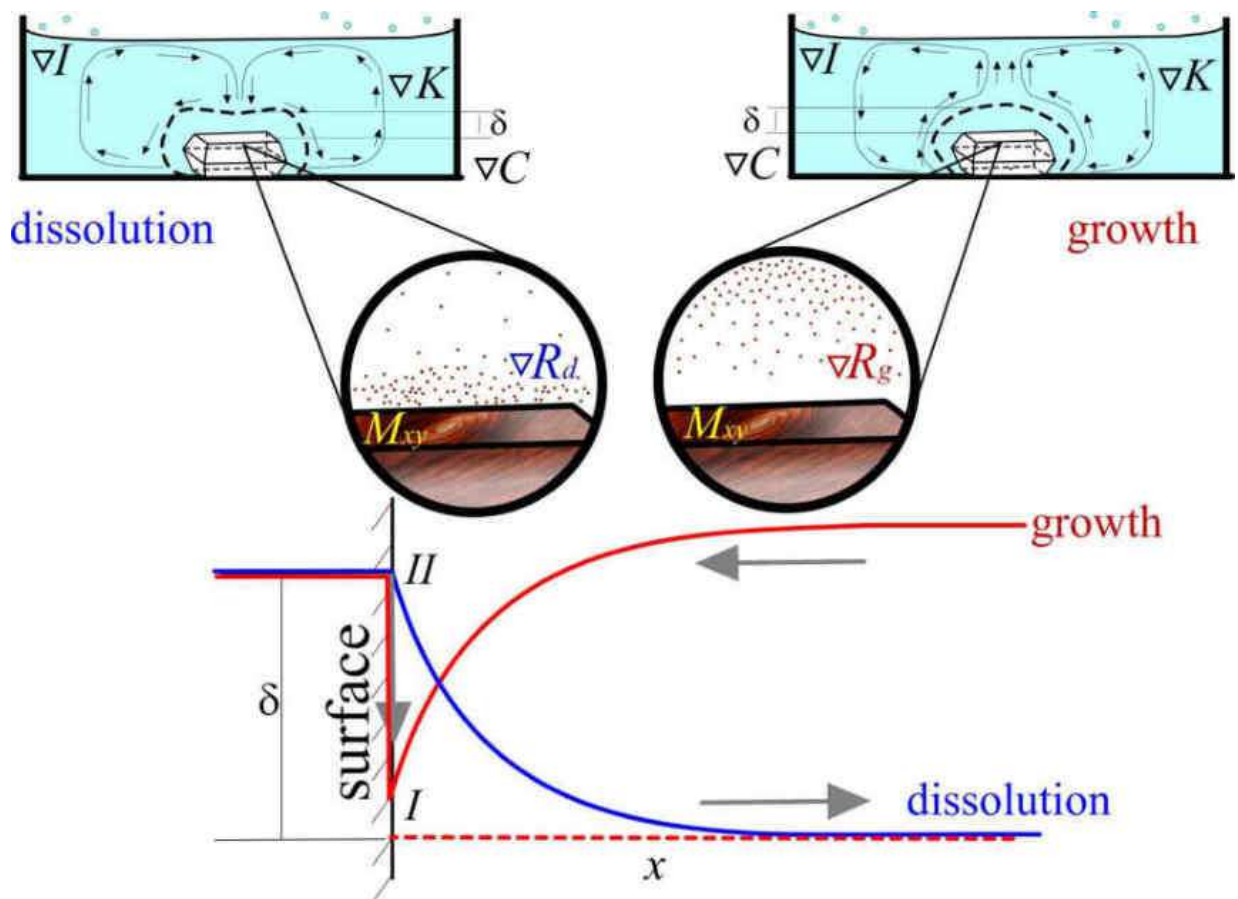


Figure 3.9 – Explanation of the role of the main potential gradient in limiting the process of layer-by-layer growth and dissolution near equilibrium. The near surface concentration profiles for these two processes are shown below

The flow is proportional to its rate and concentration, the rate of movement of the molecules is related to the acting force equal to the gradient of the potential by the coefficient $\frac{D}{kT}$. Thus, the first Fick's equation for the flow during growth and dissolution in three dimensions takes the form:

$$J = J_D + J_I + J_K + J_R + J_M = \quad (3.1)$$

$$= -D \left(\nabla C(x, y, z, t) + \frac{C(x, y, z, t) \nabla I}{kT} + \frac{C(x, y, z, t) \nabla K}{kT} \right) + D_{d,g} \frac{C(x, y, z, t) \nabla R}{kT} + J_M$$

where J_D, J_I, J_K are the flows generated by diffusion in the layer, evaporation and convection, J_R and J_M are the flows generated by the processes directly *at* and *on* the surface by growth-dissolution and surface migration, t is time, k is the Boltzmann constant, T is the temperature, ∇ is the Nabla operator, D is the diffusion coefficient, $D_{d,g}$ is the diffusion coefficient directly at the edge, which is different for growth and dissolution (an increase in concentration reduces the mean free path and leads to more frequent collisions, reducing the diffusion coefficient).

The first three terms for weak dissolution and the subsequent weak growth are practically the same, as is the case for convection, although the direction of the convection currents is different for growth and dissolution. In the equation there are no \pm signs in front of the first, third, fourth and fifth terms, but it is clear that the flows are in opposite directions during growth and dissolution. The equality in absolute value of the first three terms is ensured by low concentrations, the same evaporation in both cases (Figure 2.30, Section 2.5.2, Chapter 2) and the same and very low viscosity (Figure 2.6, Section 2.2.2, Chapter 2). Low viscosity makes the diffusion coefficient large, as can be seen from the following expression:

$$D = \frac{kT}{6\pi\mu r h}, \quad (3.2)$$

where D is the diffusion coefficient, μ is the viscosity and r is the radius of the molecule in solution.

In the case of dissolution, convection currents flow away from the face, rise to the surface of the solution, capture the excess formed by evaporation and then descend from

the sides to the crystal. In the case of growth, the depleted solution accumulated at the bottom rises to the free surface of the liquid, captures the excess produced by evaporation, and again descends to the face of the crystal. Looking at the normal rates in the experiment (Figure 3.8), despite their different behaviour and the initial growth spurt, the steady-state value of the rate for both growth and dissolution is symmetrical – about 0.001 nm/sec, i.e. convection does not have a large influence on these two processes, and the global inflow and outflow of matter as a result of convection is the same.

Thus, the processes of fast volume diffusion, weak evaporation and convection do not limit the processes observed in this AFM experiment. Only the last two terms in red in equation (3.1) are significant, i.e. the growth of this substance in solution at low rates and concentrations occurs, as expected, in the kinetic regime. The excess of substance ∇R_d due to dissolution and the depletion of substance ∇R_g above the crystal surface due to growth are responsible for the gradients ∇R in the penultimate term. It can be assumed that these terms for growth and dissolution differ insignificantly: during dissolution the diffusion coefficient is lower, but at the same time the concentration at the surface is higher, which cancel each other out when multiplied. However, diffusion at the surface itself affects both processes. It does not have time to remove the substance during dissolution, as evidenced by the different depths of the dissolution waves in Figure 3.2 of Section 3.1.1, the jump in rate at the beginning of growth as a result of mass addition of the substance in Figure 3.7 of Section 3.1.2, and significant fluctuations during dissolution. This near-surface diffusion cannot cope with growth either: Figure 3.8 of Section 3.1.2 shows that after the jump, the growth rate decreases unevenly over 40 minutes, with unstable fluctuations, until it reaches a plateau where evaporation begins to compensate for the decrease in rate.

The factors causing the gradients ∇R_g and ∇R_d operate near the edge at a distance much smaller than the thickness of the diffusion layer, which according to (Bredikhin et al., 1987), provided it is independent of the horizontal coordinate, can be calculated as:

$$\delta \sim \left(\frac{\mu^{2/3} D^{7/3}}{g \frac{\rho}{\rho_0} \left(\frac{\partial \rho_0}{\partial C} \right) R} \right), \quad (3.3)$$

where D is the volume diffusion coefficient, μ is the viscosity, g is the gravitational acceleration, ρ and ρ_0 are the densities of the crystal and solution, C is the concentration, R is the normal growth rate. In the present experiment, it is not necessary to take the coordinate into account when calculating the thickness of the diffusion layer, since growth and dissolution take place on the same steps of a hillock. Taking into account the very low normal growth rate in the denominator and the very high diffusion coefficient D , the estimate of the diffusion layer thickness gives a large value – a few millimetres. The absence of dioxide in solutions both during cluster growth and dissolution (Figure 2.7, Section 2.2.2, Chapter 2) and the equality of the parameters included in equation (3.3) indicate the same diffusion layer thickness for dissolution and subsequent growth, which is reflected in Figure 3.9.

The last term of equation (3.1) in Figure 3.9 contains the parameter M_{xy} , which is responsible for the two-dimensional diffusion over the surface before incorporation during growth and before desorption during dissolution.

The direct binding of a substance during growth goes through the following stages:

1. Attachment to the surface (adsorption)
2. Desorption, the probability of which is inversely proportional to the lifetime before desorption, which in turn is proportional to the adsorption energy and the frequency of thermal oscillations.
3. If the particle remains, it migrates along the surface – two-dimensional diffusion of the molecule to the step.
4. Adsorption at the edge of the step
5. One-dimensional diffusion along the step to the fracture
6. Addition at the fracture with formation of basic bonds

In the case of dissolution, the gradient for which the parameter M_{xy} is responsible is extremely small, but it still exists because the separation of the substance during dissolution goes through the following stages (Sangval, 1990):

1. The appearance of reacting ions or solvent molecules on the surface.
2. Their capture and migration along the surface
3. Formation of a surface complex with them
4. Adsorption of the surface complex by the surface
5. Formation of the activated complex and its adsorption
6. Dissociation of activated complex into reaction products
7. Adsorption of the reaction products onto the surface
8. Desorption of final reaction products
9. Diffusion of desorbed products into the solution

It can be assumed that for dioxidine as a molecular substance with a considerable molecular mass of 222.2 atomic mass units ($3.69 \cdot 10^{-22}$ g), which is also a crystal hydrate, surface migration during growth does not play such a large role due to delays caused by the formation of bonds with water molecules.

Thus, in the experiment on the transition from weak dissolution to weak growth through the saturation point, carried out using AFM in a dioxidine solution with low viscosity, low solubility and no clusters, physical factors such as volume diffusion, evaporation and convection do not play a role in recording the processes of layer-by-layer growth and dissolution. The factors limiting the recorded processes of layer-by-layer growth and dissolution are only those whose action occurs in the immediate vicinity of the surface and on the surface itself, i.e. according to the kinetic mechanism of growth. The influence of these factors is not fundamentally different for growth and dissolution, but taking into account the extremely close values of solution concentration in these two processes, it is the only physical reason for the differences in behaviour and the asymmetry of the kinetic characteristics of growth and dissolution found in the experiment. This allows us to conclude that the processes of growth and dissolution are irreversible at the nanoscale. Other types of crystals growing from solutions with higher viscosity and solubility and forming clusters should show even more asymmetry and irreversibility of growth and dissolution at the nanoscale.

3.1.4 Transition from dissolution to growth through the saturation point. Conclusions

1. Direct observations of the processes of monomolecular step motions using AFM have shown that, technically, the substance does not always integrate during growth into the exact locations on the surface that it left during dissolution. During dissolution, hollow nuclei are formed mainly at defects. During the transition to growth it is important on which defect the dissolution occurred: point defects, inclusions, sometimes even edge dislocations can disappear as a result of dissolution and the centre of dissolution will no longer be a stressed area with an increased chemical potential. If dissolution has occurred on screw dislocations, which can extend over the entire crystal, the material will never integrate into the centre of the pit formed on such defects. The substance also has difficulty attaching to the top of the dislocation hillock at the very beginning of growth, making it difficult for new turns and steps to form on the top immediately after the system has passed the saturation point.

2. The step–wave mechanism of dissolution of real crystals on hidden defects, despite the theoretically predicted depth of steps equal to the elementary unit characteristic of a given substance, can be realised even near the saturation point by different depths of dissolution wave steps – the deepest at the beginning and the smallest closer to the saturation state.

3. During near equilibrium dissolution, in contrast to growth, bundles of narrow and shallow dissolution regions can be formed which extend in a particular crystallographic direction. Their shape is determined by the superposition of the etching vectors characteristic of the surface of a given syngony and substance and the propagation vectors of specific steps.

4. Closed steps of a polygonal dislocation hillock on the face of a molecular crystal near the saturation point do not show significant differences or complete identity of shape during dissolution and subsequent growth. Straight edges of steps may become locally curved and right angles of steps may become pointed/rounded during both growth and dissolution.

5. The moment of transition from dissolution to growth on the dislocation pit on the dioxidine face is not characterised by a "stop", i.e. visual equilibrium: the outer steps of the pit have already begun to grow and the centre of the pit is still dissolving. At the moment of transition from dissolution to growth on the dislocation hillock on the dioxidine face there is also no stop, although in this case a "stop" is likely in the 4.5 minute interval between scans. Stop is in quotes because strictly physical equilibrium does not mean the absence of processes, but the equality of the number of attachments and detachments.

6. The assumptions of simultaneous growth and dissolution in the transition zone around the saturation point and of pure dissolution and pure growth far from the saturation point were not justified. The AFM data show that, at a relative distance from the saturation point, there is significant growth during general dissolution and individual dissolution during general growth. On the other hand, the transition from the growth zone to the dissolution zone close to the saturation point is characterised by pure processes, which may be related to the achieved uniformity of the substance distribution due to its sufficient quantity in the immediate vicinity of the facet surface.

7. The assumption of visual symmetry of the tangential and normal growth and dissolution rates and their modular equivalence at the same distance from the saturation point was not confirmed. The average rate itself changes significantly and has large and unstable fluctuations that only decrease close to the saturation point. On the contrary, the graph of the growth rate first shows a jump and then a monotonous decrease, characterised by small and constant fluctuations at a distance from the saturation point. Similar conclusions about the non-equivalence of the processes for the normal rate are confirmed by direct measurements, since the hillock during growth, within one hour after passing the saturation point, did not regain the contour it had during dissolution one hour before reaching the saturation point.

8. The analysis of the instrumental influence on the experimental results (Section 2.6.2 of Chapter 2), taking into account the mixing of the solution by the scanning unit and the heating effect of the laser, does not contradict the conclusions about the irreversibility of the growth-dissolution processes.

3.2 Dynamics and kinetics of layer-by-layer growth and dissolution without mechanical impact

3.2.1 Growth of monomolecular steps on screw dislocations

In order to draw correct conclusions about the influence of mechanical factors on the kinetics of processes and the morphology of the crystal surface, it is necessary to compare such experiments with unaffected experiments. To assess the consequences of scratching the top of a dislocation hillock with monomolecular steps, it is necessary to imagine how similar hillocks grow under normal conditions (Piskunova, 2018 b). In the previous section, the second half of the experiment was devoted to the very beginning of growth without any effect on the polygonal steps of the dislocation hillock. After the transition to growth, its steps did not change shape and did not deviate from the directions dictated by the general shape of the hillock. Figure 3.10 shows a plot of the average tangential rate and its variations for this experiment.

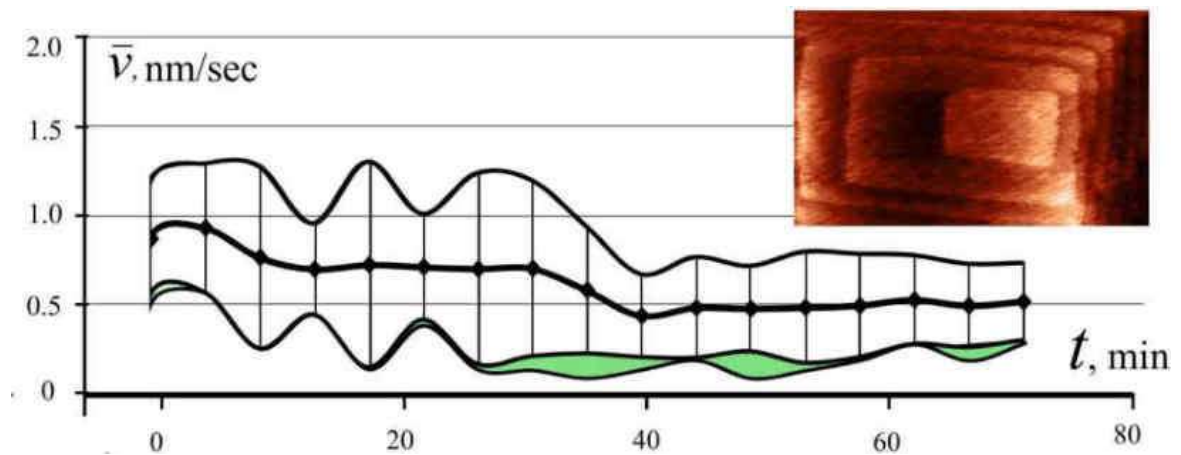


Figure 3.10 – Average tangential rate of monomolecular steps and its fluctuations (plotted up and down at each point) for growth on a Frank-Read dislocation hillock immediately after passing the saturation point. 7,300 rate values were used. Green patches – addition introduced by dissolution events during growth

Random increases in fluctuations are damped in this experiment, which is consistent with Prigogine's description of a stable non-equilibrium state (Prigogine, Kondepudi, 2002). Closed steps are emitted from the top of the hillock in Figure 3.10 because it is formed on two dislocations of opposite sign (the spirals twist towards each other and, according to Frank, provided the distance between the dislocations is greater than the radius of the critical nucleus, their steps will merge). If the hillock is formed on dislocations of the same sign (twisting of the spirals in one direction), the picture can be different depending on the growth conditions and the shape of the hillock.

For example, the steps can move in pairs (Figure 3.11 (a)) or separately, but on an elongated hillock a "pigtail" pattern is formed at the bends (Figure 3.11 (b)). It is also thought that such a difference in the relative position of the steps can be caused by the distance between the exits of the screw dislocations (Bletskan, 1979): if it is less than $2\pi r_c$, where r_c is the radius of the critical nucleus (in the case of dioxidine, the radius of the molecule), then the steps will move in pairs; if it is greater than $2\pi r_c$, they will look as in Figure 3.11 (b).

The following experiment without any influence shows the growth of such a hillock, the steps of which form a "pigtail" at the bends (Figure 3.12). Its apex contains the exits of two dislocations of the same sign. It is obvious that the steps of such a hillock, even when growing without any influence, do not look ideal on such a scale; they can influence each other by pulling the feed, causing parts of some steps to move forward temporarily, but then they align again. Initially, only 8 steps fit on one slope of the hillock in the scanning area, whereas after 70 minutes 16 steps are moving in the same area. Nevertheless, the hillock as a whole retained the shape of the steps and the direction of their propagation throughout the observation period. The graph of the average tangential rate and its fluctuations for this experiment is shown in Figure 3.13.

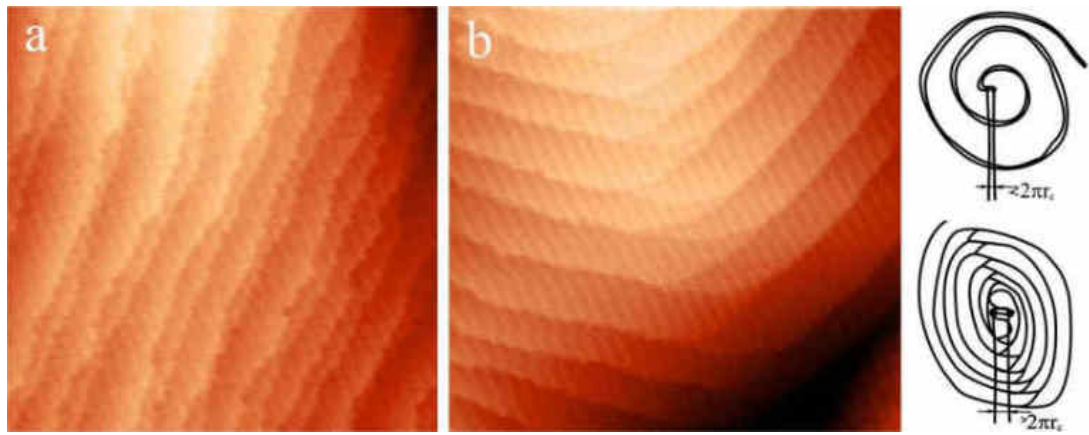


Figure 3.11 – Monomolecular steps produced by two adjacent dislocations of the same sign (twisting of the spirals in one direction). The steps can move in pairs (a) or separately, but on an elongated hillock a "pigtail" pattern is formed at the bends (b)

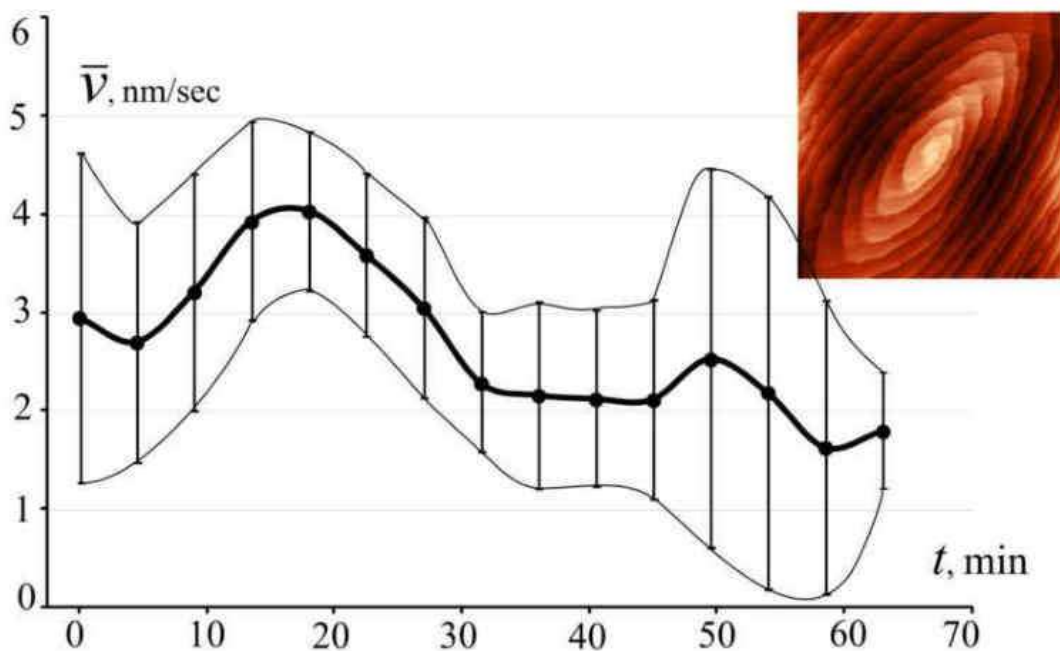


Figure 3.13 – Average tangential rate of monomolecular steps and its fluctuations (plotted up and down at each point) for growth in the experiment from Figure 3.12. Over 3000 rate values were used. The fluctuations are due to the mutual influence of steps on a complex hillock formed on two dislocations

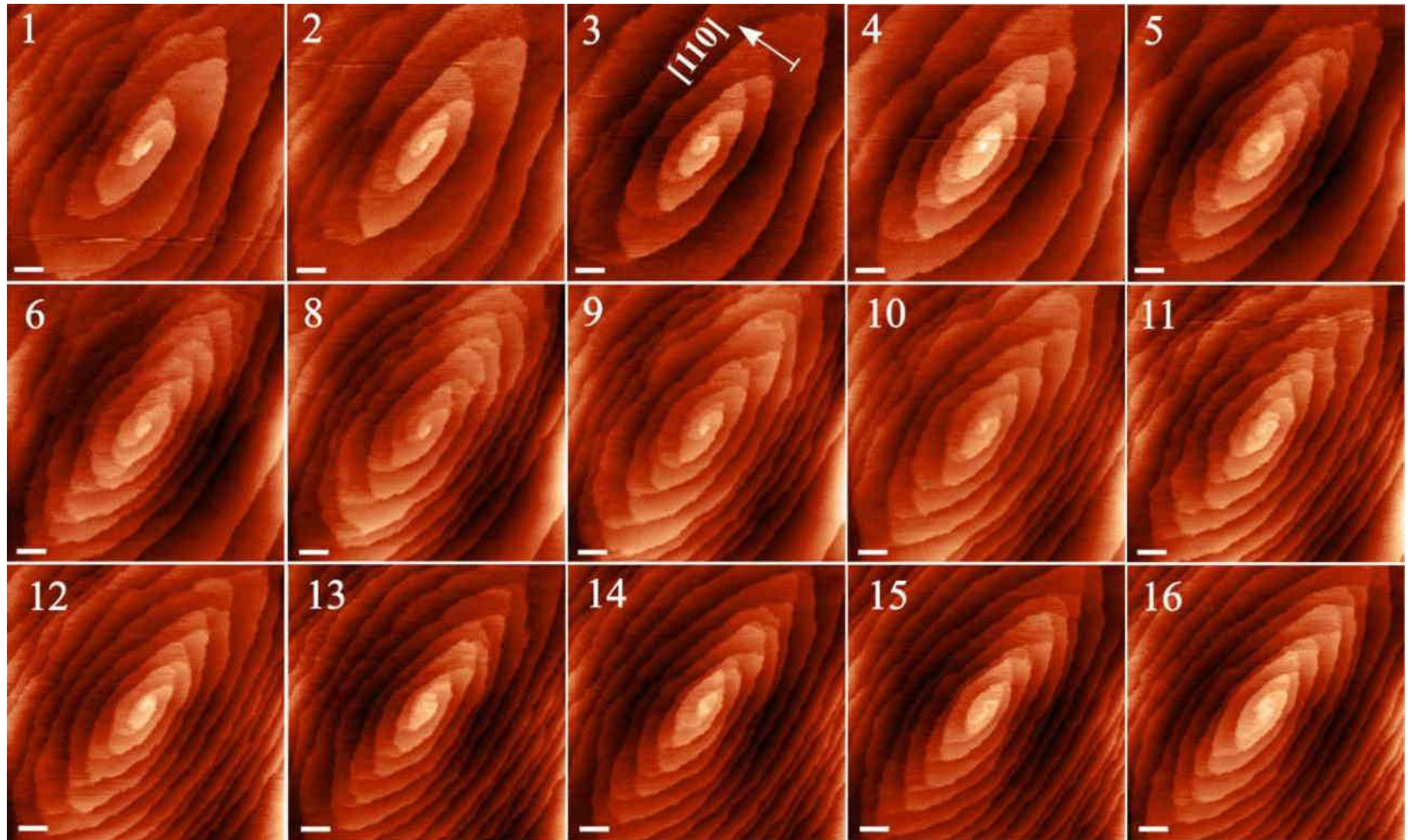


Figure 3.12 – Growth without influence on a hill formed by two dislocations of the same sign. Time interval between sequentially numbered images – 4.5 min. Scale bars – 1 μm

The rate fluctuations are associated with the mutual influence of the steps on the complex hillock formed on two dislocations as described above.

An even more complex hillock was observed in the following non-exposure experiment (Figure 3.14). It clearly shows how the steps from the counter-rotating spirals merge into the Frank-Read hillocks.

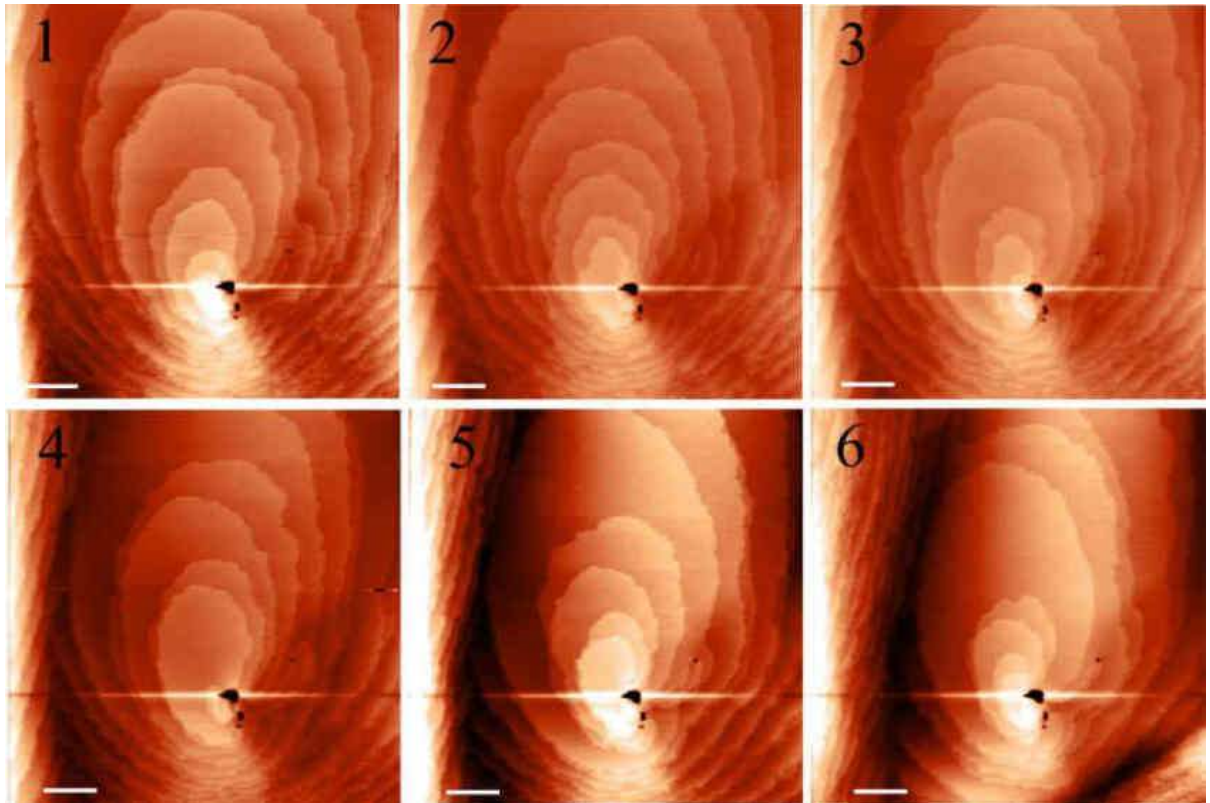


Figure 3.14 – Growth of monomolecular steps of a complex hillock. The time interval between sequentially numbered images is 4.5 minutes. Scale bars are 2 μm

The hillock in Figure 3.14 is formed by a large number of dislocations:

- the bundle of 7 dislocations, marked with the symbol "1" in Figure 3.15, twisting the steps clockwise,
- the union of two dislocations, marked with the symbol "2", twisting the steps anti-clockwise,
- the bundle of at least five dislocations that rotate the steps counterclockwise (symbol "3").

– the bundle of three dislocations (symbol "4") twisting the steps counterclockwise,

The white arrow in Figure 3.15 shows where the steps of different dislocations merge into one step at some distance. Despite such a complex structure and high rates, the hillock retains its shape throughout the observation period. Large holes are visible at the top of the hillock; their origin is due to multiple single exits from dislocation sources of the same sign.

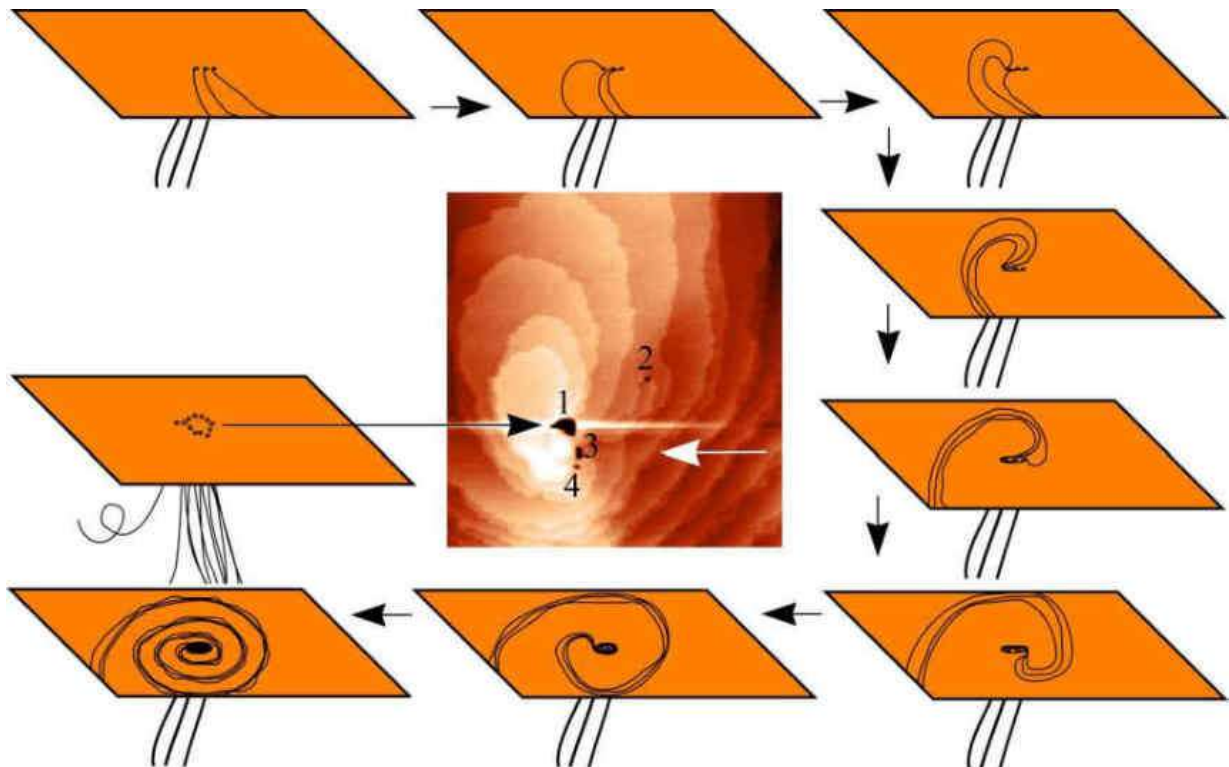


Figure 3.15 – Schematic of the formation of a large hole when steps wrap around all exits in a dislocation bundle. In the centre: "1" – hole from a bundle of seven dislocations twisting the steps clockwise, "2" – hole from two dislocations (counterclockwise), "3" – hole from a bundle of five dislocations (counterclockwise), "4" – round hole from three dislocations twisting the steps counterclockwise. The white arrow shows the merging of the steps

The diameter of the channel of a single elementary dislocation (Burgers vector equal to 1) may differ from the visible hole at its exit point on the surface. This depends on the growth time of the hillock. The channel itself is a thin capillary, but if the site of

its exit on the surface is bypassed many times by an elementary step during growth, the width of the channel can reach tens of nanometres, depending on the nature of the substance and the growth rate. If there are many dislocation exits and they are spaced some distance apart (but not more than $2\pi r_c$, where r_c – radius critical nuclei), then the steps emitted by them will wrap around all the exits one by one, eventually forming a large hole (Figure 3.15). Such a hillock, as in Figure 3.14, is formed precisely on a set of nearby dislocations; it does not owe its origin to a large shear when dislocations with a large Burgers vector are formed. This is evidenced by the large holes formed on its top according to the scheme (Figure 3.15) and the elementary height of the steps. The graphs of the average tangential rate and its fluctuations on the dislocation hillock from Figure 3.14 are shown in Figure 3.16. Since the rate distributions were bimodal, the data were divided into two parts: for the "upper" steps emitted by the more active dislocation at the top of the scan window (dislocation "1" in Figure 3.15), and for those whose movement occurs at the bottom of the scan window – the "lower" steps.

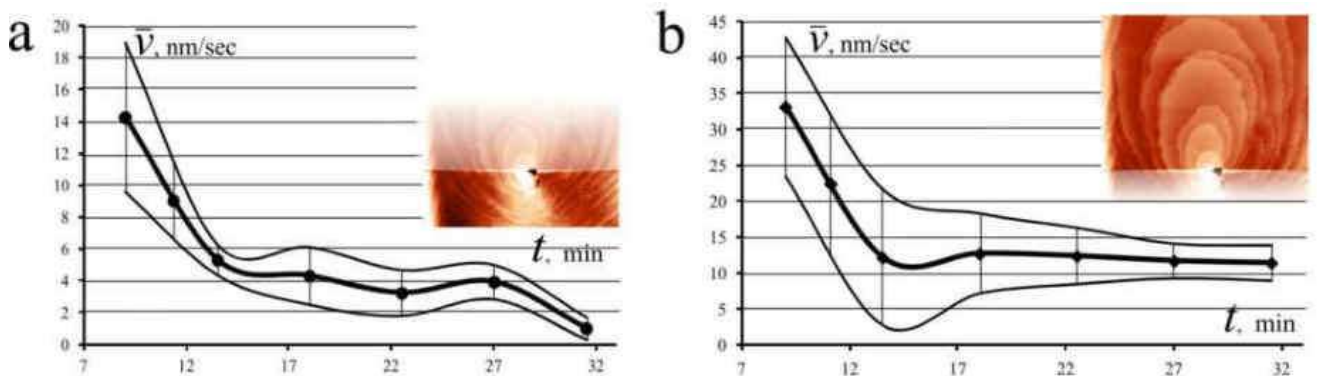


Figure 3.16 – Average tangential rate of monomolecular steps on a complex hill (Figure 3.14) and its fluctuations (plotted up and down at each point): (a) – for lower steps, (b) – for upper steps. The graphs contain about 3500 rate values.

The plots show a decrease in rate and, despite the intense growth, smooth fluctuations are observed which are very small for the lower steps.

Observations of the growth of dislocation hillocks of different types with monomolecular steps show that the hillocks retain their original shape, although the

density of the steps making up the hillock may change depending on the growth conditions.

For example, Figure 3.17 shows a simple hillock with a single monomolecular polygonal step twisted clockwise, which during 117 minutes of observation reduced the density of the twists but retained its outline. The polygonality is characteristic of hillocks at low supersaturation, but towards the end of the observation the rate increased and apparently its fluctuations increased, so that the top of the hillock began to be inadequately drawn (the 25th and 26th frames in Figure 3.17).

The following Figure 3.18 shows a hillock formed by two screw dislocations whose monomolecular steps twist counterclockwise. As can be seen, the hillock retains its shape during growth. Foreign steps creep up the hillock from below (Figures 10–15 in Figure 3.18). When it was fully submerged under these steps, its dislocation exit (marked with a circle at (18) in Figure 3.18) was transmitted through 12 monomolecular layers. Figure 3.19 shows a surface area of $10 \times 9 \mu\text{m}^2$ on which many screw hillocks grow, all their steps twisting counterclockwise. In the left part of the figure a chain of screw dislocations can be seen, the minimum distance between them being 250 nm. All the hillocks retain their original shape despite their mutual influence. After 99 minutes, a chain of hillocks is also recorded in this area (the last image in Figure 3.19). The growth of a complex hillock is shown in Figure 3.20. This hillock is formed by about 17 screw dislocations, all the monomolecular steps emitted by them twist clockwise. The hillock also retains its shape for almost 90 minutes.

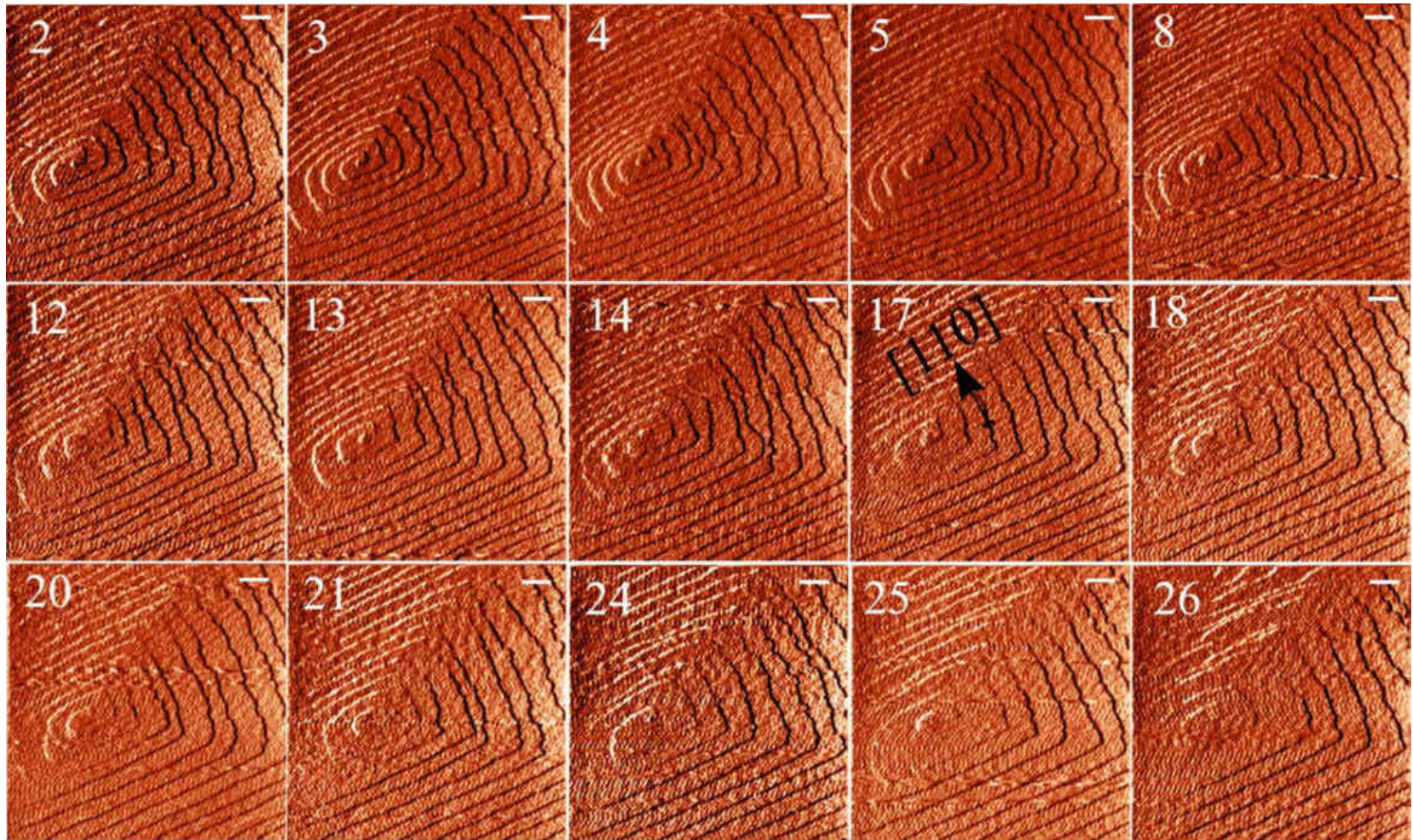
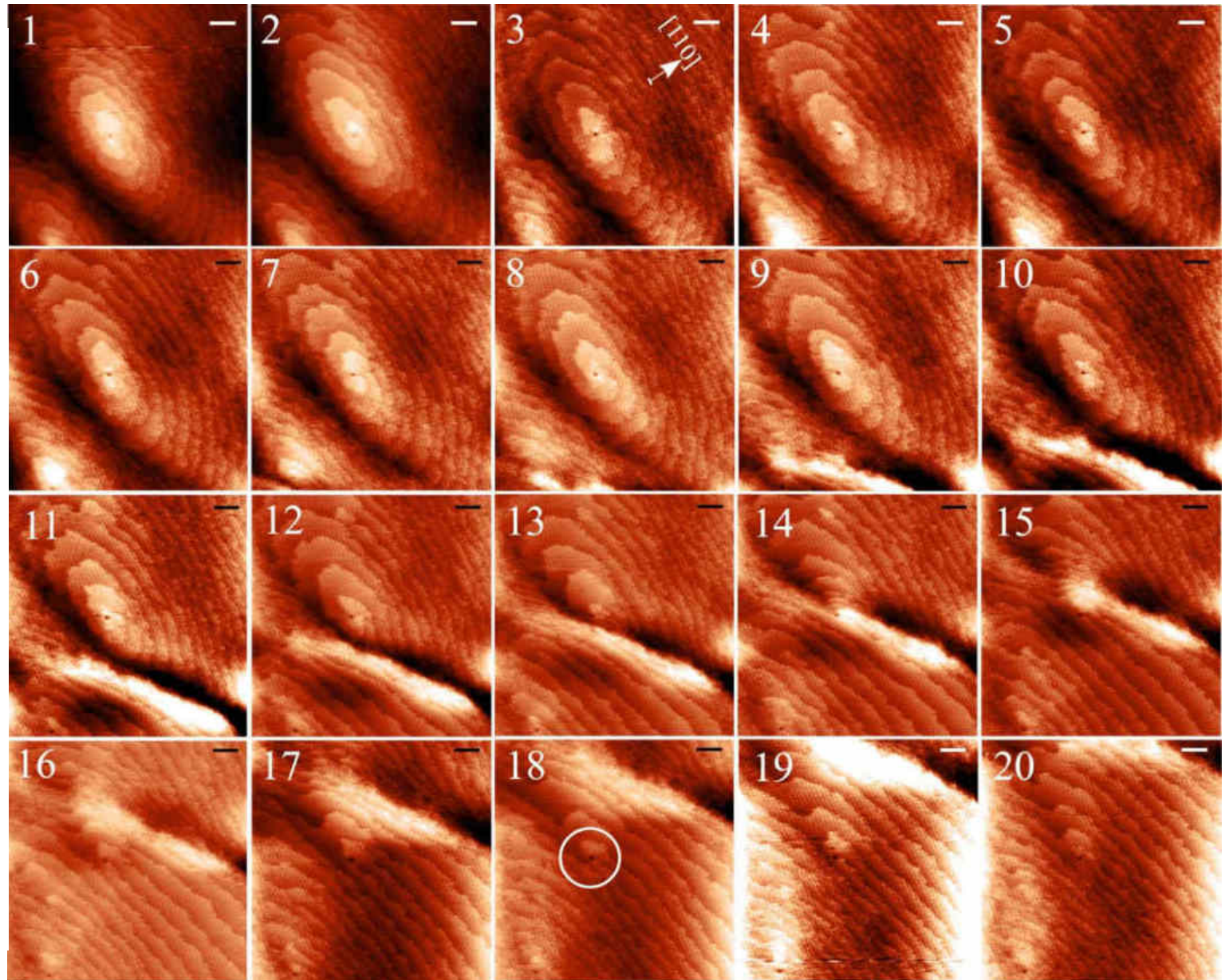


Figure 3.17 – Growth of a polygonal hillock on a screw dislocation (Burgers vector equal to 1) with a screw step of monomolecular height twisted clockwise. Scale bar 500 nm. Time interval between consecutively numbered images – 4.5 min, total observation time 117 minutes

Figure 3.18 – Growth of a hillock formed by two screw dislocations: the monomolecular steps twist counterclockwise. When the hillock was absorbed, its dislocation exit (marked with a circle in (18)) was transmitted through the grown 12 monomolecular layers. Scale bars are 500 nm. The time interval between consecutively numbered images is 4.5 minutes



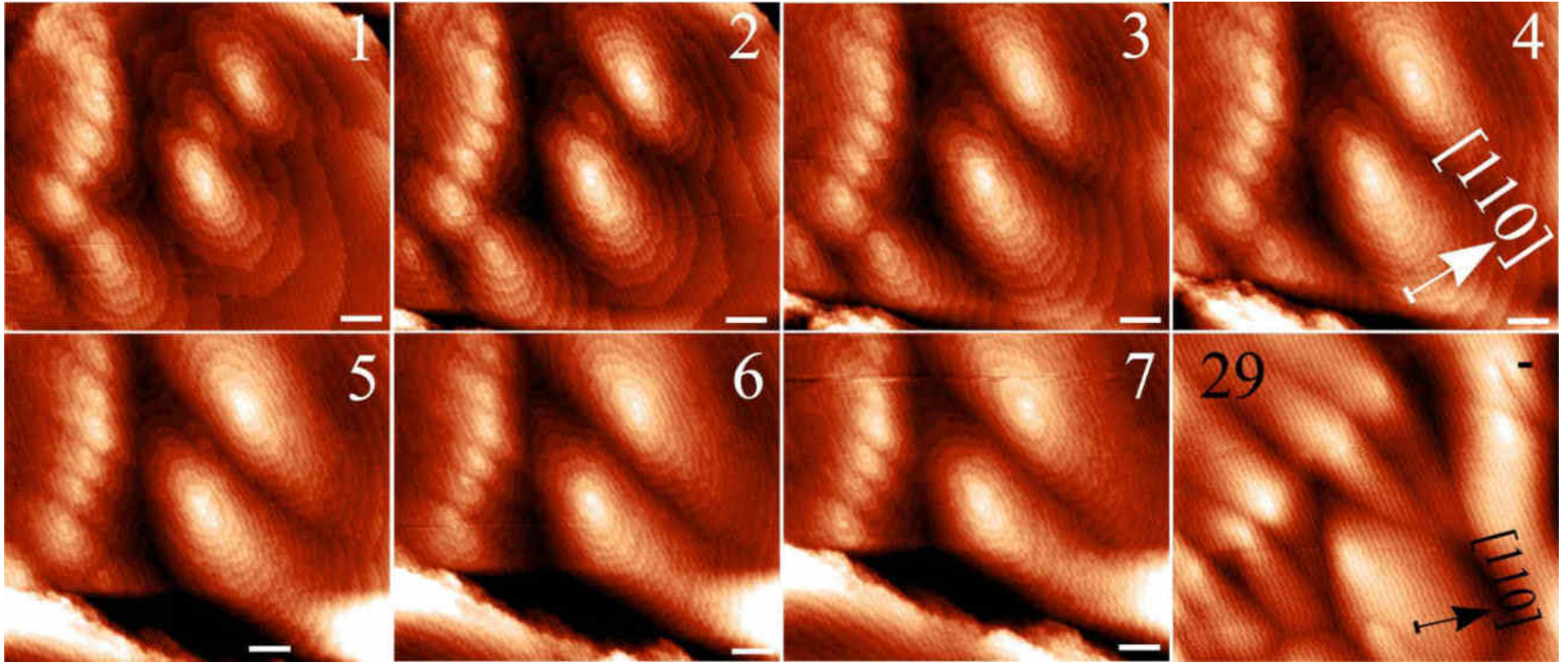
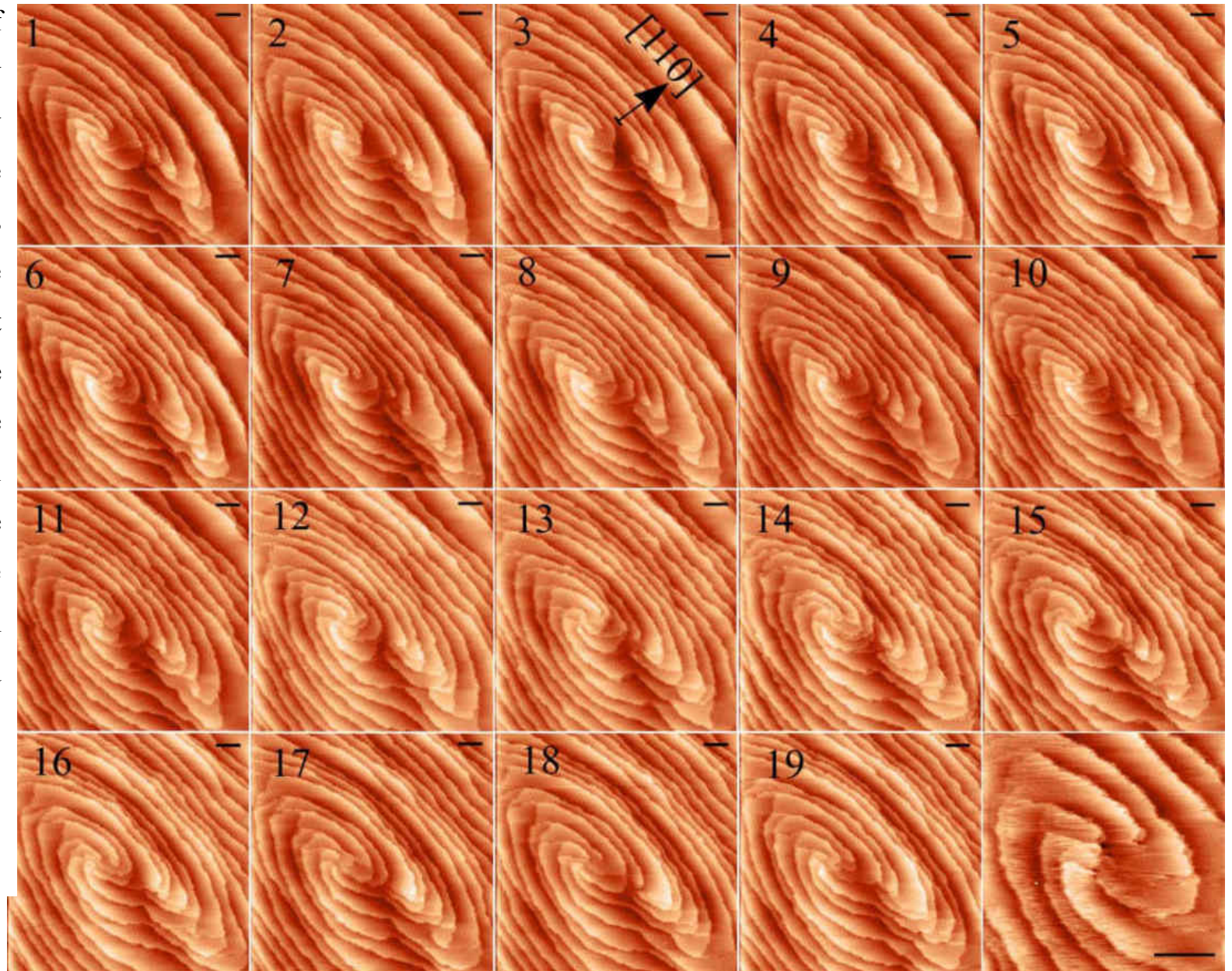


Figure 3.19 – Simultaneous growth on a $10 \times 9 \mu\text{m}^2$ area of a series of helical hillocks whose steps rotate counterclockwise. All steps in the images are monomolecular. The last image shows the same site as the first, after 99 minutes, on a larger scale: the chains of hillocks are preserved. The scale bars are $1 \mu\text{m}$. The time between successively numbered images is 4.5 minutes

Figure 3.20 – Growth of a hillock formed by about 17 screw dislocations. The monomolecular steps they emit rotate clockwise. The last figure shows the distance between the exits of individual dislocations. The scale bars are 1 μm . The time interval between sequentially numbered images is 4.5 minutes



3.2.2 Growth of macrosteps and large hillocks

If it is clear from the appearance of the hillocks in the previous section that they are due to screw dislocations, it is not so obvious when macrosteps and microcrystals are observed on the surface (Figure 3.21). On closer inspection, however, all the large islands are of dislocation nature and the large steps are composed of elementary steps (Figures 3.22, 3.23, 3.24 and 3.25). Macrosteps and even the edges of epitaxially growing microcrystals can be slowed down at the exit of screw dislocations as obstacles (Figure 3.26). Dislocations can also create hillocks of macrosteps; Figure 3.27 shows a hillock with a large Burgers vector.

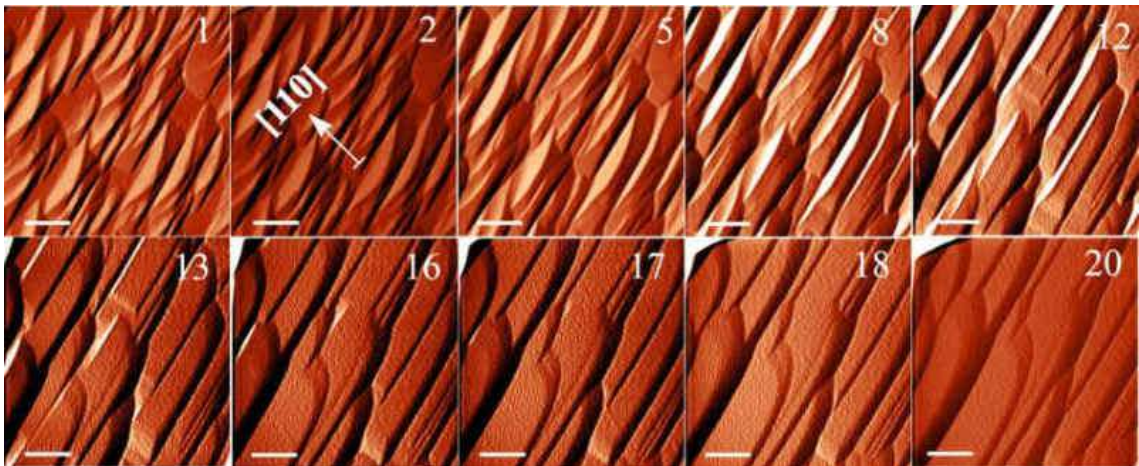


Figure 3.21 – Large island growth. Scale bars 5 μm . Time interval between sequentially numbered images – 4.5 minutes

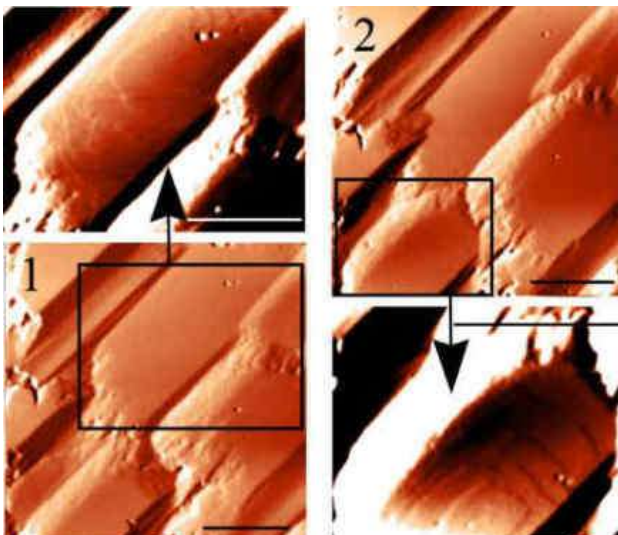


Figure 3.22 - Dislocation nature of large islands. A Sobel filter was used to detect monomolecular feet. The time interval between sequentially numbered images is 4.5 minutes. Scale bars are 2 μm

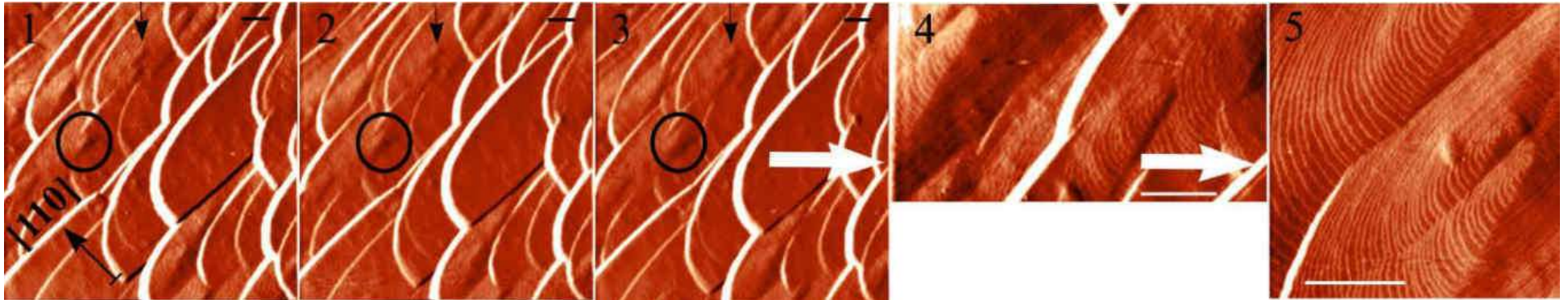


Figure 3.23 – Dislocation nature of large islands. Scale bars 5 μm . Time between sequentially numbered images – 4.5 minutes

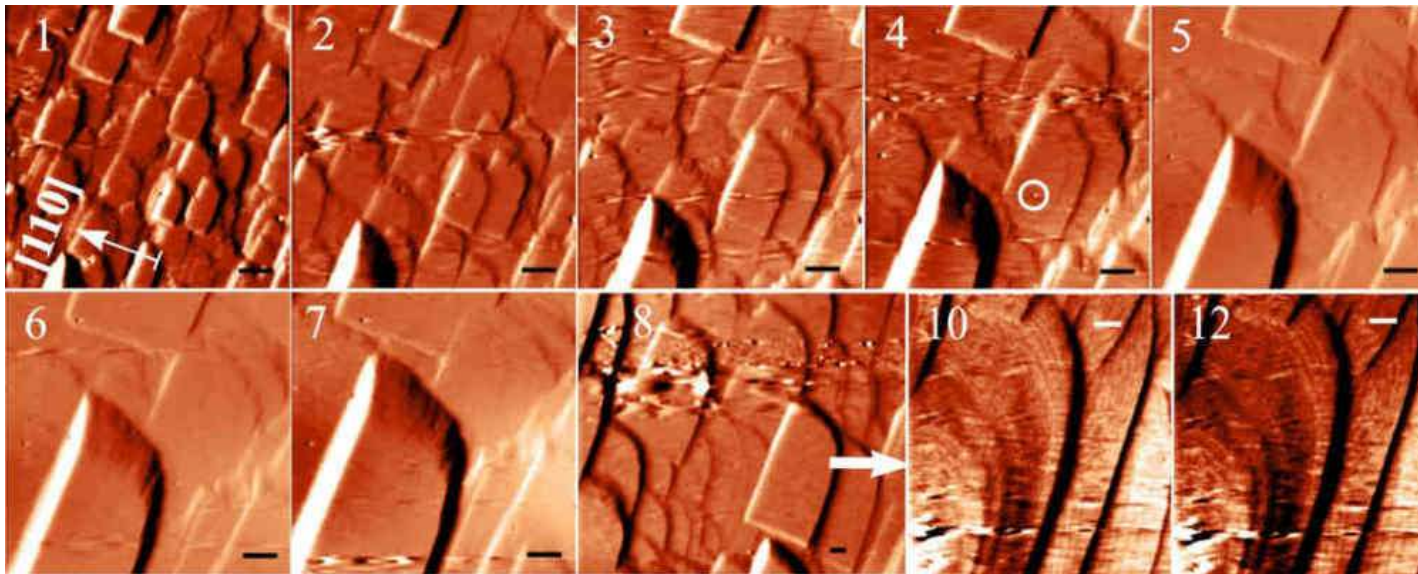


Figure 3.24 – Growth of large islands on screw dislocations (in the 4th picture the exit of the dislocation source is marked with a circle), elementary steps are visible in pictures 10 and 12.

Scale bars are 2 μm

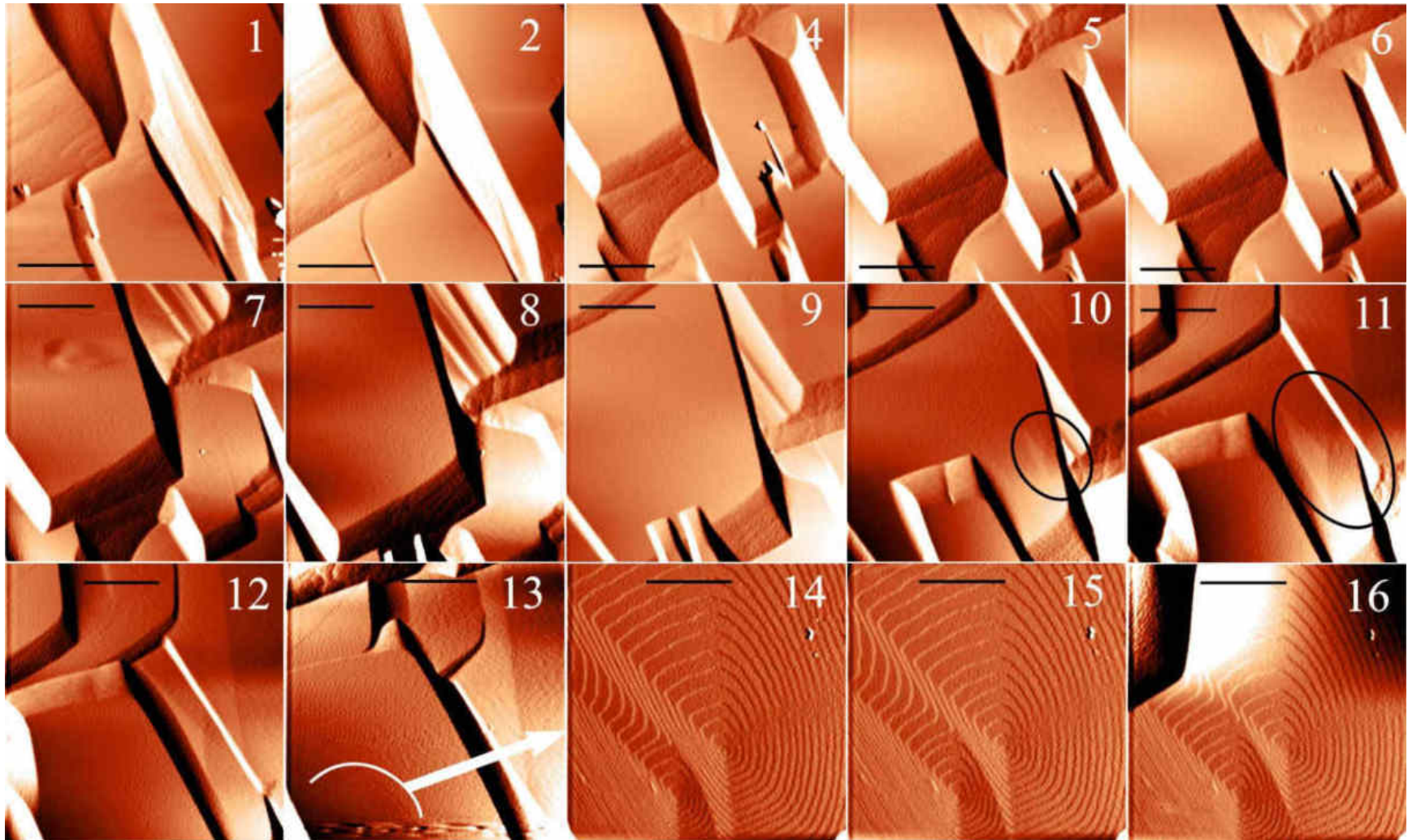


Figure 3.25 – Dislocation nature of large islands. The circles in (10) and (11) mark the polygonal hillock of a screw dislocation translated through layers. In (14–15) the dislocation structure of another large flat island is shown. The scale bars are $10\ \mu\text{m}$. The time interval between sequentially numbered images is 4.5 minutes

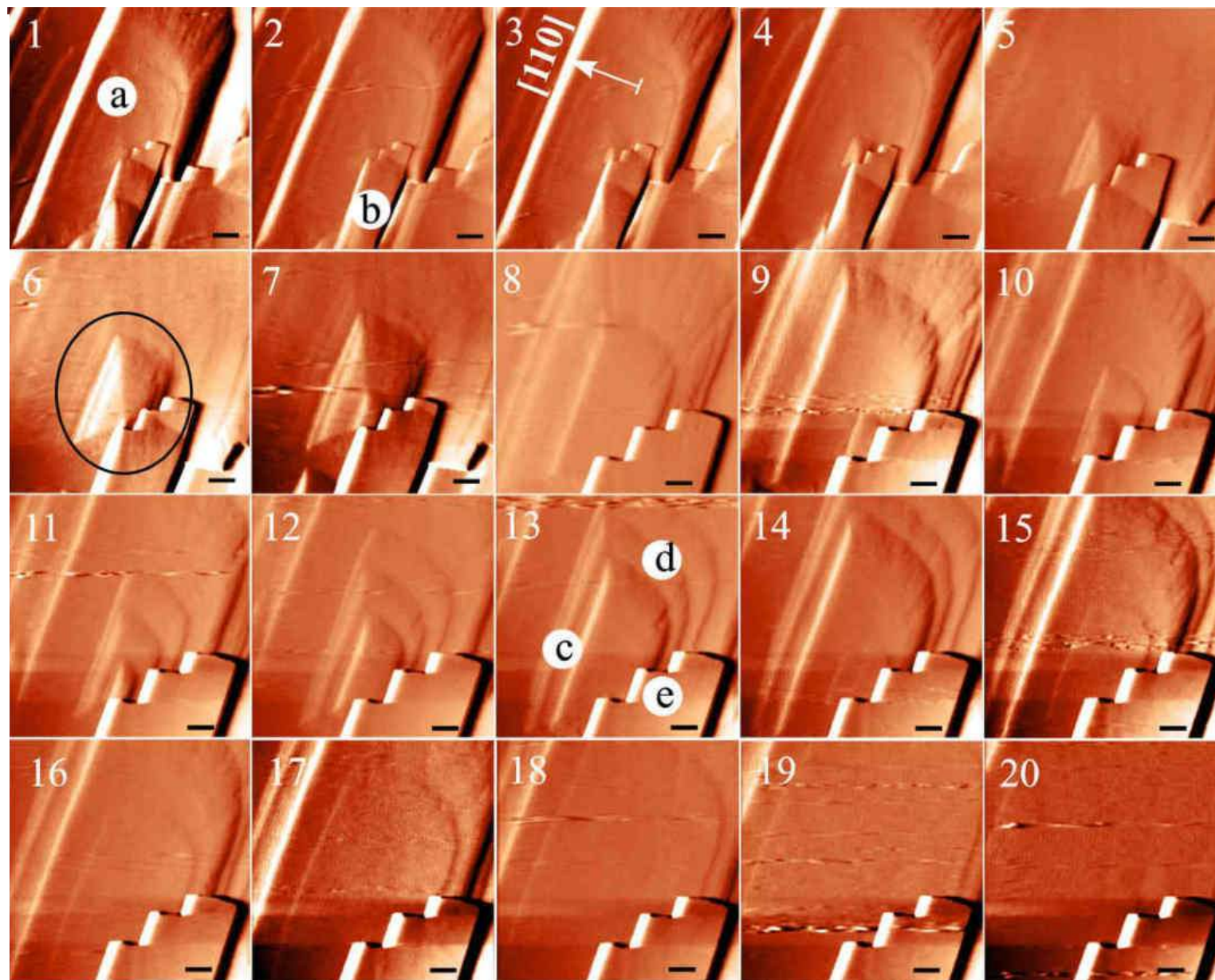
Figure 3.26 – The edge of the upper microcrystal was obstructed during growth by the exit point of a screw dislocation (marked with a circle in (6)) on the lower crystal.

The tangential growth rates of the lower crystal (symbol "a") are initially 1-9 nm/sec and those of the upper crystal (symbol "b") are 4-5.9 nm/sec.

The rates of the screw steps on the lower crystal are
 "c" - 3.3-4.6 nm/sec,
 "d" - 9 nm/sec.

The edge of the upper crystal ("e") does not move.

Scale bars are 5 μm . The time interval between sequentially numbered images is 4.5 minutes



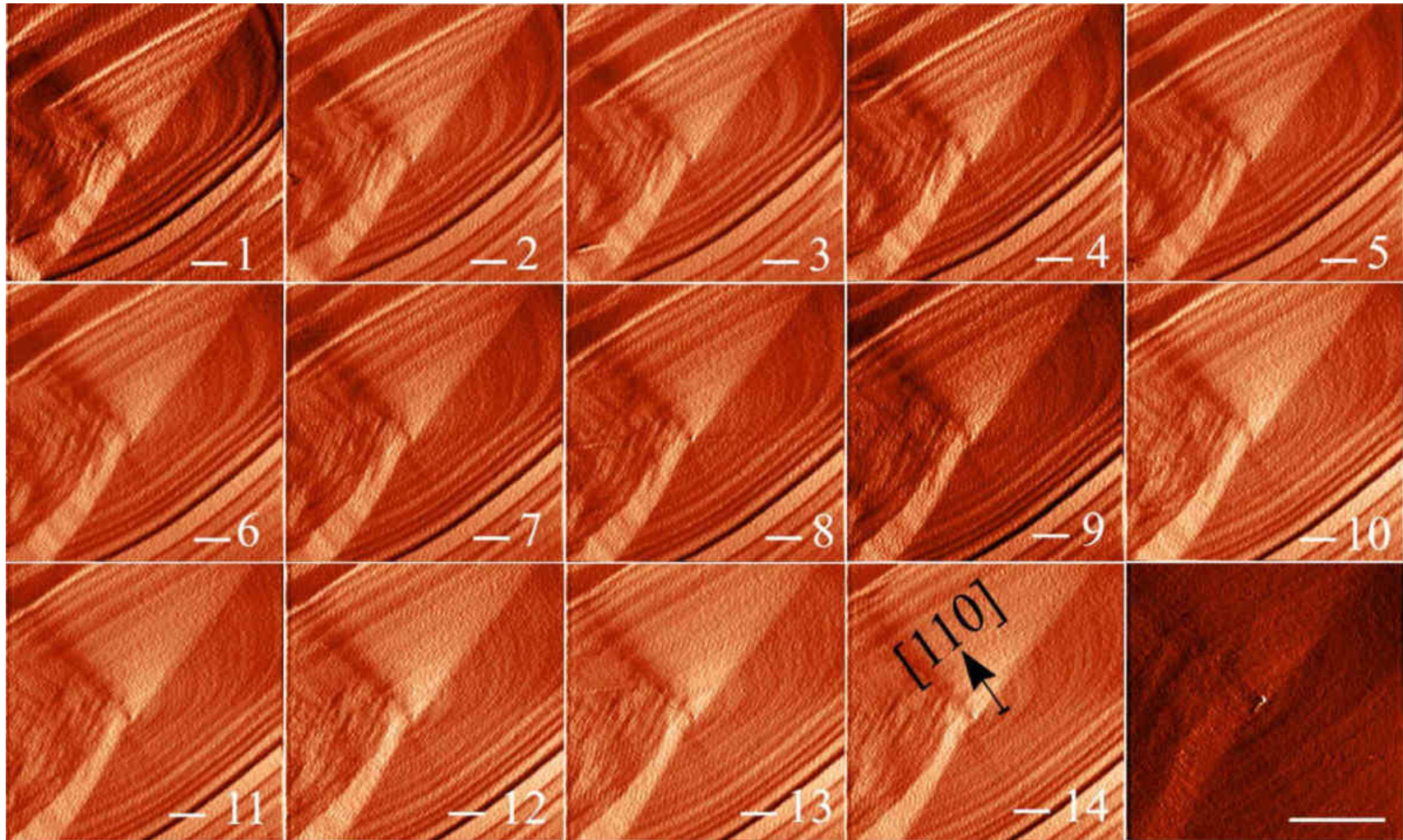


Figure 3.27 – Growth of a large hillock on a screw dislocation. Elementary steps are not recorded (the last image is at the top of the hillock) but they form step density waves of 3.5, 6, 8 and 10 nm. Scale bars are 5 μm . The time interval between sequentially numbered images is 4.5 minutes

3.2.3 Dissolution without mechanical impact

The dissolution of a real crystal begins with the formation of hollow nuclei on defects, this is true for both high and low degrees of undersaturation. In the former case, deep etching reveals a massive crystalline layer in places that hide defects. A process visually similar to chemical polishing is initiated when the dissolution of the massive layer prevails over the tangential reduction of steps on a relatively flat substrate (Figure 3.28).

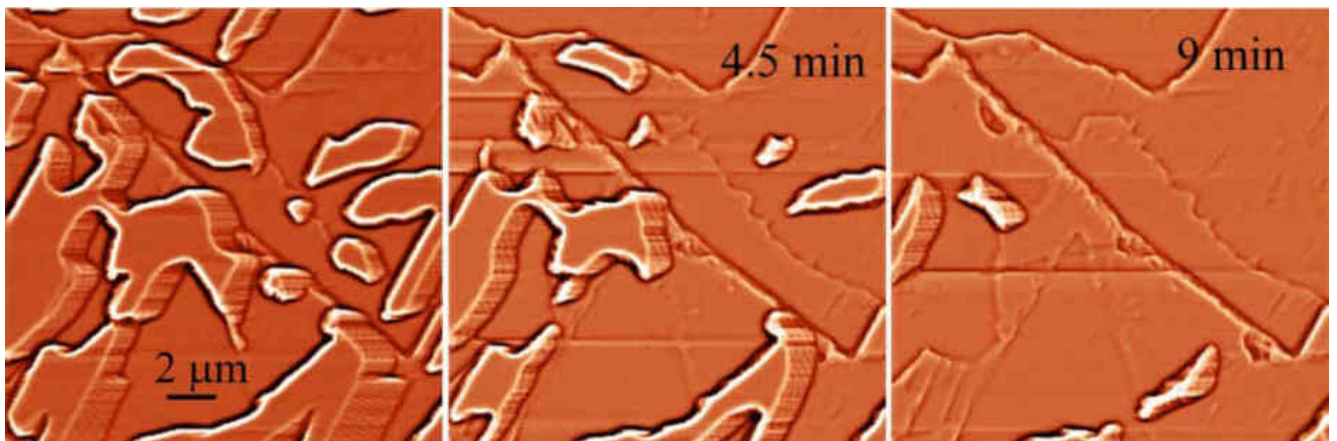


Figure 3.28 – Dissolution at relatively large undersaturations: formation of deep dissolution nuclei simultaneously in many defect areas and dissolution of a large layer.

Scale bars are 7 μm . The images show the time from the first image

Further dissolution is also initiated by defects, but because the material content near the surface has increased and gradients have been established, dissolution on thin steps and defects occurs at a slower rate, relief details do not quickly leave the observation zone and such dissolution can be recorded step by step by AFM (Figures 3.29 and 3.30)

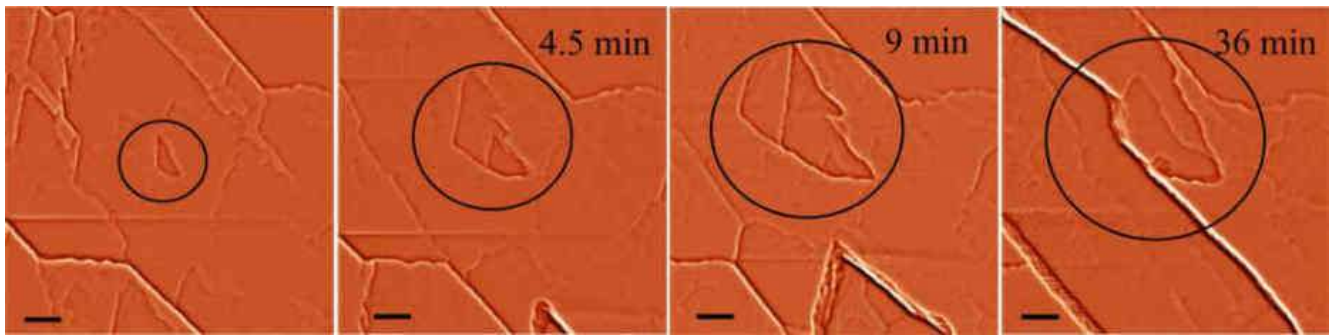


Figure 3.29 – Resolution at small undersaturations on a screw dislocation. Scale bars are 7 μm . The images show the time from the first snapshot

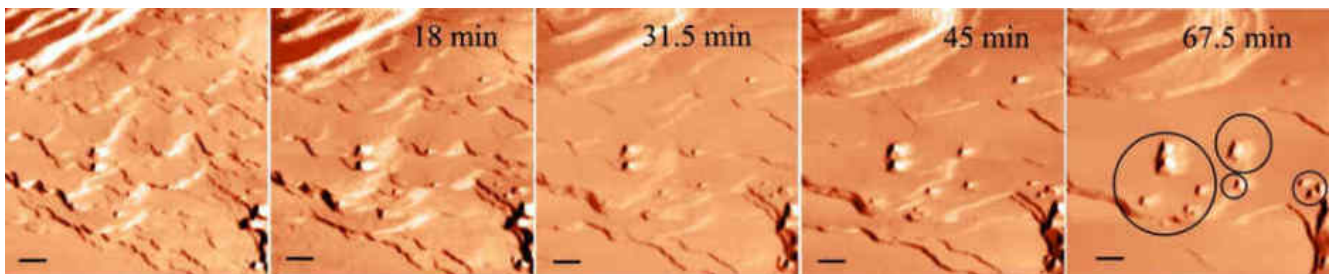


Figure 3.30 – Dissolution with exposure of defective areas (marked with circles in the last image). Scale bars are 1 μm . The images indicate the time from the first image

3.3 Effect of scratches

3.3.1 Effect of scratches on the surface dissolution

Letter “O”

This section presents experiments in which a deliberate, enhanced, directed motion of an indenter, the AFM tip itself, is applied to the surface during growth and dissolution. Section 2.3.2.1 of Chapter 2 shows that such an impact causes the appearance of grooves—scratches up to 1 μm wide.

Before the scratch in the shape of the letter “O” was applied to a specific area of the surface in a slightly undersaturated solution, monomolecular steps (Figure 3.31)

dissolved at a rate of up to 0.6 nm/sec. The measurements were made against reference objects – dislocation exit points (shown as ovals in Figure 3.31).

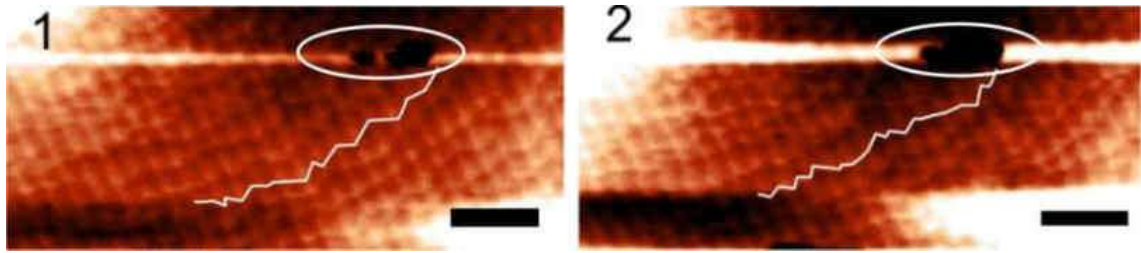
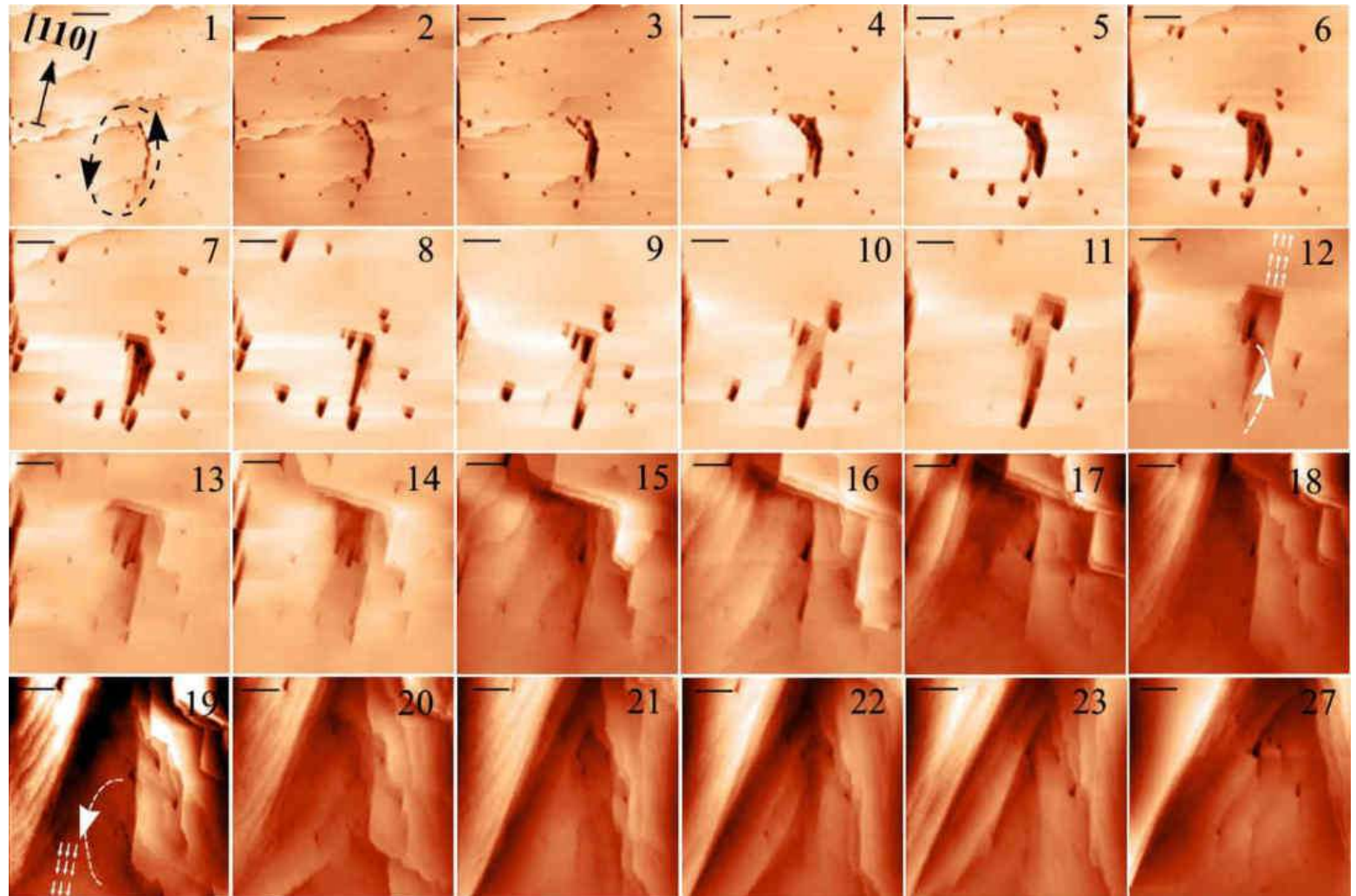


Figure 3.31 – Enlarged image of the surface dissolution prior to the application of an letter “O” shaped scratch. The step profile at time (1) and its profile after 4.5 minutes (2) are shown. Dislocations are marked with an oval. Scale bar – 2 μm

The AFM tip then applied the outline of the letter “O” to the surface, but the left part of the letter did not appear as a scratch because the tip moved in the direction of the steps, encountered virtually no resistance and therefore did not create any defects (Figure 3.32). The changes that occurred to the surface in an hour and a half indicate that the impact of the tip, in addition to the visible scratch, stimulated the appearance of edge dislocations far from the contact point (an explanation of this effect is given in Figure 2.9 in Section 2.3.2.1 of Chapter 2). The tip movement from the right bottom up provoked a displacement and created edge dislocations, resulting in a scratch growing in a near equilibrium solution with a tangential rate of up to 8.8 nm/sec. The tip movement from the left, from top to bottom, did not form a scratch, but apparently created shear stresses (their direction is shown by arrows in Figure 3.32, picture 19) and triggered the dissolution of the lower part of the area. The dissolution canyon does not repeat the contours of the scratch, but is extended in both directions strictly in the direction of $[110]$ – $[11\bar{0}]$, i.e. in the direction of the disturbances created far from the scratch.

Figure 3.32 – Dissolving an almost flat surface on a scratch in the shape of the letter “O” in a slightly undersaturated solution. The left part of the letter did not appear as the tip moved in the direction of the steps. The 12th image shows the initial outlines of the scratches and the direction of the formation of edge dislocations (arrows). The scale bars are 5 μm . The time interval between sequentially numbered images is 4.5 minutes



3.3.2 Effect of scratches on layer-by-layer growth characteristics

Layer-by-layer growth area

Before scratching, large steps of almost equal height (about 23 nm) moved almost equidistantly in one direction at rates of 0.9–1.8 nm/sec (Figure 3.33 "before"). The AFM tip then drew two parallel lines of 5 μm length in this area – from top to bottom on the left and from bottom to top on the right – on which scratches quickly appeared in the solution at a supersaturation of 1%. The different widths of the scratches are due to the different energy and number of defects created by the tip: on the left the tip moved in the direction of the steps and the scratch on the left is thinner, while on the right the tip moved against the direction of the steps and the scratch on the right is almost 1 μm wide. The rate of the feet on the surrounding surface decreased to 0.8 nm/sec, while in the area of the scratches the steps started to move at a rate of up to 3 nm/sec. The next image shows that the steps on the surface quickly absorbed the left groove, although their profile was broken at this point. The right scratch is still visible after 13.5 minutes. The morphological stability of the surface was lost after the application of the scratches, the steps lost their original contours and directions, the order of their distribution was disturbed even where there was no direct contact, obviously due to the edge dislocations generated by the effect. The plots of the distribution of relief details by height show that 30 minutes after the application of the scratch, many steps with a height of about 23 nm were regrouped, creating larger steps (callouts in Figure 3.33). The next Figure 3.34 shows a dislocation hillock with two scratches applied to its top.

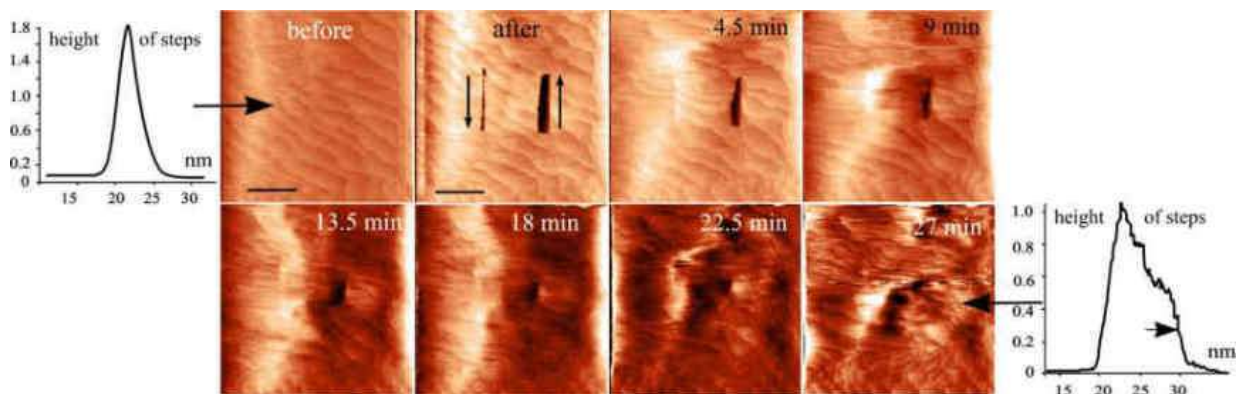
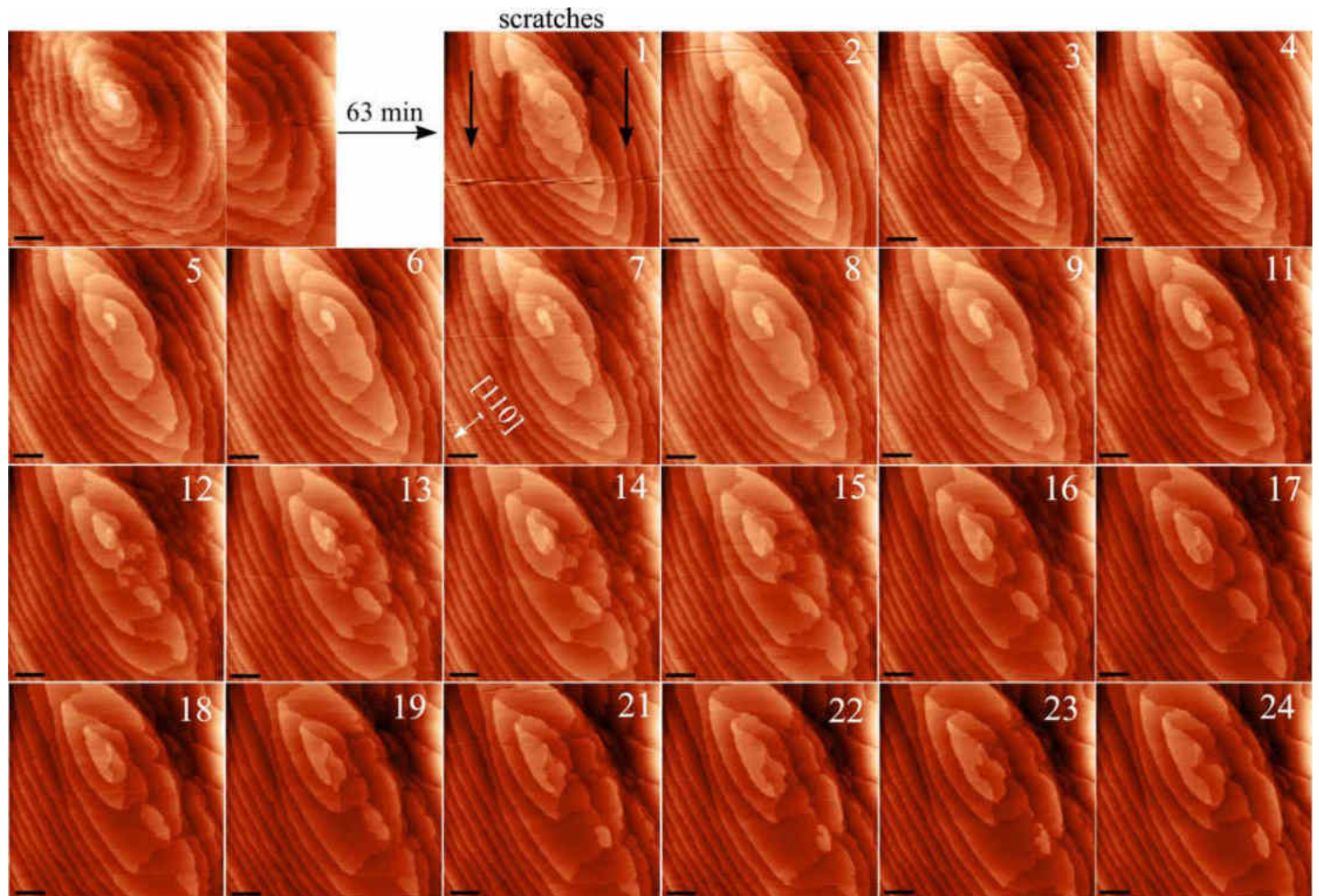


Figure 3.33 – Loss of morphological stability in the Layer-by-layer growth area after scratching. Scale bars are 5 μm . On the top – the time since scratching

Figure 3.34 –
Scratches are drawn from top to bottom to the right and left of the top of the dislocation hillock. On the left the needle moved in the direction of the steps, on the right against them. The scale bars are 2 μm . The time interval between sequentially numbered images is 4.5 minutes



Top of a dislocation hillock

The apex of a dislocation hillock in a solution with a supersaturation of slightly less than 1% emitted monomolecular steps that were grouped in pairs and grew at a rate of up to 0.9 nm/sec before the scratch was applied (Figure 3.34). At the 63rd minute of the experiment, two 5- μm lines were drawn with the AFM tip to the left and right of the apex. The left tip moved in the direction of the steps of the hill and the right tip moved against the direction of the steps. The impact resulted in important morphological and kinetic changes. The initial order of the steps, particularly on the right, was disrupted and the profile of the steps was significantly distorted.

The shape of the steps was distorted even in areas of the surface that were not subjected to direct impact. On the right side, where the needle moved against the direction of the steps, a combination of growth and dissolution was visually observed, including in adjacent areas of the same step at a distance of less than 1 μm (Figure 3.35).

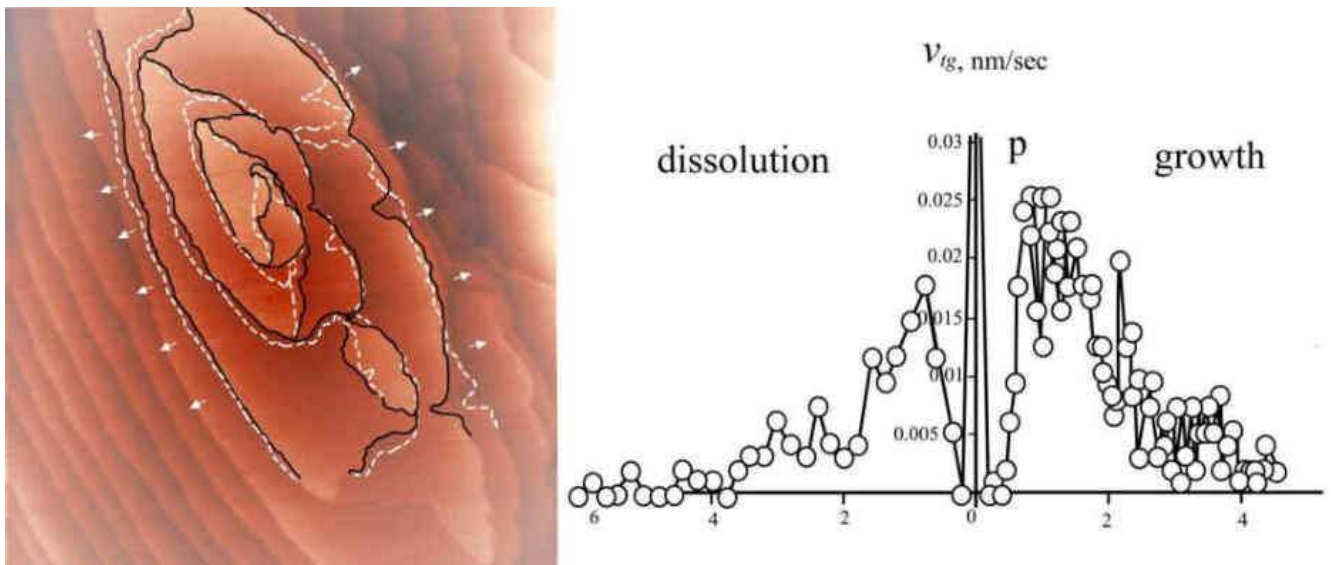


Figure 3.35 – An example of simultaneous growth and dissolution in adjacent areas: the white outline shows the shape that the steps outlined in black will take in 4.5 minutes.

The steps have not moved outwards (grown) everywhere; in some areas their retreat (dissolution) is visible. The distribution of rates for the given pair of images is shown on the right; the average rates of growth and dissolution are practically the same

Simultaneous growth and dissolution were observed using interferometry in the work (Sherwood, Ristic, 2001) where the top of the hillock on sodium chloride was pre-exposed to radiation. Figure 3.36 graphically shows the proportion of dissolving areas during growth on a scratch for the experiment in Figure 3.34; it is evident that dissolution is registered at the very beginning, although it is not visually apparent. To calculate the tangential growth rates and their variations, the results for the left and right parts of the hill have been separated. This is due to significant differences in behaviour, as the needle did not move with the steps on the right, but against them. The coordinates of the dissolving areas were not included in the calculation of growth; the average growth rates and average dissolution rates are shown separately on the graphs (Figure 3.37); they show almost rhythmic fluctuations which have not been observed in similar experiments.

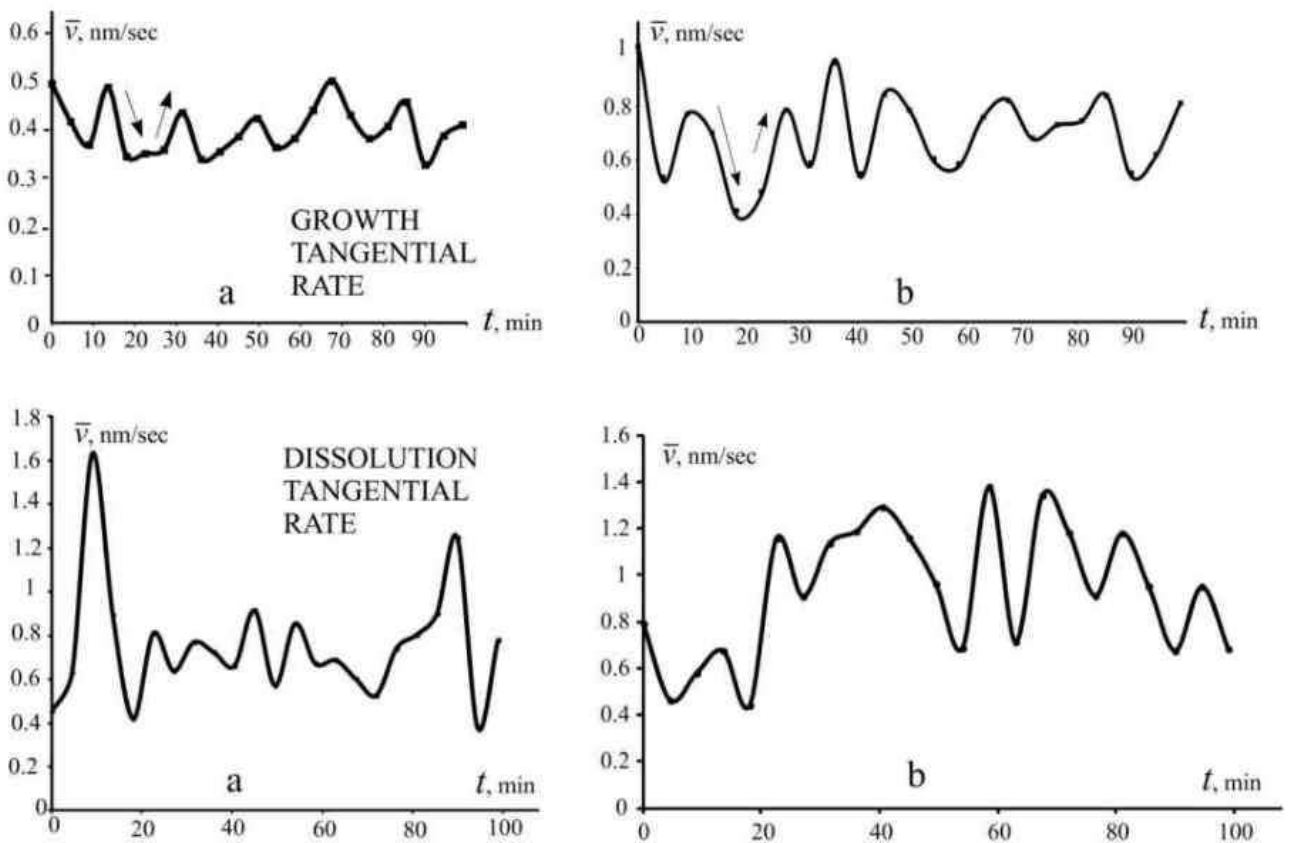


Figure 3.37 – Oscillating nature of average tangential growth and dissolution rates in the scratch experiment: (a) – on the left side of the hill, (b) – on the right.

Approximately 10,000 rate values were used for each plot

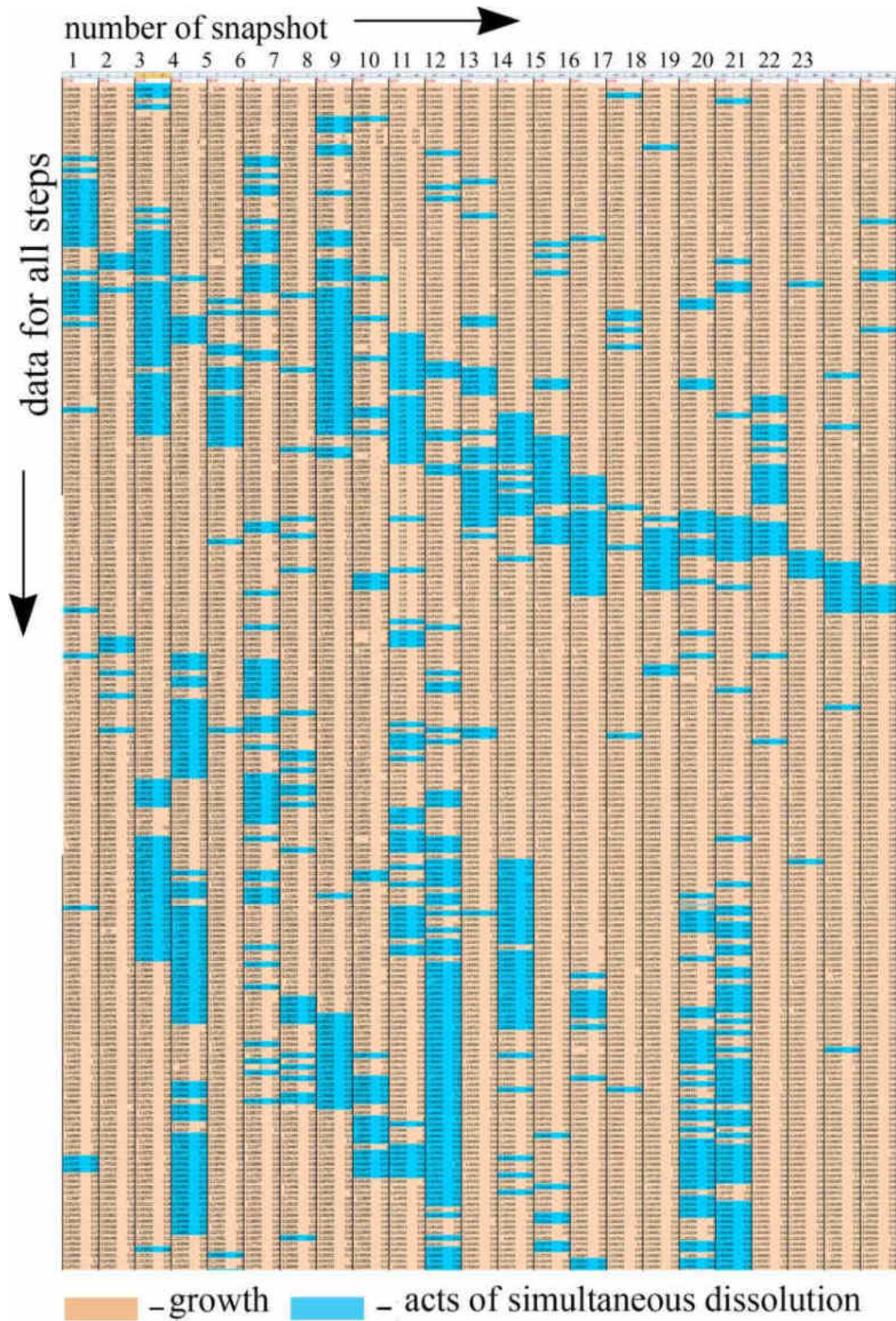


Figure 3.36 – Graphical representation of the dissolution fraction according to AFM data (cells with dissolution point rates are filled in blue) against the background of simultaneous growth (shaded in beige) after applying a scratch for the experiment in

Figure 3.34

No correlation was found between growth and dissolution. There is a correlation between the growth rates on the left and on the right, which reaches 0.95 at the end of the experiment. This means that the rates on the left and right increase and decrease simultaneously. The correlation between the dissolution rates on the left and on the right is negative at each time point and sometimes reaches (-0.86) . This means that the decrease in the dissolution rate on the left is accompanied by an increase in dissolution on the right. Dissolution during the main growth in this experiment is the result of large fluctuations, so the average dissolution rates have been added to the fluctuations in the growth rate plotted at each time point. However, it is clear that even without this addition, the fluctuations, especially on the right, are very large (Figure 3.38 (b)).

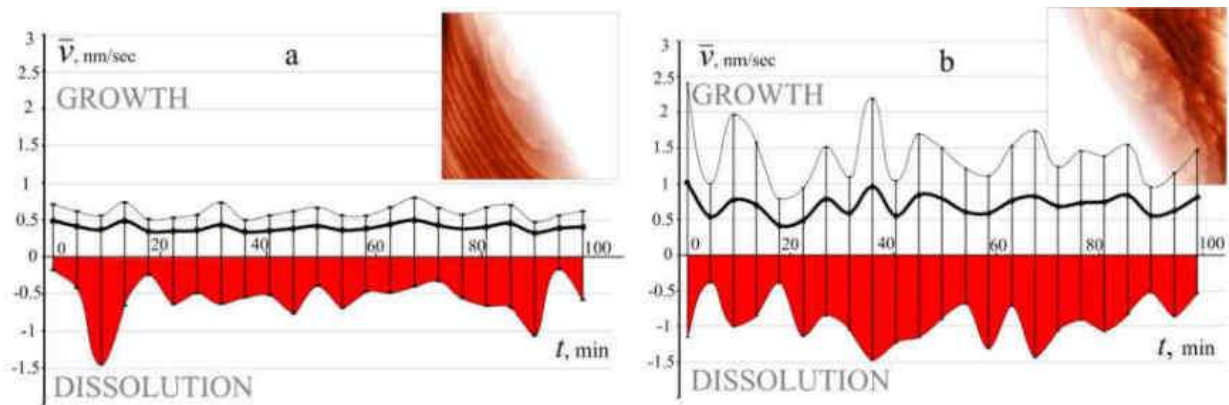


Figure 3.38 – Average tangential growth rates of a hillock (Figure 3.34) after a scratch and their fluctuations plotted up and down at each point: (a) – for the left side of the hillock, (b) – for the right side. The part of the fluctuation that allows dissolution during growth is highlighted in red

The average distances between the steps at each time point and the average normal growth rate, as well as their fluctuations, were then calculated (Figure 3.39).

The discovered oscillatory nature of both tangential and normal rate, which has not been observed in similar experiments, as well as the huge fluctuations and the recorded phenomenon of simultaneous growth and dissolution after scratching, suggest the manifestation of self-organisation at the nanoscale – self-oscillations of the rate. A significant increase in the fluctuations is the main sign of the departure of the system

from the state of thermodynamic equilibrium. At equilibrium, fluctuations serve only as small corrections to the mean values; the second law of thermodynamics neutralises any random increase.

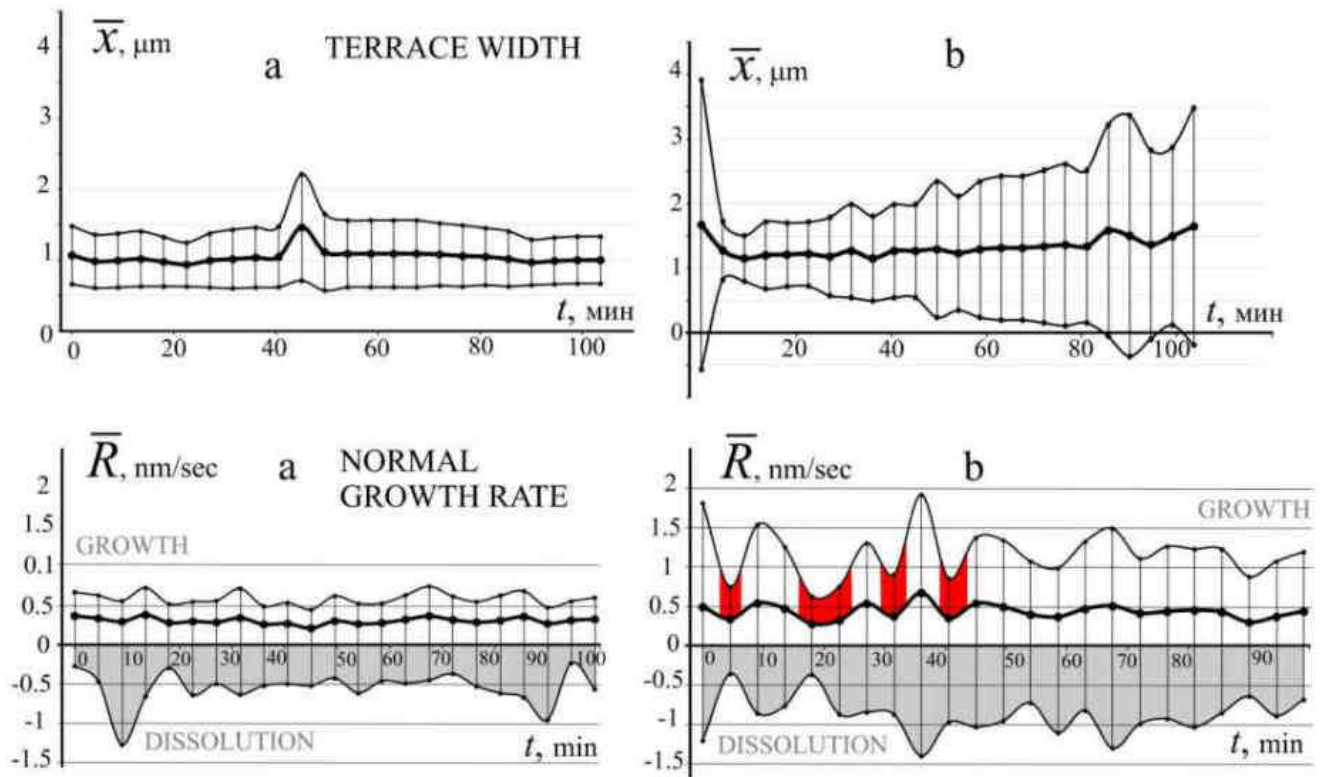


Figure 3.39 – Average distances between adjacent steps and average normal growth rate and their fluctuations plotted up and down at each point after scratching: (a) – for the left side of the hillock, (b) – for the right side. Zero on the time line of the graphs corresponds to the moment of scratching. Red shows the areas of fluctuation reset due to self-oscillations, followed by increases

However, as soon as fluctuations begin to significantly change the mean values in open non-equilibrium systems, self-organisation processes can arise as a result of the coordinated interaction of subsystems (Prigogine, Kondepudi, 2002). In this case, these are self-oscillations of the rate. The theory of self-oscillations has been developed since the 1930s; they are not damped, since any dissipation is completely compensated by the influx of energy from the outside (Andronov et al., 1959); such an influx in this case ensures the entry of matter from the solution due to weak uniform evaporation.

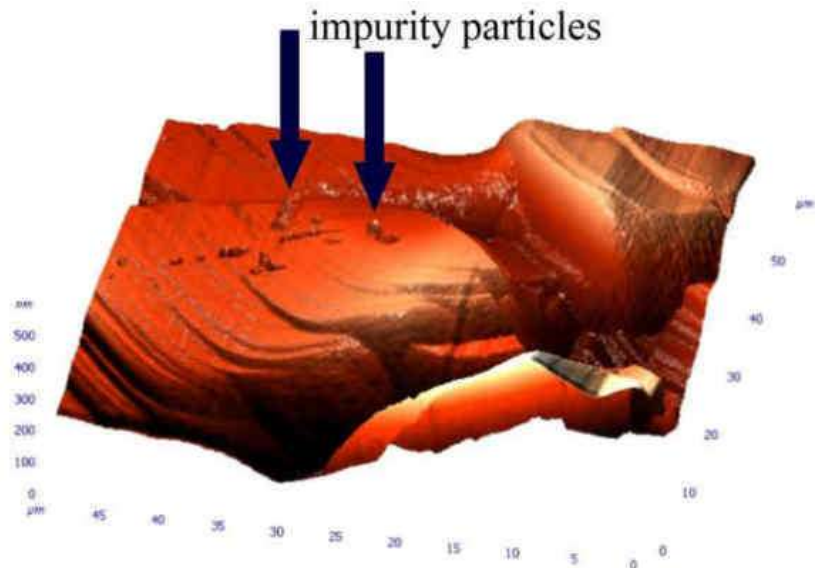
Examples of self-oscillations are the oscillations of a clock pendulum due to a suspended weight, the oscillations of a violin string under the influence of a uniformly moving bow, etc.

The conclusion about the activation of self-organisation processes based on the calculation results applies to both sides of the hill, although the contours of the steps on the left are visually smoother, the corresponding graphs show practically periodic oscillations (Figure 3.37 (a)). Comparison of the data obtained with no impact experiments suggests that it was the scratching that provoked the fluctuation-dissipative restructuring of the surface. The fluctuations immediately after scratching were so large that the system was forced to restructure the energy-consuming mechanism of surface construction, leading to chaos; cooperative flows of energy and matter emerged, leading to a decrease in fluctuations. All of this happened before the first picture was taken after the scratch. What is shown in the graphs is the result of such a restructuring, when the system adopted for itself a certain intermediate but satisfactory state, which has the nature of self-oscillations. The aim was to reduce the amplitude of the fluctuations, which happened, but not for long, as the fluctuations increased again (red parts in Figure 3.39 (b)). After the 40th minute, the fluctuations almost stop reducing the amplitude, but their magnitude still exceeds the growth rate, indicating that the next restructuring in the system cannot be ruled out. It is possible that self-oscillations are precursors of another phenomenon of self-organisation, kinematic waves of step density, which are not uncommon in crystal growth (Vekilov P. G., Alexander, 2000; Thürmer et al., 1999).

3.4 Incorporation of the solid foreign particles

This section presents the results of an AFM study of the effect of solid impurities captured by a growing crystal on the dynamics and kinetics of layer-by-layer growth on its surface (Piskunova, 2023 a, 2023 b). In Figure 3.40, a group of foreign particles on the (010) face of dioxidine growing in a solution with a relative supersaturation of just

over 1% is marked with an oval. Some of the particles are already immersed in the crystal, while others are still almost 400 nm above the surface. The substance does not adhere to these particles but to the steps on the surface, causing their edges to move. When they reach the particles, the steps do not adhere tightly to them, and after some time holes–wells are formed above the particles



(Figure 3.40). One of the reasons for the loose adhesion of the growing layers to the impurity particles is the poor adhesion of the impurity material to the material of the surrounding crystal. The wells above the particles do not overgrow due to the high energy barrier as in the case of the screw dislocation channel (explained in Figure 1.3). Therefore the wells, like the dislocation channels, are propagated through the covering layers for a long time and remain reference objects in the images.

3.4.1 Dislocation formation on the captured particle

After 100 minutes from the start of the experiment, all the particles and even the wells above them were overgrown and the surface was almost flat. At the same time, at one of the points where first a solid particle and then a well were observed, the appearance of a hillock was noted (the 32nd snapshot in Figure 3.40A).

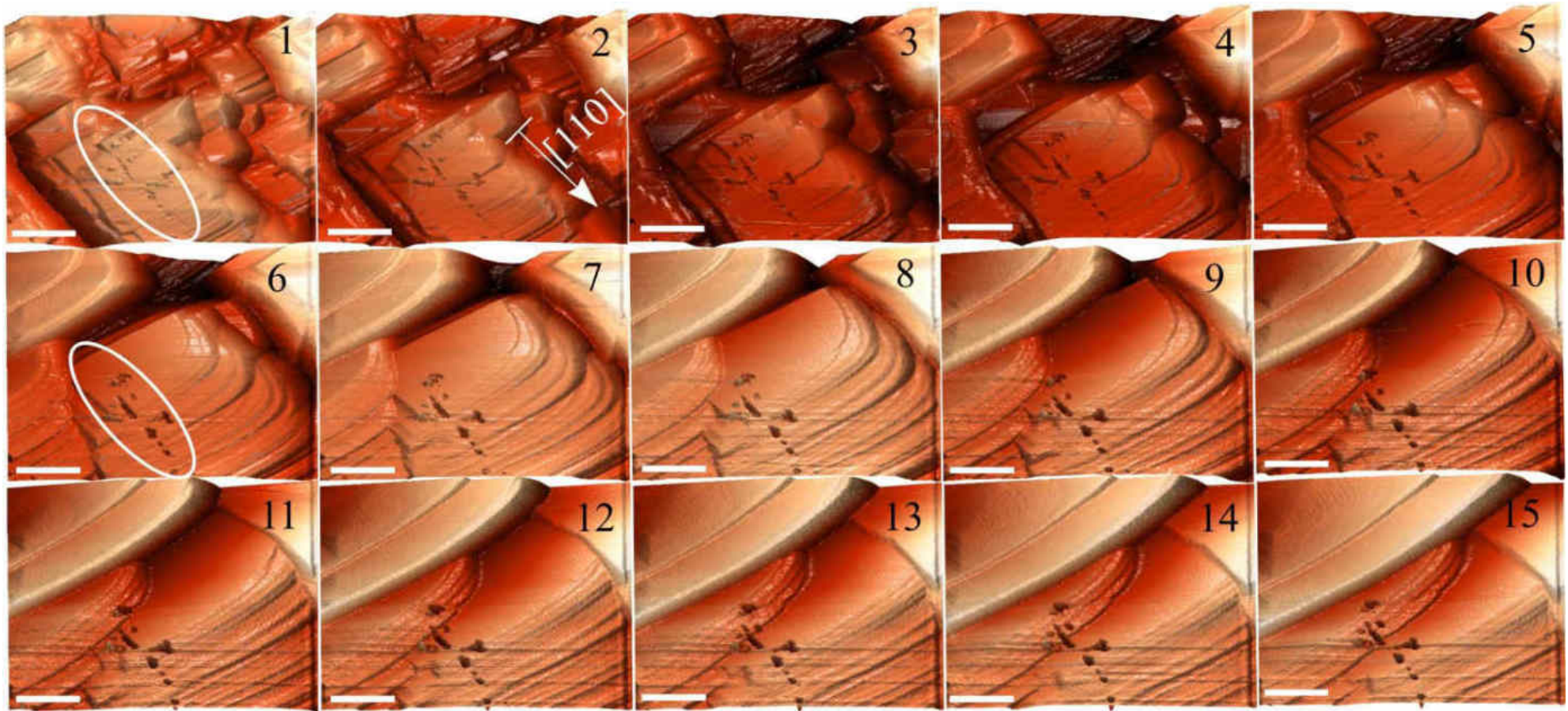


Figure 3.40 – AFM images of a dioxidine surface with foreign particles growing into it (marked with ovals at (1–16)). Holes are visible above the particles which do not grow over for a long time. The time interval between the sequentially numbered images is 4.5 minutes. The scale bars are 10 μm .

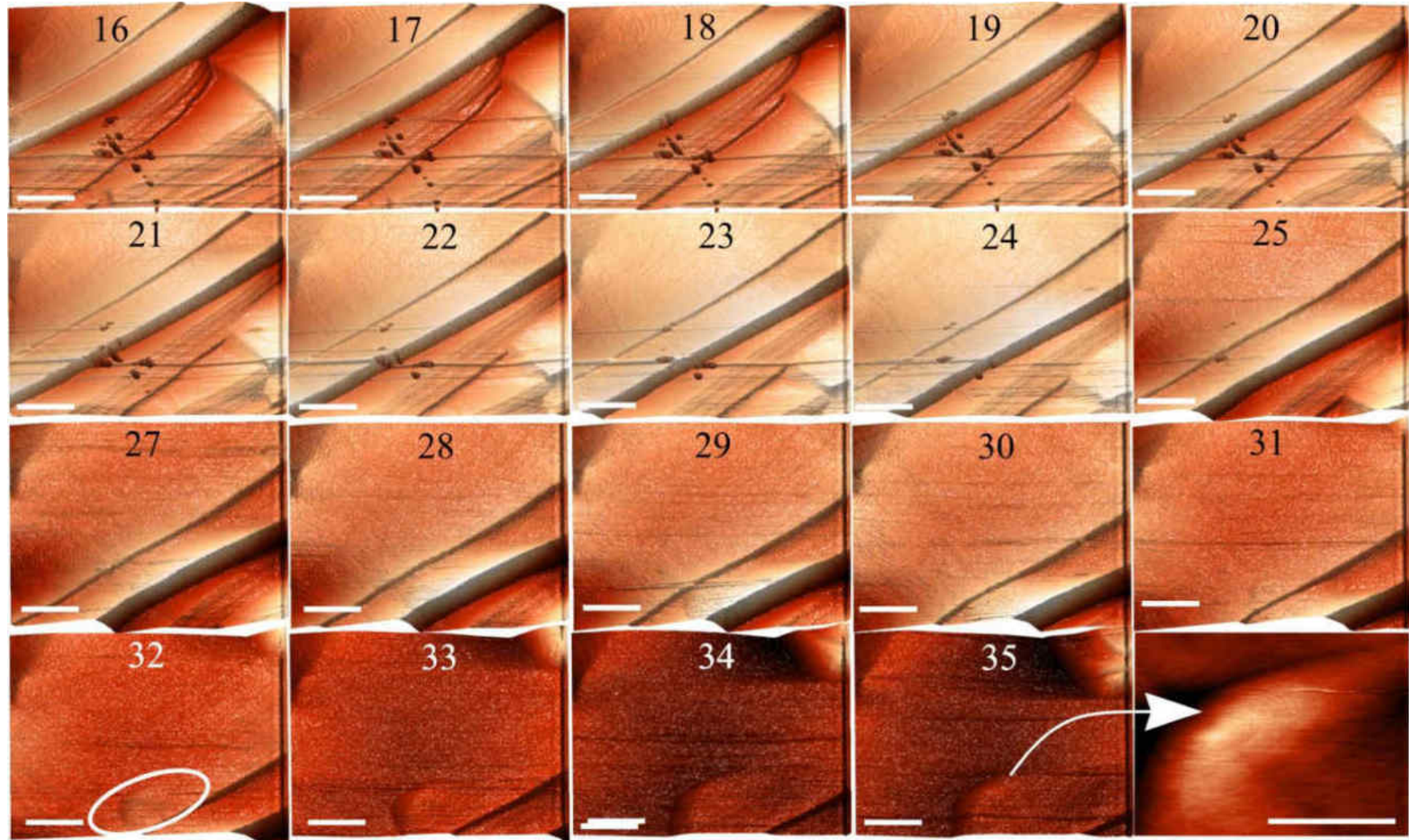


Figure 3.40A – From the 32nd image, the formation of a hillock (marked with an oval at (32)) above the captured particles can be seen. The last enlarged image shows the dislocation nature of the hillock. The time interval between the sequentially numbered images is 4.5 minutes. The scale bars are 10 μm

Closer inspection revealed that a spiral hillock had formed on a screw dislocation above the overgrown particle (the last image in Figure 3.40A). It grew at a uniform rate and its shape remained asymmetric because the main steps advanced from one side (Figure 3.41). This hillock appeared exactly at the coordinate where the impurity particle had previously been (Figure 3.42).

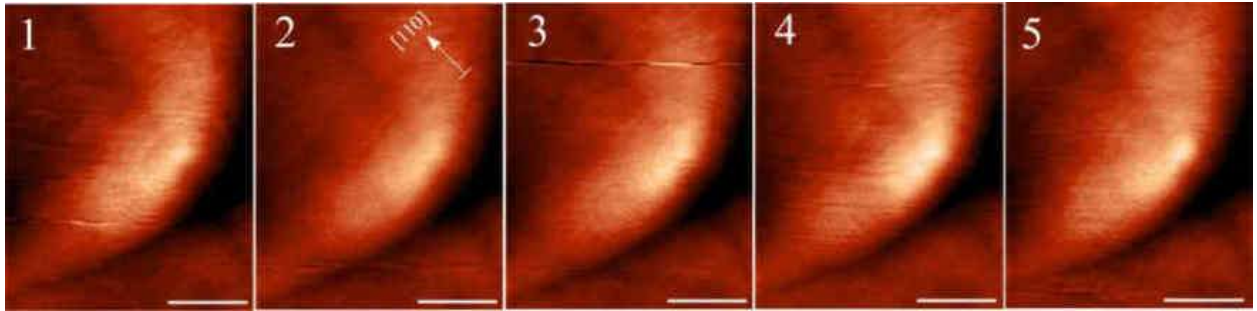


Figure 3.41 – Sequential images of hillock growth on a screw dislocation formed as a result of the crystal trapping a solid foreign particle. The time between sequentially numbered images is 4.5 minutes. Scale bars are 5 μm

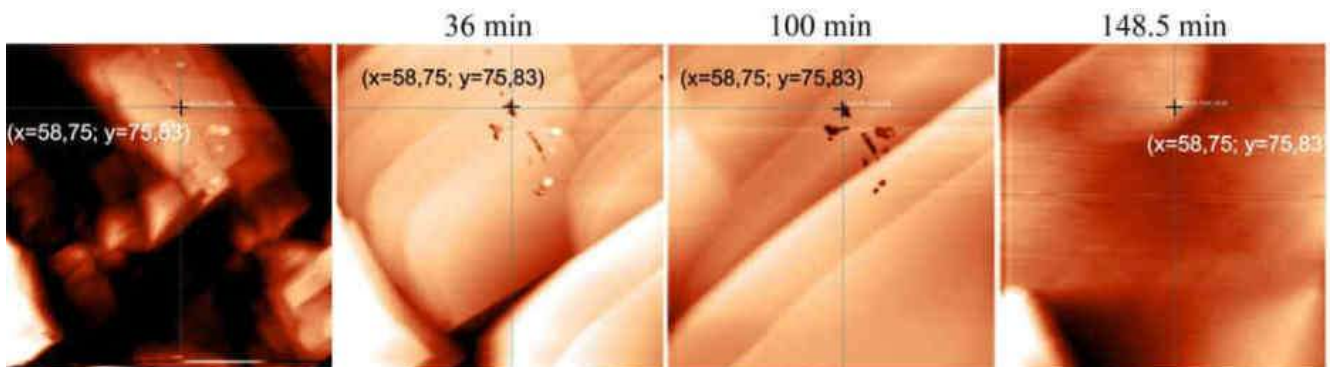


Figure 3.42 – Coordinate (58.75; 75.83) corresponds to the position of the particle, then to the hole above the particle, then to the centre of the spiral hillock corresponding to the screw dislocation that occurred at that point. The time elapsed since the first image is marked above the images

It is important to note that approximately 35 particles of similar size were imaged simultaneously on this section of the face, but under identical conditions a dislocation occurred on only one particle. The experiment recorded in detail the process of dislocation pile-up at the solid particle trapping coordinate. Before explaining the

mechanism of dislocation formation under such conditions, it is necessary to consider another phenomenon discovered using AFM – propagation of the dislocation through macrolayers.

3.4.2 Dislocation propagation through growth layers

A dislocation is a topological defect, it cannot end inside the crystal, which means that dislocations must be inherited by each subsequent layer and propagate along the crystal in a direction approximately perpendicular to the facet growth front. Numerous methods for studying growth processes and post-growth observations confirm this postulate (Klapper, 1991; Smolsky, Rudneva, 1993; Malkin et al, 1996; Bai et al, 2007; Klapper, 2010). However, the process of intergrowth has never been directly observed at the nanoscale. In this experiment, we were able to record this process in detail. Figure 3.43 shows successive images of the growth of a dislocation hillock (marked with an arrow), which initially consisted of 8 monomolecular steps. At some point this hillock was completely covered by a large step, 100 molecules high, creeping up from below on the right. The top of the covered hillock, which had just disappeared under the macrostep, immediately reappeared as if it had appeared on the outer surface of the macrostep (Figure 3.43, snapshot 4). A new spiral hillock emerged from the emerging tip (Figure 3.43, snapshots 5–10). Rate measurements showed that this new dislocation hillock had an advantage over the proper steps of the macrolayer in terms of attaching matter.

The mechanism of the propagation phenomenon is the transfer of stresses in the form of plastic deformation (shear) along the dislocation line from the depth of the crystal to the nearest point of the free surface. The increased chemical potential for the addition of the substance causes a small segment of the free surface step to stop at this point. As the substance continues to be added around the stop point, such a step with a fixed edge can wrap around this point, forming a new screw hillock on this dislocation.

Knowing the thickness of the layer through which the stresses have been transferred, it is possible to quantitatively estimate the real energy of the dislocation with the minimum Burgers vector for this surface. According to (Dvoryantseva et al, 1990) only four hydrogen bonds are broken along the height of the unit cell in the projection on the (100) face of dioxidine. Assuming that the energy of a hydrogen bond (Thakuria, 2017) is on average 6 kcal/mol (0.26 eV), we obtain a value of just over 60 eV for dislocation growth in Figure 3.43. This corresponds to the breaking of bonds along only one line, and since the screw shear occurs in a specific plane, this value will be many times greater. This figure is not the energy of the entire lower dislocation (it is calculated by integrating over the shear plane, which has a depth to the point of origin of the dislocation), but corresponds only to the excess energy that allowed the dislocation to transmit stress through the macrolayer. Almost all natural crystals have bonds that are stronger than hydrogen or van der Waals bonds and therefore have higher dislocation energies. For example, the dislocation energy for wurtzite has been calculated by Belabbas to be 4.70 eV/Å (Belabbas et al., 2005).

Temperature in natural systems also plays an important role: at high values, only large stresses relax and cause dislocations to occur, whereas stresses such as those found in a laboratory experiment under room conditions do not require relaxation under high PT conditions. The energy stored by dislocations at great depths in the Earth can reach considerable values. When it is brought to the surface, the pressure and temperature differences induce stresses equal in magnitude and opposite in sign to those relieved by the formation of dislocations during growth (Modern Crystallography, 1980). The release of this energy can cause macroscopic deformations, and large crystals inevitably become filled with cracks, despite slow extraction and careful transport.

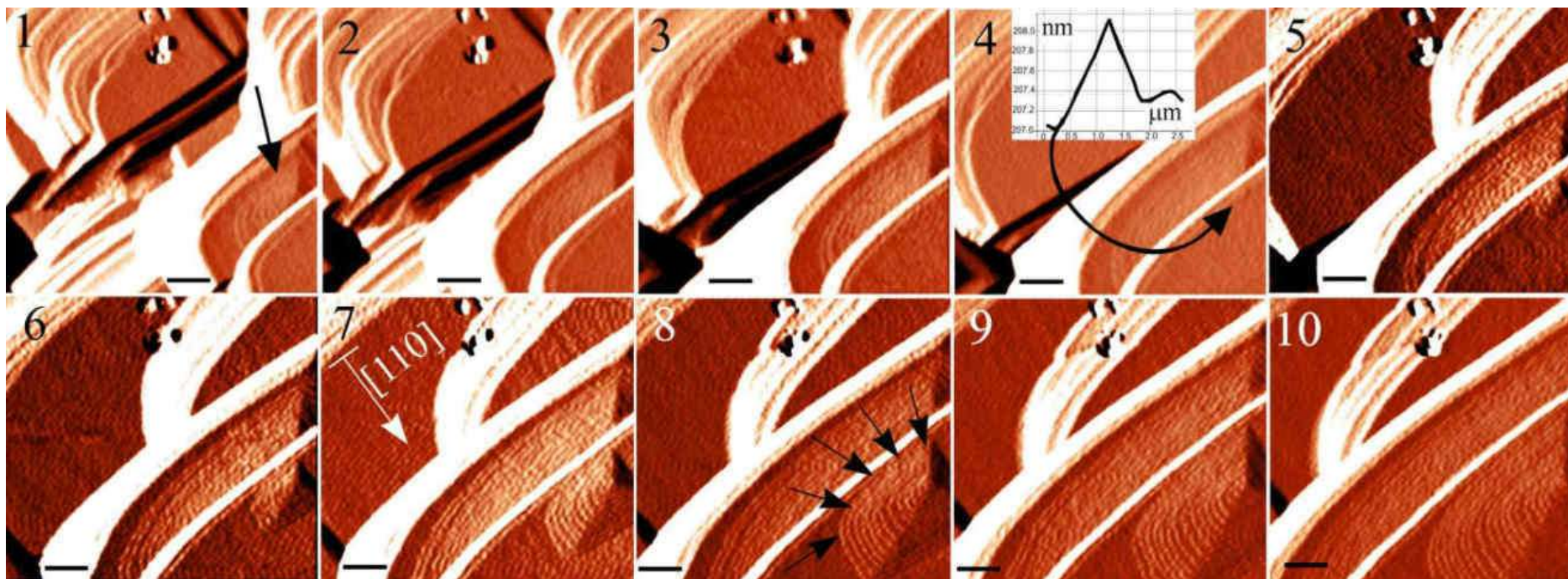


Figure 3.43 – AFM images demonstrating the phenomenon of dislocation propagation through the covering growing layers: (1) – the arrow shows the dislocation hillock (8 molecules high); (4) – the moment when the top of the hillock is covered by a layer 100 molecules high and this top appears at the top of the layer (the inset is a profile section at this point); (5–12) – the development of a new spiral hillock from the emerging point (shown by arrows in the 8th image). The time between the consecutively numbered images is 4.5 minutes. Scale bars – 5 μm

3.4.3 Dislocation formation before cavity sealing

In the experiment described (Figure 3.40), 35 foreign particles of approximately the same size and shape were introduced into the crystal at the same time and on the same surface. Only one of the particles produced a dislocation. Literary examples confirm that not every solid impurity or liquid inclusion should produce a defect (Viti, Frezzotti, 2001; Johnson et al, 2004). What factors are required to ensure the formation of a dislocation on an inclusion?

Figure 3.44, which is an enlargement of Figure 3.40 using filtration, shows that the first dislocation appears above the particle even before the well above it is completely sealed. This is evidenced by the monomolecular closed steps that appeared at some point around the well (shown by arrows in Figure 3.44 (2)). They spread out considerably during the time it takes to seal the hole. In such a short time a screw step from a dislocation would not have time to go around the large hole even once. Therefore, it can be argued that the Frank–Read dislocation (the growth analogue of the Frank–Read dislocation source) is responsible for these circular steps (Frank, Read, 1950; Rimer et al., 2010; Choudhary et al., 2020), which consists of at least two dislocations of opposite sign that can be on opposite edges of the hole. It is likely that the stress around the particle exceeded a critical value prior to complete sealing, causing symmetrical displacements along the walls of the cavity.

Thus the hillock above the particle in Figure 3.40 is not the result of the dislocation occurring during the sealing of the particle, but the result of the inheritance of an existing dislocation when it is completely covered by the macrostep. Calculation of the dislocation energy in this case, taking into account the thickness of the macrostep (200 nm), gives a value slightly greater than 200 eV. This difference with a similar dislocation (60 eV) is explained by the energies of its primary dislocations: the complex Frank–Read dislocation accordingly stores more energy.

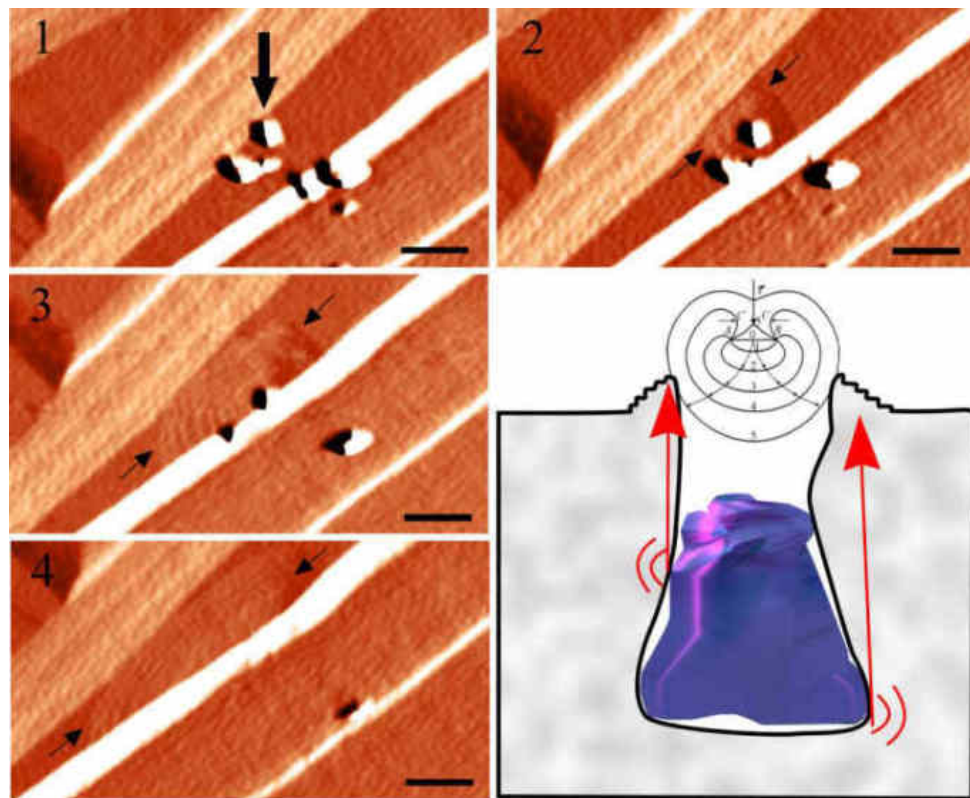


Figure 3.44 – Circular steps surrounding the hole from the particle (arrows on the 2nd image) indicate that the dislocations forming the Frank–Read source were formed before the hole was sealed. The images are enlarged and a Sobel filter is applied. The time interval between sequentially numbered images is 4.5 minutes. Scale bars are 5 μm . On the right is a schematic representation of the stresses around the particle that have caused displacements along the cavity walls, forming the Frank–Read dislocation

3.4.4 Mechanism of formation dislocation initiated by solid inclusion

It has long been suggested that dislocations can be generated by solid inclusions. Macroscale observations and etching have shown that dislocations in projection are located exactly above the captured inclusions. The first such observations were made by Fortey in 1954. One of the last major studies of dislocation formation on particles was carried out by Neuroth and Klapper (2020) using optical microscopy and post-growth *X*-ray diffraction topography. Nanoscale observations of dislocation formation in real time (AFM) on a specially embedded impurity particle were first reported by Zhong et

al. (2018). The authors believed that the mechanism of dislocation formation was fully consistent with that first described in 1980 by A. A. Chernov in his work "Modern Crystallography", which was published in English translation in 1984. The formation of a dislocation in it is explained by the curvature of the atomic planes and their misalignment as they join above the inclusion, caused by the adhesion (or epitaxy) of the growing material to the inclusion surface (Figure 3.45). Theoretically, a screw dislocation should only form after complete overgrowth of the inclusion or particle. The diagram given by Chernov (Figure 3.45 (a)) shows a tight fit of the growth layers to the inclusion surface, with no empty space (solution) between them, exactly as in Zhong et al. This mechanism is considered to be dominant in the literature (Klapper, 2010; Zhong et al., 2018; Klapper, Rudolph, 2015; Thurmer, Nie, 2013; Chang et al., 2021; Zhong et al., 2019). Dudley in 1999 extended this description to all types of inclusions (solution, void, solid impurity), without distinguishing the mechanism of dislocation occurrence on them, explaining the reason as a mismatch of lattice planes resulting from a higher feed rate of the protruding edge compared to the reentrant edge (Figure 3.45 (c)).

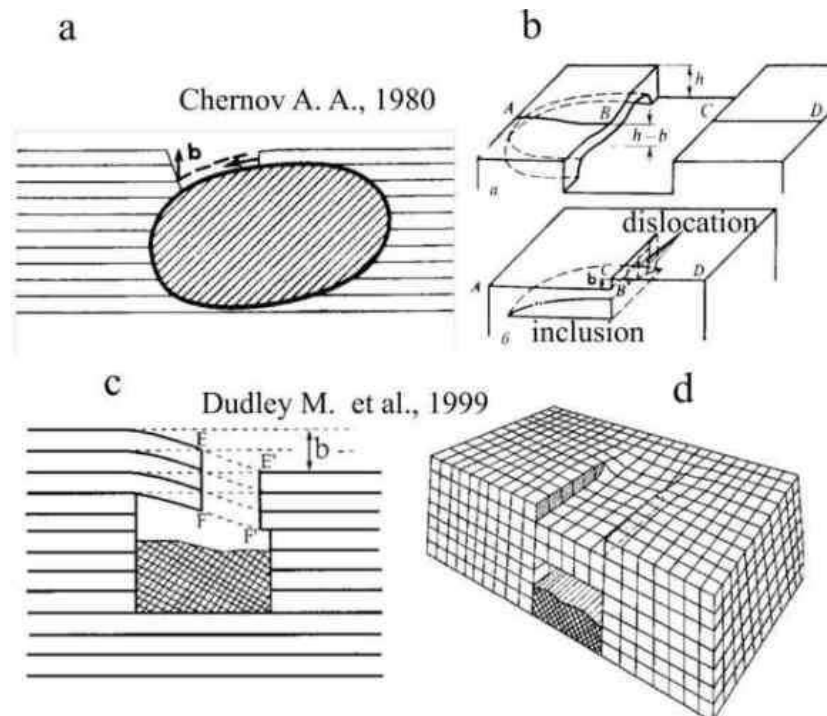


Figure 3.45 – Mechanisms of dislocation formation on a solid particle: misalignment of flat grids due to a higher feed rate of the edge protruding above the inclusion compared to the reentrant edge of the overgrown material (a, c) or due to sagging (b, d)

Simply put, if the foreign material is a "void or transport gas", there will be a "downward bending of the overhanging protrusion" (Dudley et al., 1999). However, there has been no experimental confirmation of the mechanisms described.

The studies carried out in this work allow us to add to the mechanisms described above. The most important addition is that dislocations on solid inclusions in a crystal can occur even before the inclusions are sealed. Moreover, the mere fact of sealing the cavity with growth layers does not guarantee the formation of a dislocation. This was demonstrated by an experiment in which the process of overgrowing 35 identical holes each should have led to a "downward sagging of the overhanging protrusion" and further misalignment of the planar lattices.

A possible guarantee of the occurrence of a screw dislocation on a solid inclusion is the occurrence of dislocations before the inclusion cavity is sealed. In this case, the task of creating a dislocation is reduced to its growth, and this will always happen since a screw dislocation cannot end inside the crystal.

A Frank-Read dislocation covered by a growth layer may not grow as a Frank-Read dislocation but as a single thread simple dislocation, as in the experiment in Figure 3.40. This is a slightly more complex mechanism involving the addition of intermediate dislocations. The process by which two dislocations form one with a different Burger vector during closure is well described in epitaxial growth theory. The macrostep covering the inclusion pit in Figure 3.44 can be considered as an epitaxial layer with an exact lattice match that is only broken above the pit. The pair of heterochiral dislocations that make up the Frank-Read source did not annihilate during closure because there is a resulting dislocation. In addition, their dislocation lines must approach each other within a few nanometres for annihilation to occur (Vegge, Jacobsen, 2022). The 2.5 μm diameter well and the particle within it act as a constraint, preventing the dislocations from approaching each other. Each of the dislocations at such a distance could then act as a separate dislocation and two hillocks would form. In the experiment, however, a single hillock is observed with energy almost four times greater than that of a similar spiral. This indicates that the two dislocations did not act independently but reacted together. The total Burgers vector of the dislocations that are

components of the Frank-Read dislocation is zero, but since no annihilation occurred, it can be assumed that additional factors were involved in the reaction, such as edge misfit dislocations that formed at the boundary of two layers: the overgrown crystalline layer and the well of solution surrounding the particle (Modern Crystallography, 1980). As a result, the dislocation is mixed on either side of the hole and takes on an L-shape (Figure 3.46).

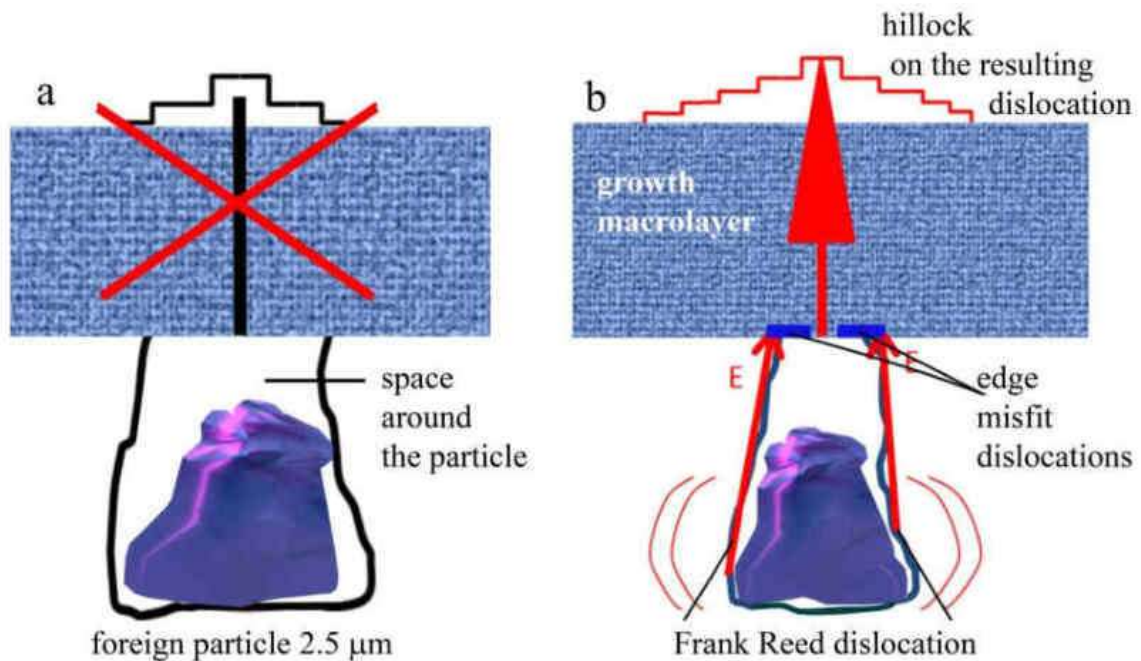


Figure 3.46 (a) – The overgrowth of a particle or cavity with a solution in itself does not guarantee the occurrence of linear defects. (b) – If dislocations have formed around the particle before the cavity is sealed, there will always be a resulting dislocation in the macrolayer covering the cavity as a result of dislocation growth.

These dislocations merge into one at the boundary, much as is described for epitaxial film growth (Modern Crystallography, 1980). The overgrowth of a Frank-Read source consisting of more than two dislocations will occur by the same mechanism.

Thus, the proposed mechanism for the formation of a screw dislocation when a growing crystal captures a solid inclusion with low adhesion suggests three stages: the formation of one or more (most likely a pair) dislocations in the immediate vicinity of the cavity with a particle before its sealing in the first stage, the addition of edge

dislocations to them at the moment of cavity closure in the second stage, and the formation of the resulting dislocation after sealing in the third stage with its subsequent growth. It is shown that the mere fact of inclusion sealing does not necessarily end with the occurrence of a screw dislocation. Perhaps the fact that not every inclusion causes critical stresses before complete overgrowth explains the paradoxically weak defectiveness of the growth surface with a significant amount of solid impurities captured by the crystal.

The sagging of the edge and the mismatch of the flat grids in the mechanism of dislocation formation on the inclusion are related to the general ideas about the formation of a screw dislocation from the closure of layers of different heights, as first shown in the work of G.G. Lemmlein and E.D. Dukova in 1956 (Figure 3.47). However, the closure of layers in itself does not form a dislocation; a point is needed at which one end of the step (of height mismatch) stops forever and begins to bend, i.e. a point to which the substance does not adhere. In the experiment of the paper (Lemmlein, Dukova, 1956) this point already existed (shown by the red arrow in Figure 3.47), i.e. the dislocation was already there, it just did not manifest itself.

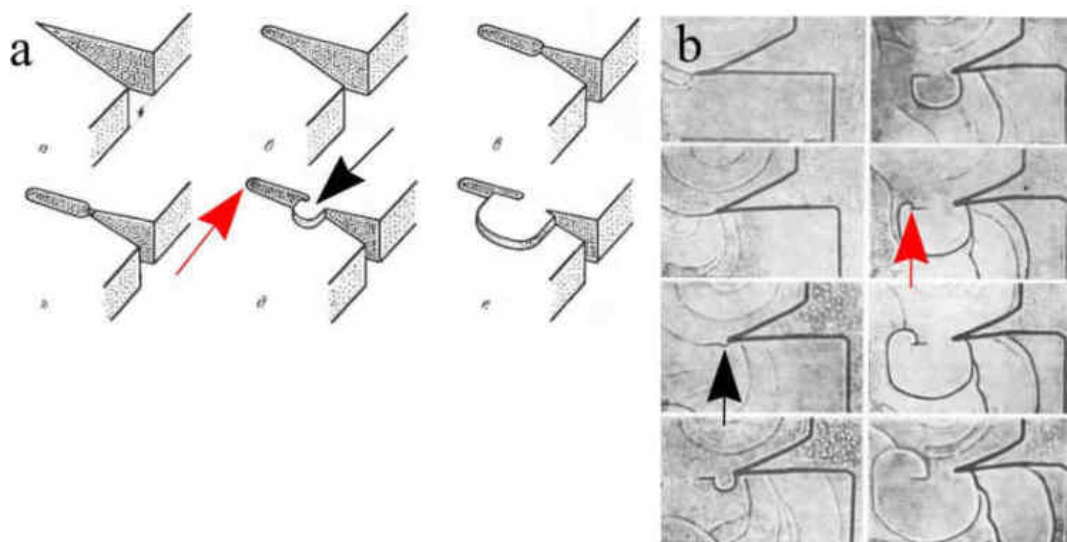


Figure 3.47 (a) – Diagram of the formation of a screw dislocation according to (Lemmlein, Dukova, 1956), (b) – the corresponding experiment with the closure of branches of a paratoluidine dendrite. It is possible that the dislocation did not originate at the closure site (black arrows), but already existed in the reentrant angle between the branches (red arrows). The end of the resulting step reached the reentrant angle, stopped there and the step spiralled to form a hillock

The growth closure of opposing blocks, large or thin steps of different heights, does not in itself form a dislocation because it does not generate stress (Figure 3.48). Even if there is a defect nearby, where the step can theoretically stop at one end and curl into a spiral hillock, as in Figure 3.49, where such a point is a hole (a three-dimensional defect) above the solid particle (shown as a circle in the 4th picture).

The step formed by the height mismatch when the steps closed did not retain one of its edges at this point because there is no stress (increased chemical potential for the addition of a substance) at this point, the substance is added there and the step therefore easily passes through it.

Thus, according to direct AFM observations, the formation of a hillock on a screw dislocation is more energy intensive than the misalignment of flat lattices due to the closure of layers, even when the different layer heights are due to the sagging of edges over inclusions. The stored energy allows the dislocation to propagate (be transferred) through layers hundreds and thousands of units thick.

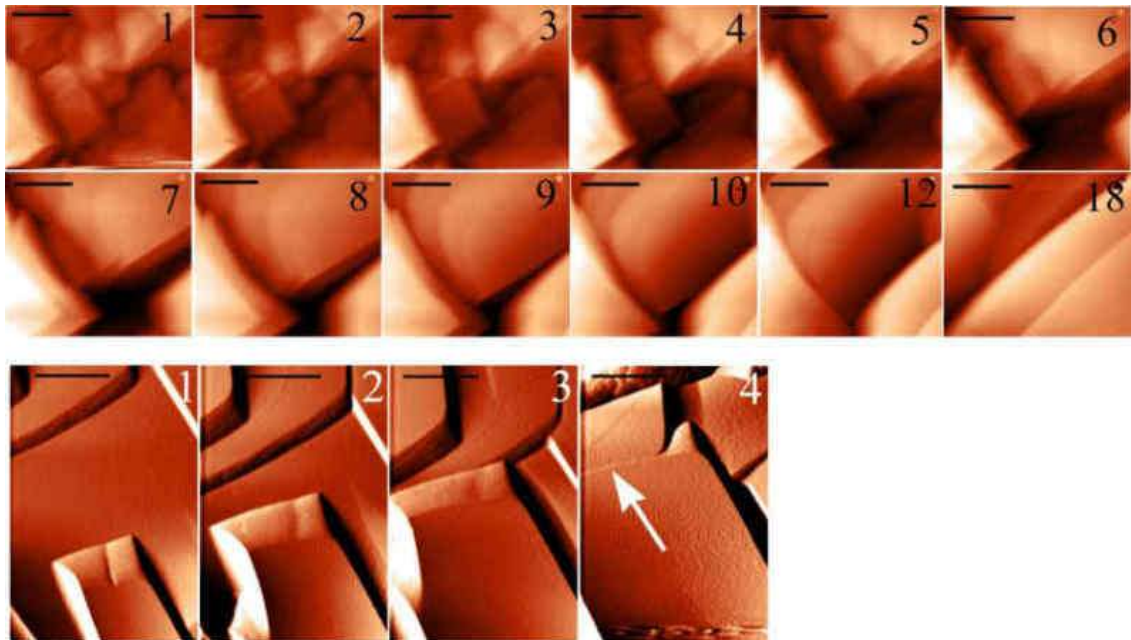


Figure 3.48 – The closure of opposite steps of different heights in different experiments does not form a dislocation as no stress is generated. The time between sequentially numbered images is 4.5 minutes. Scale bars are 10 μm . The arrow indicates the difference in height

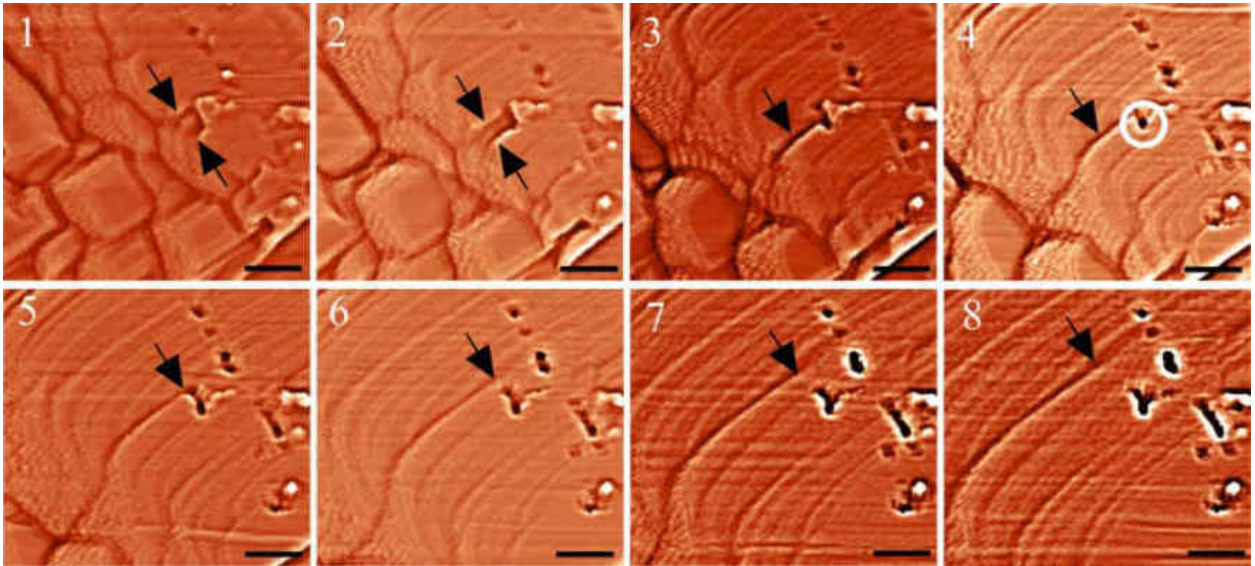


Figure 3.49 – Closure of steps (shown by arrows) with height difference. The hole (three-dimensional defect) above the solid particle (shown by the circle in the 4th image) has not slowed down the end of the step because there is no stress at this point.

The time between consecutive images is 4.5 minutes. The scale bars are 5 μm

3.4.5 3D reconstruction of inclusion in the crystal

Based on the AFM data obtained, a 3D reconstruction of the inclusion cavity containing a particle was made (Figure 3.50). The entrapped particle is visible inside the cavity; the properties of its material and the characteristics of its entrapment led to the creation of a space around it in which the solution should be located. The entire cavity is sloped because the growth steps in this experiment only approached the particle from one side. The cavity and the particle below the midline (marked in Figure 3.50) were modelled on the condition that if the hole has a diameter of 2 μm , then the particle at one of the lower levels is also not smaller than 2 μm . The shape of the bottom of the cavity is unknown, as the particle could have been pushed out for a long time by the growth front. In this case, the particle shields part of the diffusion flow, the surface under the particle loses stability, and then the bottom is unlikely to have a flat shape. It was shown long ago using AFM that there are hollow channels in the core of a screw

dislocation (De Yoreo et al, 1997). In the experiment in Figure 3.40, the hollow channel is not resolved due to the scanning scale, but it is marked in the 3D reconstruction as the presence of the dislocation has been demonstrated. The putative misfit dislocations and the Frank-Read dislocation are not reflected in the 3D reconstruction. Figure 3.50 simply gives an idea of what the inner walls of the cavity with a captured particle look like. In nature, a freshly captured inclusion with any filling will not have clear walls either. Only after hundreds of years of ageing under certain P–T conditions can the cavity walls become faceted, a property characteristic of natural crystals when a hollow inclusion takes the form of a negative crystal (Johnson et al., 2004; Chi et al., 2021).

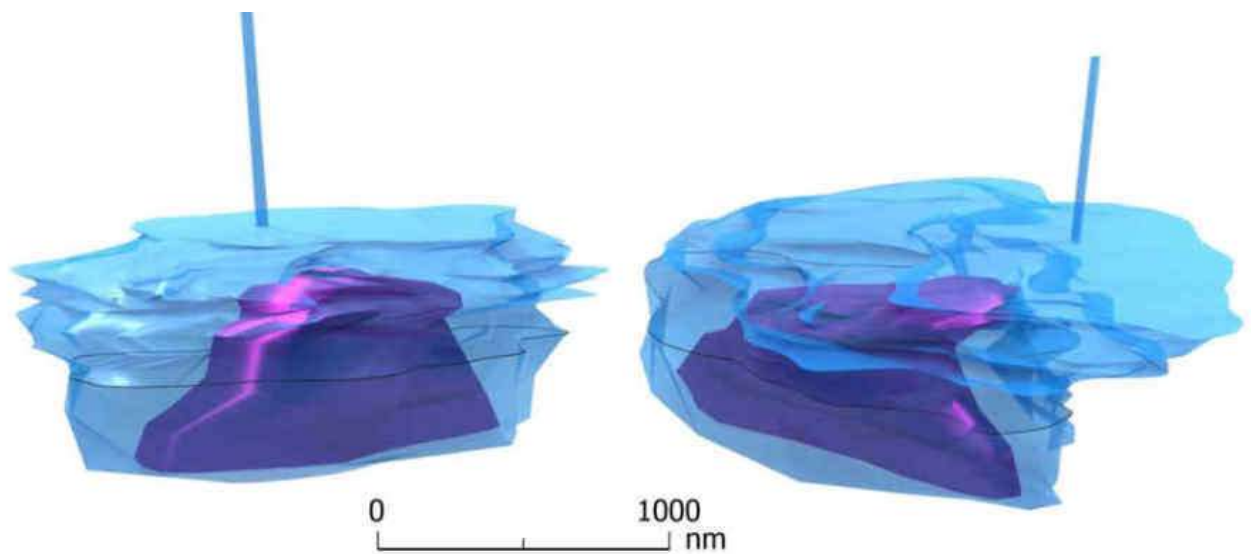


Figure 3.50 – 3D reconstruction of a real inclusion cavity with a particle (based on AFM data). The screw dislocation axis is represented as a tube of finite width. The particle and cavity are modelled below the black midline. The volume of the upper (real) part of the particle is $0.12 \mu\text{m}^3$, the volume of the real part of the cavity (together with the particle) is $0.92 \mu\text{m}^3$

3.4.6 Average growth rates and their fluctuations during solid particle capturing

The constancy of the normal rate and the tendency of its fluctuations towards zero, indicating the approach of the system to the state of steady growth, were not observed in

any of the experiments. In fact, the author believes that it is impossible to register absolute steady-state growth using AFM, mainly due to the small size of the scanning window. In addition, the AFM scanning unit constantly mixes the boundary diffusion layer of the crystal, preventing stabilisation of the concentration gradient. Nevertheless, a general trend can be seen from the graphs; for example, a comparison of the kinetic data in the unexposed and scratched experiments shows that the former are much closer to steady state. In the exposure experiments, the nature of the fluctuations is markedly different: they are unstable and often exceed the rate value itself. Such behaviour may indicate the activation of self-organisation processes. Similar patterns were logically expected when impurities were introduced. Contrary to expectations, the fluctuations on impurities turned out to be small (Figure 3.51). They represented a small deviation from the rate value. At the 40th minute of the experiment, the cascade of small steps slowed down on the first particle; around the 80th minute, the first macrostep reached the first large hole; at the 110th minute, the last hole was sealed; and after the 120th minute, rapid growth began on a large number of steps of one molecule in height. The increase in parameter values at the indicated points was necessarily followed by a return to the previous values. Thus, all stages of the process of formation of a screw dislocation on a captured solid particle were followed. The results obtained allowed to extend the existing description of the mechanism of dislocation formation on inclusions. In contrast to the scratch experiment, the introduction of a large number of large solid particles, each of which overgrows with the formation of a large cavity, does not lead to an increase in the growth rate fluctuations. On the contrary, the fluctuations are insignificant and their behaviour is comparable to that of experiments without exposure. The introduction of mechanical impurities did not cause a strong destabilisation of the kinetic parameters, but a monotonic increase in both the tangential and normal growth rates by almost a factor of two was observed. Such a significant increase in rate was not observed in any of the experiments, which is understandable: the solution in the AFM cell is gradually depleted and evaporation is weak and uniform. The appearance of a screw dislocation in the middle of this experiment, which is a strong source of monomolecular steps, should be accompanied by an increase in the rate. The emitted

rounded steps have a high density and many kinks – entering angles that are most favourable for the attachment of building units. The experiment showed that a simple dislocation with monomolecular steps on an area of $50 \times 50 \mu\text{m}$ is sufficient for the tangential and normal rates to increase almost twofold within two hours, without replenishing the substance in the solution. The results contribute to a better understanding of the surface processes that occur at low supersaturation in the final stages of the growth of natural crystals with a large number of impurities.

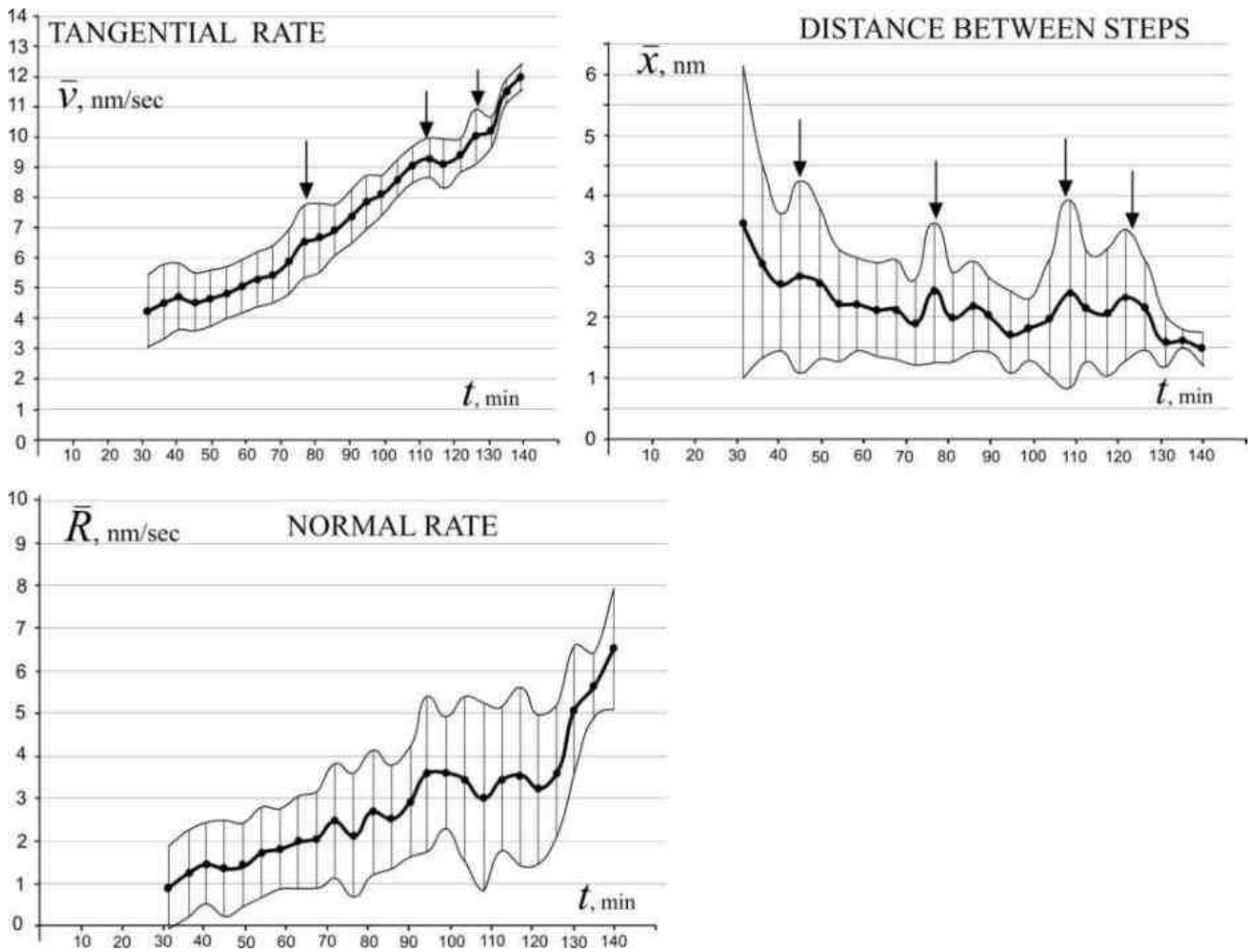


Figure 3.51 – Experiment on the trapping of a solid particle by a growing crystal: average tangential and normal rates, average distance between steps. Fluctuations for each parameter are plotted up and down at each point. Arrows indicate the times when parameter fluctuations occur (explained in the text). Each point on the graph is the result of processing 600–900 rate values

3.5 Layer-by-layer growth processes at the crystal intergrowth boundary

This section presents the results of the experiment to directly observe Layer-by-layer growth at the boundary between two identical faces (010) of two dioxidine crystals grown together at an angle of 120° in the XY plane (Figure 3.52). In the XZ plane there was a small angle between the twins – their boundary was incoherent.

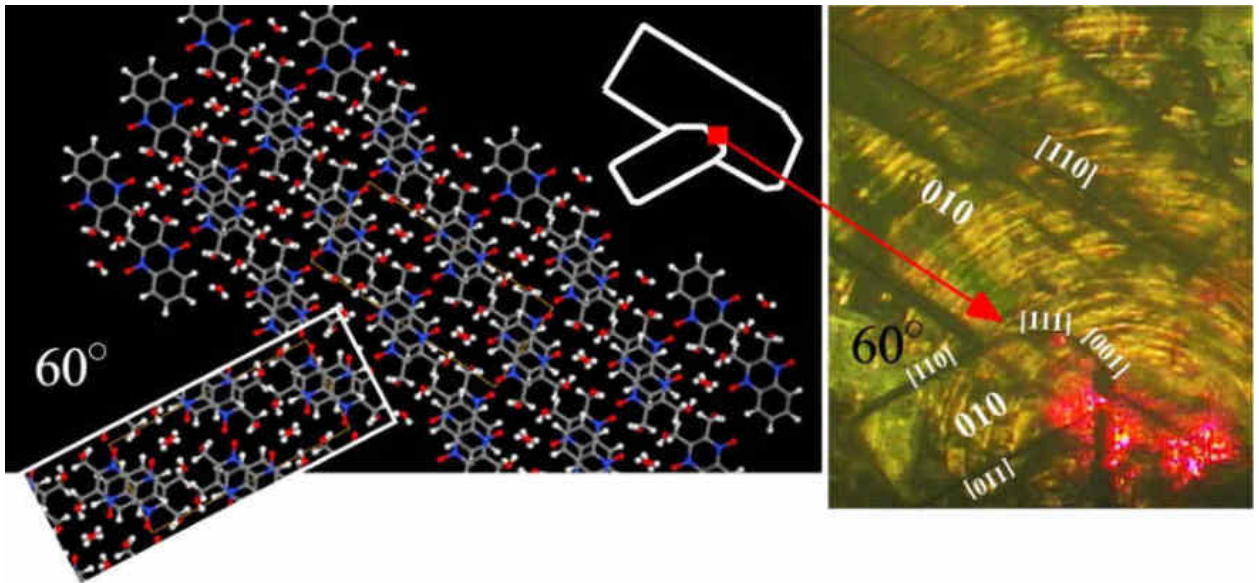


Figure 3.52 – Location of the scanning section of the boundary between the (010) faces in a crystal intergrowth in a twin position

It is known that intergrowth boundaries, as well as twin and block boundaries, are concentrators of large internal stresses. The occurrence of dislocations at these sites, their transition through the twin boundary, splitting and other features of dislocation interaction are important aspects of the theory of strengthening alloys (Chassagne et al., 2011; Samaee et al., 2021). In such work, dislocations are observed by transmission electron microscopy and X -ray methods. During growth at room temperature and pressure, complex dislocation movement is hardly possible, but it has been shown that during crystallisation under room conditions, dislocations also occur at the intergrowth boundary and play no less a role.

Figure 3.53 shows AFM images of the processes at the interface between two crystals in the twin position in a solution with just under 1% supersaturation for 6 hours.

The interface between the crystals is indicated by white arrows in the first image. During joint growth, the steps of the upper crystal reached the interface but did not cross it, only thickening the edge of the upper crystal. Screw dislocations were detected along the entire interface on the lower crystal using AFM (shown by arrows in Figures 3.53 (19) and 3.53B (58)). These were caused by stress between the individuals in the intergrowth. Figure 3.53A shows how strong one of the dislocation hillocks of the lower crystal becomes. This hillock, reinforced by the steps of the upper crystal, soon occupied almost the entire scanning window (Figure 3.53A (24)).

The remaining dislocations of the lower crystal sometimes grew through the steps of this hillock (marked with white arrows in photograph 58 of Figure 3.53B and visible in snapshot 64 of Figure 3.53C). In Figure 3.53C the dominant dislocation on the lower crystal looks visually like a shell flank (symbol "I" in snapshot 77). Thus, the absence of a coherent boundary, as well as complete structural mismatch, does not prevent the steps of monoclinic crystals in intergrowths from flowing onto each other. The flow of the steps does not erase the boundary, it is clearly visible in snapshot 77 of Figure 3.53C (symbol "I") and looks like a groove on a smooth surface. Why is the boundary between individuals in an intergrowth visible even where the steps flow? The surface of each crystal in such a fusion or twin, trying to reduce its area, pulls the joint from the inside, forming a groove, until its own tension is balanced by the surface tension. The rest of the boundary is a deep crack (symbol "II" in the 77th snapshot of Figure 3.53B), and this is what the boundary looks like during the inductive interaction of individuals, when the crystals advance and retreat at each other's edges.

Figure 3.53 – Successive AFM images of the boundary between two individuals in a crystal intergrowth in a twinned position in slightly supersaturated solution (the boundary is indicated by the white arrows in (1)).

The step rates on the upper crystal over 90 minutes, shown in this part of the figure, reached 8 nm/sec (the average rate is 4.2 nm/sec).

Dislocations at the edge of the lower crystal constantly generated steps, new turns of which are indicated by arrows in (10) and (19). The rates on the lower crystal, despite being smaller, are much higher - up to 14 nm/sec (the average rate over 90 minutes is 6.5 nm/sec).

Scale bars are 10 μm , the time interval between consecutive images is 4.5 minutes

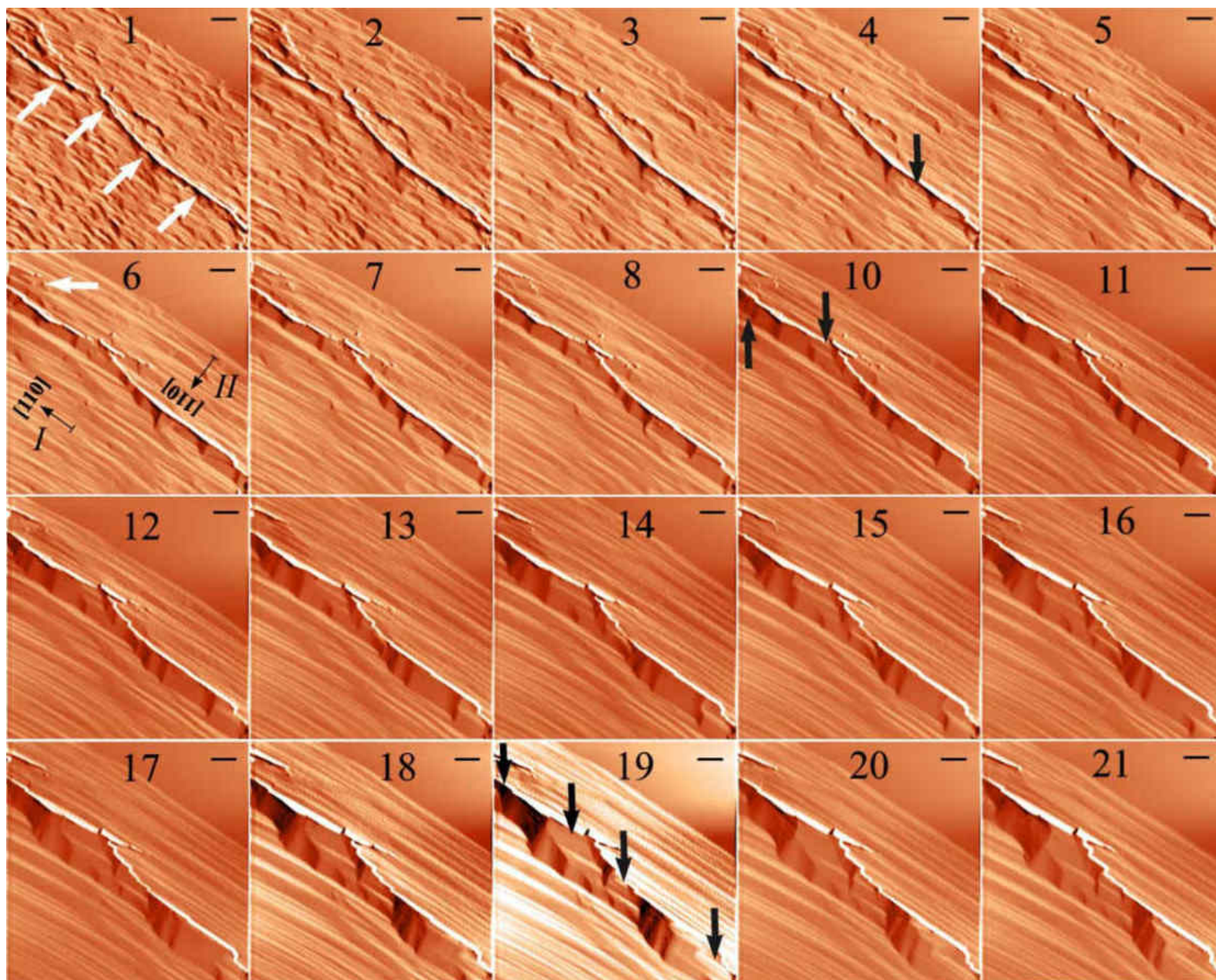


Figure 3.53A – Successive AFM images of the boundary between individuals in an intergrowth in the twin position. The arrow in the first image shows the area where the steps of the upper crystal merge with the hillock of the lower crystal. In the direction parallel to their profile they reinforced the steps of the hillock (symbol "II" in (24)), in the perpendicular direction they led to the formation of "sheaves" (symbol "⊥" in (24)). By the end of the third hour, the steps on the lower crystal are growing at rates of up to 60 nm/sec, the average rate increasing to 31 nm/sec, due to dislocations creating greater opportunities for attachment. The average rate on the top crystal is 27 nm/sec. Scale bars are 10 μm , the time interval between consecutive images is 4.5 minutes

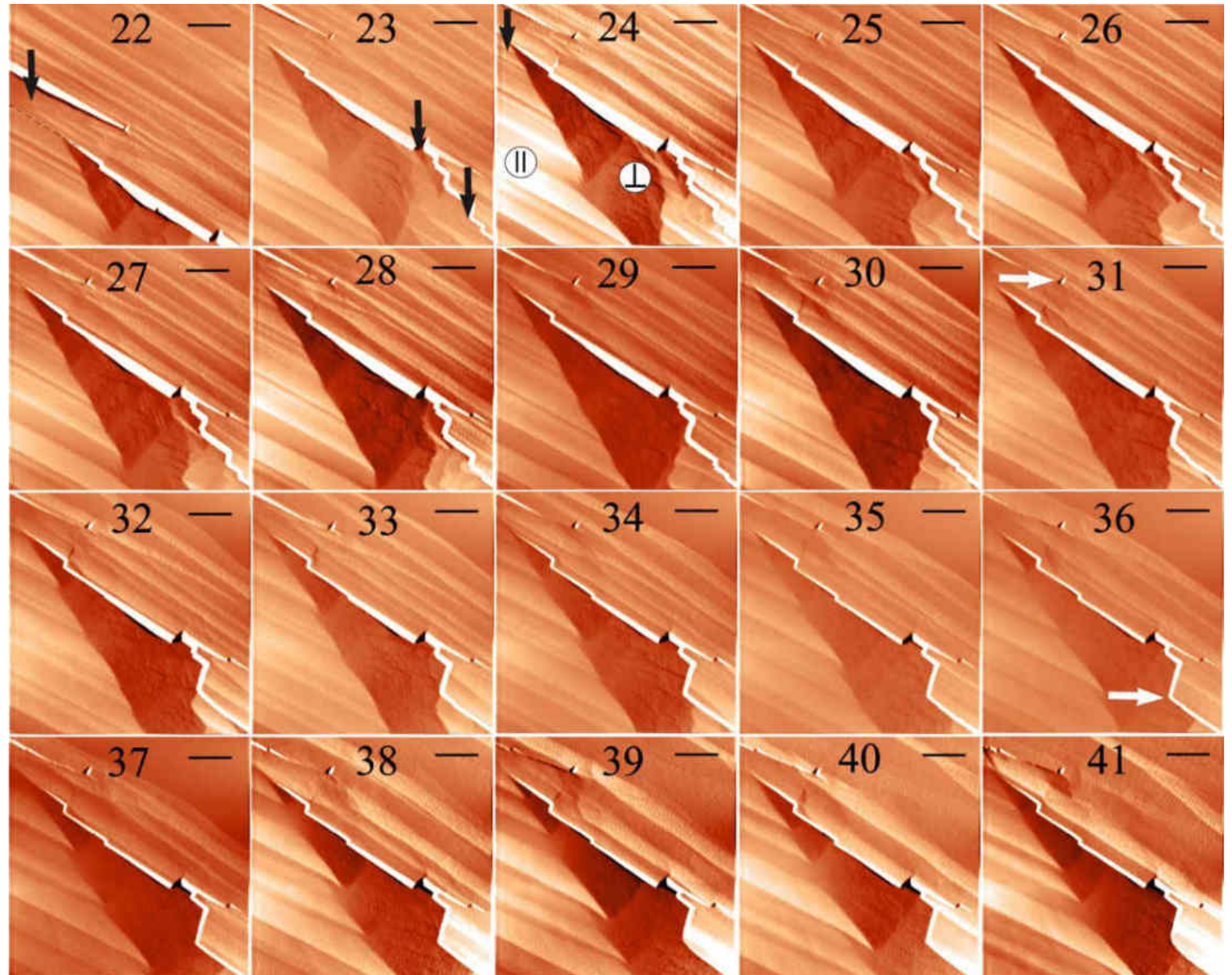


Figure 3.53B – Successive AFM images of the boundary between individuals in a crystal intergrowth in the twin position. The hillock of the lower crystal, with the peak in the upper left corner, reinforced by the steps of the upper crystal, becomes dominant. However, other boundary dislocations of the lower crystal sometimes grew through it (indicated by white arrows in Figure 58). After the 4th hour, the average rate of the steps of the lower crystal reaches 49 nm/sec and that of the upper crystal 39 nm/sec.

The scale bars are 10 μm , and the time interval between consecutive numbered images is 4.5 minutes

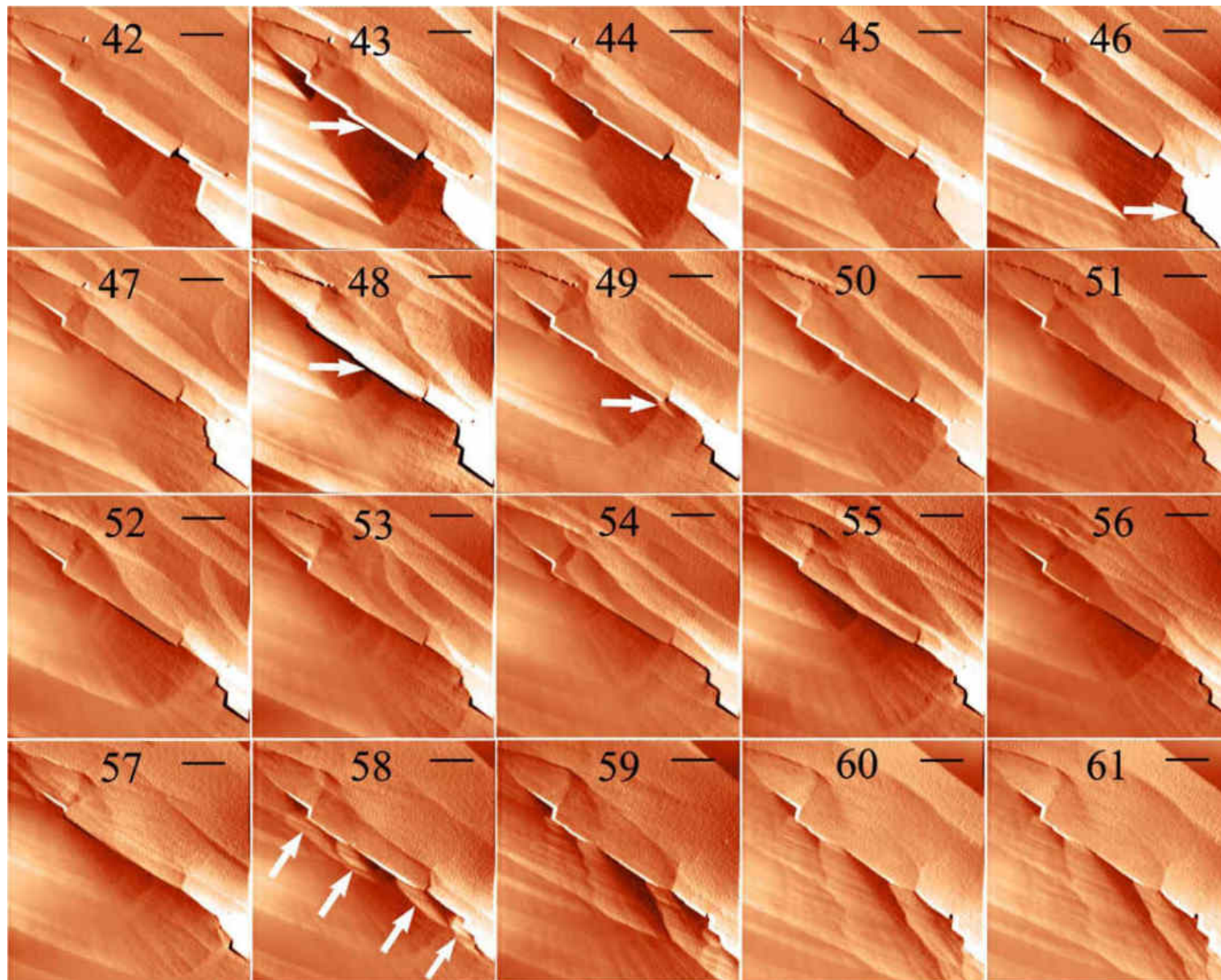
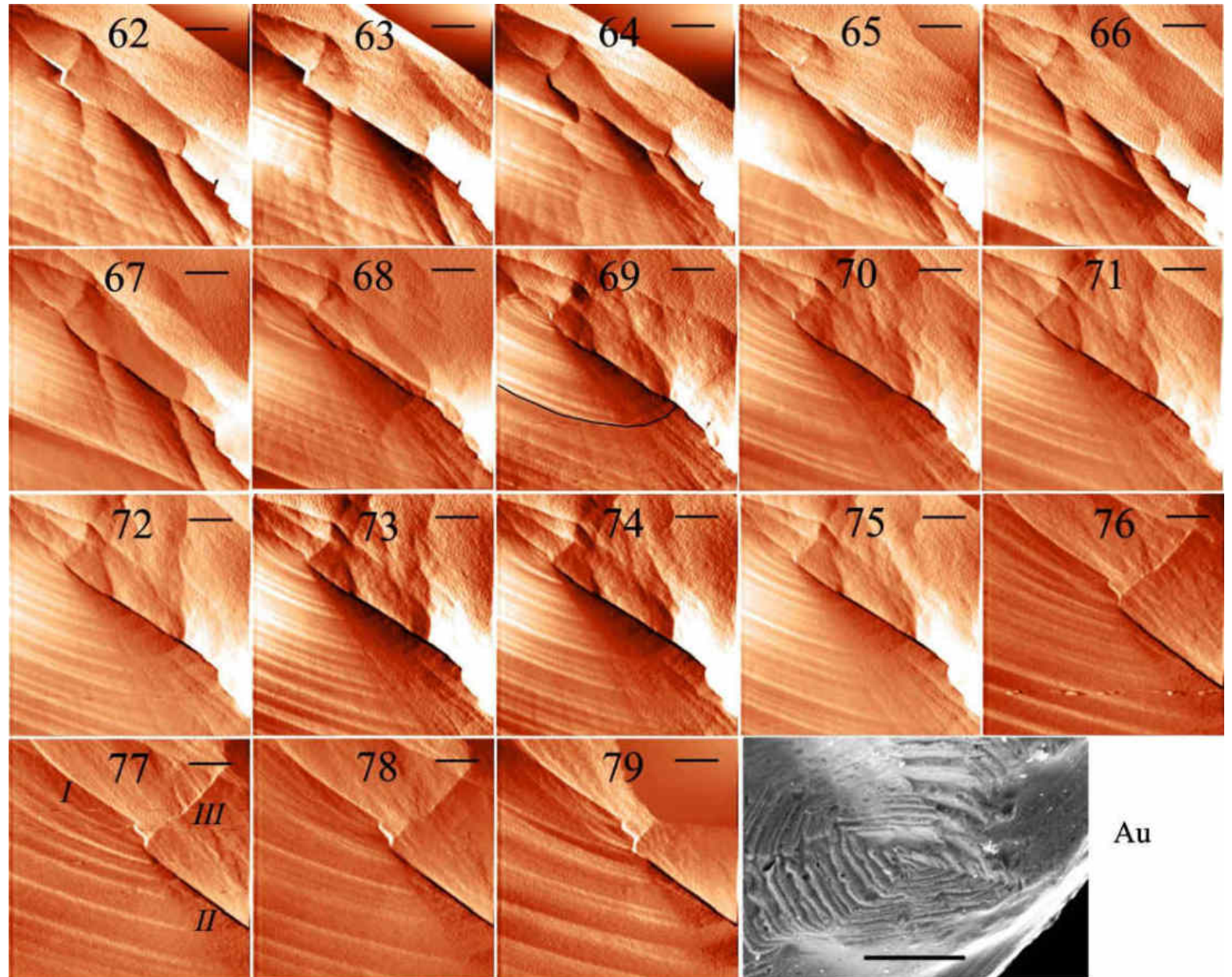


Figure 3.53C – The boundary between individuals in a crystal intergrowth in a twinned position. The dominant dislocation on the lower crystal looks visually like a shell flank. The interface between individuals can be a shallow groove (symbol 'I' in the 77th figure) or a deep crack (symbol 'II'). The pressure of the lower crystal on the upper one has led to edge displacements which, in combination with screw displacements, result in a convex seam (symbol 'III'). The scale bars are 10 μm , and the time interval between consecutive numbered images is 4.5 minutes. The last image is a SEM image of a gold grain with a similar boundary between individuals (but containing two dislocations), in which the twin seam is clearly visible



This retreat-advancement of the steps of the upper and lower crystals can be seen in Figure 3.54.

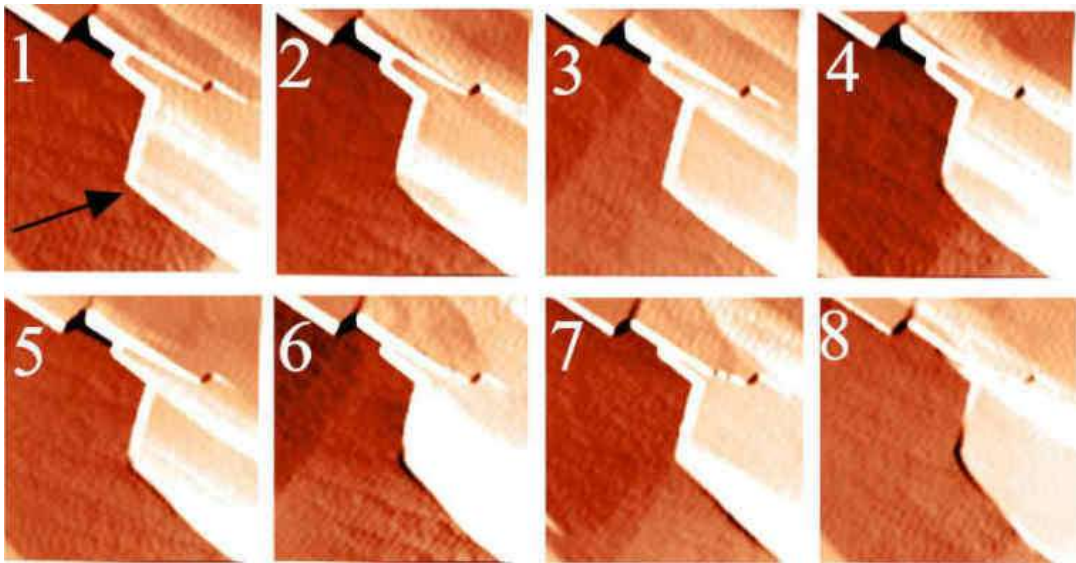


Figure 3.54 – Border of individuals with intergrowth of crystals in twin position: the advance (1, 3, 7) of the upper crystal is replaced by the advance of the edge of the lower crystal (2, 4, 5, 6, 8). Scale bars 10 μm , time interval between sequentially numbered images 4.5 minutes

Step crossing is a rare phenomenon, basically the steps of one crystal cannot cross the boundary with another crystal because of stoppers, which are the exits of dislocation channels along the entire boundary (Figure 3.55). These stoppers "held" the boundary within the initial boundaries in many areas for almost all of the 6 hours of observation (Figure 3.56).

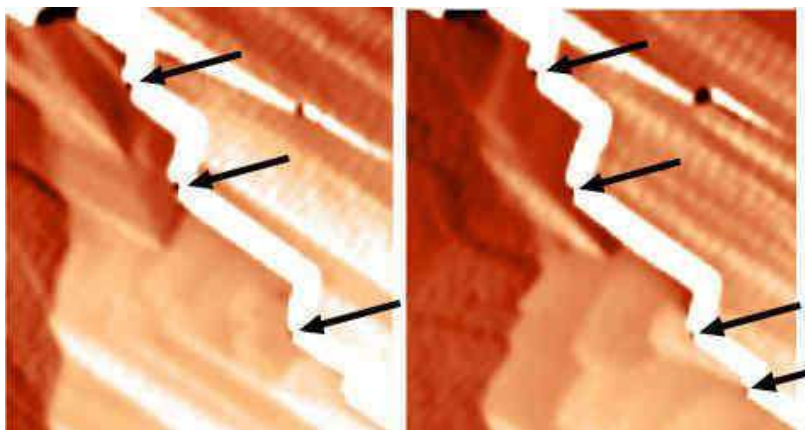


Figure 3.55 – Dislocation channels on the lower twin as stops for the advancement of the edge of the upper crystal from the intergrowth

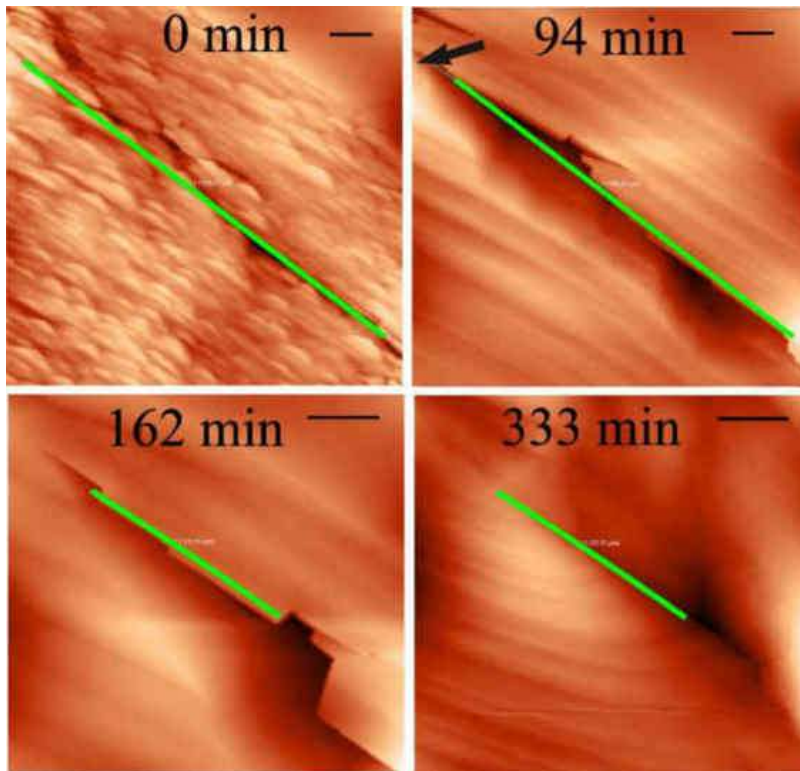


Figure 3.56 - The boundary between individuals in a crystal intergrowth in a twinned position during six hours of observation. Where the steps of the upper crystal did not meet resistance, they flowed onto the lower crystal, reinforcing its own dislocation hillock (shown by the arrow)

Crossing steps onto the neighbouring crystal creates a leakage, the optical image of which before and after the experiment is shown in Figure 3.57. The leakage should bind the crystals in the intergrowth more strongly.

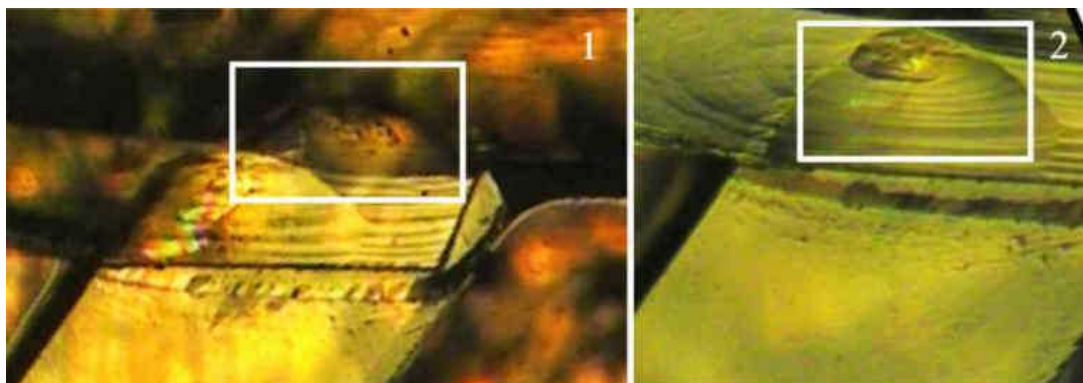


Figure 3.57 – Optical image of the boundary of individuals in a crystal intergrowth in a twinned position before scanning (1) and after scanning (2), where the formation of an leakage is visible

Growth on dislocations along the boundary on one crystal can exert pressure and cause edge displacement on another crystal in the intergrowth. Combined with the intrinsic screw dislocations of the second crystal, such a mixed defect will look like Figure 3.58 (shown as an oval).

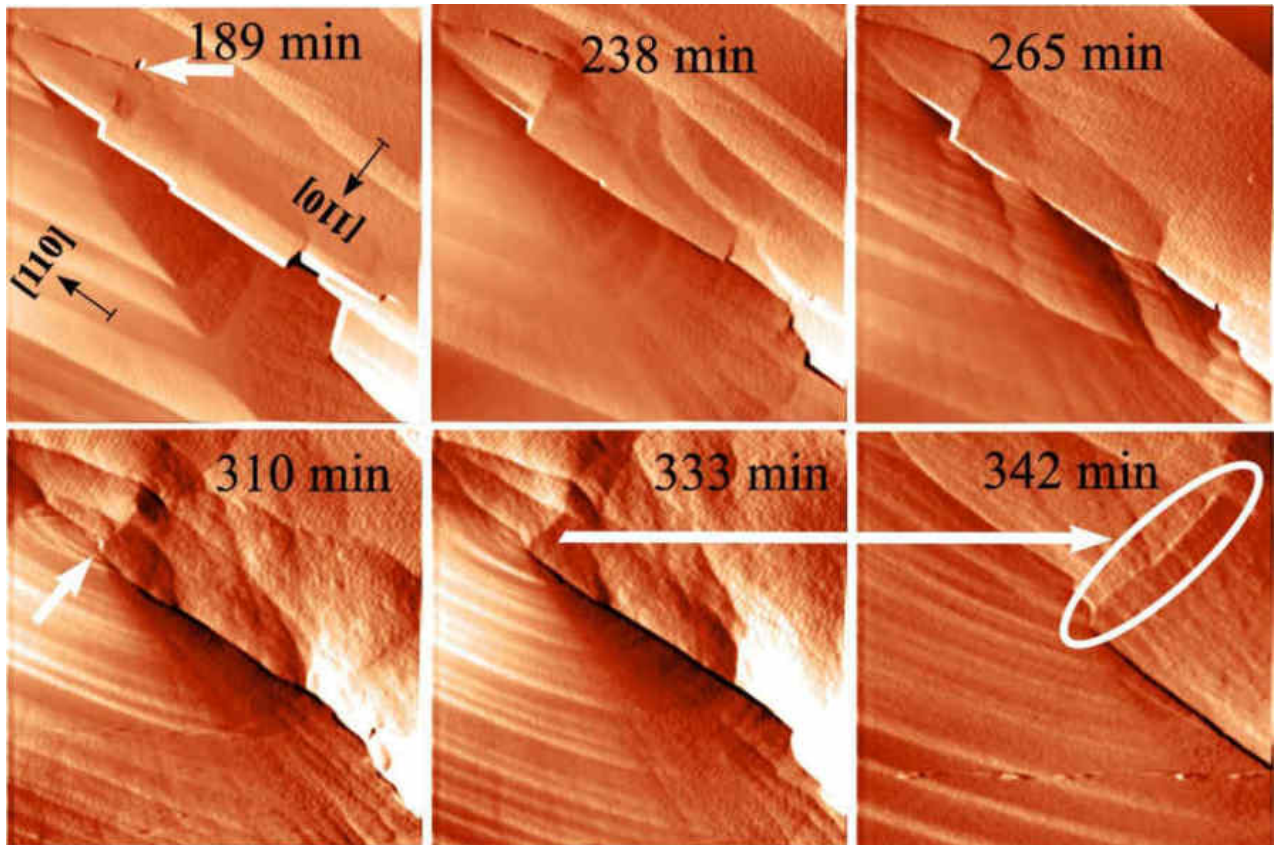


Figure 3.58 – The exit point of the dislocation on the lower crystal (shown by the arrow at minute 310) creates stresses in the upper crystal leading to edge shifts, their interaction with the screw dislocation of the upper crystal (shown by the arrow at minute 189) can form a convex seam (oval at minute 342)

In the given experiment, the formation of dislocations at the boundary was observed, due to the proximity of the boundary, the steps on the dislocations spread more downwards than upwards, resulting in the formation of half-hillocks. In the second crystal, due to the lack of mirror-like structure at the junction of monoclinic crystals, no symmetrical half-hillocks were formed. In crystals of cubic syngony, for example, symmetrical half-hillocks could be formed from two identical dislocations at

the boundary of twins. This is exactly what was found on the gold grain from the Kyvvozh gold deposit (Volsko-Vymskaya ridge, Middle Timan (Sokerin et al., 2023)), which was kindly provided to the author for SEM scanning by M.Yu. Sokerin and Yu.V. Glukhov. The last image in Figure 3.53B shows the two described half-hillocks (mirror dislocations on two crystals) and a double seam between them found on the gold. This sample proved to be very revealing in terms of growth traces, with many differently oriented levels of growth steps found on it. The height of the steps ranged from 100 to 1000 nm (Figure 3.59), apparently flowing from crystal to crystal in the intergrowth. Many screw hillocks of dislocation nature were found on this sample (Figure 3.60), mainly Frank-Read dislocations. The dislocation axes are differently oriented which characterises the mutual arrangement of the crystals in the intergrowth. Large steps (grouped into macro steps) in the AFM data indicate slow growth under conditions of depleting feed. Intact traces of layered growth on such a soft material as gold indicate that the sample has not undergone transfer and dissolution, supporting the authors of the find's conclusion that this gold is close to the primary source, which is important in the search for gold ore deposits.

The dislocations on gold in the last frame of Figure 3.53B are similar to those observed in the *in-situ* experiment. The analogy can be drawn despite the fact that the gold twinning suggests a deformation nature. However, the causes of dislocations at the boundaries of intergrowths and twins and the mechanisms of their growth evolution are similar for crystals of different genesis. The conclusion that the gold grain contains intergrowths, or rather twins, is also not contradicted by the authors of the find, who found intermittent dashed lines on the Debyeograms of this sample. Unlike the solid lines characteristic of powders and the single dots characteristic of single crystals, dashed lines are characteristic of suborientation of crystals in intergrowths (Glukhov et al. 2024). Twinning could have been facilitated by thermal stress and mechanical compression, as well as the presence of impurities (gold in this sample contains a significant amount of silver).

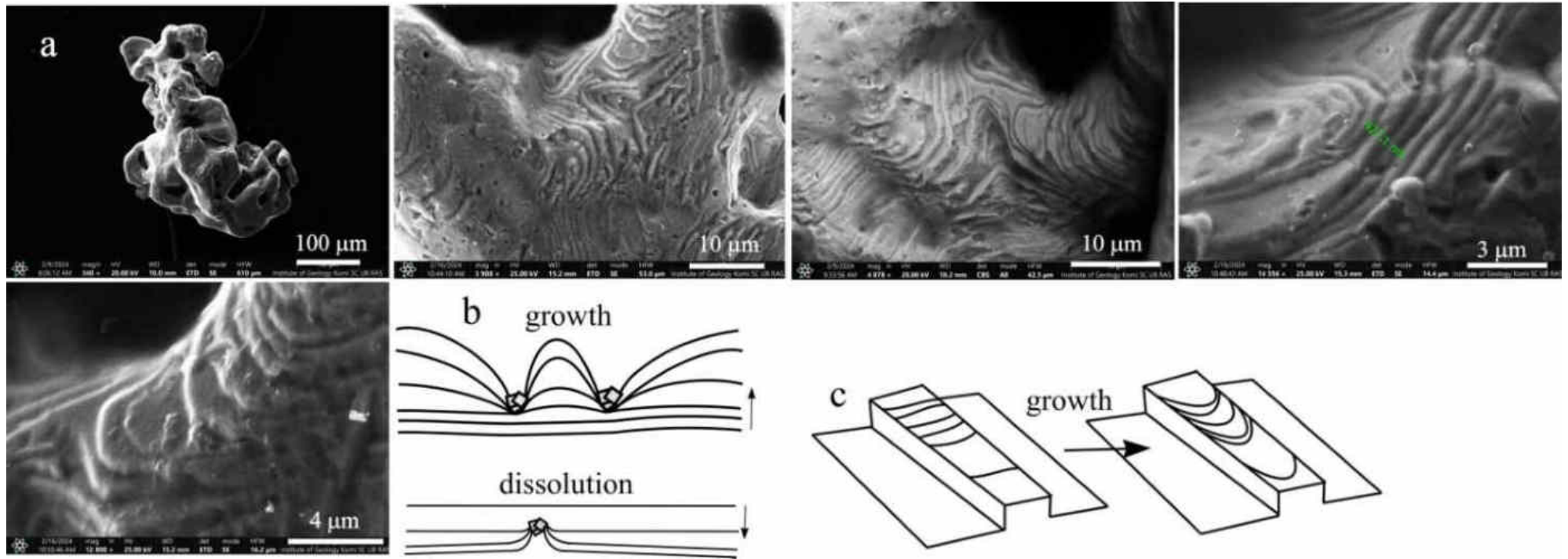
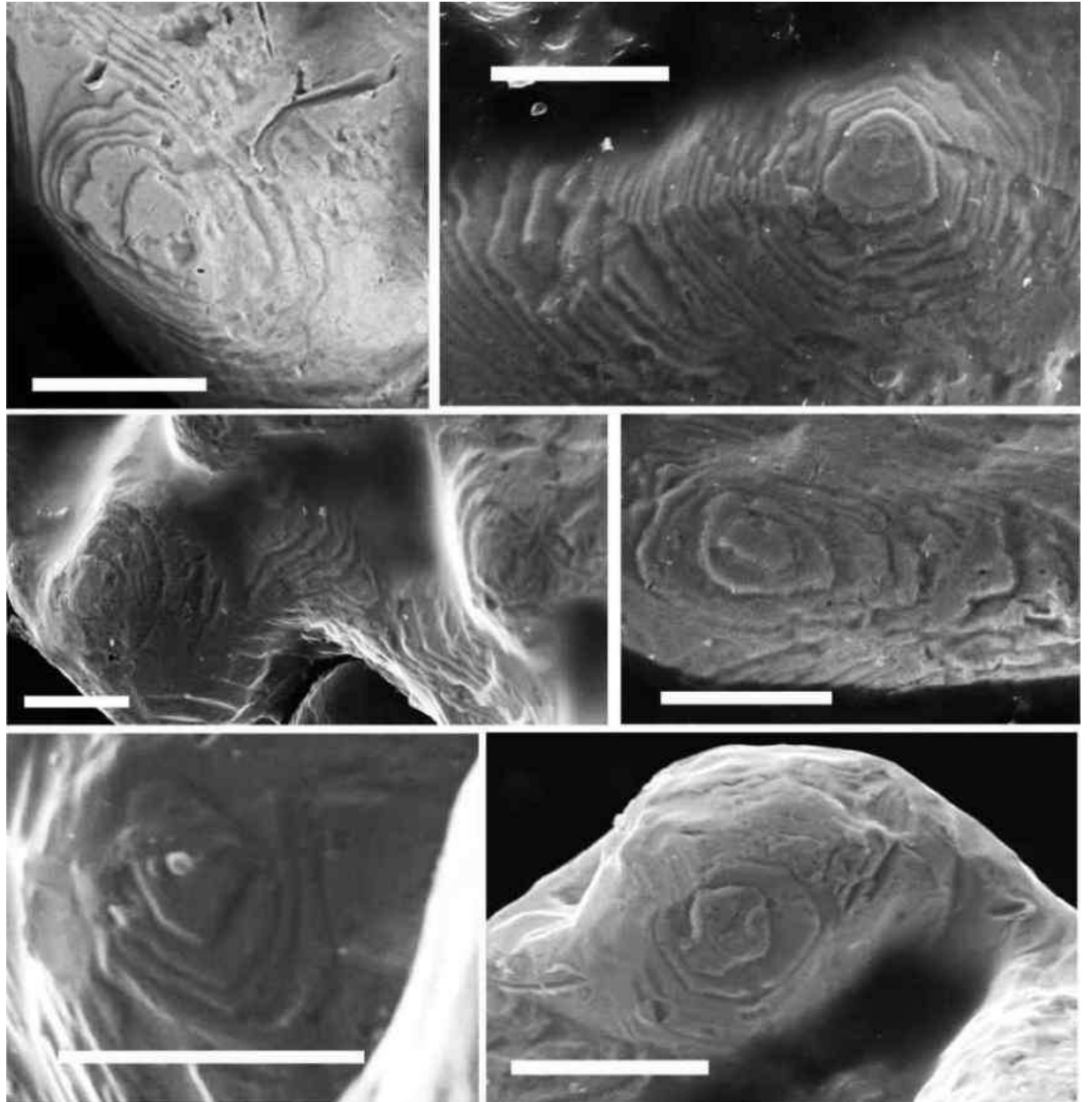


Figure 3.59 – A sample of gold from the Kyvvozh gold placer field (a) (provided by M.Yu. Sokerin and Yu.V. Glukhov) with growth steps 100-1000 nm high on its different planes (SEM). Below is a diagram showing the shapes of the growth and dissolution steps when interacting with obstacles (b) and on ridges (c)

Figure 3.60 – Dislocation hillocks on different planes of a gold grain from the Kyvvozh gold placer field (SEM) (sample for study provided by M.Yu. Sokerin and Yu.V. Glukhov). Scale bars 10 μm



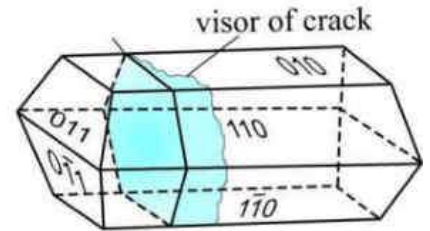
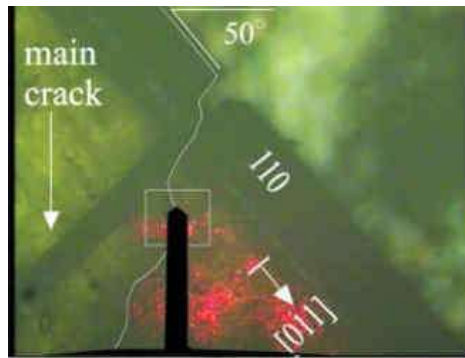
3.6 Processes of layer-by-layer growth and dissolution in the crack area

This section presents the results of observations of growth and dissolution processes on the (010) face in the area of specially created cracks.

Crack with a visor

In the first experiment, the crack was created with a thin visor and the scanning was not done above the main crack visible in the light, but at the edge of the visor.

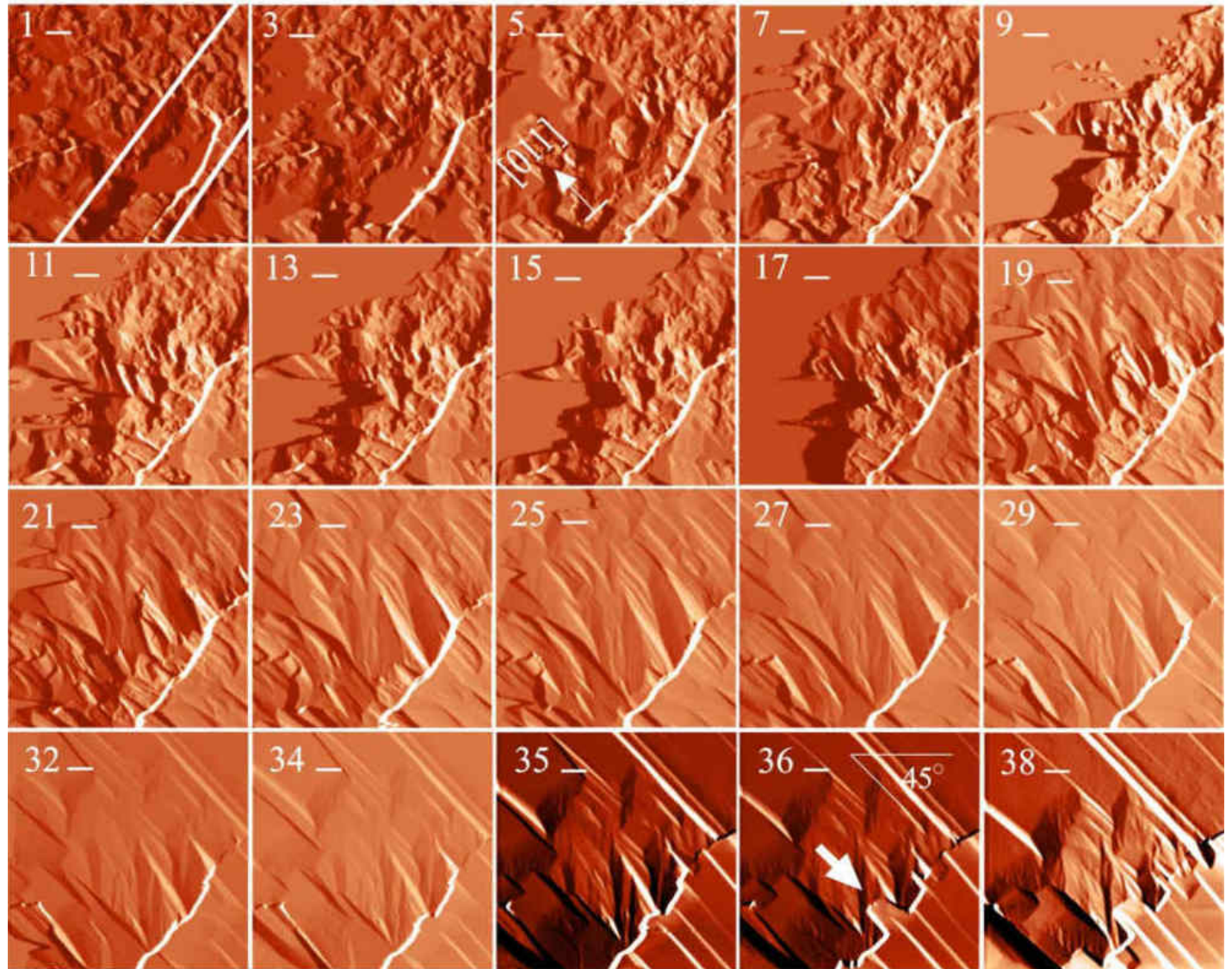
The solution for the experiment was prepared saturated for the given temperature, but weak dissolution was observed during the first three



scans (images 1 and 3 in Figure 3.61). During the time it took to adjust the apparatus, the edge of the visor dissolved and a height difference appeared. Growth began from the 5th image but the crack boundary did not move, steps approached it from both sides but did not cross the boundary itself, unable to overcome the increased chemical potential in the crack area. In the 35th, 36th and 38th snapshots of Figure 3.61 some parts of a large step finally threw bridges over the crack. In the next Figure 3.61A, the counter-movement of large steps towards the crack continued, and in the 52nd snapshot they were completely closed. Figure 3.61B shows that on the crack, which was completely overgrown by snapshot 62, many screw dislocations with inclined axes had formed.

Figure 3.61 – Healing of a crack whose partially dissolved boundary is highlighted by lines in the first image. In the 35th, 36th and 38th snapshots, some parts of a large step have thrown bridges across the crack (indicated by an arrow in the 36th snapshot). By the 130th minute of observation, the steps to the left of the crack were growing at an average rate of 16 nm/sec, while the steps to the right had an average rate of slightly less than 10 nm/sec.

Scale bars are 10 μm , the time interval between consecutive images is 4.5 minutes



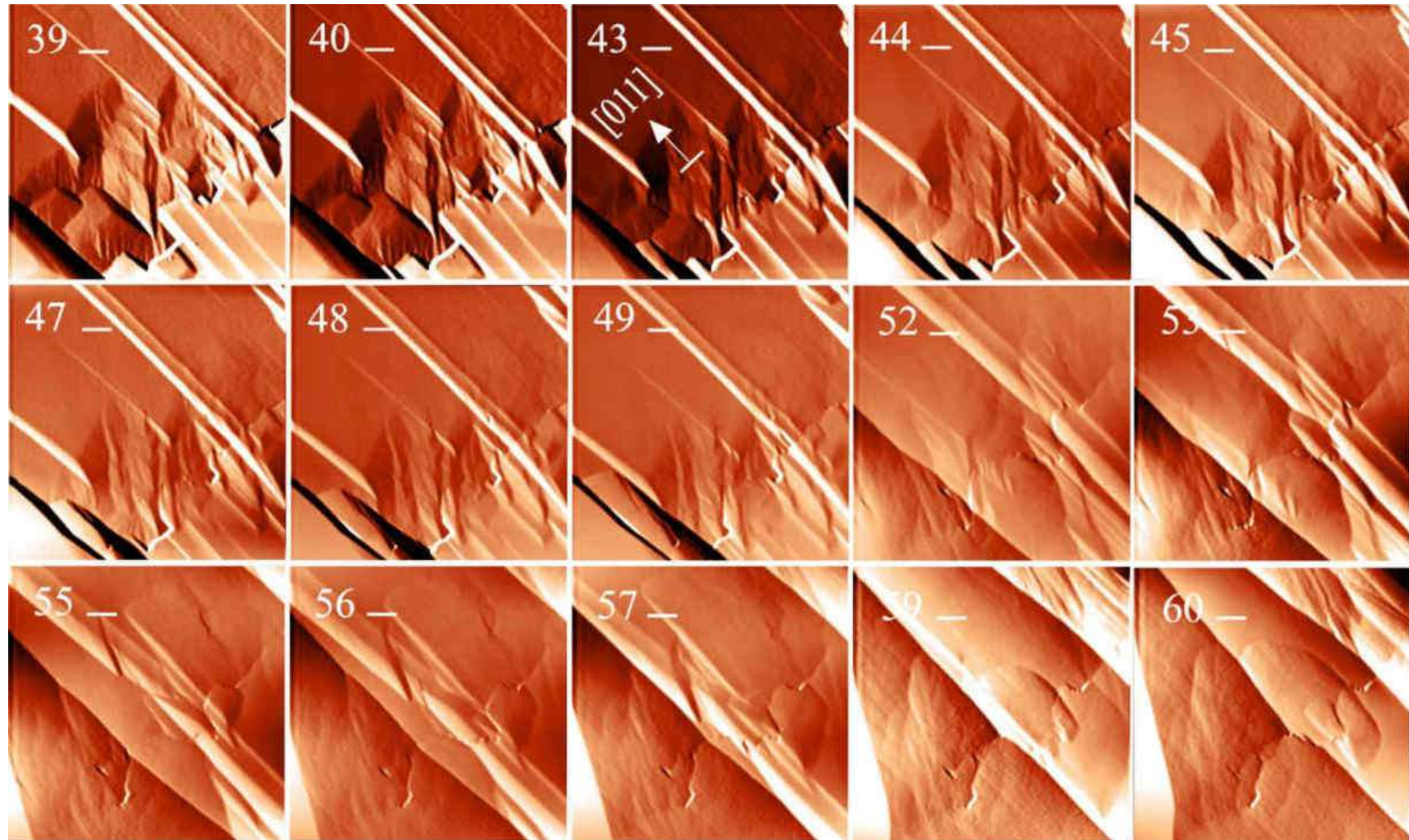


Figure 3.61A – Crack healing, large steps moving towards the crack are visible, their complete closure occurs in the 52nd snapshot. Scale bars are 10 μm , the time interval between sequentially numbered images is 4.5 minutes

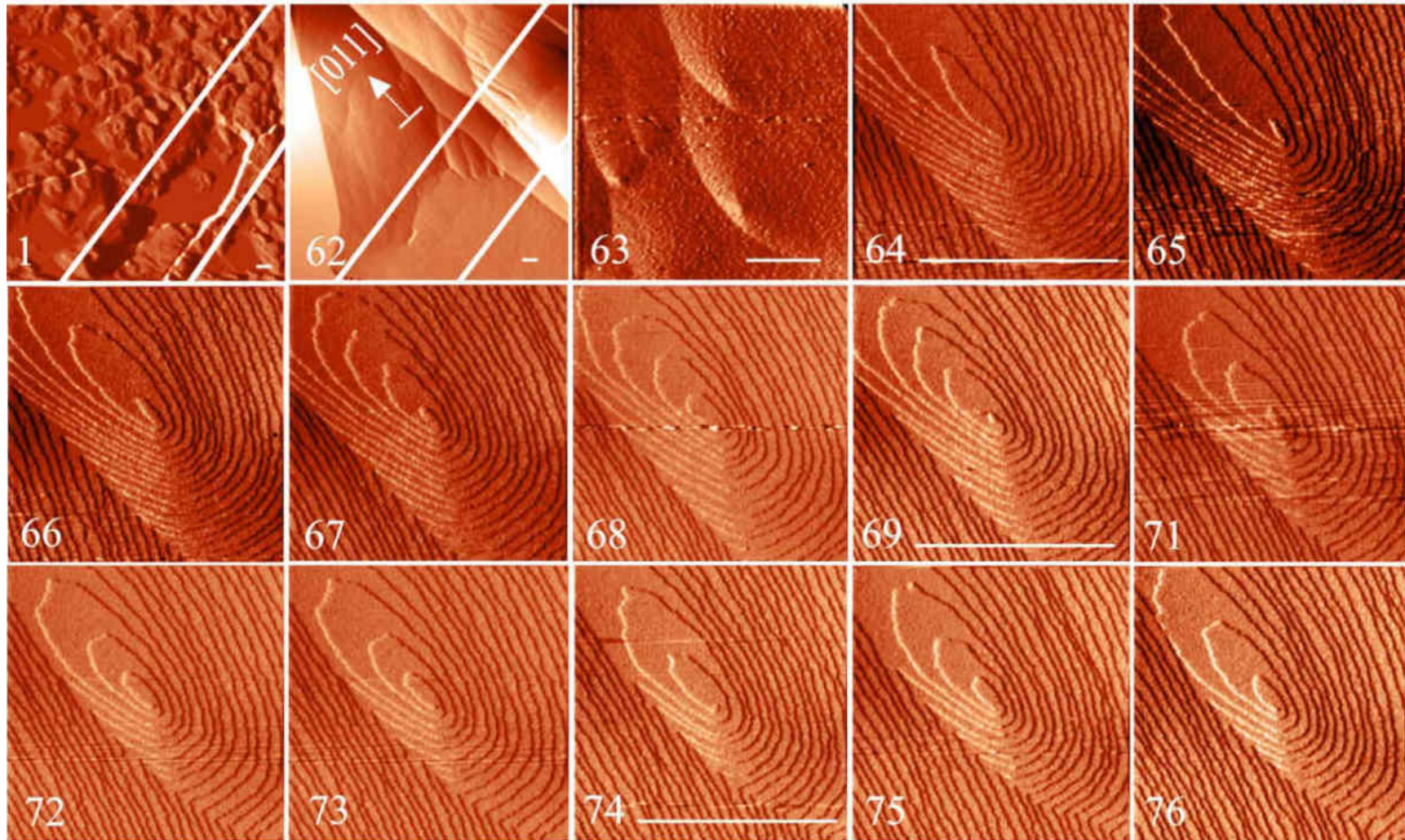
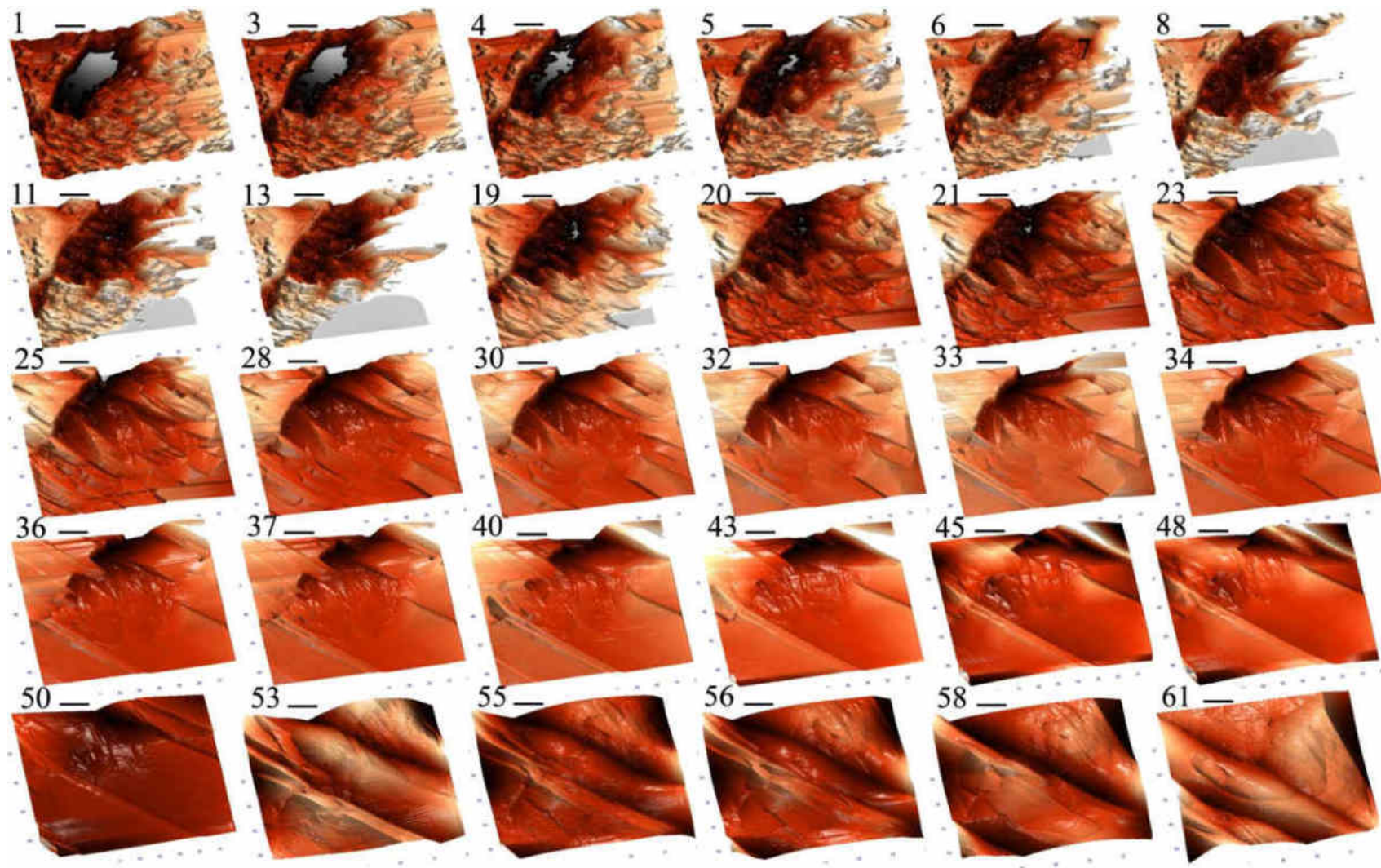


Figure 3.61B – The partially resolved crack (lines in the 1st image) had completely healed by the 62nd snapshot (after 279 minutes). The 63rd snapshot shows an enlarged view of the healed crack: a chain of inclined–axis screw dislocations (64–76) had formed along it. The scale bars are 5 μm , and the time interval between successively numbered images is 4.5 minutes. This experiment is shown below in 3D from another angle.



It is interesting to note that a chain of screw dislocations formed just above the main crack (Figure 3.62), exactly in accordance with the mechanism described for dislocation growth through the overgrown layers; in this case the stresses were transmitted through a thin visor. The epitaxially growing layers on the visor slowed down at the stressed points and curled up into screw hillocks.

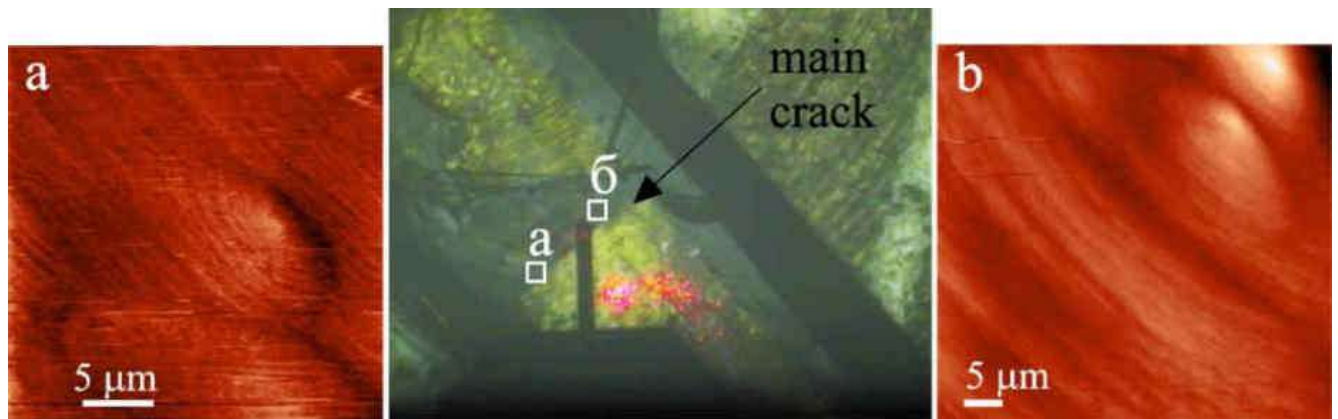


Figure 3.62 – Chain of dislocations formed above the main crack, photographed at two of its locations – (a) and (b)

Vertical displacement crack

In the next experiment, in a solution with a supersaturation of just over 1%, a crack with a large (7 μm) height difference healed rapidly. The crack boundary here is also an obstacle to the free movement of the steps, but at some point a protrusion also extended from the foot of the high edge, which facilitated the throwing of the bridge (10th snapshot in Figure 3.63).



A crack is not only a displacement along the normal, but also a displacement in the lateral plane: if the grids at the crack boundary no longer coincide, and therefore growth in this area can no longer proceed as before, the crack becomes an obstacle to the movement of the steps, especially if there is a height difference. However, experiments

on growth on a crack have shown that in some areas there are breakthroughs with protrusions that become a kind of bridge, making it easier to cross the crack. Obviously, some areas along the crack have a lower chemical potential compared to the neighbouring areas, more compensated bonds due to partial coincidence of the structure.

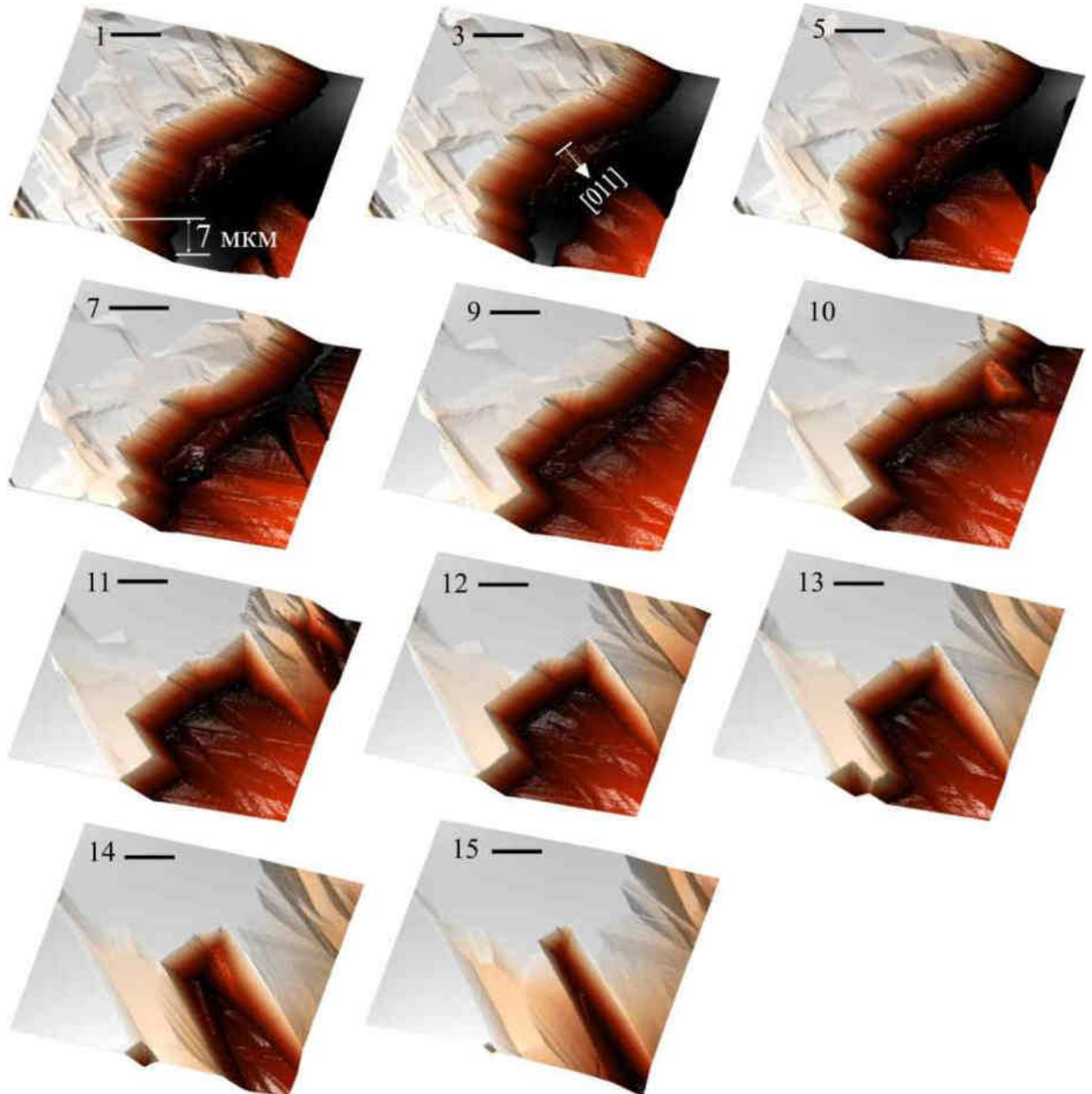


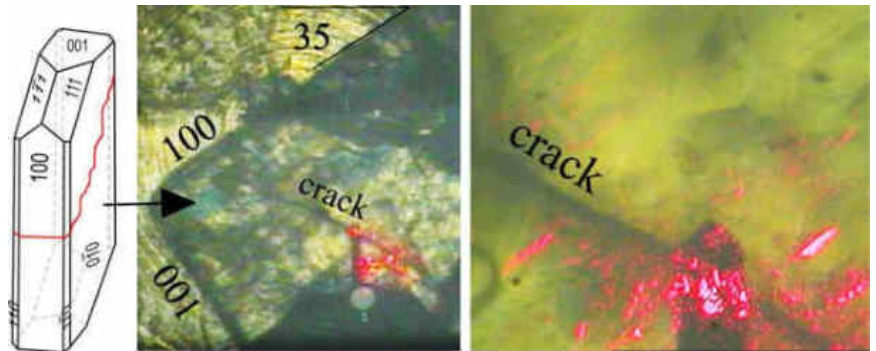
Figure 3.63 – Healing of a crack with a large height difference. The 10th image shows how a protrusion has emerged from the foot of a high edge and has begun to grow at a rate of up to 13 nm/sec. The scale bars are 10 μm , and the time interval between consecutive images is 4.5 minutes

In this way, the crack heals completely, unlike the boundary of the intergrowths, and heals without a seam, but with the formation of defects. Screw dislocations occurred both at the boundary of the individuals in the intergrowth and at the crack, but above the healed crack the dislocations were the result of the realisation of stresses, and in the twins the appearance of dislocations along the boundary on one crystal became the reason why the steps of the second crystal could not cross it.

Dissolution on the crack

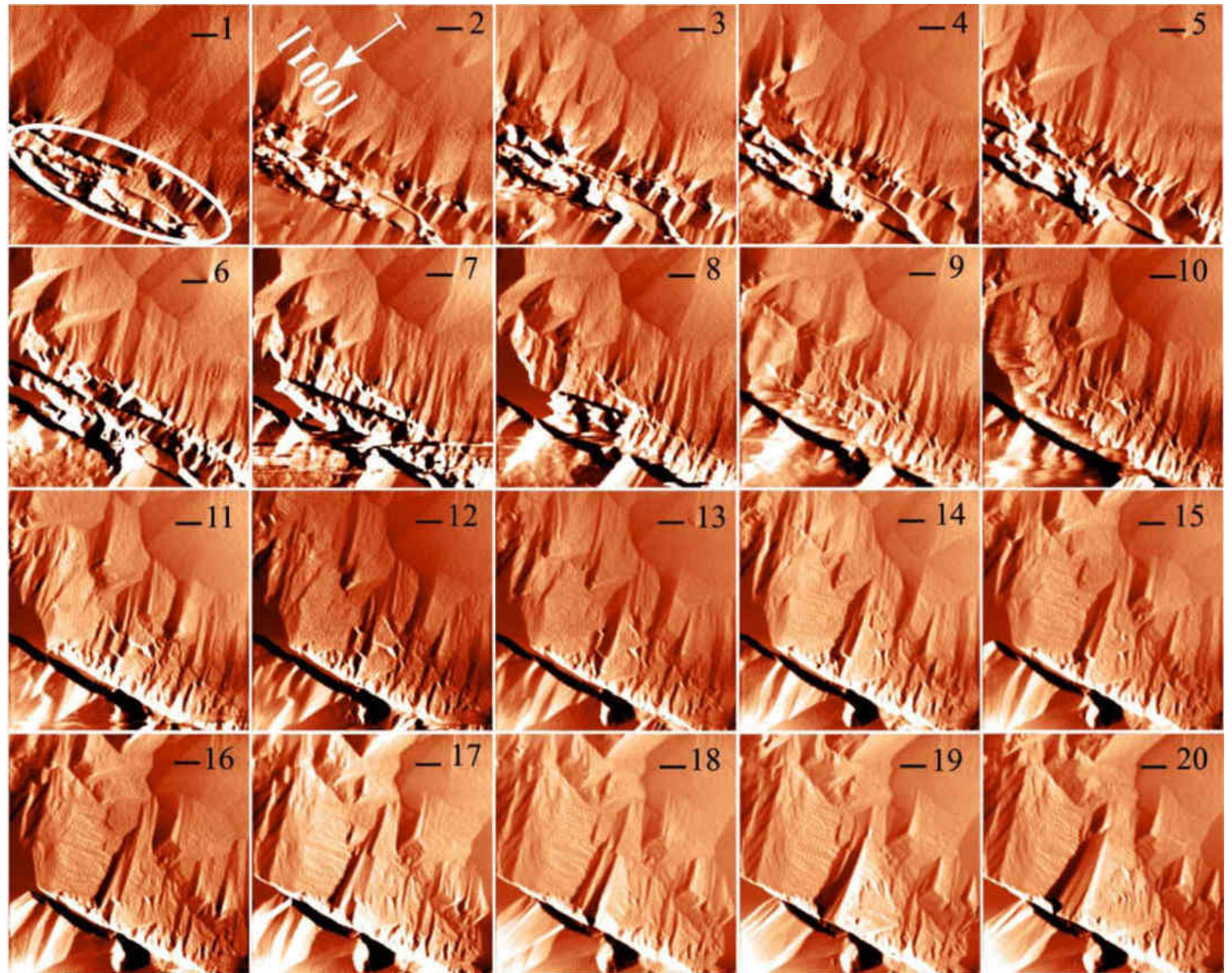
The following experiment examined dissolution in the region of a specially created crack.

Figures 3.64, 3.64A and 3.64B clearly show that the crack is not a site of selective dissolution.



Only areas with edge defects perpendicular to the crack along its entire depth dissolve intensively: even after three hours, dissolution is visible on such perpendicular lines (Figure 3.65). The diagram in Figure 3.66 shows the difference between dissolution on a growth defect (screw dislocation) and dissolution on a post-growth defect (crack). Despite its considerable width compared to the diameter of the dislocation channel, the crack does not expand during dissolution because there are no stresses around it of the same magnitude as around the dislocation channel. The pit on the dislocation becomes wider with time in accordance with the step wave mechanism (Figure 3.2, section 3.1.1). The crack, on the other hand, does not expand; the crystal face is ground off globally as it dissolves, with only a slight slope towards the crack due to the edge defects described (symbol "k" in Figure 3.66).

Figure 3.64 – Dissolution on the specially created crack (indicated by an oval in the first image). The scale bars are 10 μm and the time interval between successively numbered images is 4.5 minutes



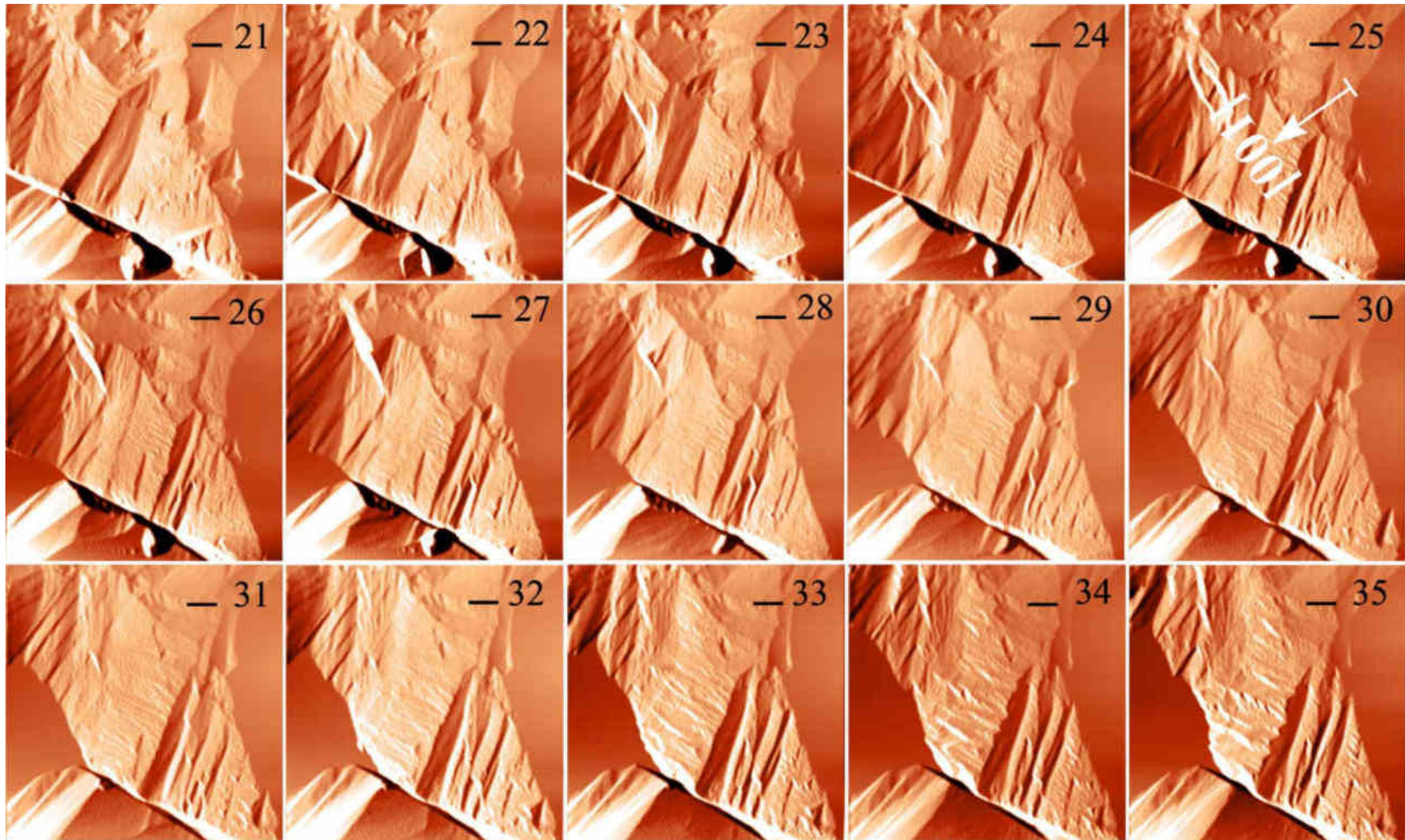


Figure 3.64A – Continuation of dissolution on the specially created crack area. The width of the crack does not change. The scale bars are 10 μm and the time interval between successively numbered images is 4.5 minutes

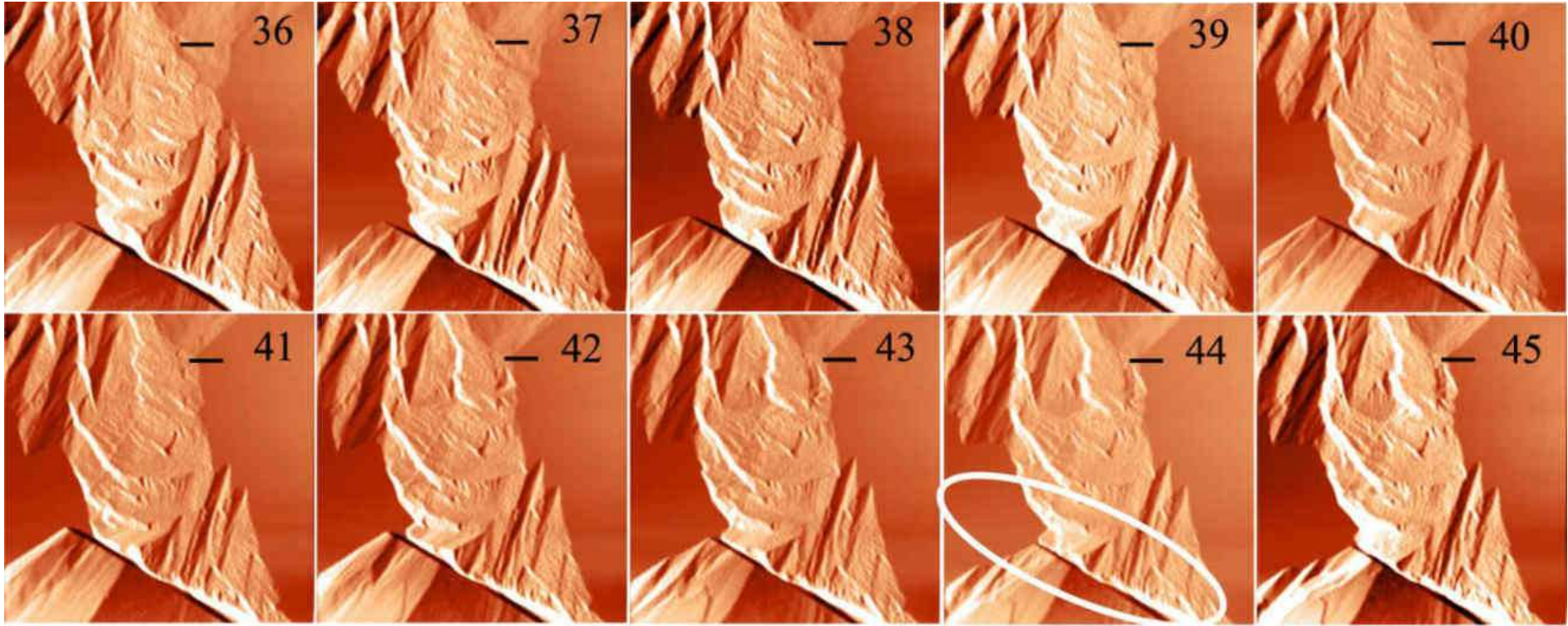


Figure 3.64B – Continuation of dissolution on the specially created crack area. The width of the crack does not change (indicated by an oval in the 44th frame, corresponding to the 198th minute of observation). The scale bars are 10 μ m and the time interval between sequentially numbered images is 4.5 minutes

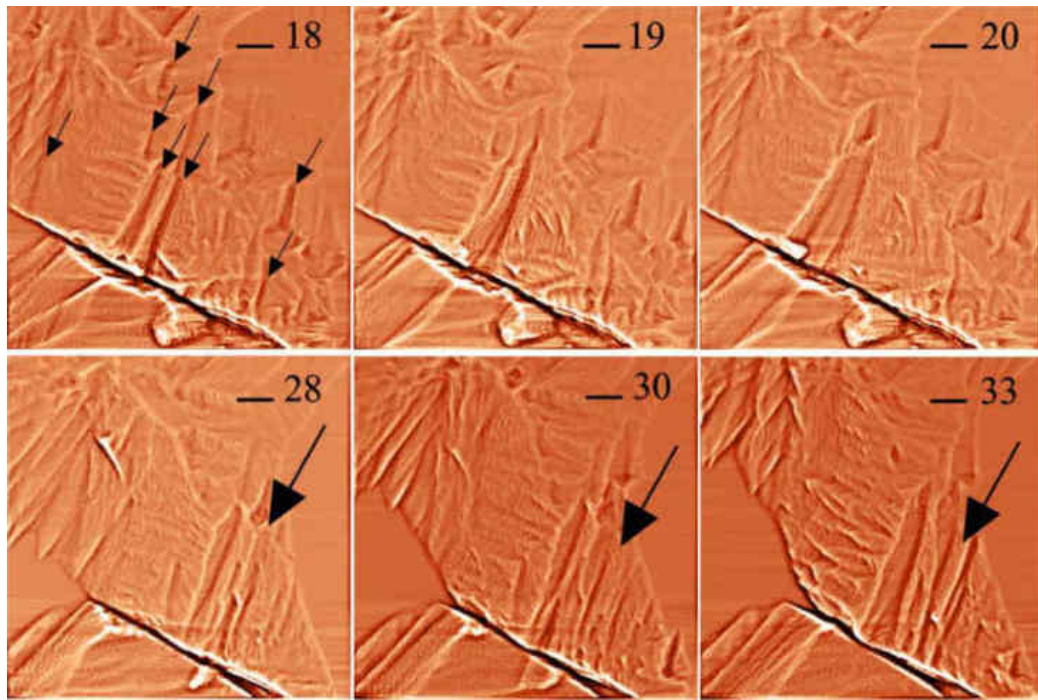


Figure 3.65 – Dissolution in the crack area. Arrows indicate edge damage perpendicular to the crack. Scale bars are 10 μm , time between sequentially numbered images is 4.5 minutes

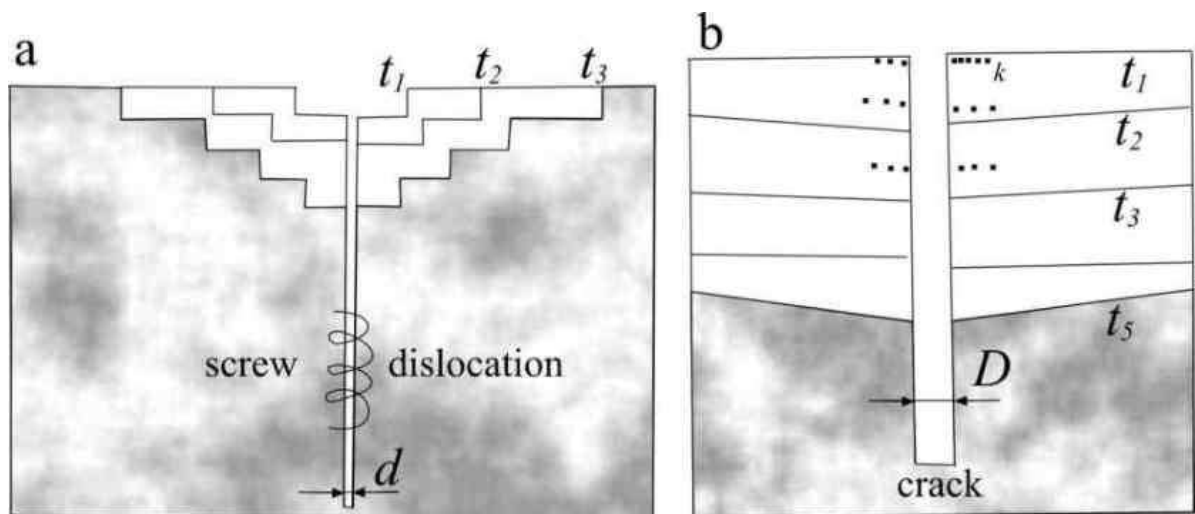
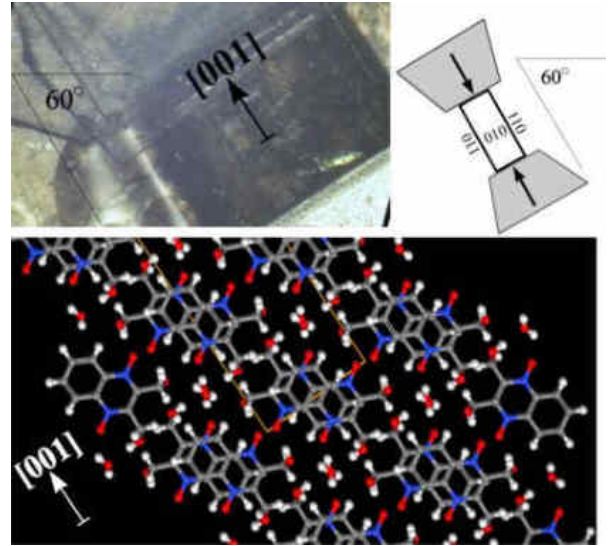


Figure 3.66 – Difference between dissolution on a screw dislocation (growth defect) (a) and dissolution on a crack (post-growth defect) (b). The nature of the stored stresses around the dislocation channel causes the pit centred in the channel to widen with time $t_1, t_2, t_3 \dots$. There are no stored stresses around the crack, only very weak post-growth edge dislocations (symbol "k") which slightly affect the dissolution relief. Despite the fact that the crack width D is significant compared to the channel width d , the pit on the crack does not widen (b)

3.7 Observation of a constrained crystal face in solution

This section presents experiments to observe the layer-by-layer growth and dissolution of the constrained surface (010) of dioxidine. The growth and dissolution had a clear direction and this direction coincided with the compression vectors. Such behaviour was observed in all the compression experiments, but only the most illustrative results are presented in the paper. In one of the experiments, the dioxide surface was compressed by blocks, as shown in the figure. Studying the face in the near equilibrium solution showed that the features of the face relief up to 400 nm high grow on one side and simultaneously dissolve on the diametrically opposite side (Figure 3.67). The direction of simultaneous growth and dissolution coincided with the direction of the compression vectors. In this experiment, edge dislocations occurred in the direction of compression and since the material does not adhere to the stressed region, elongated holes appeared in the projection of the edge dislocations on the surface. The last three images in Figure 3.67A show that the monomolecular steps bend around these holes during growth, increasing their depth. The occurrence of dislocations due to compression and stretching of crystals has long been demonstrated experimentally by optical, X-ray and *in-situ* interferometric methods (Ristic et al, 1997; Zikic et al, 1998).



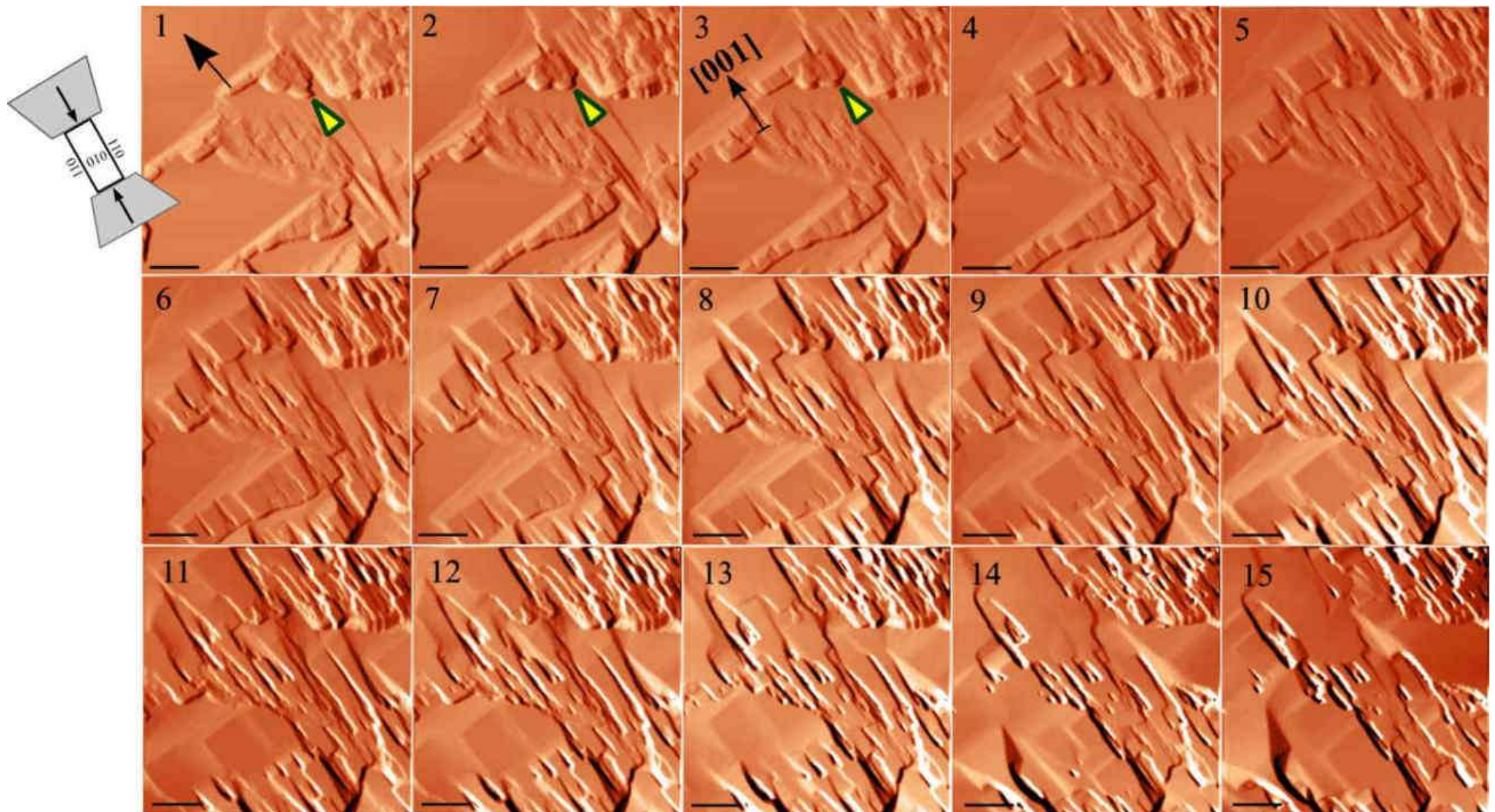


Figure 3.67 – Constrained face in a near-equilibrium solution, relief details up to 400 nm high grow at a rate of 2–4.5 nm/sec on one side (black arrow in the first figure) and simultaneously dissolve at a rate of 1.5–4.3 nm/sec on the diametrically opposite side (yellow arrows). The direction of such growth and dissolution coincides with the direction of the compression vectors. The time interval between the images is 4.5 min. Scale bars are 5 μm

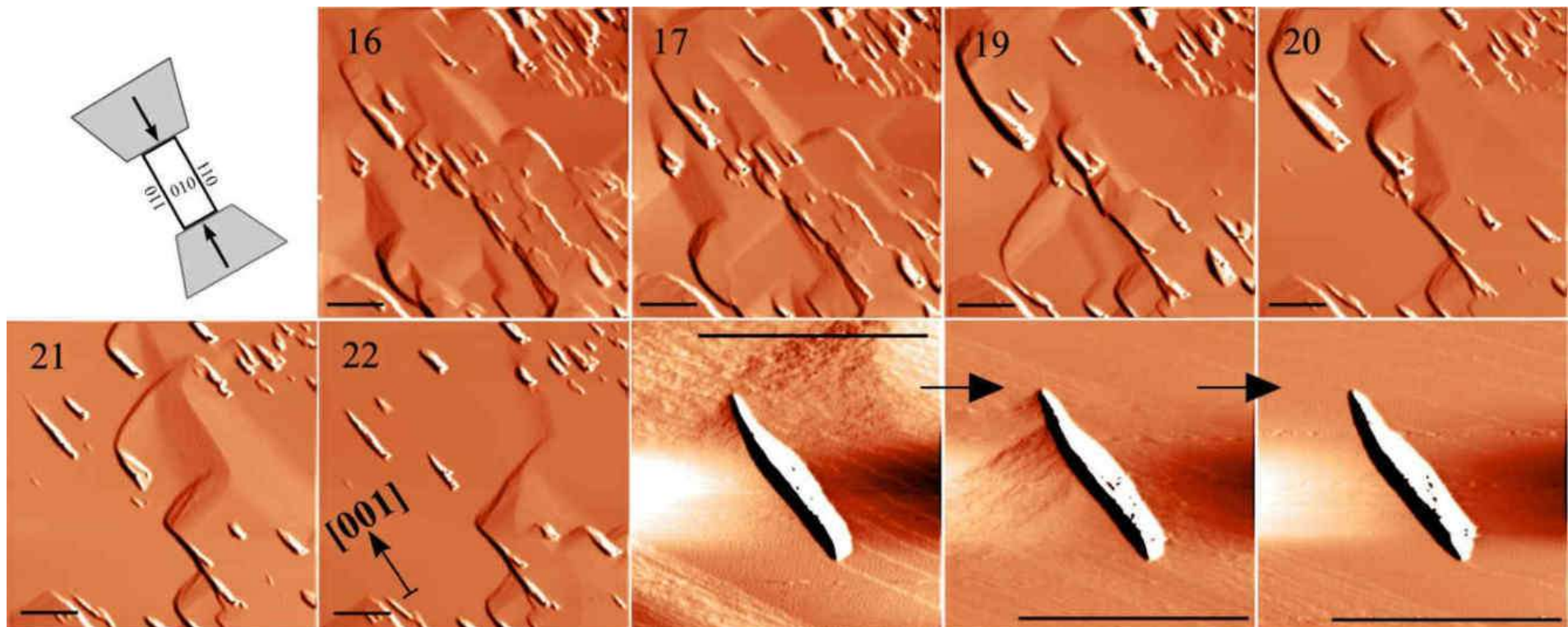


Figure 3.67A – Growth of a constrained face. Edge dislocations are formed in the direction of compression and, as the material does not join the stressed region, elongated holes are formed above them. Monomolecular steps with a tangential rates of 1.5 to 5 nm/sec bypass these holes, decorating the edge dislocations and deepening them progressively (last three images). The time interval between successively numbered images is 4.5 minutes. Scale bars – 5 μm

To check whether the chosen direction of dissolution and growth was characteristic of a particular crystallographic direction, the next experiment was to compress the crystal from the other two faces, as shown in Figure 3.68. Slight dissolution on the (010) face of dioxidine and growth (at rates of 2–5 nm/sec at first, then 10–11 nm/sec) were also observed, the direction of which coincided with the compression vectors. As the steps along the reoriented surface now move from left to right, peculiar traces appear behind the resulting edge perturbations (Figure 3.68).

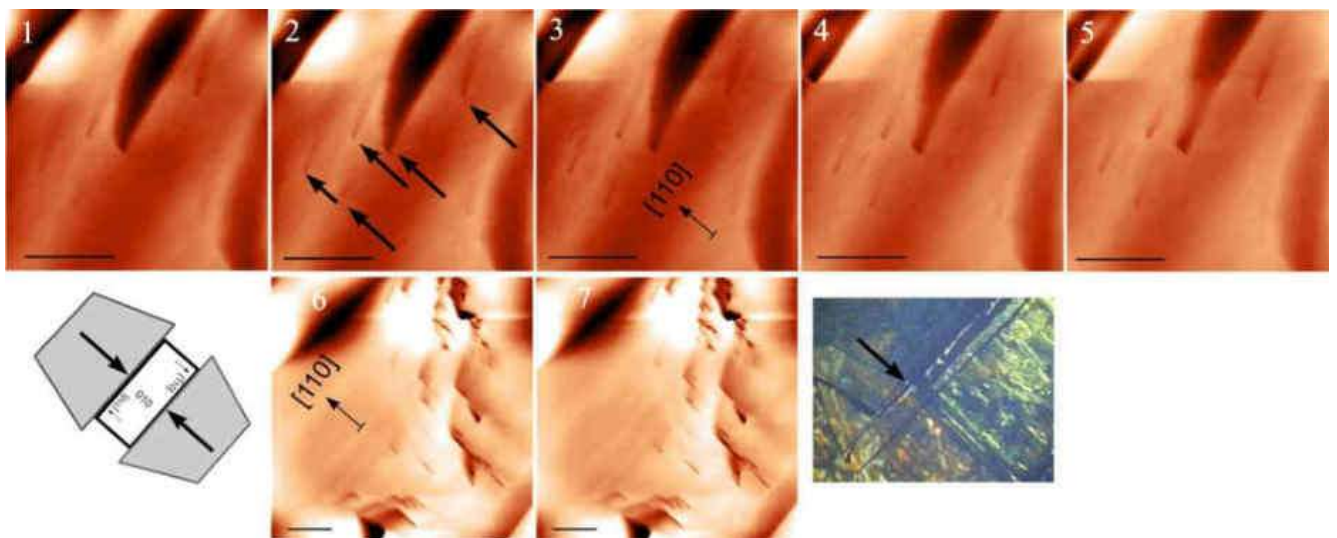


Figure 3.68 – Edge dislocations (shown by arrows) have been created in the direction of compression to which the substance does not attached during growth. Steps growing upwards and to the right form a trail behind the holes. The time interval between images is 4.5 min. Scale bars are 10 μm

This effect was repeated in the next experiment. The oval in the 11th image in Figure 3.69 shows edge dislocations whose plane is oriented in the direction of compression.

The next experiment was continued with the cell rotated 90 degrees to the edge to facilitate needle access. A dislocation pile with massive steps (about 35 nanometres high) and an unusually shaped hole at the top was discovered (Figure 3.70). The shape of the hole is due to the fact that edge perturbations caused by compression have been

attached to the screw dislocation (diagram in Figure 3.71). The growth rates of the steps on this hill are very high – from 19 to 600 nm/sec. In another experiment in a slightly supersaturated solution, growth occurred with overgrowth of edge dislocation projections, with the formation of elongated depressions, also oriented in the direction of the compression vectors (shown by arrows in Figure 3.72). As the steps, which grow at a rate of 4.5 to 8.7 nm/sec and bypass the edge dislocations, do not move strictly in the direction of compression but to the left, a trace is also formed behind each hole. The depth of the holes increases with time – 40–60–80–90 nm.

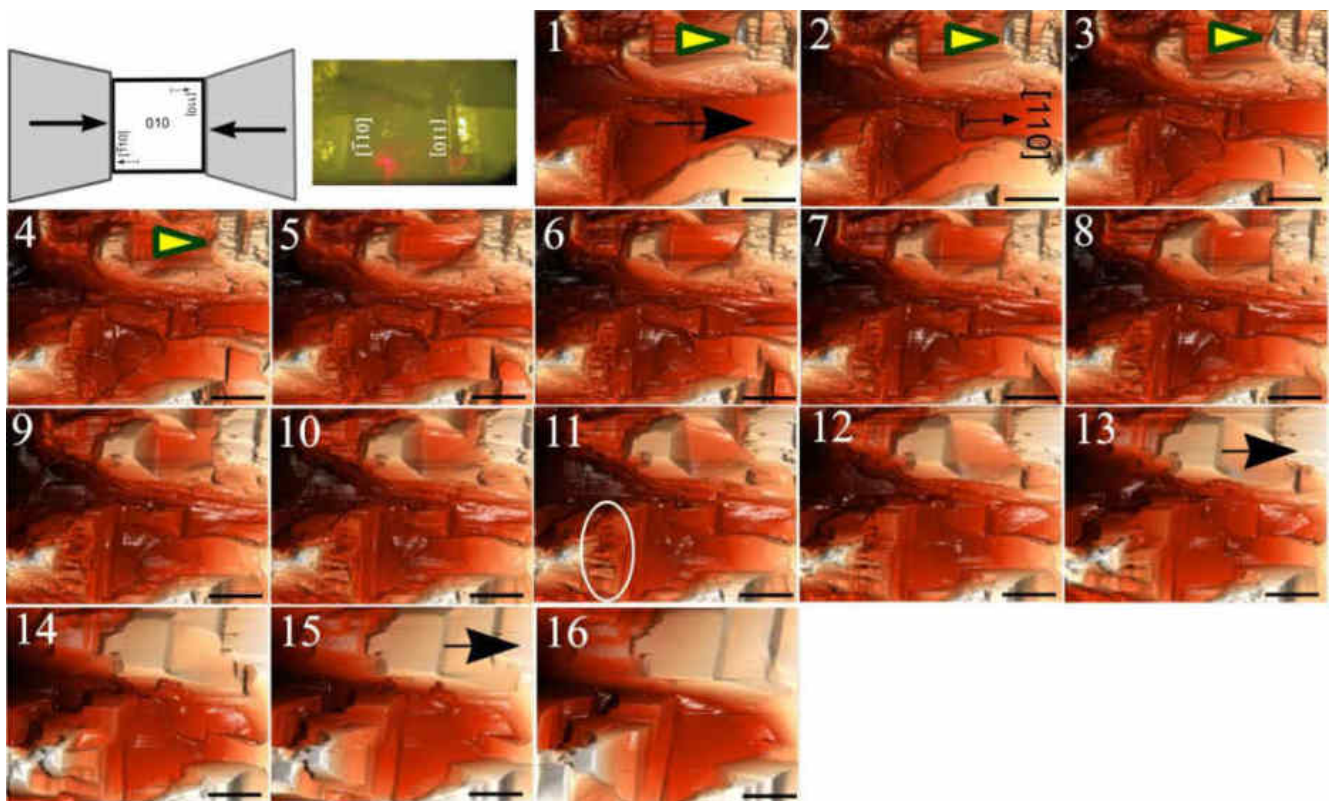


Figure 3.69 – Light dissolution (yellow arrows in the first images) and growth (black arrows in the 13th and 15th images) occur exactly in the direction of compression. The oval in the 11th image shows edge dislocations oriented in the direction of compression.

The time interval between frames is 4.5 minutes. The scale bars are 10 μm

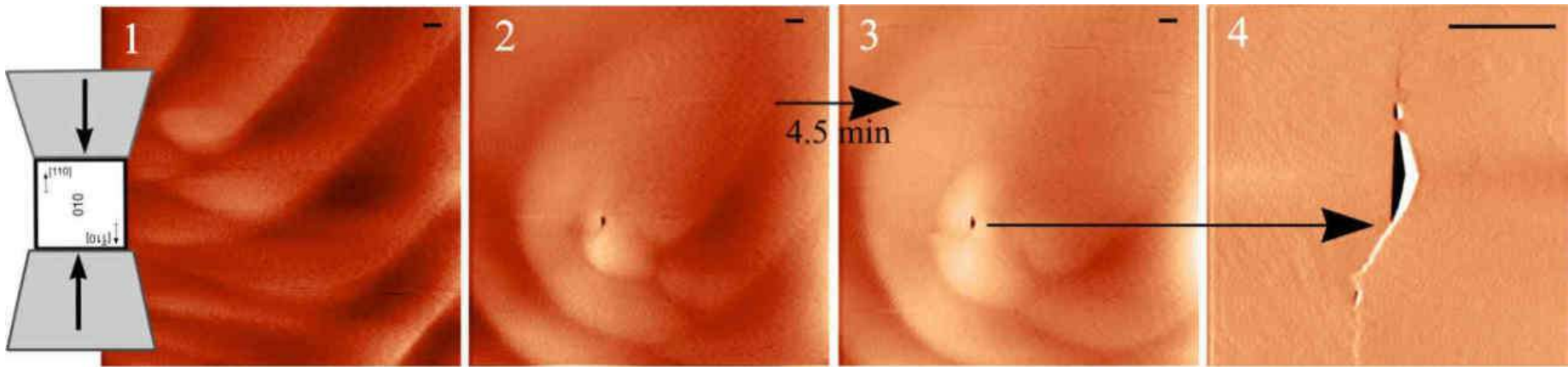


Figure 3.70 – Large dislocation hillock on a compressed surface and a hole at the top, elongated in the direction of the compression vectors. Scale bars – 10 μm

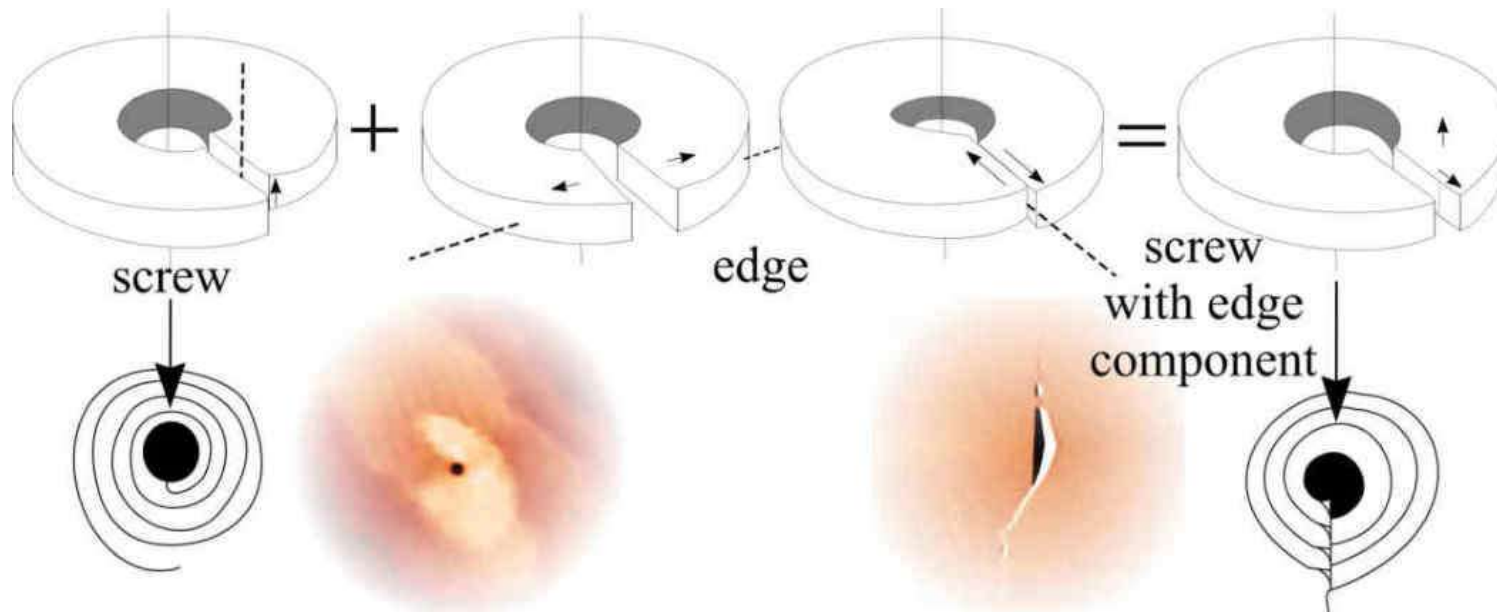


Figure 3.71 - Shape of a hole on a screw dislocation and on a screw dislocation with an edge component caused by face compression

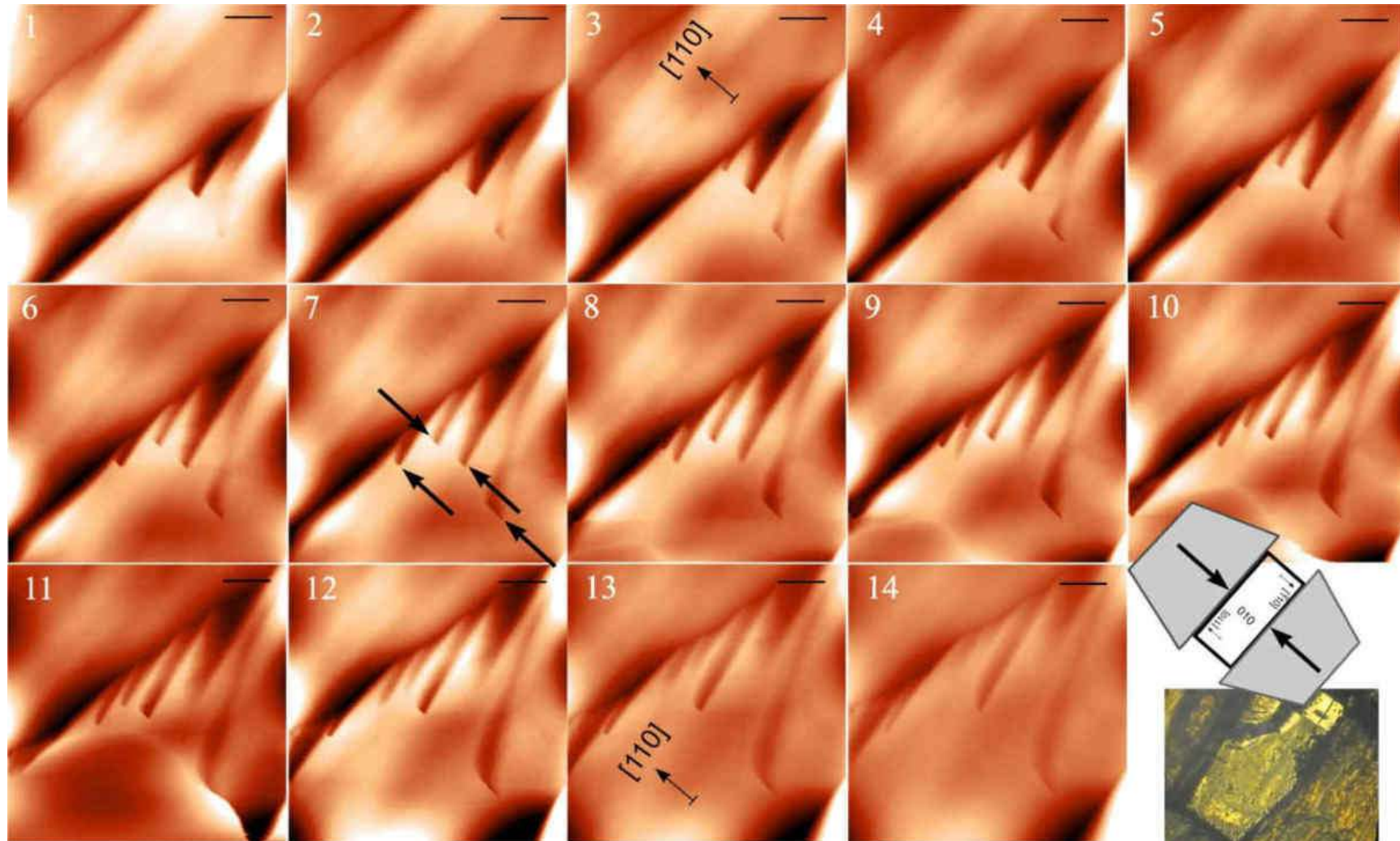


Figure 3.72 – Edge dislocations (shown by arrows) have arisen in the direction of compression, and the substance does not attach to them. The steps moving from the left form a trail behind the holes, and the elongated holes themselves remain reference objects in the image. The time interval between the images is 4.5 minutes. Scale bars are 10 μm

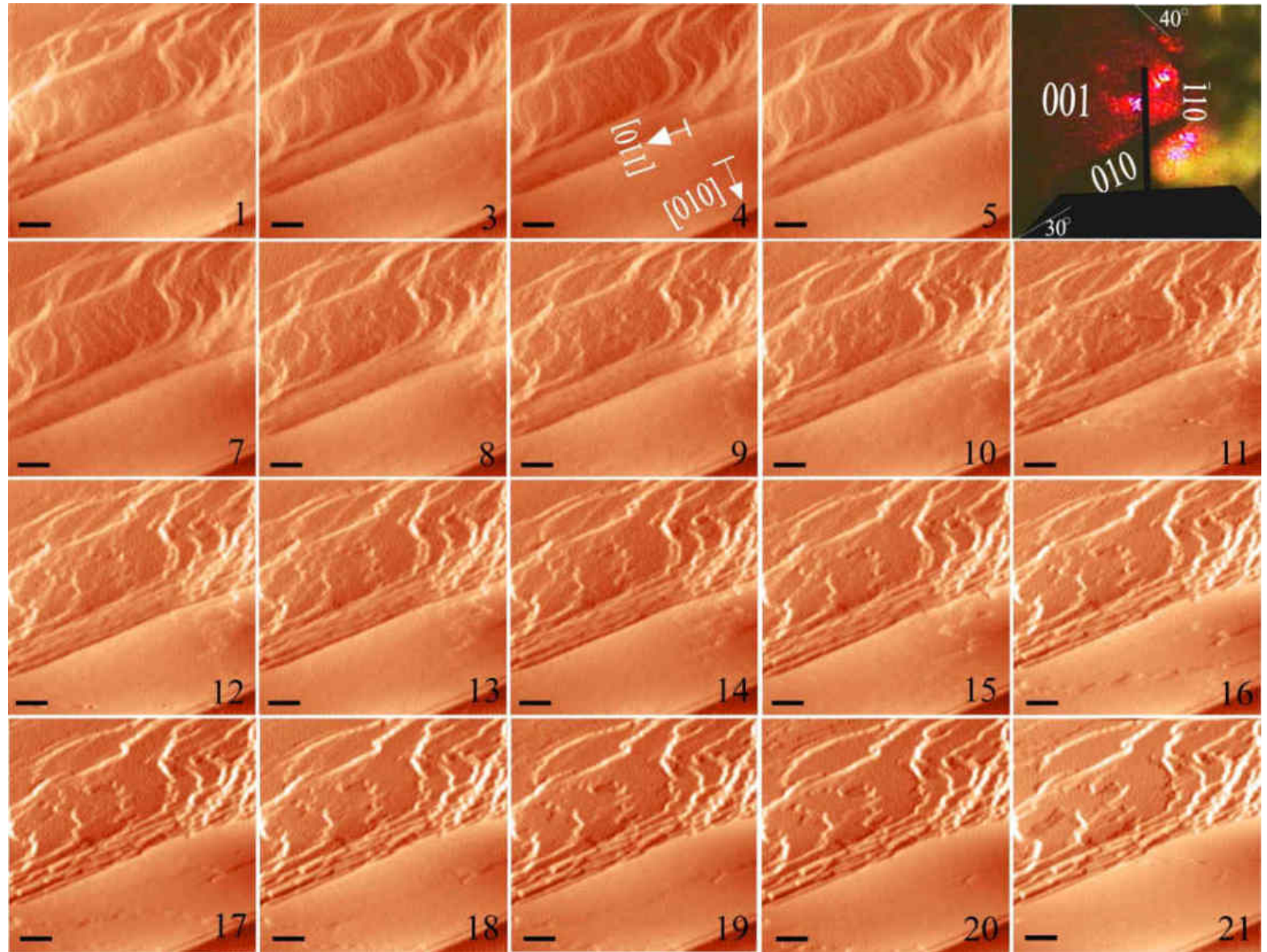
3.8 Processes of layer-by-layer growth (regeneration) and dissolution on the cleavage surface. Influence of neighbouring crystals

Regeneration

In the first experiment, a crystal fracture surface parallel to the $\{001\}$ plane was observed immersed in an equilibrium solution. After slight dissolution, segmental growth began, with elementary steps moving in the $[110]$ direction while other areas remained unchanged (Figure 3.73). On the same surface, weak growth of relief details (indicated by arrows in Figure 3.74) was observed simultaneously at several points on the surface, with the details extending in the $[1\bar{1}0]$ direction.

In several other experiments, similar growth of narrow, rare fragments was recorded in the $[01\bar{0}]$ direction (Figure 3.75) or $[010]$. This type of overgrowth of the fractured surface is associated with its initial non-parallelism to the $\{001\}$ plane and the multi-headed completion of the surface to a singular plane.

Figure 3.73 – Segmental overgrowth of a fracture surface parallel to the $\{001\}$ plane by monomolecular steps moving in the $[110]$ direction. The edge of the steps is uneven with multiple protrusions also elongated in the $[110]$ direction. The time interval between sequentially numbered images is 4.5 minutes. The scale bars are 500 nm



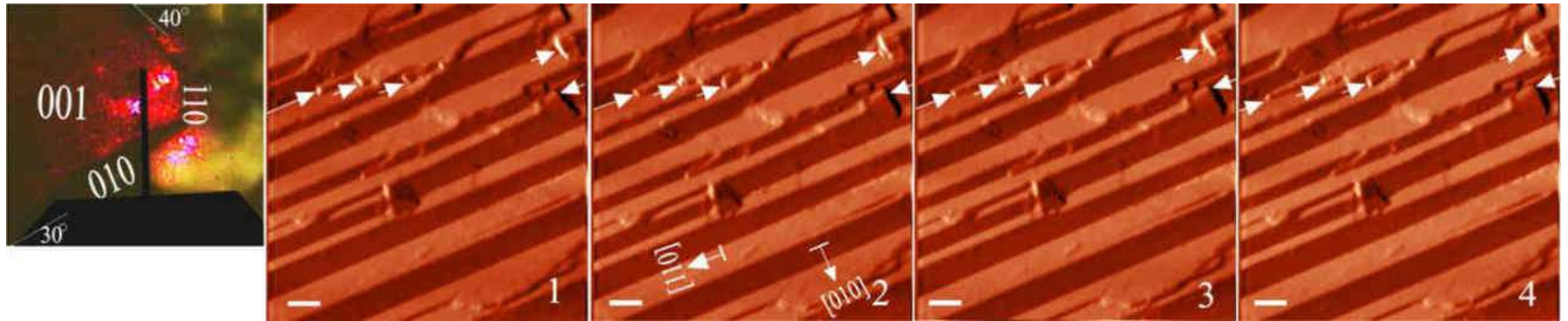


Figure 3.74 – Weak segmental growth of relief details (indicated by arrows) in the direction $[1\bar{1}0]$ on the fracture surface parallel to the $\{001\}$ plane. The time interval between images is 4.5 min. Scale bars are $2\ \mu\text{m}$

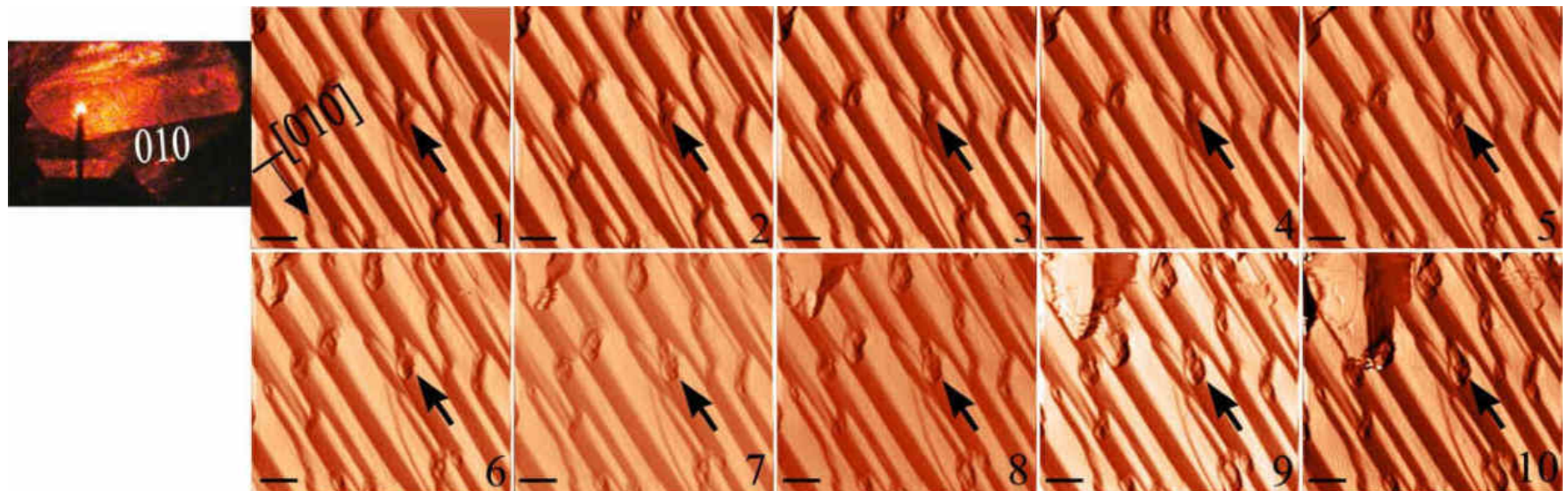


Figure 3.75 – Beginning of fracture regeneration parallel to the $\{001\}$ plane. Individual large narrow steps (indicated by arrows) extend strictly in the $[01\bar{0}]$ direction. The interval between frames is 4.5 minutes. Scale bars are $5\ \mu\text{m}$

Influence of neighbouring crystals

It was planned to observe elementary processes at the site of close contact between two crystals over a long period of time in order to establish the characteristics of the formation of induction surfaces. However, many attempts to use AFM to observe the boundary between two closely pressed natural faces (100) or (010) of different crystals were unsuccessful, as satisfactory contact was prevented by "bevels" in the form of even the narrowest faces (110). However, on one of the joined crystals, a dislocation hillock was discovered with an interesting pattern of dislocation exit from several elongated holes 500 to 1000 nm wide (Figure 3.76). The steps of the hillock had a height of 25 to 50 nm and grew at a rate of tens of nm/sec. Since such elongated holes on the top have only been observed under conditions of special compression of the face (Figure 3.70), it is logical to assume that the tightly compressed neighbouring crystal acted in a similar way at the nanoscale, adding several edge shifts to the screw dislocation. These edge perturbations changed the usual appearance of dislocation holes at the top of the hill. As there are multiple dislocation exits at the top of the hillock, the appearance of the top is much more complex than that of the hillock in Figure 3.70, but the reasons for the elongation of the holes are similar.

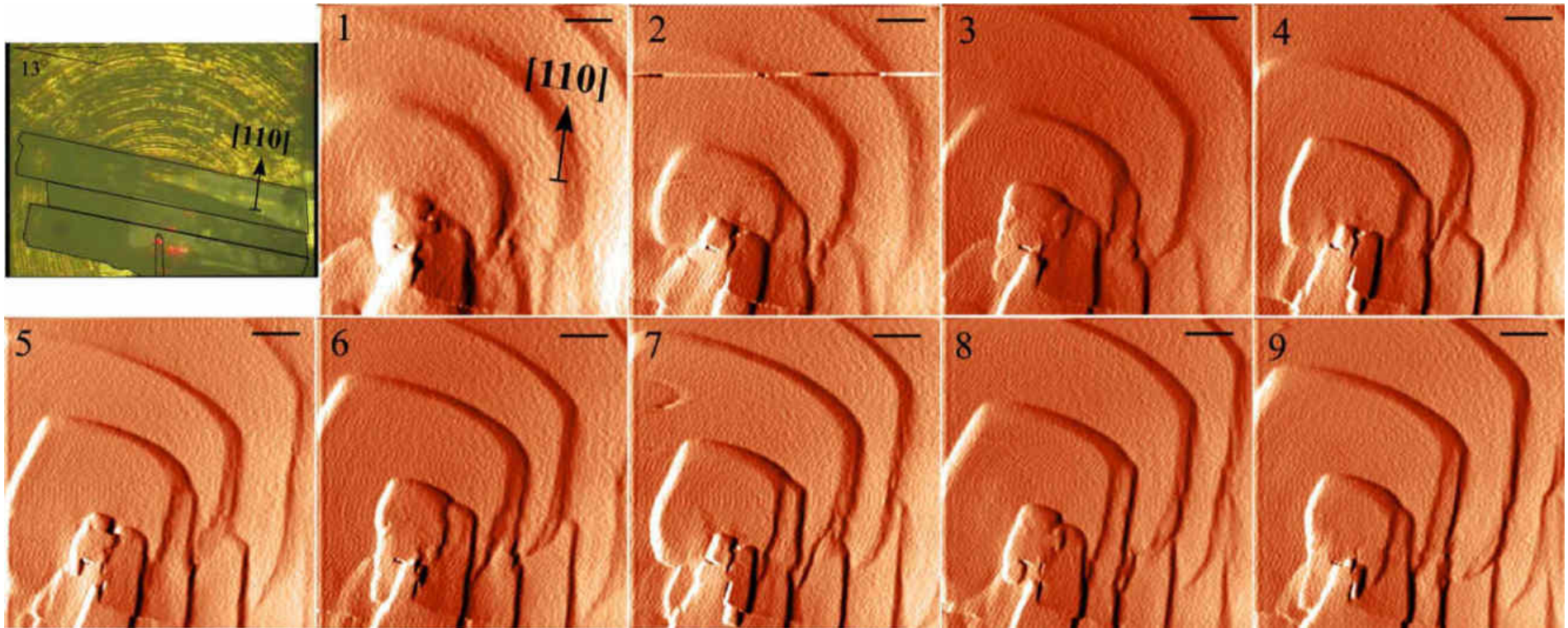


Figure 3.76 – Dislocation hillock on the face of one of the pressed crystals, is similar to the hillock on the surface specially compressed from both sides (Figure 3.70), the pressure of the neighbouring individuals has added several edge shifts to the screw dislocation, making the holes at the top of the hillock non-circular. The time interval between images is 4.5 minutes. The scale bars are 10 μm

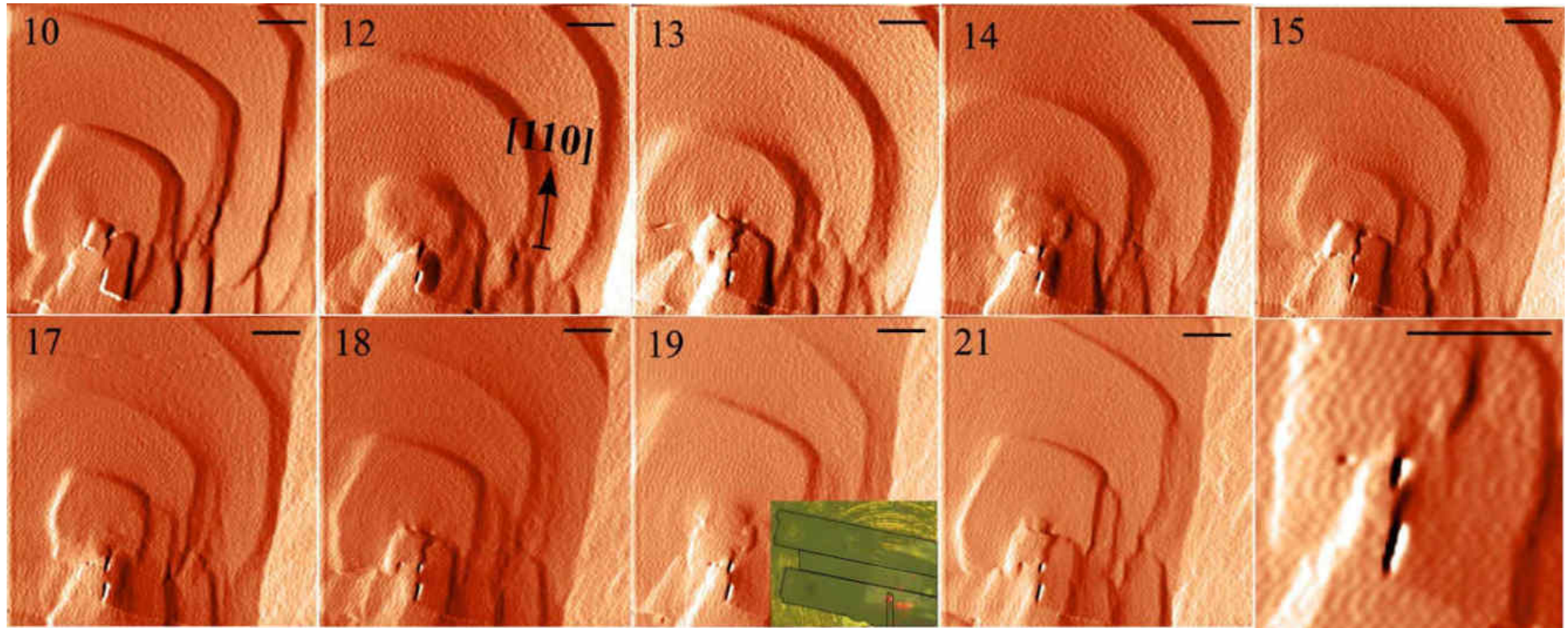


Figure 3.76A – Dislocation hillock on the face of one of the pressed crystals, is similar to the hillock on the surface specially compressed from both sides (Figure 3.70), the pressure of the neighbouring individuals has added several edge shifts to the screw dislocation, making the holes at the top of the hillock non-circular. The time interval between sequentially numbered images is 4.5 minutes. The scale bars are 10 μm

Chapter 4. *Ex-situ* AFM Study of Mineral Crystals: Evidence of Growth and Dissolution on Defects

The study of micro- and nanoscale traces of growth processes on the natural faces of natural crystals using various methods, based on the results of direct AFM observations of the growth and dissolution processes of model crystals, allows us to identify some of the factors that influenced the formation of specific mineral crystals in the final stage of their growth in nature (Piskunova, 2018 a). These data will then help a geologist to reconstruct larger scale processes and geological environments.

It is more accurate to compare AFM images of "live" processes with AFM images of dry surfaces. AFM does not require the surface to be sprayed, for example, spraying would not allow the detection of natural inorganic nanoparticles on quartz crystals (Piskunova, 2020). In addition, AFM does not require a vacuum, but most importantly, AFM is a truly three-dimensional method, whereas the interaction of an electron beam with relief details can cause artificial changes in contrast and misrepresent relief height. AFM studies of natural crystals are a very complex task, because even the most ideal of them have experienced transfer. The optically shiny growth surface on the micrometre scale turns out to be covered with oxidation films, traces of dissolution, chips, abrasions, etc. (Sokerina, 2011, 2013) In the final stage, which can last tens to hundreds of years for hydrothermal crystals, the crystals grow slowly under conditions of diminishing nutrients. Under these conditions, the steps on their surface tend to group and form macrosteps. In this case, impurities have a particularly strong effect and, due to the low rates, manage to block the fractures on the steps and the hillocks grow predominantly upwards rather than outwards, becoming too high to scan in AFM. Although such images do not contain neat dislocation spirals, they are valuable because they show how crystals form in nature.

Pyrite (Polar Ural, Russia)

Cubic pyrite metacrystals up to 1.5 cm in size collected by V.I. Silaev from the Polar Ural massive silty mudstones (Middle Palaeozoic deposits of the Eastern (Palaeocean) structural zone) were transferred to the funds of the Geological Museum of the Institute of Geology of the Komi Scientific Centre, probably by M.N. Kostyukhin (Figure 4.1(a)). The exact geological reference of the samples has not been preserved. It was found that the paired faces of the crystals differed significantly in micromorphology (Figure 4.1 (b) and (c)), although all the faces of the cube belong to one simple shape and should be identical in sculpture. Initially, an X-ray study was carried out, which showed that the samples belonged to pyrite and that there were no pseudomorphs. AFM scanning revealed polygonal growth spirals folded into steps with a relatively smooth front on the faces of one type ((b-AFM) in Figure 4.1) and hillocks with rounded steps on the faces of another type (Figure 4.1 (b-AFM)).

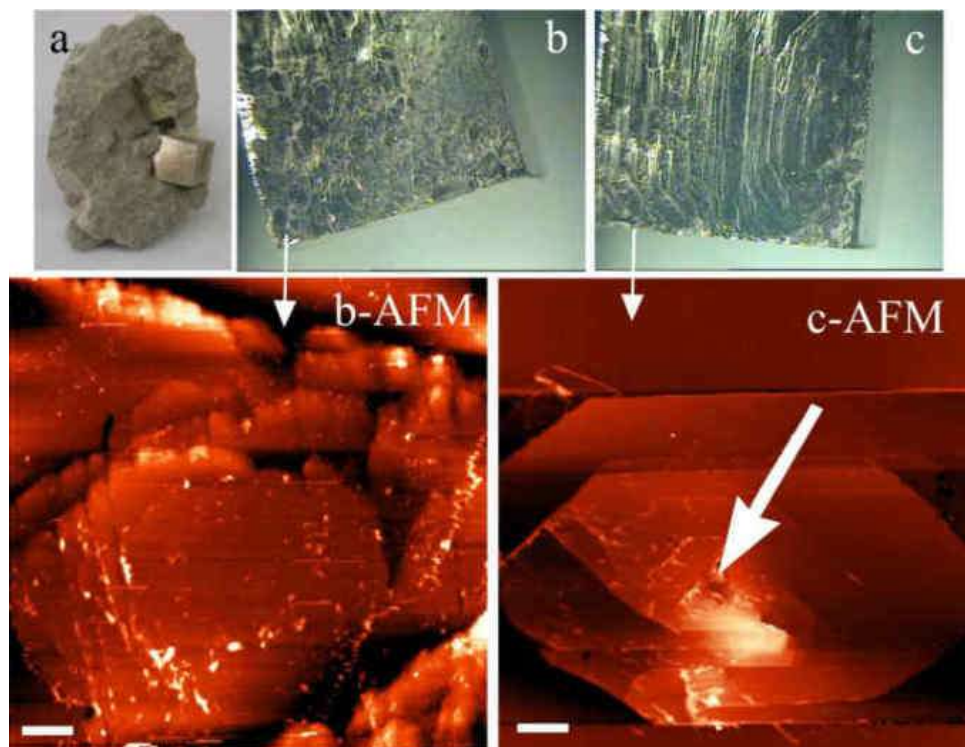


Figure 4.1 – Pyrite from Polar Ural silty mudstones (a) with different facet sculpturing (b, c). Bottom – AFM image of typical growth hillocks found on these types of facets.

The arrow in (c-AFM) shows the semi-dissolved top of the polygonal hillock at the dislocation exit point. Scale bars are 10 μm

Evidence of non-equilibrium adsorption of impurities was also found; the rounded hillock surface had significantly more solid inclusions (Figure 4.2 (a)). The size of inclusions on such surfaces (quartz, illite and calcite according to Raman spectroscopy) did not exceed 4 μm . In contrast, surfaces of the type (Figure 4.1 c) were characterised by relatively large (up to 20 μm) inclusions of illite, anhydrite and calcite (Treyvus et al., 2011a). Apparently, one of these inclusions left a characteristic imprint with a layered relief as recorded by AFM (Figure 4.2 (b)).

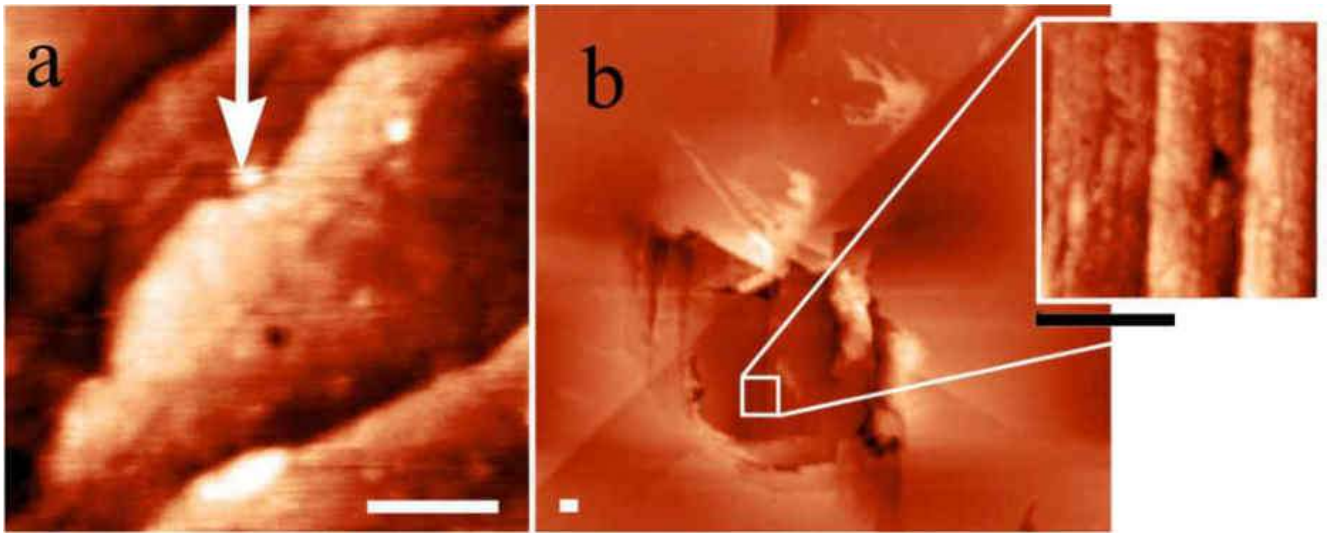


Figure 4.2 – AFM images of surfaces of different sculptures of a pyrite crystal from Polar Ural siltstones: (a) – growth bend of a step during braking on a solid inclusion on a surface with rounded hillocks (Figure 4.1 (b)). A hole from a dislocation channel is visible in the centre of the image; (b) – a pit from a fallen solid inclusion with layered relief of the walls on a face with polygonal hillocks (Figure 4.1 (c)). Scale bars 500 nm

Pyrite (Iberian Mountains, Spain)

Cubic crystals from Navajun in the Iberian Mountains (30 km north-east of Soria, Spain) were given to the author for study by Academician N.P. Yushkin. The rock containing the described pyrite crystals is characterised as a Mesozoic metapelite with a low degree



of metamorphism. They also showed different sculptures of opposite pairs of faces: flat polygonal steps on one side and steep-sided hillocks up to 2 mm high on the other. According to the AFM data, the steps on the first type of faces, 9 to 200 nm high, are of a dislocation nature (Figure 4.3).

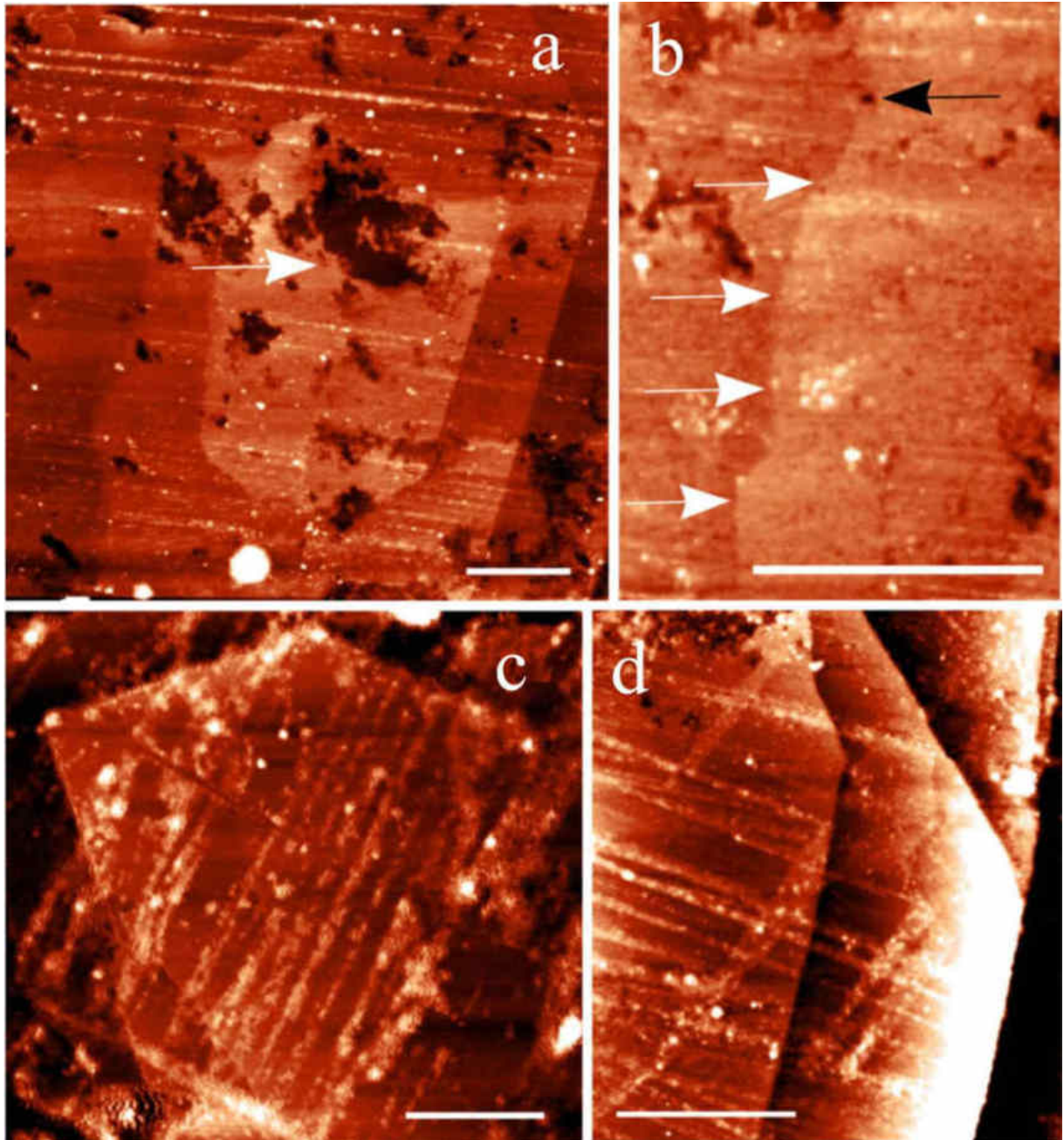


Figure 4.3 – AFM images of polygonal dislocation hillocks (a, c, d) on flat pyrite surfaces (Navajun, Spain). The arrow in (a) shows dissolution at the exit of the dislocation spiral. In (b) the white arrows indicate a thin step ejected from the dislocation exit (black arrow). Scale bars 20 μm

Many areas of the pyrite faces were covered with films showing a nanoscale globular structure (Figure 4.4). In the SEM, such a film thickness is not available for elemental analysis, it can be assumed that these are iron oxides.

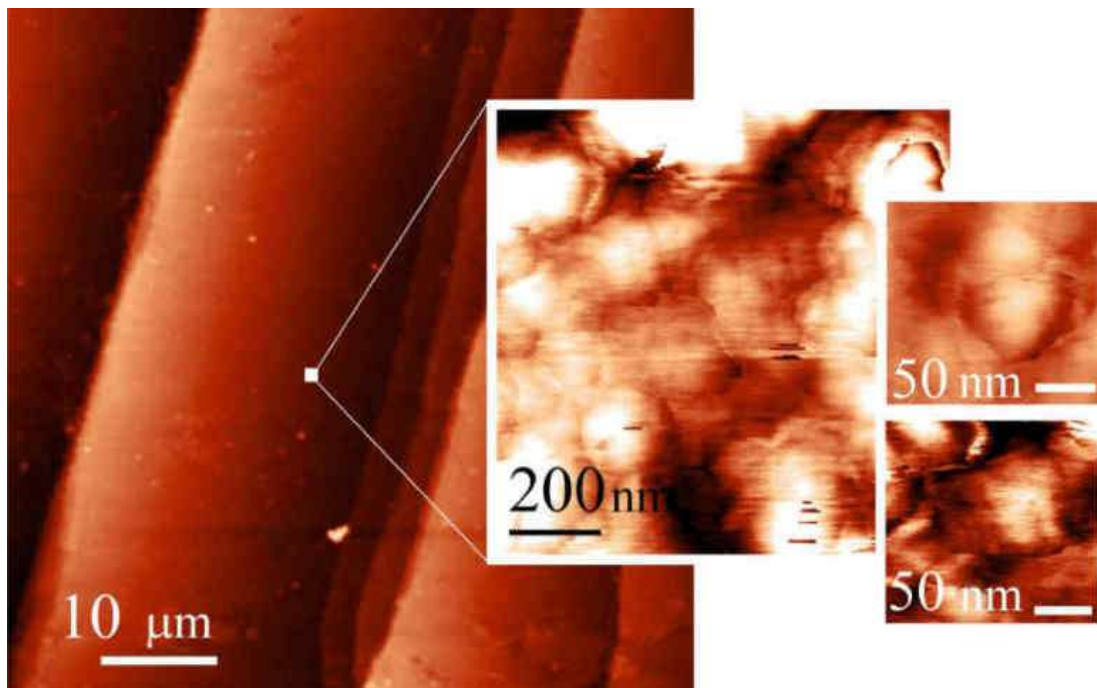


Figure 4.4 – Steps on the pyrite surface, with terraces between covered by globular oxide films

The knobbly pairs of crystal faces from Navahun showed complex combinations of dislocation outcrops on the tops of steep-sided hillocks (Figure 4.5).

AFM data, together with goniometer measurements and a map of slip planes for each crystal, allowed E.B. Treyvus to suggest the influence of directional pressure for the Ural pyrites and for all 20 samples of Spanish pyrites (Treyvus et al., 2011a, 2011b). For some crystals, the pressure was perpendicular to one of the three pairs of their faces; they showed the most striking differences in pairs of faces, in contrast to crystals that were apparently not so strictly oriented in the direction of the pressure. The consequences of plastic deformations during the process of non-free growth of these pyrite crystals are the twins found among them, the misorientation of the microblocks, three times greater in angle than that of the relatively perfect faces, the differences in the microsculpture of the faces and the nature of the inclusion of impurities in them.

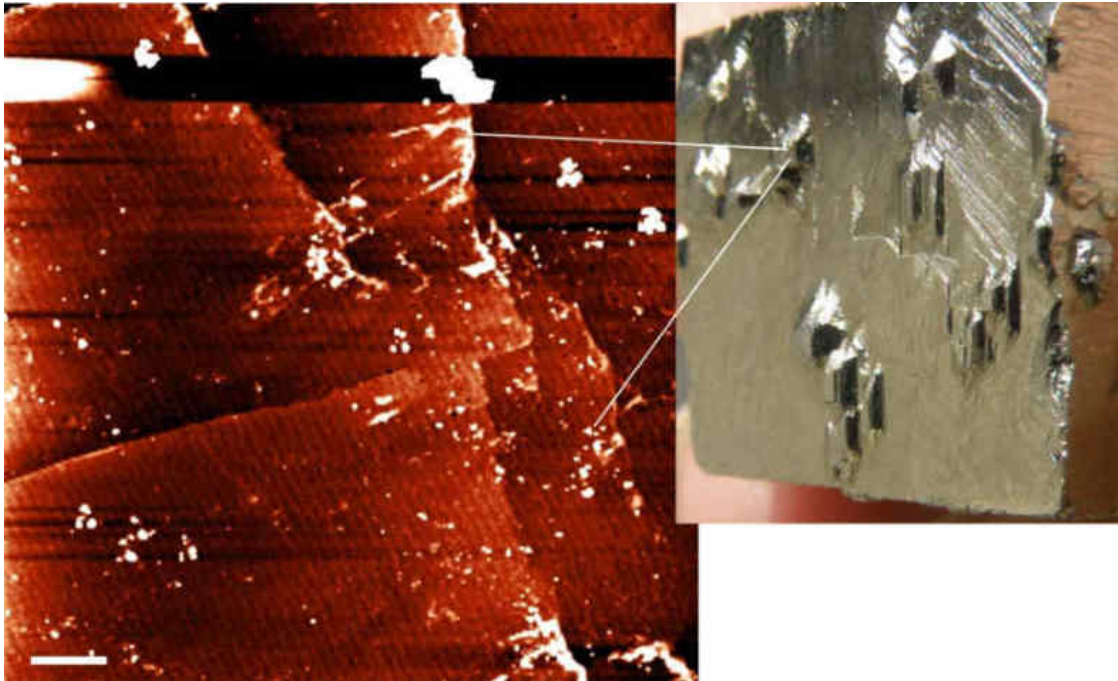


Figure 4.5 – AFM image of the top of a hillock on the pyrite face (Navajun, Spain): a complex structure of multiple dislocation outcrops and large steps emitted by them.

Scale bar 5 μm

Alabandine

Alabandine crystals sent for study by V.I. Silaev were mined at the Vysokogorny deposit, located in the Okhotsk volcanic belt of the South Verkhoyansk metallogenic province. They are very large crystals of cubic syngony, with an octahedral and hexaoctahedral habit, up to 7 cm in diameter. The crystals have grown from hydrothermal solutions and are saturated with a large number of impurities, including industrially valuable ones (Silaev et al., 2013). For example, indium metals are represented by micrometre (1–250 μm) inclusions uniformly distributed in alabandine. The growth surfaces are covered with porous films in many places, but some evidence of defect–



stimulated growth and dissolution on alabandine crystals has been detected by AFM. These include 4–7 nm high steps (the first image in Figure 4.6), uniformly oriented dissolution pits initiated by solid impurities (Figure 4.6 (b)) and an incompletely dissolved solid cubic inclusion (Figure 4.6 (d)). Judging by the etch pits, the crystal had undergone a small amount of dissolution, but this was replaced by growth in the final stage: image (c) shows a half-filled pit.

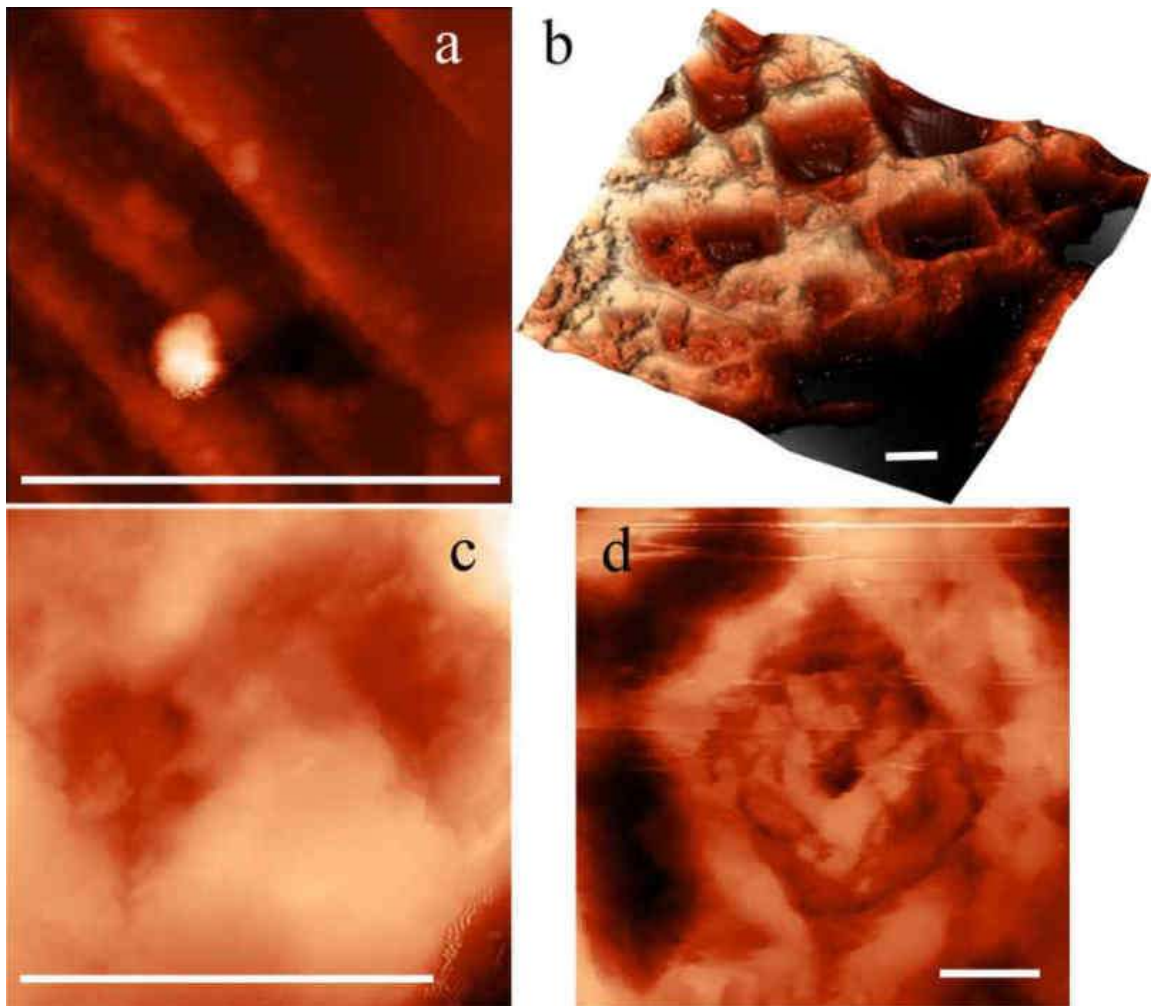


Figure 4.6 – AFM images of the (100) surface of alabandine (Vysokogornoye Mt., Yakutia): (a) – growth steps 4–7 nm high, (b) – identically oriented dissolution pits initiated by solid impurities, (d) – incompletely dissolved solid cubic inclusion. Traces of overgrowth of the etch pit are visible in (c). Scale bars 5 μm

Topaz



Topaz $\text{Al}_2[\text{SiO}_4](\text{F},\text{OH})_2$, crystallizes in orthorhombic syngony, this sample of solution–melt genesis from granite pegmatites of the Sherlovogorskoye deposit (Transbaikalia), kindly provided by O.V. Udoratina. Figure 4.7. shows an inclusion on the face of the topaz which, according to AFM data, has a globular structure. An AFM image of a topaz crystal surface with a microrelief indicating dissolution in a directed flow of medium is shown in Figure 4.8. The edge of the polygonal pit on the prism face (120) facing the flow (direction [110]) is much more jagged (Figure 4.8 (d)) than its edge (d) on the 'leeward' side (direction [010]).

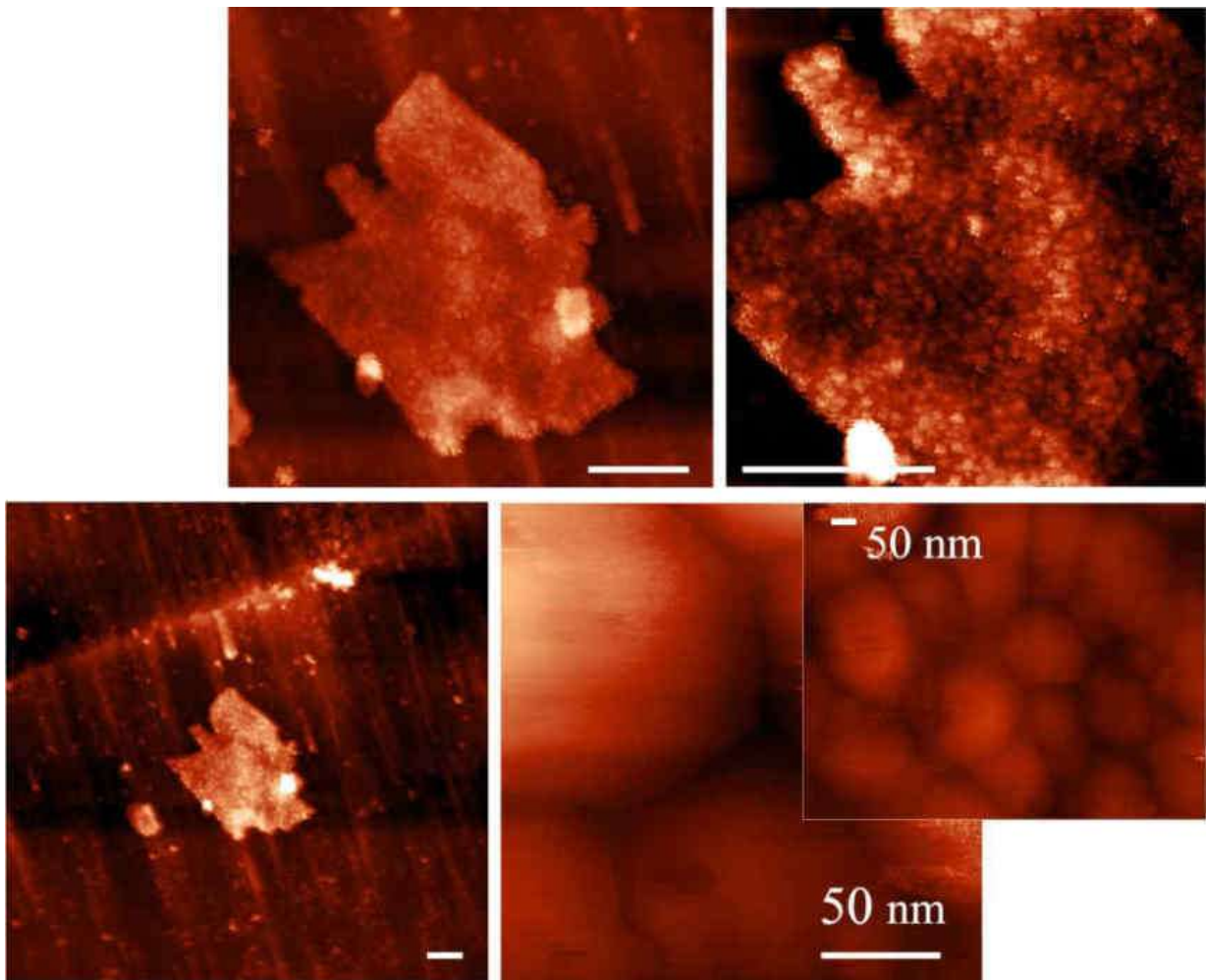


Figure 4.7 – Globular structure of a xenomineral inclusion on a topaz face (globule size ~150 nm). Unmarked scale bars 4 μm

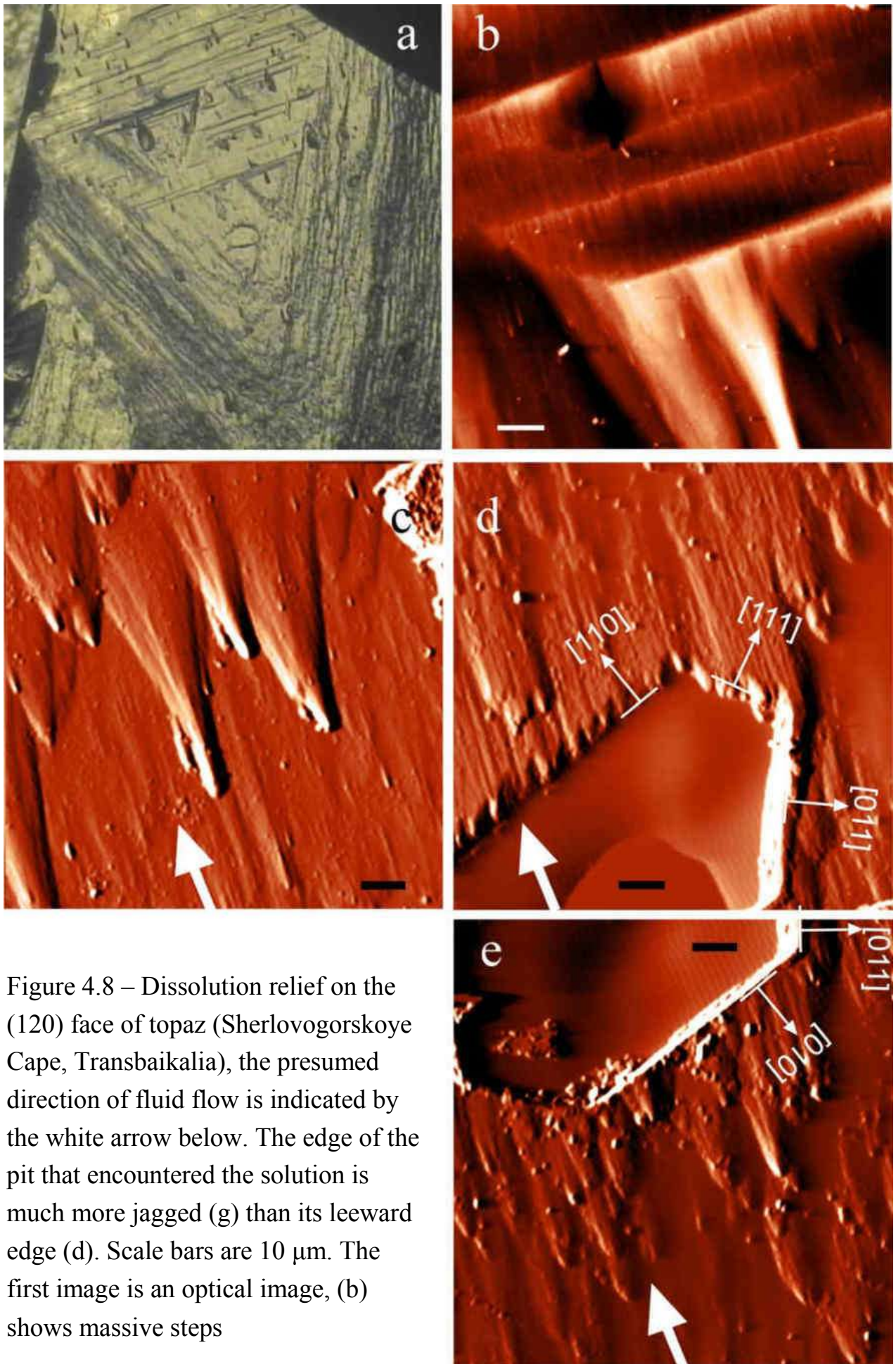


Figure 4.8 – Dissolution relief on the (120) face of topaz (Sherlovogorskoye Cape, Transbaikalia), the presumed direction of fluid flow is indicated by the white arrow below. The edge of the pit that encountered the solution is much more jagged (g) than its leeward edge (d). Scale bars are 10 μm . The first image is an optical image, (b) shows massive steps

Phenakite

Phenakite crystals (Be_2SiO_4 , trigonal syngony) from the Ural emerald mines (Mariinskoye (Malyshevskoye) and Sretenskoye (Sverdlovskoye) emerald-beryllium deposits) belong to Nikolaev A.G. and Popov M.P. This phenakite grew from high-temperature pneumatolite–hydrothermal solutions. The AFM images in Figure 4.9 show nano- and microscale evidence of layer-by-layer growth and dissolution on defects on the $(112\bar{0})$ face of the phenakite. The smallest step size measured is 2.5 nm.

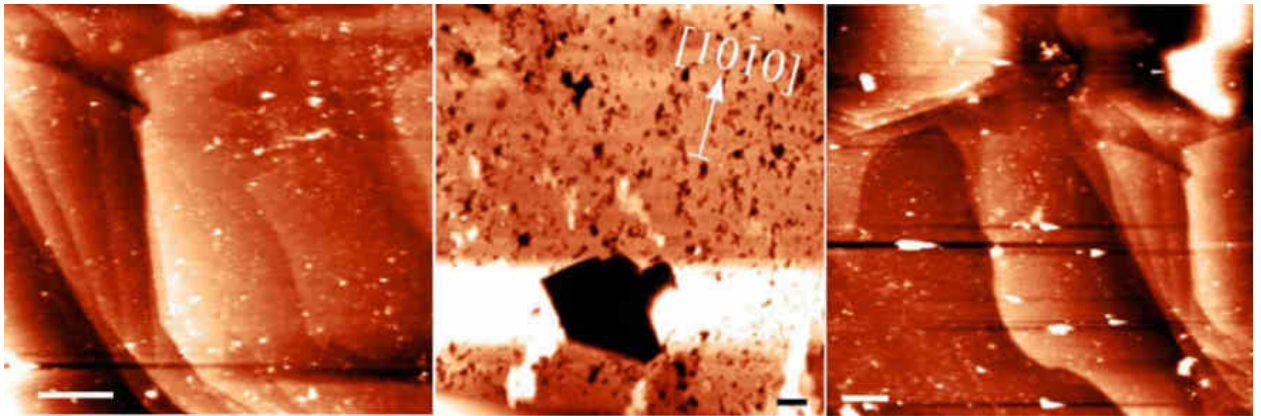


Figure 4.9 – Face $(112\bar{0})$ of phenacite crystal, evidence of Layer-by-layer growth and dissolution on defects. Steps 2.5, 4, 9, 20, 26 nm high. Scale bars 5 μm

Datolite

Using AFM, very large hillocks on screw dislocations were found on the $(011)/(122?)$ face of datolite $\text{CaB}(\text{SiO}_4)(\text{OH})$, extending in the $[001]$ direction, on which only step density waves are distinguishable (Figure 4.10). These greenish crystals of monoclinic syngony grew from high temperature solutions (fluid) and were brought by O.V. Udoratina from the Dalnegorsk skarn borosilicate deposit (Primorye).



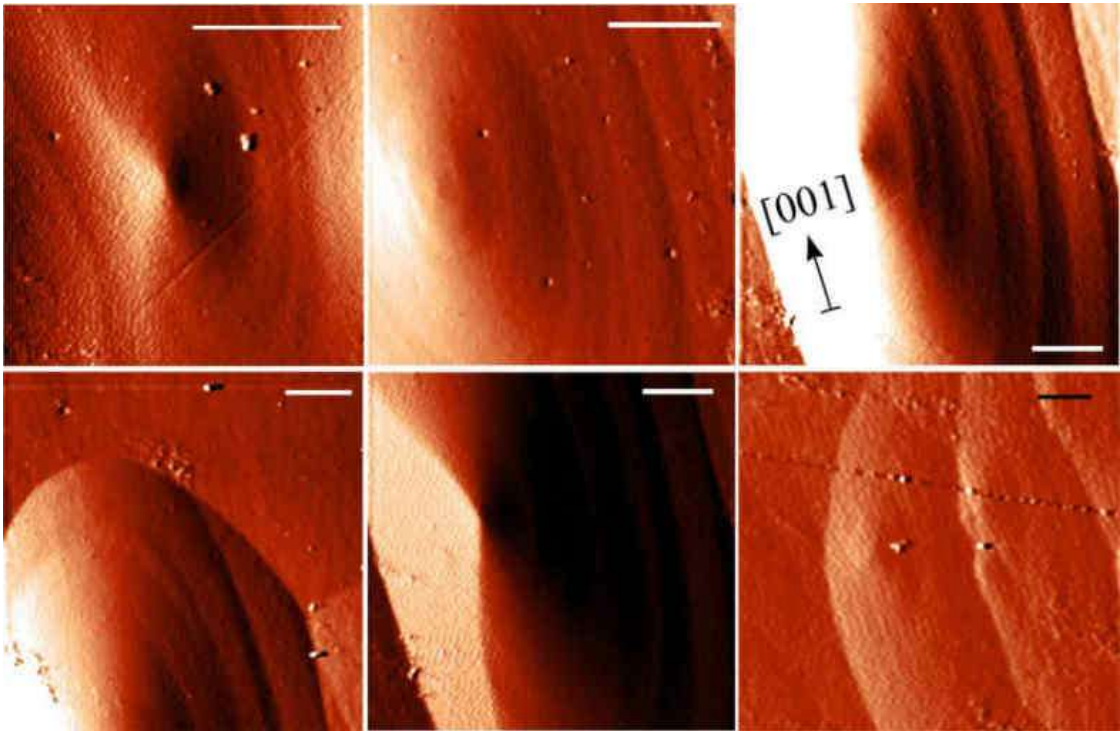


Figure 4.10 – Large dislocation hillocks on the (011)/(122?) face of datolite (Dalnegorsk, Primorye), elongated in the [001] direction. Scale bars 10 μm

Quartz

This section presents quartz of hydrothermal origin. The face of the negative rhombohedron of the rock crystal from quartz veins of the Zhelannoye deposit (Kozhinsky district, subpolar Urals) is shown in Figure 4.11.

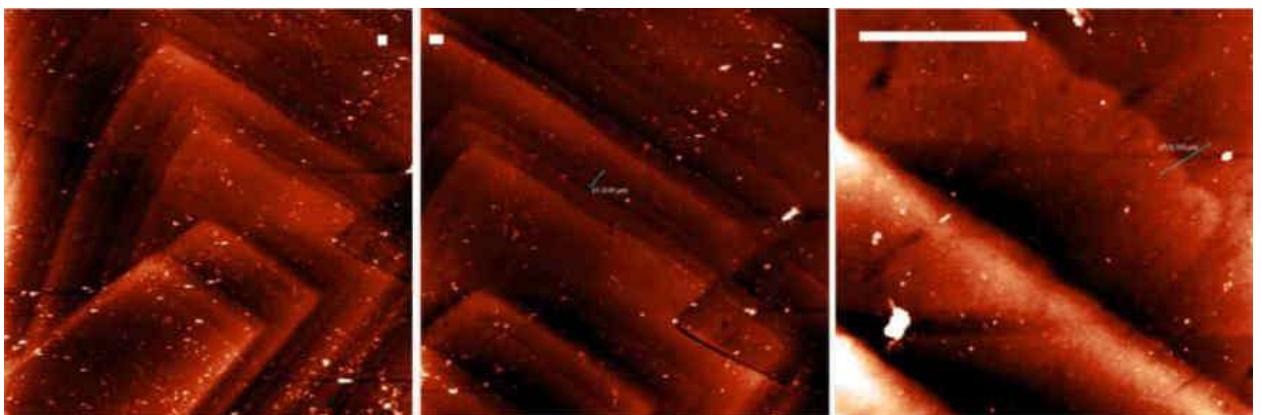


Figure 4.11 – Large (up to 50 nm) and thin (3 nm) steps on a growth hillock on the (011 $\bar{1}$) face of a quartz crystal (Zhelannoe Mt., Subpolar Urals). Scale bars 2 μm

The faces of positive rhombohedrons of small redeposited quartz crystals from gold-bearing quartz veins of the Sinilga occurrence are shown in Figure 4.12.

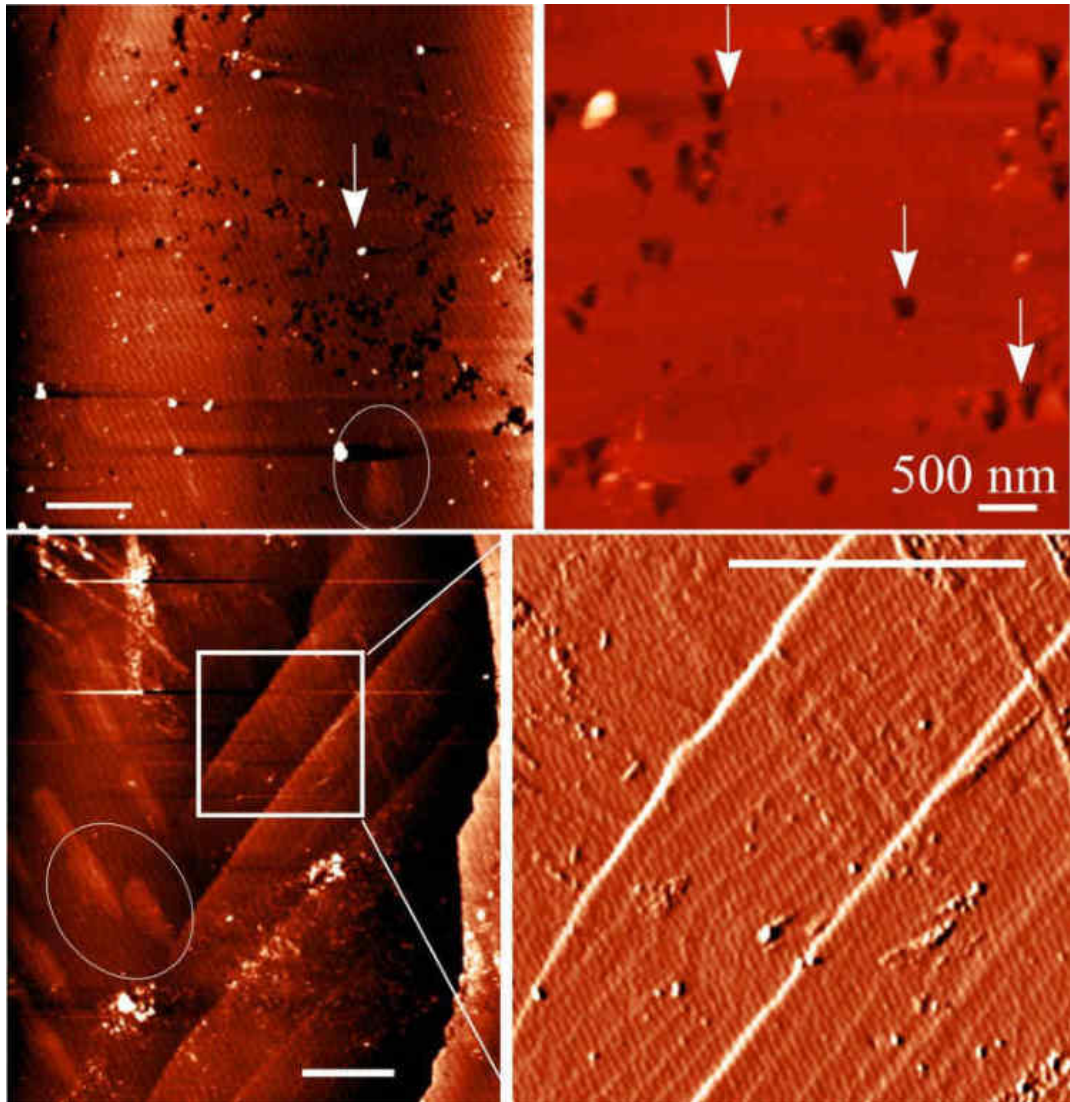


Figure 4.12 – Facets ($101\bar{1}$) of quartz crystals (Sinilga occurrence, subpolar Urals), top – triangular pits (indicated by arrows) with the sharp end facing the top of the crystal; bottom – large steps are folded into thin steps 1.2 nm high. Ovals show dislocation hillocks with the blunt end facing the top of the crystal. Scale bar in the 2nd image – 500 nm, in the others – 4 μm

This deposit is located in the central part of the subpolar Urals, in the upper reaches of the Pelingichi River. Quartz crystals were sent to N.V. Sokerina for study. On the positive rhombohedron of the Sinilga quartz, distinct dislocation growth spirals

(Figure 4.13) were discovered, composed of elementary steps (step height about 6 Å). These spiral hillocks have a width of up to 3.5 μm at the base and are almost triangular in shape and oriented upwards. Such hillocks were found due to the small size of the crystals and the fact that they encrusted the walls of the cavern, under which they were well preserved. Even a rough calculation of the number of oriented pits and screw hillocks, and hence screw dislocations, gives a value for their concentration in some areas of the order of 10^6 cm^{-2} . A high density of dislocations may indicate high rates, temperature differences and the influence of impurities during the formation of quartz of this generation.

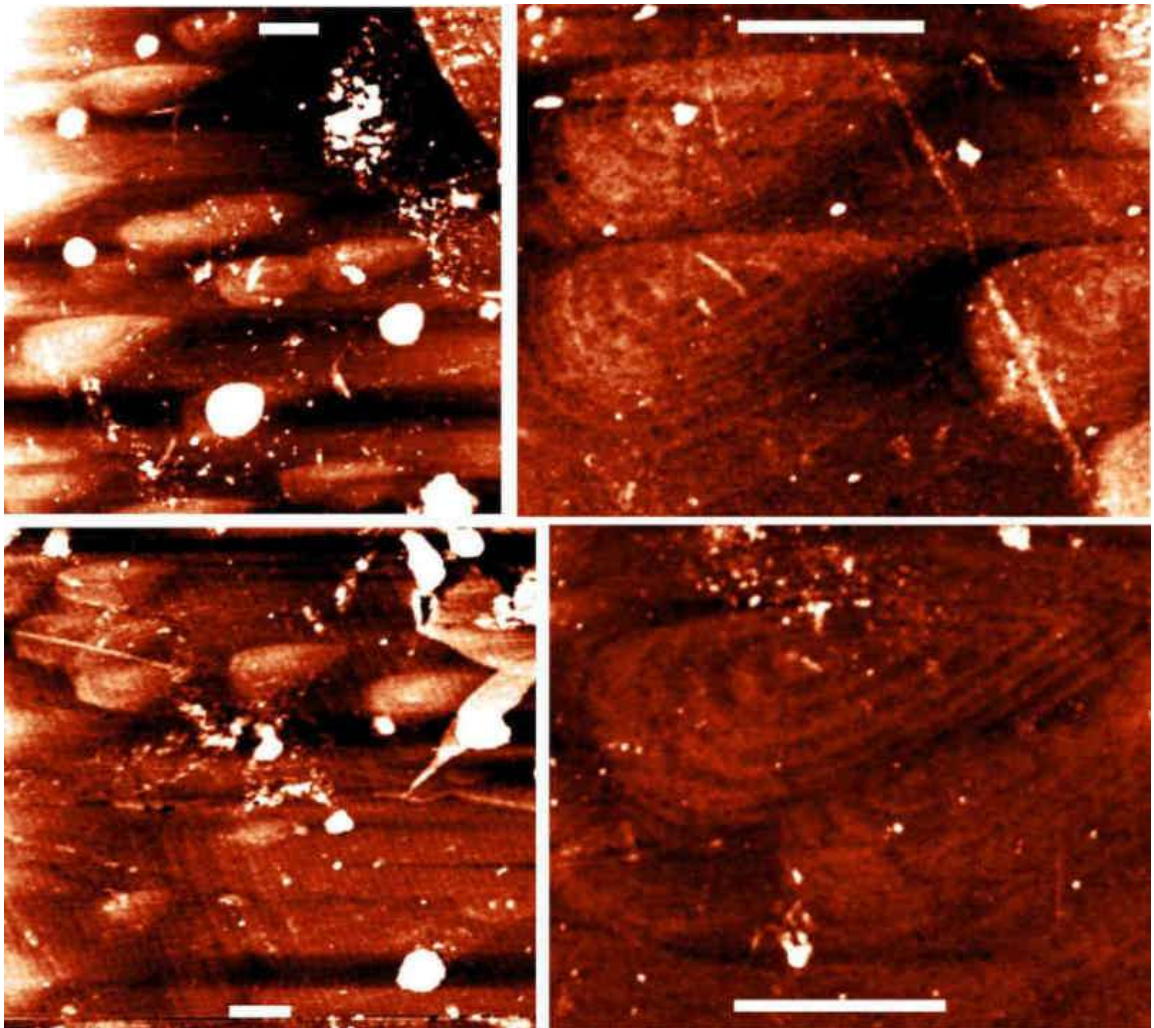


Figure 4.13 – Face $(101\bar{1})$ of a quartz crystal (Sinilga occurrence, subpolar Urals) with triangular dislocation hillocks, the base of which is oriented towards the apex of the crystal. The height of the steps on the spirals is 6 Å. Scale bars are 2 μm

Zircon

Zircon crystal from granitoids of the Mankhambo Massif (subpolar Urals) provided by O.V. Udoratina. Zircon ZrSiO_4 crystallises from melts in the tetragonal syngony. AFM has revealed triangular and hexagonal etch pits on defects (Figure 4.14) and elementary growth steps (Figure 4.15) on the (100) faces of zircon. The unit cell parameters of zircon are 6.604 and 5.979 Å, the height of the steps recorded on zircon is 5 Å, but several measurements carried out using AFM data showed an even smaller value (Figure 4.15).

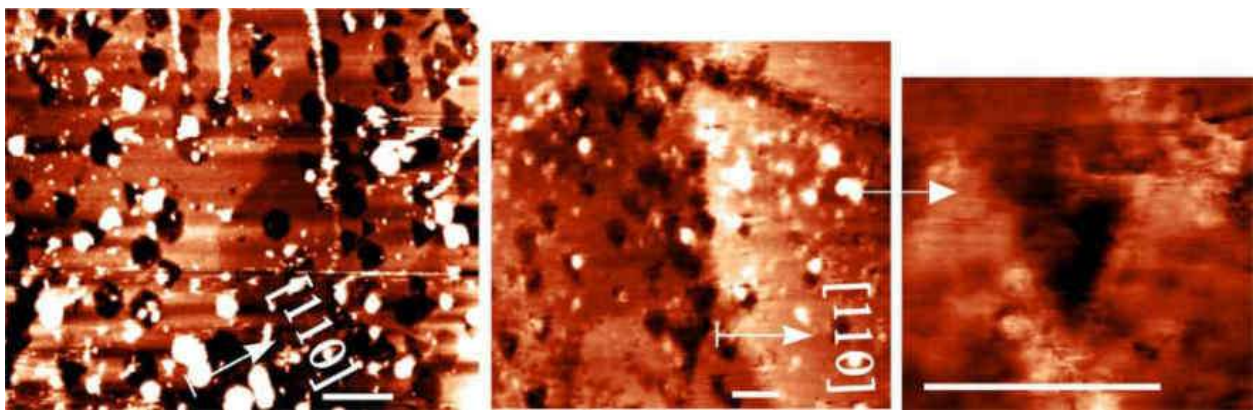


Figure 4.14 – Face (100) of phenacite crystal, triangular and hexagonal etch pits on defects. Scale bars 1 μm

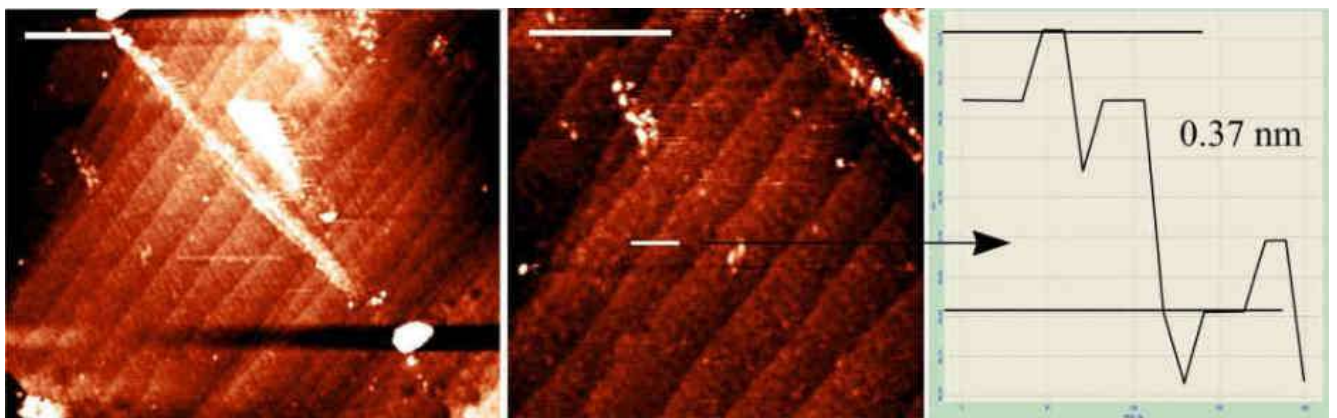


Figure 4.15 – Elementary growth steps on the (100) face of zircon (Manhambo Massif, Subpolar Urals). Scale bars 500 nm

Conclusion

At the micro- and nanoscale, the atomic force microscope is now an important source of data and a unique tool that allows direct (in-situ) observation of the solution processes occurring at the surface of a crystal during its growth and dissolution. This paper describes the results of over forty AFM experiments, ranging from 1.5 to 6 hours in duration, to study the processes of layer-by-layer growth and dissolution on the surface of a molecular crystal of dioxidine under ambient conditions. During the course of the study, the tasks set were completed, the relief and evolution of the crystalline surface in solution were studied at the micro- and nanoscale under different conditions, the processes accompanying the movement of monomolecular and macrolayers (steps) of growth on the surface, their interaction with each other and with obstacles when different mechanical factors act on the surface were followed. In AFM there are no standardised methods for modelling the influence of extraneous factors on crystal growth. For this work, methods were developed and experiments performed to determine the effect on surface processes of 1) short term mechanical action causing scratches; 2) large impurity particles; 3) cracks; 4) neighbouring crystals in intergrowths; 5) compression of the crystal face from different sides.

By processing the coordinates of thousands of points on the edge of each step, the average rates of the steps and their fluctuations were calculated. The processes of formation and evolution of growth mounds on screw dislocations of different types and scales were recorded step by step.

The mechanisms of dislocation germination (inheritance) through massive growth layers, the mechanisms of edge dislocations during face compression, with the directed effect of the needle on the surface during growth and dissolution, the mechanisms of screw dislocations at the boundary between crystals in intergrowths and during crack healing were analysed.

A three-step mechanism is proposed for the theoretical explanation of the process of formation of a screw dislocation on a solid particle, the essence of which lies in the relaxation of stresses around the impurity particle through the formation of dislocations even before its overgrowth. Thus, various types of special mechanical action on the surface of a crystal in solution are accompanied by the appearance of new point, linear and three-dimensional structural defects, which begin to significantly affect the morphology of the crystal surface on the micro- and nanoscale, as well as the dynamics and kinetics of growth and dissolution processes.

The transition from dissolution to growth through the saturation point on the steps of the same dislocation pit and on the monomolecular steps of the same dislocation hillock is traced; as a result of the observations, it is proved that growth and dissolution are irreversible, non-equivalent processes in both dynamics and kinetics at the nanoscale. It is found that for dioxidine the direction of movement and the pressure of the scanning needle do not influence the outlines of the monomolecular steps and the processes of their distribution over the surface. The instrumental influence consists mainly of laser heating and mixing of the solution layer above the surface as a result of the reciprocating motion of the needle. The analysis of this influence showed that the instrumental heating and mixing does not create new phenomena on the surface, but only weakens the phenomena recorded in the experiments, making the main conclusions of the work even more convincing.

An analysis of the influence of diffusion and convection in the AFM cell showed that in solutions of dioxidine, which has low viscosity, low solubility and no clusters, physical factors such as volume diffusion, evaporation and convection do not play a role in the registration of layer-by-layer growth and dissolution processes using AFM. The only flows that limit the recorded processes of layer-by-layer growth and dissolution are those created by gradients in the immediate vicinity of the surface and on the surface itself, i.e. according to the kinetic growth mechanism.

Ex-situ AFM studies of the growth surfaces of several natural crystals have revealed identical evidence of defect-stimulated growth and dissolution at the nano- and microscale for crystals of different genesis (from different crystal-forming

environments) - growth stages, including elementary ones, dislocation spiral mounds and dissolution pits on defects. Further AFM studies of the elementary processes of crystal growth and dissolution and the influence of various factors on them, in addition to the establishment of new theoretical mechanisms of nanoscale growth phenomena and the deciphering of the processes of natural crystal formation, can contribute to an effective solution of the problems facing the growth industry today.

Acknowledgments. The studies were carried out in the Laboratory of Experimental Mineralogy of the Institute of Geology named after Academician N.P. Yushkin of the Komi Scientific Centre of the Ural Branch of the Russian Academy of Sciences, using the equipment of the Geonauka Collective Use Centre. The author expresses his deep and comprehensive gratitude to the scientific advisor Academician Askhab Magomedovich Askhabov and the entire staff of the Institute, in particular Natalia Sergeevna Inkina, Ksenia Aleksandrovna Braun, Aleksey Aleksandrovich Kryazhev, engineers Stanislav Vladimirovich Rudnitsky, Ivan Vyacheslavovich Soloviev, Maxim Vladimirovich Yakimov and Andrey Valentinovich Ploskov, who provided technical assistance. The author is grateful to engineer Viktor Aleksandrovich Radaev for carrying out the AFM and SEM studies and for training in the use of an atomic force microscope. The author is grateful to Dmitry Vyacheslavovich Kuzmin for his help in studying the solutions. The author thanks Olesya Igorevna Forsyuk for fruitful cooperation.

Great appreciation is expressed to the co-authors and all those who provided mineral crystals for study: Ph. D. (Geology and Mineralogy) Kryuchkova Lyudmila Yuryevna, D.Sc. (Geology and Mineralogy) Rakin Vladimir Ivanovich, D.Sc. (Geology and Mineralogy) Silaev Valery Ivanovich, Ph.D. (Geology and Mineralogy) Udoratina Oksana Vladimirovna, Ph.D. (Geology and Mineralogy) Nikolaev Anatoly Germanovich, Ph.D. (Geology and Mineralogy) Sokerina Natalia Vladimirovna, Ph.D. (Geology and Mineralogy) Sokerin Mikhail Yuryevich, Ph.D. (Geology and Mineralogy) Glukhov Yuri Valentinovich. Special thanks for constructive comments and remarks are due to colleagues from the Crystallography Department and the

Resource Centre of St. Petersburg State University who took part in the discussion of the work.

The author is grateful to his mother Tatyana Pavlovna Markova and his children Anastasia and Denis for their support. The author honours and will always remember the contributions of his father Nikolay Prokopyevich Markov, Academician Nikolay Pavlovich Yushkin, D.Sc. (Geology and Mineralogy) Arkady Eduardovich Glikin and Ph.D. (Geology and Mineralogy) Evgeny Borisovich Treivus.

This work was carried out in accordance with the research topics of the Institute of Geology of the Komi Scientific Center of the Ural Branch of the Russian Academy of Sciences since 2008 to 2024 years. In this period the author was an executor of grants from the Russian Foundation for Basic Research (08–05–00346–a, 11–05–00432–a, 14–05–00592a, 19–05–00460), Fundamental Research Programs of the Presidium and the Department of Earth Sciences of the Russian Academy of Sciences No. 12–U–5–1026, 12–T–5–1022, 12–P–5–1011, 12–P–5–1027, 15–18–5–45, 15–18–5–46, 18–5–5–44, as well as Grants of the President of the Russian Federation for leading scientific schools of the Russian Federation: NSh–3266.2008.5, NSh–7198.2010.5, NSh–1310.2012.5, NSh–4795.2014.5.

References

1. **Aleksandrov, V.D.** Analysis of melting and crystallization processes of crystal hydrates using melting thermograms / V.D. Aleksandrov, Sh.K. Amerkhanova, V.A. Postnikov [et al.] // Interuniversity collection of scientific papers “Physicochemical aspects of studying clusters, nanostructures and nanomaterials” : – Tver : Tver State University. – 2015. – Issue. 7. – P. 5–15. [in Russian].
2. **Andreev, V.K.** Thermocapillary instability / V.K. Andreev, V.E. Zakhvataev, E.A. Ryabitsky – Novosibirsk : Nauka. – 2000. –126 p. [in Russian]
3. **Bletskan, D. I.** Mechanism of growth of layered single crystals of AIVBVI AIVB2VI from the gas phase / D. I. Bletskan // Ukrainian Physical Journal. – 1979. – Vol. 24, No. 9. – P. 1321–1324. [in Russian].
4. **Gvozdev, N. V.** Atomic force microscopy of crystals of lysozyme of orthorhombic modification / N. V. Gvozdev // dissertation ... candidate of physical and mathematical sciences: 01.04.07. – Moscow, – 2001. – 87 p. [in Russian].
5. **Glikin, A. E.** Micromosaic distribution of components and features of the genesis of mixed crystals in solutions / A. E. Glikin, L. Yu. Kryuchkova, Yu. A. Plotkina // Reports of the Academy of Sciences. – 2010. – Vol. 433, No. 1. – P. 85. [in Russian].
6. **Lemmlein, G. G.** Experimental production of vicinals on a growing crystal / G. G. Lemmlein // Reports of the USSR Academy of Sciences. – 1934. – Vol. 2. – P. 554.
7. **Lemmlein, G. G.** Morphology and genesis of crystals. / G. G. Lemmlein – Moscow: Nauka – 1973. –327 p. [in Russian].
8. **Lemmlein, G. G.** Formation of screw dislocations during crystal growth / G. G. Lemmlein, E. D. Dukova // Crystallography. – 1956. –Vol. 1, No. 3. – P. 352–355. [in Russian].
9. **Maillard, J.–P.** Application of Fourier spectroscopy in the near infrared region to astronomical problems / Maillard J.–P. –M.: Mir. – 1972. – P. 128–200. [in Russian].
10. **Mashina, E.V.** Mechanism of cholesterol monohydrate crystal growth in choleliths / E.V. Mashina, N.N. Piskunova, A.M. Askhabov [et al.] // Zapiski

Rossiiskogo Mineralogicheskogo Obshchestva (Proceedings of the Russian Mineralogical Society. – 2015. – No. 5. – P. 112–119. [in Russian].

11. **Petrova, E.V.** Growth and dissolution of calcium oxalate monohydrate crystals / E.V. Petrova // Dis. ... Cand. of Phys. and Mathematics : 01.04.07 : – Moscow. – 2004. – 120 p. – RSL OD, 61 : 05–1/142. [in Russian].

12. **Rashkovich, L. N.** Fluctuations in the velocity of step motion and the formation of a dislocation spiral on the (101) face of the monoclinic modification of lysozyme / L. N. Rashkovich, N. V. Gvozdev, M. I. Silnikova [et al.] // Crystallography. – 2002. – Vol. 47, No. 5. – P. 925–932. [in Russian].

13. **Rashkovich, L. N.** Fluctuation of steps on the faces of potassium dihydrogen phosphate crystals in solution / L. N. Rashkovich, O. A. Shustin, T. G. Chernevich // Solid State Physics. – Moscow – 2000. – Vol. 42, No. 10. – P. 1869–1873. [in Russian]

14. **Sangwal, K.** Crystal etching. Theory, experiment, application / K. Sangwal // – M. : Mir. – 1990. – P. 179. [in Russian].

15. **Sebisi, T.** Convective heat transfer. Physical principles and computational methods / T. Sebisi, P. Bradshaw – Transl. from English. – Moscow : Mir. – 1987. – 589 p. [in Russian].

16. **Silnikova, M. I.** Atomic force microscopy of rhombic and monoclinic modification of lysozyme / M. Silnikova I., N. V. Gvozdev // International conference named after G. G. Lemlein “Crystallography and mineralogenesis” – St. Petersburg. – 2001. – P. 360. [in Russian].

17. **Sokerina, N. V.** Conditions of quartz crystal growth at the Zhelannoye deposit, Subpolar Urals (based on data from a study of fluid and solid inclusions) / N. V. Sokerina, N. N. Piskunova // Geochemistry. – 2011. – No. 2. – P. 192–201. [in Russian].

18. **Sokerina, N. V.** Conditions of gold mineralization formation at the Sinilga occurrence, Subpolar Urals (based on data from a study of fluid inclusions) / Sokerina N. V., Shanina S. N., Piskunova N. N. [et al.] // Zapiski Rossiiskogo Mineralogicheskogo Obshchestva (Proceedings of the Russian Mineralogical Society. – 2013. No. 6. – P. 89-105. [in Russian].

19. **Smolsky, I. L.** Effect of the Morphology of Growing Facets on the Orientation of Growth Dislocations in KDP Crystals / I. L. Smolsky, E. B. Rudneva // Crystallography. – 1993. – Vol. 38, No. 4. – P. 248–256. [in Russian].

20. **Chernov, A. A.** Modern Crystallography. Volume 3 / A. A. Chernov, E. I. Givargizov, H. S. Bagdasarov [et al.] – Moscow: Nauka. – 1980. – 407 p. [in Russian]

21. **Piskunova, N. N.** Study of Crystal Growth and Dissolution Processes Using Atomic Force Microscopy Methods. / N. N. Piskunova – Yekaterinburg: Ural Branch of the Russian Academy of Sciences. – 2007. – 135 p. [in Russian].

22. **Piskunova, N. N.** Crystals from medicinal solutions as model objects for studying elementary processes of growth and dissolution / N. N. Piskunova // Proceedings of the International Mineralogical Seminar "Mineralogical Perspectives". – Syktyvkar. – 2011. – P. 132–134. [in Russian].

23. **Piskunova, N. N.** Iron oxide nanoparticles in thin films on the surface of natural quartz crystals / N. N. Piskunova // DAN. Earth Sciences. – 2020. – Vol. 492, No. 2. – P. 31–34. [in Russian].

24. **Piskunova, N. N.** Direct observation of growth processes on a crystalline surface initiated by impurity capture / N. N. Piskunova // Zapiski Rossiiskogo Mineralogicheskogo Obshchestva (Proceedings of the Russian Mineralogical Society. – 2023 a. – Vol. 152, No. 3. – P. 82–97. [in Russian].

25. **Piskunova, N. N.** Effect of mechanical deformations on crystal growth (according to atomic force microscopy data) / N. N. Piskunova, A. M. Askhabov // DAN. – 2017. – Vol. 474. No. 2. – P. 164-167. [in Russian].

26. **Piskunova, N. N.** Potential of atomic force microscopy in solving problems of studying crystals and their growth processes / N. N. Piskunova // Izvestia of the Komi Science Center. – 2018 c. – No. 4. – P. 39-45. [in Russian].

27. **Piskunova, N. N.** Study of self-organization processes on a damaged crystal surface using atomic force microscopy / N. N. Piskunova // Zapiski Rossiiskogo Mineralogicheskogo Obshchestva (Proceedings of the Russian Mineralogical Society. – 2022 a. – Part CLI. No. 5. – P. 112–127. [in Russian].

28.**Prigogine, I.** Modern thermodynamics. From heat engines to dissipative structures / I. Prigogine, D. Kondepudi – M.: Mir. – 2002. – 461 p. – ISBN 5–03–003538–9. [in Russian].

29.**Treyvus, E. B.** Pyrite metacrystals from the subpolar Urals with signs of plastic deformation / E. B. Treyvus, N. N. Piskunova, V. I. Silaev // Proceedings of the international mineralogical seminar "Mineralogical prospects". – Syktyvkar. – 2011a. – P. 150–153. [in Russian].

30.**Treyvus, E. B.** Sculpture of cubic faces of pyrite crystals from Spain and a possible cause of their occurrence / E. B. Treyvus, N. N. Piskunova, Yu. S. Simakova // Bulletin of the Komi Scientific Centre of the Ural Branch of the Russian Academy of Sciences. – 2011b. – No. 8. – P. 60–64. [in Russian].

31.**Chernov, A. A.** X–ray topographic study of the ADP crystal growth process / A. A. Chernov, I. L. Smolsky, V. F. Parvov // Crystallography. – 1980. – Volume 25, Number 4. – P. 821–828. [in Russian].

32.**Chernov, A. A.** Crystal growth processes from aqueous solutions (KDP group) / A. A. Chernov, L. N. Rashkovich, I. L. Smolsky [et al.] // In the book. "Crystal growth. Volume 15" – Moscow: Science. – 1986. –P. 43–88. [in Russian].

33.**Yaminsky, I.** Protein crystals / I. Yaminsky // Science and Life. – 2004. – No. 1. – P. 58–60. [in Russian]

34.**Abbona, F.** Morphology of crystals grown from solutions / F. Abbona, D. Aquilano // In Dhanaraj, Byrappa, Prasad, Dudley (Eds) Handbook of Crystal Growth – Heidelberg : Springer. – 2010. V. 1084 (3). – P. 70.

35.**Amit, S.** Interfacial diffusion aided deformation during nanoindentation / S. Amit, E. Weinan // AIP Advances. – 2016. – №6. –P. 075002 (1–8).

36.**Araki, Y.** Atomic-resolution imaging of aragonite (001) surface in water by frequency modulation atomic force microscopy / Y. Araki, K. Tsukamoto, N. Oyabu [et al.] // Japanese Journal of Applied Physics. – 2012. – V. 51. – 08KB09.

37. **Astier, J. P.** α - amylase crystal growth investigated by in-situ atomic force microscopy / J. P. Astier, D. Bokern, L. Lapena [et al.] // J. of Crystal Growth. – 2001. – V. 226. – P. 294–302.
38. **Aswal, D. K.** In-situ observation of melting/dissolution, nucleation and growth of $\text{NdBa}_2\text{Cu}_3\text{O}_x$ by high temperature optical microscopy / D. K. Aswal, M. Shinmura, Y. Hayakawa [et al.] // J. of Crystal Growth. – 1998. – V.193. – P. 61–70.
39. **Bai, J.** Study of the defect elimination mechanisms in aspect ratio trapping Ge growth / J. Bai, J.-S. Park, Z. Cheng [et al.] // Appl. Phys. Lett. – 2007. –V. 90, №10. – P. 101902 (3).
40. **Bartelt, M.** Growth and dissolution morphology and surface dynamics of molecular crystals: experiments and modeling / M. Bartelt, C. Orme, A. Vilacampa [et al.] // G.G. Lemlein`s International Conference «Crystallography and Mineralogenesis» – S.-Pb. – 2001. – P. 40–41.
41. **Belabbas, I.** Atomic structure and energy of threading screw dislocations in wurtzite GaN / I. Belabbas, M. A. Belkhir, Y. H. Lee [et al.] // Phys. Stat. Sol. – 2005. – V. 2, №7. – P. 2492–2495.
42. **Bisker-Leib, V.** Modeling crystal shape of polar organic materials: applications to amino acids / V. Bisker-Leib, M. F. Doherty // Cryst. Growth Des. – 2003. – V.3, №2. – P. 221–237.
43. **Bozhilov, K. N.** Time-resolved dissolution elucidates the mechanism of zeolite MFI crystallization / K. N. Bozhilov, T. T. Le, Z. Qin [et al.] // Science Advances. – 2021. – V. 7, №25. – eabg0454.
44. **Bose, S.** Dissolution Kinetics of sulfate minerals: linking environmental significance of mineral water interface reactions to the retention of aqueous CrO_4^{2-} in natural waters / S. Bose – PhD thesis. Environmental Sciences PhD : Wright State University.– 2008. – https://corescholar.libraries.wright.edu/etd_all/230M.Sc.
45. **Bredikhin V.I.** Mass transfer processes in KDP crystal growth from solutions / V. I. Bredikhin, V. P. Ershov, V. V. Korolikhin [et al.] // J. of Crystal Growth. – 1987. – V. 84. №3. –P. 509–514.

46. **Capellades, G.** Impurity incorporation in solution crystallization: diagnosis, prevention, and control / G. Capellades, J. O. Bonsu, A. S. Myerson // *Cryst. Eng. Comm.* – 2022. – V.24. – P. 1989–2001.

47. **Chakrabarti, R.** Dual mode of action of organic crystal growth inhibitors / R. Chakrabarti, P. G. Vekilov // *Crystal Growth & Design.* – 2021. – V. 21, №12. – P. 7053–7064.

48. **Chakrabarti, R.** The elementary reactions for incorporation into crystals / R. Chakrabarti, L., V. G. Verma, Hadjiev [et al.] // *Proceedings of the National Academy of Sciences.* – 2024. – V. 121, №7. – e2320201121.

49. **Chaliha, D.** In-situ atomic force microscopy (AFM) investigation of kaolinite dissolution in highly caustic environments / D. Chaliha, J. F. Gomes, P. Smith [et al.] // *CrystEngComm.* – 2022. – V. 24. – P. 2042–2049.

50. **Chang, Y.-R.** Atomic Step induced screw dislocation driven spiral growth of SnS / Y.-R. Chang, N. Higashitarumizu, H. Kawamoto [et al.] // *Chem. Mater.* – 2021. – V. 33. – P. 186–194.

51. **Chasnitsky, M.** Atomic force microscopy imaging of ice crystal surfaces formed in aqueous solutions containing ice-binding proteins / M. Chasnitsky, S. R. Cohen, Y. Rudich [et al.] // *Journal of Crystal Growth.* – 2023. – V. 601. – 126961.

52. **Chassagne, M.** Atomic-scale simulation of screw dislocation/coherent twin boundary interaction in Al, Au, Cu and Ni / M. Chassagne, M. Legros, D. Rodney // *Acta Materialia.* – 2011. – V. 59, №4. – P.1456-1463.

53. **Chernov, A. A.** Steps in solution growth: dynamics of kinks, bunching and turbulence / A. A. Chernov , L. N. Rashkovich , P. G. Vekilov // *Journal of Crystal Growth.* – 2005. – V. 275, №(1-2). – P. 1–18.

54. **Chernov, A. A.** Fluctuations and Gibbs-Thomson law – the simple Physics / A. A Chernov, J. J. De Yoreo, L. N. Rashkovich // *J. Optoelectr. Adv. Mat.* – 2007. – V.9. – P. 1191 – 1197.

55. **Chernov, A. A.** *Modern Crystallography III: Crystal Growth* (Springer Series in Solid-State Sciences, 36) / A. A. Chernov With Contribution of E. J. Givargizov, K. S. Bagdasarov, V. A. Kuznetsov [et al.] // Softcover reprint of the original 1st ed. – 1984 (

- <https://link.springer.com/book/10.1007/978-3-642-81835-6>). Berlin : Springer ; – 2011. –ISBN-13: 978-3642818370; – ISBN-10: 3642818374. – 537 p.

56. **Choudhary, M. K.** In-situ imaging of two-dimensional surface growth reveals the prevalence and role of defects in zeolite crystallization / M. K. Choudhary, R. Jain, J. D. Rimer // Proceedings of the National Academy of Sciences. – 2020. –V. 117, №4. – P. 28632–28639.

57. **Chi, J.** Face-specific occlusion of lipid vesicles within calcium oxalate monohydrate / J. Chi, W. Zhang, C. V. Putnis [et al.] // Crystal Growth & Design. – 2021. – V. 21. – P. 2398–2404.

58. **Chi, G.** Common problems and pitfalls in fluid inclusion study: a review and discussion / G. Chi, L.W. Diamond, H. Lu [et al.] // Minerals. – 2021. –V. 11, №7.

59. **Chirawa, J.-I.** Technique for the video display of X – RAY topographic images and its application to the study of crystal growth / J.-I. Chirawa // J. of Crystal Growth. – 1974. – №(24–25). – P. 61–68.

60. **Choudhary, M. K.** In-situ imaging of two-dimensional surface growth reveals the prevalence and role of defects in zeolite crystallization / M. K. Choudhary, R. Jain, J. D. Rimer // Proceedings of the National Academy of Sciences USA. – 2020. – 202011806.

61. **Cho, K. R.** mechanistic pathways for the molecular step growth of calcium oxalate monohydrate crystal revealed by in-situ liquid-phase atomic force microscopy / K. R. Cho, J.-H. Lee, H.-S. Seo [et al.] // ACS Appl. Mater. Interfaces. – 2021. – V. 13, №31. – P. 37873–37882.

62. **Cho, K. R.** In-situ liquid-phase afm observation of the molecular step spiral generation on the (1–1–01) surface of calcium oxalate monohydrate crystal / K. R. Cho // Crystals. – 2023. – V. 13, №6. – P. 889.

63. **Clark, J.N.** Three-dimensional imaging of dislocation propagation during crystal growth and dissolution. / J.N. Clark, J. Ihli, A.S. Schenk [et al.] // Nat. Mater. – 2015. – V. 14. – P. 780–784.

64. **Corrias, M.** Automated real-space lattice extraction for atomic force microscopy images / M. Corrias, L. Papa, I. Sokolović [et al.] // *Machine Learning Science and Technology*. – 2023. – V. 4, №1. – 015015.

65. **Darkins, R.** Critical step length as an indicator of surface supersaturation during crystal growth from solution / R. Darkins, I. J. McPherson, I. J. Ford [et al.] // *Crystal Growth & Design*. – 2022. – V. 22. – P. 982–986.

66. **De Yoreo, J.J.** Limits on surface vicinality and growth rate due to hollow dislocation cores on KDP {101} / J.J. De Yoreo, T.A. Land, J.D. Lee // *Phys. Rev. Lett.* – 1997a. – V.78, №23. – P. 4462–4465.

67. **De Yoreo, J. J.** The effect of dislocation cores on growth hillock vicinality and normal growth rates of KDP {1 0 1} surfaces / J. J. De Yoreo , T. A. Land, L. N. Rashkovich [et al.] // *Journal of Crystal Growth*. – 1997b. – V. 182, №(3-4). – P. 442-460.

68. **De Yoreo, J. J.** Using atomic force microscopy to investigate solution crystal growth / J. J. De Yoreo, C. A. Orme, T. A. Land // *Advances in Crystal Growth Research*. – 2001. – P. 361–380.

69. **Dove, P. M.** Compatible real-time rates of mineral dissolution by Atomic Force Microscopy (AFM) / P. M. Dove, F. M. Platt // *Chemical Geology*. – 1996. – V.127, №4(31). – P. 331–338.

70. **Dove, P. M.** Mechanisms of classical crystal growth theory explain quartz and silicate dissolution behavior / P. M. Dove, N. Han, J. J. De Yoreo // *PNAS*. – 2005. – V.102, №43. – P. 15357–15362.

71. **Dove, P.** Kinetics of mineral dissolution and growth as reciprocal microscopic surface processes across chemical driving Force / P. Dove, N. Han // *Perspectives on Inorganic, Organic and Biological Crystal Growth : From Fundamentals to Applications Directions : based on the lectures presented at the International summer school on crystal growth, Park City, Utah. – 2007 / Ed. by Skowronski M., De Yoreo J.J., Wang C.A. – Melville; N.Y. : Am. Inst. Phys. Conf. Ser. – 2007. №916. – P. 215–234.*

72. **Dong, S.** An atomic force microscopy study of calcite dissolution in seawater / S. Dong, W. M. Berelson, J. F Adkins [et al.] // *Geochimica et Cosmochimica Acta*. – 2020. – V.47. – 149.

73. **Dvoryantseva, G. G.** Connection between the Structure and the Antibacterial activity of the n-Oxides of Quinoxalines. Molecular Structure of Dioxidine and Quinoxidine / G. G. Dvoryantseva, S. V. Lindeman, M. S. Aiexsanyan [et al.] // *Pharm Chem J*. – 1990. – V. 24, №9. – P. 672–677.

74. **Dudley, M.** The Mechanism of micropipe nucleation at inclusions in silicon carbide / Dudley M., Huang X. R., Huang W. [et al.] // *Appl. Phys. Lett.* – 1999. – V. 75, №6. – P. 784–786.

75. **Elts, E.** In Silico prediction of growth and dissolution rates for organic molecular crystals: a multiscale approach / E. Elts, M. Greiner, H. Briesen // *Crystals*. – 2017. – V. 7, №10. – P. 288–311.

76. **Elhadj, S.** Solvent-mediated repair and patterning of surfaces by AFM / S. Elhadj, A. A. Chernov, J. De Yoreo // *Nanotechnol.* – 2008. – V. 19. – 105304 (1–9).

77. **Forty, A.I.** Direct observations of dislocations in crystals / A.I. Forty // *Advances Phys.* – 1954. – V. 3. – P. 1–60.

78. **Frank, F. C.** The kinematic theory of crystal growth and dissolution processes / F. C. Frank // *In Growth and Perfection of Crystals*, R. H. Doremus, B. W. Roberts, and D. Turnbull (Eds.). – New York : Wiley. – 1958. – P. 411–419.

79. **Frank, F. C.** Multiplication processes for slow moving dislocations / F. C. Frank, W. T. Read // *Phys. Rev.* – 1950. – V. 79, №4. – P. 722–723.

80. **Friddle, R. W.** Subnanometer atomic force microscopy of peptide-mineral interactions links clustering and competition to acceleration and catastrophe / R. W. Friddle, M. L. Weaver , S. R. Qiu [et al.] // *Proceedings of the National Academy of Sciences*. – 2010. – V. 107, №1. – P. 11–15.

81. **Geng, X.** Alginate as a green inhibitor of barite nucleation and crystal growth / X. Geng, R. D. Sosa, Mi. A. Reynolds [et al.] // *Mol. Syst. Des. Eng.* – 2021. – V.6. – 508.

82. **Geng, Y.L.** Atomic force microscopy studies on growth mechanisms of LAP crystals grown in solution containing excessive amount of l-arginine / Y. L. Geng, D. Xu, D.L. Sun [et al.] // *Materials Chemistry and Physics*. – 2005. – V. 90, №1. – P. 53–56.
83. **Gershonowitz, J. B.** Hillock interactions during calcite growth observed using in-situ atomic force microscopy / J. B. Gershonowitz // Thesis Presented to the Faculty of the Graduate School of Cornell University. – 2019.
84. **Giocondi, J.** An atomic force microscopy study of super-dislocation micropipe complexes on the 6H – SiC (0001) growth surface / J. Giocondi, G. S. Rohrer, M. Skowronski [et al.] // *J. of Crystal Growth*. – 1997. – V. 181, №4. – P. 351–362.
85. **Glikin, A. E.** On the genetic nature of isomorphism: Mechanism of component selection during crystal growth / A. E. Glikin // *Geol. Ore Deposits*. – 2007. – V. 49. – P. 806–810.
86. **Gurena, M. G.** Direct imaging of coupled dissolution-precipitation and growth processes on calcite exposed to chromium-rich fluids. / M. G. Gurena, C. V. Putnis, G. Montes-Hernandez [et al.] // *Chemical Geology*. – 2020. – V. 552. – 119770.
87. **Hadjittofis, E.** Influences of crystal anisotropy in pharmaceutical process development / E. Hadjittofis, M. A. Isbell, V. Karde [et al.] // *Pharm. Res.* – 2018. – V.35, №5. – P. 100–122.
88. **Heiman, R. B.** Auflösung von kristallen. Theorie und technische anwendung / R. B. Heiman – Springer-Verlag : Wien, New York, USA. – 1975. – P.45–65.
89. **Hendley, C.** Mechanistic insights into diblock copolymer nanoparticle – crystal interactions revealed via in-situ atomic force microscopy/ C. Hendley, T. Fielding, A. Lee [et al.] // *J. Am. Chem. Soc.* – 2018. – V. 140, №25. – P. 7936–7945.
90. **Hill, A. R.** CrystalGrower: a generic computer program for Monte Carlo modeling of crystal growth / A. R. Hill, P. Cubillas, J. T. Gebbie-Rayet [et al.] // *Chemical Science*. – 2021. – V. 12, №3. – P. 1126-1146.
91. **Hillner, P. E.** Atomic force microscope: a new tool for imaging crystal growth processes / P. E. Hillner, S. Manne, P. K. Hansma [et al.] // *Faraday Discuss.* – 1993. – V. 95.– P. 191–197.

92. **Jiang, W.** Switchable chiral selection of aspartic acids by dynamic states of brushite / W. Jiang, H. Pan, Z. Zhang [et al.] // Journal of the American Chemical Society. – 2017. – jacs.7b03116–.
93. **Johnson, E.** One-dimensional random walk of nanosized liquid Pb inclusions on dislocations in Al / E. Johnson, M. T. Levinsen, S. Steenstrup [et al.] // Phil. Mag. – 2004. – V. 84, №(25-26). – P. 2663–2673.
94. **Johnston, W. G.** Dislocation etch pits in nonmetallic crystals" / W. G. Johnston // In Progress in Ceramic Science. J. E. Burke (Ed.). – New York : Pergamon Press, Inc. – 1962. – 11. – 245 p.
95. **Jupille, J.** Analysis of mineral surfaces by atomic force microscopy / J. Jupille // Reviews in Mineralogy and Geochemistry. – 2014. – M. 78, №1. – P. 331–369.
96. **Kamiya, N.** Effect of trace lanthanum ion on dissolution and crystal growth of calcium carbonate / N. Kamiya, H. Kagia, F. Tsunomoria [et al.] // J. Cryst. Growth. – 2004. – V. 267. – P. 635–645.
97. **Karino, W.** Atomic force microscopic studies of stabilization of NaCl (1 1 3), (1 1 2) and (1 1 0) surfaces in ethanol, CdCl₂/ethanol and HgCl₂/ethanol / W. Karino, H. Koda, K. Nakamura [et al.] // Journal of Crystal Growth. – 2008. – V. 310. – P. 676–681.
98. **Klapper, H.** X-ray topography of organic crystals / H. Klapper // In Crystals : Growth, Properties and Applications. Karl (Ed.). – Berlin : Springer. – 1991. – 13. – P. 109–162.
99. **Klapper, H.** Generation and propagation of defects during crystal growth / H. Klapper // In: Handbook of Crystal Growth. Dhanaraj, Byrappa, Prasad, Dudley (Eds.). – Heidelberg : Springer. – 2010. – 1084(4). – P. 93–132.
100. **Klapper, H.** Defect generation and interaction during crystal growth / H. Klapper, P. Rudolph // In: Handbook of Crystal Growth. Rudolph (Ed.). – Sheffield : Springer. – 2015. – P. 1093–1141.
101. **Klasa, J.** An atomic force microscopy study of the dissolution of calcite in the presence of phosphate ions / J. Klasa, E. Ruiz-Agudo, L. J. Wang [et al.] // Geochimica et Cosmochimica Acta. – 2013. – V.117. – P. 115–128.

102. **Klepikov, I. V.** Growth nature of negative relief forms of diamonds from ural placer deposits / I. V. Klepikov, E. A. Vasilev, A. V. Antonov // *Crystallography Reports*. – 2020. – V. 65, №2. – P. 300–306.
103. **Konnert, J. H.** Observation of growth steps, spiral dislocations and molecular packing on the surface of lysozyme crystals with the atomic force microscope / J. H. Konnert, P. d'Antonio, K. B. Ward // *Acta Cryst.* – 1994. – DS0. – P. 603–613.
104. **Kryazhev, A. A.** Investigation of substance aggregation effect on variation of NO₃ anions and OH-Groups Vibrations in aqueous solution by raman spectroscopy / A. A. Kryazhev // Chapter in Book «Springer Proceedings in Earth and Environmental Sciences. XIII General Meeting of the Russian Mineralogical Society and the Fedorov Session» Y. Marin (Ed.) : SPEES. – 2023. – P. 646–653.
105. **Kustov, A. V.** Thermodynamics of solution and partition of dioxidine n water and the water/1-octanol biphasic system. / A. V. Kustov, N. L. Smirnova // *Journal of Molecular Liquids*. – 2017. – V.248. – P. 842–846.
106. **Kuwahara, Y.** In-situ AFM study of crystal growth on a barite (001) surface in BaSO₄ solutions at 30 °C / Y. Kuwahara, W. Liu, M. Makio [et al.] // *Minerals*. – 2016. – V. 6, №4. – P. 117.
107. **Kuznetsov, Y. G.** AFM studies of the nucleation and growth mechanisms of macromolecular crystals / Y. G. Kuznetsov, A. J. Malkin, A. McPherson // *J. of Crystal Growth*. – 1999. – V. 196. – P. 489–502.
108. **Kuwahara, Y.** AFM study on surface microtopography, morphology and crystal growth of hydrothermal illite in izumiyama pottery stone from Arita, Saga Prefecture, Japan / Y. Kuwahara, S. Uehara // *The Open Mineralogy Journal*. – 2008. – V. 2, №1. – P. 34–47.
109. **Land, T. A.** Recovery of surfaces from impurity poisoning during crystal growth / T. A. Land, T. L. Martin, S. Potapenko [et al.] // *Nature*. – 1999. – V. 399, №3. – P. 442–445.
110. **Land, T. A.** The evolution of growth modes and activity of growth sources on canavalin investigated by in-situ atomic force microscopy / T. A. Land, J. J. De Yoreo // *Journal of Crystal Growth*. – 2000. – V. 208. – P. 623–637.

111. **Lasaga, A. C.** Variation of crystal dissolution rate based on a dissolution stepwave model / A. C. Lasaga, A. Luttge // *Science*. – 2001. – V. 291, №5512. – P. 2400–2404.
112. **Lee-Thorp, J. P.** Effect of Step anisotropy on crystal growth inhibition by immobile impurity stoppers / J. P. Lee-Thorp, A. G. Shtukenberg, R. V. Kohn // *Cryst. Growth Des.* – 2017. – V.17, №10. – P. 5474–5487.
113. **Li, N.** Quantification of dislocation nucleation stress in TiN through high-resolution in-situ indentation experiments and first principles calculations / N. Li, S. K. Yadav, X.-Y. Liu [et al.] // *Sci. Rep.* – 2015. – V. 5. – P. 15813 (1–8).
114. **Liu, Q.** Progress in the applications of atomic force microscope (AFM) for mineralogical research / Q. Liu, Y. Fu, Z. Qin [et al.] // *Micron*. – 2023. – V. 170. – P. 103460.
115. **Lovette, M. A.** Crystal shape modification through cycles of dissolution and growth: Attainable regions and experimental validation / M. A. Lovette, M. Muratore, M. F. Doherty // *American Institute of Chemical Engineers Journal*. – 2012. – V. 58, №5. – P. 1465–1474.
116. **Lucre`ce, H.** The influence of impurities and additives on crystallization / H. Lucre`ce, A. Nicoud, S. Myerson // *In Handbook of Industrial Crystallization*. Myerson, Erdemir, Lee (Eds.) – 2019. – 4. – P. 115–135.
117. **Luttge, A.** Crystal dissolution kinetics and Gibbs free energy / A. Luttge // *Journal of Electron Spectroscopy and Related Phenomena*. – 2006. – V. 150. – P. 248–259.
118. **Madras, G.** Reversible crystal growth–dissolution and aggregation–breakage: numerical and moment solutions for population balance equations / G. Madras, B. J. McCoy // *Powder Technology*. – 2004. – №(143-144). – P. 297 – 307.
119. **Malkin, A. J.** Atomic force microscopy studies of surface morphology and growth kinetics in thaumatin crystallization / A. J. Malkin, Yu. G. Kuznetsov, W. Glantz [et al.] // *J. Phys. Chem.* – 1996. – V. 100, №28. – P. 11736–11743.
120. **Malkin, A. J.** Viral capsomer structure, surface processes and growth kinetics in the crystallization of macromolecular crystals visualized by in-situ atomic

force microscopy / A. J. Malkin, Yu. G. Kuznetsov, A. McPherson // *J. of Crystal Growth*. – 2001. – V. 232. – P. 173–183.

121. **McPherson, A.** Macromolecular crystal growth as revealed by atomic force microscopy / A. McPherson, Yu. G. Kuznetsov, A. Malkin [et al.] // *Journal of Structural Biology*. – 2003. – V. 142. – P. 32–46.

122. **McPherson, A.** Mechanisms, kinetics, impurities and defects: consequences in macromolecular crystallization / A. McPherson, Y. G. Kuznetsov // *Acta Crystallogr F Struct Biol Commun*. – 2014. – V. 70, №4. – P. 384–403.

123. **Miyata, K.** Atomic-scale structures and dynamics at the growing calcite step edge investigated by high-speed frequency modulation atomic force microscopy / K. Miyata, Y. Kawagoe, N. Miyashita [et al.] // *Faraday Discuss*. – 2022. – V. 235. – P. 551–561.

124. **Nakada, T.** Direct AFM observations of impurity effects on a lysozyme crystal / T. Nakada, G. Sazaki, S. Miyashita [et al.] // *J. Cryst. Growth*. – 1999. – V. 196. – P. 503–510.

125. **Nakano, K.** Direct visualization of kinetic reversibility of crystallization and dissolution behavior at solution growth interface of SiC in Si-Cr solvent / K. Nakano, S. Maruyama, T. Kato [et al.] // *Surfaces and Interfaces*. – 2022. – V. 8. – P. 101664.

126. **Nelea, V.** Mechanisms of interaction of biomolecule phosphate side chains with calcite during dissolution / V. Nelea, J. Paquette, M. D. McKee // *Crystal Growth & Design*. – 2021. – V. 21, №5. – P. 2898–2910.

127. **Neuroth, G.** The generation of growth dislocations by inclusions and growth-face damages: an experimental study / G. Neuroth, H. Klapper // *Crystal Research and Technology*. – 2020. – V. 55, №2. – P. 1900159 (5).

128. **Ng, J. D.** Visualization of RNA crystal growth by atomic force microscopy / J. D. Ng, Y. Kuznetsov, A. J. Malkin [et al.] // *Nucleic Acids Research*. – 1997. – V. 25, №9. – P. 2582–2588

129. **Neugebauer, P.** Crystal shape modification via cycles of growth and dissolution in a tubular crystallizer / P. Neugebauer, J. Cardona, M. O. Besenhard, // *Crystal Growth & Design*. – 2018. – V. 18, №8. – P. 4403–4415.
130. **Pambudi, F.** Crystal growth of the core and rotated epitaxial shell of a heterometallic metal-organic framework revealed with atomic force microscopy / F. Pambudi, M. W. Anderson, M. P. Attfield // *Faraday Discussions*. – 2021. – P. 231.
131. **Pastero, L.** Morphology of calcite (CaCO_3) crystals growing from aqueous solutions in the presence of Li^+ ions. surface behavior of the {0001} Form / L. Pastero, E. Costa, M. Bruno [et al.] // *Cryst. Growth Des.* – 2004. – V. 4. – P. 485–490.
132. **Perovskii, I. A.** Nanosize morphological characteristics of synthetic powders obtained using the products of leucoxene reprocessing / I. A. Perovskii, N. N. Piskunova // *Glass and Ceramics*. – 2017. – V. 74, №(3–4). – P. 118–122.
133. **Pers, J.** AFM studies of pits formation on KBr (100) during its dissolution by water / J. Pers, B. Barwinski, M. Grodzicki [et al.] // *Materials Science-Poland*. – 2016. – V. 34, №4. – P. 863–86.
134. **Pina, C.** Molecular- scale mechanisms of crystal growth in barite / C. Pina, U. Becker, P. Risthaus [et al.] // *Letters to nature*. – 1998a, – P. 483–486.
135. **Pina, C.** Microtopography of the barite (001) face during growth: AFM observations and PBC theory / C. Pina, D. Bosbach, M. Prieto [et al.] // *J. of Crystal Growth*. – 1998b. – V. 187. – P. 119–125.
136. **Pina, C. M.** Nanoscale dissolution and growth on anhydrite cleavage faces / C. M. Pina // *Geochimica et Cosmochimica Acta*. – 2009. – V. 73, №23. – P. 7034–7044.
137. **Piskunova, N. N.** Statistical analysis of dynamics of elementary processes on the surface of the growing crystal (by the AFM data) / N. N. Piskunova, V. I. Rakin // *Journal of Crystal Growth*. – 2005. – V. 275. №(1-2). – P. 1661–1664
138. **Piskunova, N. N.** AFM-observation of elementary processes of crystal growth from solution / N. N. Piskunova, A. M. Askhabov // *Journal of Optoelectronics and advanced materials*. – 2007. – V. 9, № 5. – P. 1290–1293.

139. **Piskunova, N. N.** AFM study of instability of growing crystal surface morphology // N. N. Piskunova // *Functional Materials*. – 2010. – V. 17. № 2. – P. 196–200.
140. **Piskunova, N. N.** Combining In Situ and Ex Situ Atomic-Force Microscopy Studies to Reconstruct Natural Crystallogenic Processes / N.N. Piskunova, V. Sokerina, L. Y. Kruchkova // In : *Atomic force microscopy principles, developments and applications*. Bessie Moss and Clayton Stone (Eds). – New York : Nova Science Publishers, Inc.– ISBN: 978-1-53613-496-4. – 2018 a. – P. 47–66.
141. **Piskunova, N. N.** The Role of Defects in Crystal Dissolution Processes (AFM Data) / N.N. Piskunova // In : *Atomic force microscopy principles, developments and applications*. Bessie Moss and Clayton Stone (Eds). – New York : Nova Science Publishers, Inc.– ISBN: 978-1-53613-496-4. – 2018 b. – P. 101–116.
142. **Piskunova, N. N.** The effect of nanoindentation on crystal growth rate fluctuations investigated by in-situ atomic force microscopy // N. N. Piskunova// *Journal of Crystal Growth*. – 2021. – V. 575. –126359
143. **Piskunova, N. N.** Nanoscale crystal growth processes triggered by captured solid impurity particles // N. N. Piskunova// *Journal of Crystal Growth*. – 2023 b. – V. 603. – 127013.
144. **Piskunova, N. N.** Non-reversibility of crystal growth and Dissolution: Nanoscale direct observations and kinetics of transition through the saturation point // N. N. Piskunova // *Journal of Crystal Growth*. – 2024 b. –V. 631. –127614.
145. **Piskunova, N. N.** Study of the Effects of Different Factors on Crystal Growth from Solution: Data of Atomic Force Microscopy / N. N. Piskunova // *Geochemistry International*. – 2024 a. – V. 62, №. 6. – P. 634–646.
146. **Poornachary, S. K.** Impurity effects on the growth of molecular crystals: experiments and modeling / S. K. Poornachary, P. S. Chow, R. B. H. Tan // *Adv. Powder Technol.* – 2008. – V. 19. – P. 459–473.
147. **Pramanick, A. K.** Near-grain-boundary characterization by atomic force microscopy / A. K. Pramanick, A. Sinha, G. V. S. Sastry [et al.]// *Ultramicroscopy*. – 2009. – V. 109, №6. – P. 741–747.

148. **Putnis, C. V.** Crystallization via nonclassical pathways : nanoscale imaging of mineral surfaces crystallization via nonclassical pathways volume 2 : aggregation, biomineralization / C. V. Putnis, L. Wang, E. Ruiz-Agudo [et al.] // *Imaging & Application ACS Symposium Series*. – Washington : American Chemical Society. – DC. – 2021.
149. **Qi, H.** Mechanism of solid/liquid interfacial reactions. The Maleic Acid Driven Dissolution of Calcite: An Atomic Force Microscopy Study under Defined Hydrodynamic Conditions / H. Qi, M. F. Suarez, B. A. Coles [et al.] // *J. Phys. Chem. B*. – 1997. – V. 101. – P. 5557–5564.
150. **Rashkovich, L. N.** Influence of Fe^{3+} and Al^{3+} ions on the kinetics of steps on the {100} faces of KDP / L. N. Rashkovich, N. V. Kronsky // *J. of Crystal Growth*. – 1997. – V. 182. – P. 434–441.
151. **Rashkovich, L.N.** The mechanism of step motion in growth of lysozyme crystals / L. N. Rashkovich , N. V. Gvozdev , I. V. Yaminsky // *Crystallography Reports*. – 1998. – V. 43, №4. – P. 696–700.
152. **Rashkovich, L.N.** In-situ atomic force microscopy of layer-by-layer crystal growth and key growth concepts / L. N. Rashkovich , J. J. De Yoreo , C. A. Orme [et al.] // *Crystallography Reports*. – 2006. – V. 51, №6. – P. 1063–1074.
153. **Rekhviashvili, S. Sh.** On the thermodynamics of contact interaction in an atomic force microscope / S. Sh. Rekhviashvili // *Tech. Phys.* – 2001. – V. 46. – P. 1335–1338.
154. **Rimer, J. D.** Crystal growth inhibitors for the prevention of L-cystine kidney stones through molecular design / J. D. Rimer, Z. An, Z. Zhu [et al.] // *Science*. – 2010. – V. 330. – P. 337–341.
155. **Ristic, R. I.** The influence of tensile strain on the growth of crystals of potash alum and sodium nitrate / R. I. Ristic, J. N. Sherwood, T. Shripathi // *Journal of Crystal Growth*. – 1997. – V. 179, №(1-2). – P. 194–204.
156. **Rivzi, A. K.** Nucleation, growth and dissolution of faceted single crystals / A. K. Rivzi // *Doctoral thesis, EngD Chemical Engineering*. – Newcastle : Newcastle University. – 2020. <http://theses.ncl.ac.uk/jspui/handle/10443/5175>.

157. **Rudoï, Y. G.** Thermodynamic fluctuations within the gibbs and einstein approaches / Y. G. Rudoï, A. D. Sukhanov // *Phys. Usp.* – 2000. – V. 12, №43. – P. 1169–1199.
158. **Rusli, I. T.** Raman spectroscopic study of NaNO_3 solution system - solute clustering in supersaturated solutions / I. T. Rusli, G. L. Schrader, M. A. Larson // *J. Cryst. Growth.* – 1989. – V. 97, №2. – P. 345–351.
159. **Samaee, V.** Deciphering the interactions between single arm dislocation sources and coherent twin boundary in nickel bi-crystal / V. Samaee, V. Dupraz, N. Pardoën [et al.] // *Nature Communications.* – 2021. – V. 12. – 962.
160. **Sangwal, K.** Etching of Crystals: Theory, Experimental and Application / K. Sangwal // – Amsterdam : North-Holland. – 1987. – 283 p.
161. **Shen, Z.** Free energy landscape of the dissolution of gibbsite at high pH / Z. Shen, S. N. Kerisit, A. G. Stack [et al.] // *The Journal of Physical Chemistry Letters.* – 2018. – V. 9, №7. – P. 1809–1814.
162. **Schott, J.** Can accurate kinetic laws be created to describe chemical weathering? *Comptes Rendus* / J. Schott, E. H. Oelkers, P. Bénézech [et al.] // *Géoscience.* – 2012. V. 344, №(11, 12). – P. 568–585.
163. **Shindo, H.** Atomic force microscopic observation of surface processes on salts in humid air / Shindo H., Seo A., Ohashi M. [et al.] // *Proceeding of 8th World Salt Symposium.* – Haaha. – 2000. – V. 2. – P. 719–724.
164. **Shluger, A. L.** Theoretical and experimental investigation of force imaging at the atomic scale on alkali halide crystals / A. L. Shluger, R. M. Wilson, R. T. Williams // *Phys. Rev. B.* – 1994. – V. 49, №7. – P. 4915–4930.
165. **Shöâèè, M.** Crystal form, defects and growth of the metal organic framework HKUST-1 revealed by atomic force microscopy / M. Shöâèè, J. R. Agger, M. W. Anderson [et al.] // *CrystEngComm.* – 2008. – V. 10, №6. – P. 646–.
166. **Shtukenberg, A. G.** Disrupting crystal growth through molecular recognition: designer therapies for kidney stone prevention / A. G. Shtukenberg, L. Hu, A. Sahota [et al.] // *Acc Chem Res.* – 2022. – V.55, №4. – P. 516–525.

167. **Silaev, V. I.** New potentially industrial type of indium sulfide –manganese ore / V. I. Silaev, A. V. Kokin, D. V. Kiseleva, N. N. Piskunova [et al.] // Chapter in Book «Indium. Properties, Technological Applications and Health Issues». – ISBN: 978-1-62257-700-2. – Woo, Choi (Eds.). – New York : Nova Science Publishers, Inc. – 2013. – P. 261–272.
168. **Smolski, I. L.** In-situ X-ray topography for investigation of the ADP crystal growth kinetics / I. L. Smolski, A. A. Chernov, V. F. Parvov [et al.] // Abstracts Second European Conference on crystal growth. – Lancaster. – 1979. – P. 31.
169. **Snyder, R. C.** Manipulation of crystal shape by cycles of growth and dissolution / R. C. Snyder, S. Studener, M. F. Doherty // American Institute of Chemical Engineers Journal. – 2007. – V. 53, №6. –P. 1510–1517.
170. **Söngen, H.** Quantitative atomic force microscopy / H. Söngen, R. Bechstein, A. Kühnle // Journal of Physics Condensed Matter. – 2017. – V. 29, №27. – 274001.
171. **Sours, R. E.** An in-situ Atomic force microscopy study of uric acid crystal growth / R. E. Sours, A. Z. Zellelow, J. A. Swift // The Journal of Physical Chemistry B. – 2005. – V. 109, №20. – P. 9989–9995.
172. **Stack, A. G.** Accurate rates of the complex mechanisms for growth and dissolution of minerals using a combination of rare-event theories / A. G. Stack, P. Raiteri, J. D. Gale // Journal of the American Chemical Society. –2012. – V. 134, №1. – P. 11–14.
173. **Stipp, S. L. S.** Calcite surface structure observed at microtopographic and molecular scales with atomic force microscopy (AFM) / S. L. S. Stipp, C. M. Eggleston, B. S. Nielsen // Geochimica et Cosmochimica Acta. – 1994. – V. 58, №14. – P. 3023–3033.
174. **Teng, H. H.** Thermodynamics of calcite growth: baseline for understanding biomineral formation / H. Teng, P. Dove, C. Orme [et al.] // Science. – 1998. –V. 282. – P.724–727.

175. **Teng, H. H.** Controls by saturation state on etch pit formation during calcite dissolution / H. H. Teng // *Geochimica et Cosmochimica Acta*. – 2004. – V. 68, №2. – P. 253–262.
176. **Tilbury, C. J.** enhancing mechanistic crystal growth models / C. J. Tilbury, // PhD thesis in Chemical Engineering. – Santa Barbara : University of California. – 2017. https://escholarship.org/content/qt9n15495g/qt9n15495g_noSplash_4edf78f25bcb0b79767ab1fb77b8f74.pdf.
177. **Thürmer, K.** Onset of step antibanding instability due to surface electromigration / K. Thürmer, D. J. Liu, E. D. Williams [et al.] // *Phys. Rev. Lett.* – 1999. – V. 83, №26. – P. 5531–5534.
178. **Thürmer, K.** Formation of hexagonal and cubic ice during low-temperature growth / K. Thürmer, S. Nie // *Proceedings of the National Academy of Sciences*. – 2013. – V. 110, №29. – P. 11757–11762.
179. **Van der Putte, P.** Surface morphology of HCl etched silicon wafers: II. Bunch formation / P. Van der Putte, W. J. P. van Enkevort, L. J. Giling [et al.] // *J. Cryst. Growth*. – 1978. – V. 43, №6. – P. 659–675.
180. **Van Driessche, A. E. S.** Cluster-mediated stop-and-go crystallization / A. E. S. Van Driessche, J. Lutsko, D. Maes [et al.] // *Journal of Crystal Growth*. – 2023. – V. 603. – P. 127024.
181. **Vavouraki, A. I.** Crystal growth and dissolution of calcite in the presence of fluoride ions: an atomic force microscopy study / A. I. Vavouraki, C. V. Putnis, A. Putnis [et al.] // *Crystal Growth & Design*. – 2010. – V. 10, №1. – P. 60–69.
182. **Vegge, T.** Atomistic simulations of dislocation processes in copper / T. Vegge, K. W. Jacobsen // *J. Phys.: Condens. Matter*. – 2002. – V. 14, №11. P. – 2929–2956.
183. **Vekilov, P. G.** Dynamics of layer growth in protein crystallization / P. G. Vekilov, J. I. D. Alexander // *Chem. Rev.* – 2000. – V. 100. – P. 2061–2089.
184. **Viti, C.** Transmission electron microscopy applied to fluid inclusion investigations / C. Viti, M.-L. Frezzotti // *Lithos*. – 2001. – V. 55, №(1-4). – P. 125–138.

185. **Voloshin, A. E.** Morphological effects in liquid phase epitaxy (the $C_8H_5O_4K-C_8H_5O_4Rb-H_2O$ system) / A. E. Voloshin, A. E. Glikin, S. I. Kovalev, E. B. Rudneva [et al.] // *Crystallography Report.* – 2003. – V. 48. – P. 1064–1075.
186. **Waizumi, K.** Atomic force microscopy studies on growing surfaces of bovine insulin crystals / K. Waizumi, M. Plomp, W. van Enkevort // *Colloids and Surfaces B : Biointerfaces.* – 2003. – V. 30. – 73/86.
187. **Wang, L.** Direct observations of the modification of calcite growth morphology by Li^+ through selectively stabilizing an energetically unfavourable face / L. Wang, E. Ruiz-Agudo, C. V. Putnis [et al.] // *CrystEngComm.* – 2011. – V.13, №12. – P. 3962–3966.
188. **Woensdregt, C. F.** Ex-situ scanning force microscopic observation of growth and dissolution phenomena on $\{010\}$ surfaces of potassium hydrogen phthalate crystals (KAP) caused by isomorphic exchange reactions / C. F. Woensdregt, A. E. Glikin // *J. Cryst. Growth.* – 2005. – V. 283, №(3–4). – P. 523–532.
189. **Xu, M.** Dissolution kinetics of calcite at 50–70°C: An atomic force microscopic study under near-equilibrium conditions / M. Xu, X. Hu, K. G. Knauss [et al.] // *Geochimica and Cosmochimica Acta.* – 2010. – V. 74, №15. – P. 4285–4297.
190. **Yaminsky, I. V.** Atomic force microscopy study of lysozyme crystallization / I. V. Yaminsky, N. V. Gvozdev, M. I. Sil'nikova [et al.] // *Crystallography Reports.* – 2002. – V. 47. – P. S149–S158.
191. **Yau, S.-T.** Molecular Mechanisms of crystallization and defect formation / S.-T. Yau, B. R. Thomas, P. G. Vekilov // *Physical Review Letters.* – 2000. – V. 85, №2. – P.353-6.
192. **Yanagiya, S.** Joint operation of atomic force microscope and advanced laser confocal microscope for observing surface processes in a protein crystal / S. Yanagiya, N. Goto // *J. of Surface Engineered Materials and Advanced Technology.* – 2012. – V. 2. – P. 210–214.
193. **Zaitseva, N.** Growth mechanisms of large, faceted crystals grown from solutions / N. Zaitseva, L. Carman, H. Klapper // *Journal of Crystal Growth.* – 2022. – V. 597. – 126841.

194. **Zareeipolgardani, B.** Tuning biotic and abiotic calcite growth by stress / B. Zareeipolgardani, A. Piednoir, J. Colombani // *Crystal Growth & Design*. – 2019. – V. 19. – P. 5923–5928.
195. **Zhang, R.** Steady-state crystal nucleation rate of polyamide 66 by combining atomic force microscopy and fast-scanning chip calorimetry / R. Zhang, E. Zhuravlev, J. W. P. Schmelzer [et al.] // *Macromolecules*. – 2020. – V. 13. – 202053.
196. **Zhong, X.** Screw Dislocation generation by inclusions in molecular crystals / X. Zhong, A. G. Shtukenberg, T. Hueckel [et al.] // *Crystal Growth & Design*. – 2018. – V.18, №1. – P. 318–323.
197. **Zhong, X.** Dislocation generation by microparticle inclusions / X. Zhong, A. G. Shtukenberg, M. Liu [et al.] // *Cryst. Growth & Des.* – 2019. – V. 19, №11. – P. 6649–6655.
198. **Zhu, T.** Predictive modeling of nanoindentation-induced homogeneous dislocation nucleation in copper / T. Zhu, J. Lib, K. J. Van Vliet [et al.] // *J. Mech. Phys. Solids*. – 2004. – V. 52. –P. 691–724.
199. **Zikic, A. M. N.** An instrument for in-situ growth rate characterization of mechanically strained crystals / A. M. Zikic, R. I. Ristic, J. N. Sherwood // *Review of Scientific Instruments*. – 1998. – V.69, №7. –P. 2713–2719.